# Surface engineering of bio-based polymeric nanofilms for biomedical applications

Muhammad Haseeb Iqbal

# UNIVERSITÉ DE STRASBOURG

*ÉCOLE DOCTORALE PHYSIQUE ET CHIMIE-PHYSIQUE*

**Institut Charles Sadron, CNRS UPR22**

# THÈSE

présentée par :

**Muhammad Haseeb IQBAL**

soutenue le : **29 Septembre 2021**

pour obtenir le grade de : **Docteur de l'université de Strasbourg**

Discipline/ Spécialité : Science et Ingénierie des Polymères

# Surface Engineering of Bio-based Polymeric Nanofilms for Biomedical Applications

**THÈSE dirigée par :**

**Mme BOULMEDAIS Fouzia** Directrice de recherche CNRS, Université de Strasbourg, France

**RAPPORTEURS :**

**Mme GLINEL Karine** Professeure, Université Catholique de Louvain, Louvain-La-Neuve

**Mme MONGE Claire** Chargée de recherche CNRS, Université de Lyon, France

---

**AUTRES MEMBRES DU JURY :**

**M MEYER Florent** Professeur, Université de Strasbourg, France

Dedicated to my PhD mentor, friends, siblings, and parents, especially my father, a person I will always aspire to be.

# Acknowledgements

My PhD research journey would not have been possible without the support and guidance of many people. Among them, only a few are given a special mention here.

First of all, I would like to extend my gratitude to my thesis supervisor, Dr. Fouzia Boulmedais, for her continuous support and invaluable mentorship. Though there was a rough period during my second year, but thanks to her guidance and problem-solving skills, I managed to solve the research related issue. I want to thank her for her support and optimism throughout my PhD. She gave me complete freedom to do the research, meanwhile being very available and with lots of pertinent ideas. Sometimes I used to wonder, perhaps even now, about how promptly she was able to transform raw ideas into a well-structured scientific plan, and to propose solutions. She has always been thoughtful to find opportunities that I can benefit from e.g., to enrich my skills, to interact with scientific community by attending conferences etc. Thanks to her knowledge and scientific network, I have been in contact with many people in different labs and discovered various techniques in the field of biomaterials.

It was mainly due to a huge contribution from Prof. Florent Meyer, professor at faculty of medicine Strasbourg, that I was able to cherish the adventures of interdisciplinary research. In context of a collaboration, he co-supervised my PhD work and helped me get trained on cell biology. Despite of his busy schedule, he always finds time to follow-up my work. I always enjoyed our long discussions with his insightful inputs. I found him passionate about the research with a critical approach. Here, I would like to highlight the role of Christine Affolter-Zbaraszczuk, project engineer at INSERM UMR1121, with whom I have had cell biology trainings with. She has been kind and friendly, and I thank her for letting me share a lab with her. Please accept my sincere gratitude!

Many people have contributed to the individual projects of the work. At INSERM UMR1121, Dr. Philippe Lavelle is greatly acknowledged for his help in AFM, his fruitful discussions, and suggestions regarding my research work, and giving me the opportunity to deliver lectures at the faculty of medicine in Strasbourg. A big thanks goes to Dr. Bernard Senger and Prof. Vincent Ball for the valuable contributions towards physico-chemical aspects of my work. Thanks to Dominique VAUTIER for his help with fluorescence microscopy and cell culture. I would like thank Dr. Varvara Gribova for her help and guidance in the work with human myoblasts. I would like to express my gratitude to Dr. Morgane Rabineau for her help with confocal microscopy and AFM. A big thank you for the AFM probes! Thanks to Eric Mathieu for providing training on SEM and metallizer. Of course, I thank my office colleagues; Cynthia Calligaro, Lorène Tallet and Manon Allais, for their consistent help and discussions. Also, I would like to thank Dr. Nihal Engin Vrana and Prof. Pierre Schaaf for welcoming me at INSERM.

At Institut Charles Sadron, I would like to express my gratitude to André Schroder for his big help Isothermal Titration Calorimetry training and data analysis. A sincere thanks to Mélanie Legros for providing trainings at the spectroscopy platforms at ICS. I would like to thank Dr. Miryam Craido Gonzalez for showing me the use of QCM, Dr. Lionel Lopez for training me on AFM which has been of great use during my PhD work, and Dr. Jennifer Rodon Fores for her help with my training for infrared spectroscopy. My special thanks to my friends and colleagues at ICS and INSERM (including alumni), I do not want to mention single names to avoid forgetting to mention someone. I have enjoyed working with all of you over the years, as you created a wonderful environment. Please feel included in this acknowledgement as we had plenty of activities together like coffee breaks, lunches, dinners, games, city tours, Europa Park tour, seminars, group meetings, movies, and so on.

I want to thank the internship students Faratiana Jeanne Rosine Revana, Emeline Pradel, Titikpina Marzukh, and Lisa Marchadier for their contributions towards the advance of my PhD work. It was my pleasure to host you at ICS.

My sincere gratitude to our collaborators outside Strasbourg; Halima Kerdjoudj from BIOS Reims, Christian Njel from KIT Karlsruhe, Laurent Heux from CERMAV Grenoble, Gregory Francius from LCPME Nancy, Vincent Mouly and Catherine Coirault from Myology Institute Paris.

I extend many thanks to all the IMI team at Charles Sadron Institute and the INSERM UMR1121 team for my very good integration and for the pleasant and fulfilling work environment. I thank them all for the support throughout the experimental work, the very rewarding conversations about different projects and techniques.

Thanks to my sister, Noor-ul-ain, for her support especially during her one year stay in Strasbourg. Many thanks to my family for supporting me in many different ways over these years. I can always rely on you.

Lastly, Higher Education Commission (HEC) Pakistan is acknowledged for financial support and Campus France for administrative help to make my stay in France easier.

Direction de la **recherche**
et de la **valorisation**
Collège **doctoral**
Université de Strasbourg

# Déclaration sur l'honneur
# *Declaration of Honour*

J'affirme être informé que le plagiat est une faute grave susceptible de mener à des sanctions administratives et disciplinaires pouvant aller jusqu'au renvoi de l'Université de Strasbourg et passible de poursuites devant les tribunaux de la République Française.

Je suis conscient(e) que l'absence de citation claire et transparente d'une source empruntée à un tiers (texte, idée, raisonnement ou autre création) est constitutive de plagiat.

Au vu de ce qui précède, **j'atteste sur l'honneur que le travail décrit dans mon manuscrit de thèse est un travail original et que je n'ai pas eu recours au plagiat ou à toute autre forme de fraude.**

*I affirm that I am aware that plagiarism is a serious misconduct that may lead to administrative and disciplinary sanctions up to dismissal from the University of Strasbourg and liable to prosecution in the courts of the French Republic.*

*I am aware that the absence of a clear and transparent citation of a source borrowed from a third party (text, idea, reasoning or other creation) is constitutive of plagiarism.*

*In view of the foregoing,* ***I hereby certify that the work described in my thesis manuscript is original work and that I have not resorted to plagiarism or any other form of fraud.***

**Nom : Prénom :** IQBAL Muhammad Haseeb

**Ecole doctorale :** École Doctorale Physique et Chimie-Physique (ED 182)

**Laboratoire :** Institut Charles Sadron, CNRS UPR22

**Date :** 29/09/2021

# Table of Contents

# List of abbreviations

**A**

| | |
|---|---|
| AFM | Atomic force microscopy |
| Alg | Alginate |
| ATR | Attenuated total reflection |

**B**

| | |
|---|---|
| BSA | Bovine serum albumin |

**C**

| | |
|---|---|
| CD | Circular dichroism |
| CNC | Chitin nanocrystal |
| CFU | Colony forming unit |
| CHI | Chitosan |
| CLSM | Confocal laser scanning microscopy |
| Cyd | Cyclodextrin |

**D**

| | |
|---|---|
| DMEM | Dulbecco's Modified Eagle Medium |
| DAPI | 4,6-diamidino-2-phenylindole |
| DM | Differentiation medium |

**E**

| | |
|---|---|
| *E. coli* | *Escherichia coli* |
| EDTA | Ethylenediaminetetraacetic acid |
| EGCG | Epigallocatechin gallate |
| ECM | Extracellular matrix |

**F**

| | |
|---|---|
| Fe(III) | Ferric ion |
| FTIR | Fourier-transform infrared spectroscopy |
| FITC | Fluorescein isothiocyanate |
| FBS | Fetal bovine serum |

**G**

| | |
|---|---|
| GM | Growth medium |

**H**

| | |
|---|---|
| HA | Hyaluronic acid |
| HEP | Heparin |

| | |
|---|---|
| HEPES | 4-(2-hydroxyethyl)-1-piperazineethanesulfonic acid |
| HSA | Human serum albumin |
| HCl | Hydrochloric acid |
| HGFs | Human gingival fibroblasts |
| HMDS | Hexamethyldisilazane |

**I**

| | |
|---|---|
| ITC | Isothermal titration calorimetry |

**L**

| | |
|---|---|
| LbL | Layer-by-layer |
| LB | Lysogeny broth |

**M**

| | |
|---|---|
| MH | Mueller Hinton |
| MIC | Minimal inhibitory concentration |
| MRSA | Methicillin-resistant *Staphylococcus aureus* |

**N**

| | |
|---|---|
| NP | Nanoparticle |
| NaCl | Sodium chloride |
| NaOH | Sodium hydroxide |

**O**

| | |
|---|---|
| OD | Optical density |

**P**

| | |
|---|---|
| PAA | Poly(acrylic acid) |
| PAAm | Polyacrylamide |
| PAH | Poly(allylamine hydrochloride) |
| PBS | Phosphate buffered saline |
| PDA | Polydopamine |
| PDADMAC | Poly(diallyl dimethyl ammonium chloride) |
| PEG | Poly(ethylene glycol) |
| PEI | Polyethylenimine |
| PFA | Paraformaldehyde |
| PGA | Poly(L-glutamic acid) |
| PLL | Poly(L-lysine) |
| PAR | poly(L-arginine) |
| PLGA | Poly lactic-co-glycolic acid |
| PMMA | Poly(methacrylic acid) |
| PSS | Poly(styrene sulfonate) |
| PVAm | Poly(vinylamine) |

**Q**

| | |
|---|---|
| QCM | Quartz crystal microbalance |
| QCM-D | Quartz crystal microbalance with dissipation monitoring |
| QAC | Quaternary ammonium compounds |

**R**

| | |
|---|---|
| RPMI | Roswell Park Memorial Institute medium |

**S**

| | |
|---|---|
| *S. aureus* | *Staphylococcus aureus* |
| SAM | Self-assembled monolayer |
| SEM | Scanning electron microscopy |

**T**

| | |
|---|---|
| TA | Tannic acid |

**X**

| | |
|---|---|
| XPS | X-ray photoelectron spectroscopy |

# Résumé de thèse

## Introduction

Selon la définition convenue lors de la conférence de la Société Européenne des Biomatériaux en 1986, les biomatériaux sont des matériaux non viables utilisés dans un dispositif médical pour le diagnostic, la guérison, le traitement ou la prévention des maladies. Il peut s'agir de dispositifs implantés ou extracorporels (système respiratoire artificiel, dialyse...). Lorsque la pose d'un biomatériau n'est pas suffisante, l'ingénierie tissulaire permet de régénérer le tissu lésé en offrant une matrice tridimensionnelle aux cellules du patient. Trois propriétés fondamentales du biomatériau doivent être maitrisées : la biocompatibilité, la biointégration qui est l'aptitude d'un matériau à être colonisé par les cellules vivantes spécifiques ainsi que la limitation de la prolifération bactérienne.

## Objectifs de la thèse

En collaboration avec l'UMR 1121 INSERM (Strasbourg), mon travail de thèse s'est intéressé au développement de différents revêtements de biopolymères (polymères naturels) possédant des propriétés antibactériennes ou capable d'orienter et de différencier les cellules souches musculaires (myoblastes) dans le contexte de l'ingénierie musculaire. Les propriétés antibactériennes ont été évaluées sur *Staphylococcus aureus*, une bactérie virulente à Gram positif connue pour causer des infections nosocomiales liées à des dispositifs médicaux et sur *Escherichia coli*, une bactérie à Gram négatif qui est la plus fréquemment associée aux cathéters.

Ce travail de thèse est divisé en cinq chapitres.

Dans le chapitre 1, différentes techniques de fonctionnalisation de surface sont décrites en particulier les assemblages couche par couche (en anglais layer-by-layer, LbL) de protéines et leurs applications biomédicales.

Le chapitre 2 présente les produits et les méthodes utilisés dans l'ensemble de la thèse.

Le chapitre 3 décrit de manière complète l'assemblage LbL de collagène et d'acide tannique (TA/COL) aussi bien ses propriétés physico-chimiques que biologiques. Grâce à leur capacité à interagir avec les protéines via des liaisons hydrogène, les films LbL TA/COL ont été construits dans des tampons acétate ou citrate à pH 4. De façon surprenante, le tampon utilisé a un impact non seulement sur les propriétés physicochimiques mais aussi sur les propriétés antibactériennes des films. La topographie des films est différente avec une structure granulaire pour les films construits dans le tampon citrate et fibrillaire pour ceux construits dans le tampon acétate. Au contact d'une solution physiologique (0.15 M NaCl, pH 7.4), les deux types de films TA/COL libèrent une quantité comparable de TA en solution mais seules les films construits dans du tampon citrate ont montré un effet antibactérien contre *Staphylococcus aureus*. Une étude approfondie de la nature des interactions entre COL et TA et de la composition des films a été mené afin d'expliquer cette différence.

Le chapitre 4 traite du développement de films LbL TA/COL orientés à l'aide d'une méthode rapide et économique de brossage au pinceau. Les fibres de collagène alignées ont la propriété d'orienter les cellules le long de leur axe par guidage par contact. Plusieurs stratégies ont été utilisées pour aligner les fibres de collagène, par exemple la lithographie, l'électrofilage, l'impression 3D, la microfluidique, le flux de cisaillement, le champ magnétique et l'étirement mécanique. Ces techniques ont certaines limites comme la nécessité d'une instrumentation complexe qui peut dénaturer le collagène. Ici, nous avons utilisé la méthode du brossage pour déposer des couches de

collagène orientées avec la délivrance de TA, composé bioactif pour accélérer la différenciation cellulaire. Ces nanofilms s'avèrent être particulièrement intéressants pour l'alignement anisotrope, la migration et la différenciation des cellules myoblastes humaines pour l'ingénierie des tissus musculaires.

Dans le chapitre 5, nous avons exploré la possibilité de remplacer les molécules fibrillaires de COL par des nanocristaux de chitine (CNC) hautement cristallins et rigides pour développer des films LbL TA/CNC. De manière surprenante, les bactéries Staphylococcus aureus et Escherichia coli n'adhèrent pas, ne prolifèrent pas et ne forment pas de biofilms sur les nanofilms orientés contrairement aux nanofilms non-orientés, obtenu par la technique de trempage. L'activité antibactérienne a été associée à la densité de charge positive en surface des nanofilms orientés suffisante pour attirer les bactéries et à la nanotopographie présentant des pointes capables probablement de percer la membrane bactérienne.

Enfin, une conclusion générale de ce travail et quelques perspectives sont données.

## 1. Contexte du travail

### 1.1 Les films LbL de polyélectrolytes

Afin de conférer des propriétés biomédicales aux biomatériaux, l'utilisation de films multicouche de polyélectrolytes offre de grands potentiels. Ces nanofilms, généralement d'une épaisseur d'environ 10 nm à 1 µm, sont construits selon la méthode couche par couche (LbL) basée sur la physisorption (assemblages basés sur des interactions faibles, principalement électrostatiques) de polyanions et de polycations (Figure 1).[1] Le substrat (généralement chargé négativement) est plongé dans une solution de polycations pendant 5 à 20 minutes. Les chaînes de polycations, chargées positivement, s’adsorbent alors à la surface grâce aux interactions électrostatiques. La

surface est ensuite rincée par une solution tampon afin d'éliminer les chaînes de polymère non adsorbées à la surface. La surface est maintenant chargée positivement. Par conséquent, une couche de chaînes de polymères chargées négativement peut être adsorbée par trempage du substrat dans une solution de polyanions suivi par un rinçage. Des cycles consécutifs, alternant l'adsorption de polycations et de polyanions, conduisent à la construction d'un film multicouche de polyélectrolytes. Au cours de la construction du film, sa masse et son épaisseur augmentent avec le nombre de couches. En dehors de la méthode de trempage, les films peuvent être obtenus par pulvérisation,[2] spin coating ou encore par brossage.[3-4]

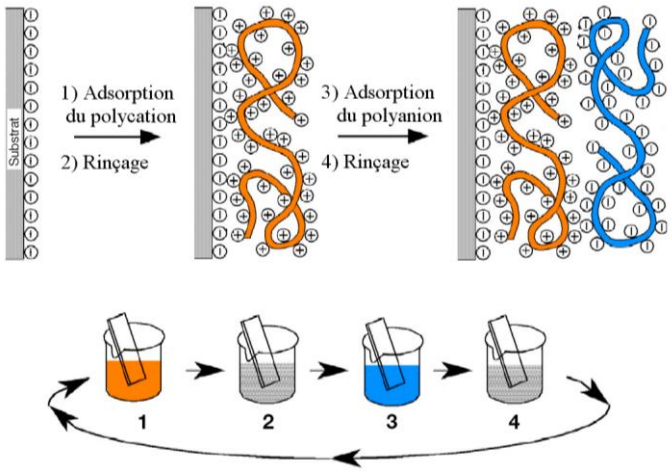


**Figure 1** : Schéma simplifié de la construction de multicouches de polyélectrolytes par adsorptions successives de polycation et de polyanion suivi par un rinçage.[1]

Les forces motrices principales de la construction de ces films multicouches sont les interactions électrostatiques. D'autres types de films ont été développés basés sur des liaisons hydrogènes ou des interactions hydrophobes. Réalisés à partir de solutions aqueuses et à température ambiante, ces films présentent des propriétés ajustables en fonction des conditions physico-chimiques de construction et permettent l'immobilisation de plusieurs (macro)molécules bioactives, tels que les

protéines.[5] Les polymères synthétiques et naturels, les ions ou particules métalliques, les enzymes, les peptides, etc. ont été largement explorés dans l'assemblage des LbL.

### 1.2 Les films LbL à base de protéines et leurs applications

Les protéines principalement utilisées pour développer des films LbL sont le collagène de type-I, la gélatine, la fibronectine, le fibrinogène, l'élastine, la laminine, le lysozyme, la caséine et l'albumine En 2001, un film LbL à base de protéine a été développé en utilisant le collagène de type I (COL), une protéine de la matrice extracellulaire, pour favoriser l'adhésion cellulaire sur les surfaces des biomatériaux. A partir de 2006, l'assemblage LbL de protéines a suscité un énorme intérêt pour le développement de biomatériaux multifonctionnels. Différentes propriétés ont été conférées aux films selon la protéine immobilisée, souvent présente naturellement dans la matrice extracellulaire. Les propriétés antibactériennes ont été obtenues en utilisant la gélatine, le lysozyme ou encore des peptides antimicrobiens. L'adhésion et la différentiation cellulaire ont été assurées par l'immobilisation de COL, gélatine, fibronectine, élastine, ou laminine pour favoriser la vascularisation (cellules endothéliales), la reconstruction osseuse (cellules ostéoblastes) ou neuronale (neurones). Ces films ont également été utilisés afin de délivrer des principes actifs comme des facteurs de croissance, polyphénols ou flavonoïdes pour favoriser la reconstruction osseuse, principalement.

## 2. Films à base de collagène et d'acide tannique aux propriétés antibactériennes

### 2.1 Contexte

L'Organisation Mondiale de la Santé ne cesse d'alerter sur l'émergence et la prolifération de souches microbiennes multi-résistantes aux antibiotiques. En Europe, un patient sur vingt contracte

une infection nosocomiale au cours de son hospitalisation, représentant la sixième cause de décès dans les hôpitaux. Une infection nosocomiale sur deux est liée à la pose d'un biomatériau, engendrant un coût supplémentaire des soins par patient. Le site chirurgical étant la porte d'entrée principale des pathogènes, un traitement antimicrobien administré localement pendant les 6 à 12 h suivant l'opération pourrait prévenir une telle infection. La surface des biomatériaux est le lieu privilégié où se déroulent les interactions avec son environnement biologique. Le défi consiste donc à contrôler ces interactions pour améliorer leur biocompatibilité et leur conférer une bioactivité. Cela peut être réalisé en adaptant les propriétés de surface du biomatériau, notamment par l'application d'un revêtement.

Le collagène (COL), protéine majoritaire de la peau, permet l'adhésion cellulaire sur une surface et favorise la biocompatibilité des films LbL. Le collagène est composé de trois chaînes α qui s'assemblent entre elles grâce à leur structure moléculaire (figure 2a). Les chaînes α sont composées de milliers d'acides aminés basés sur la répétition de la séquence Gly-X-Y, où X et Y sont principalement la proline et la 4-hydroxyproline. La présence de glycine est essentielle à chaque troisième position d'acide aminé pour permettre la formation du tropocollagène à partir des trois chaînes α. Les molécules de tropocollagène s'assemblent en une fibrille de collagène de 10 à 300 nm qui s'agrège pour former la fibre de collagène, dont le diamètre varie de 0,5 à 3 µm. L'acide tannique (TA) est un polyphénol anionique, dérivé des plantes, connu pour son activité antimicrobienne (Figure 2b). Il est connu pour sa capacité à précipiter les protéines en formant des complexes par des liaisons hydrogènes et interactions hydrophobes.[6] Il a été utilisé pour la construction de films LbL avec des enzymes, des protéines et des ions métalliques. Cependant, un seul type de film LbL à base de TA a été décrit comme possédant une propriété antibactérienne intrinsèque sans l'incorporation d'un autre composé antibactérien.

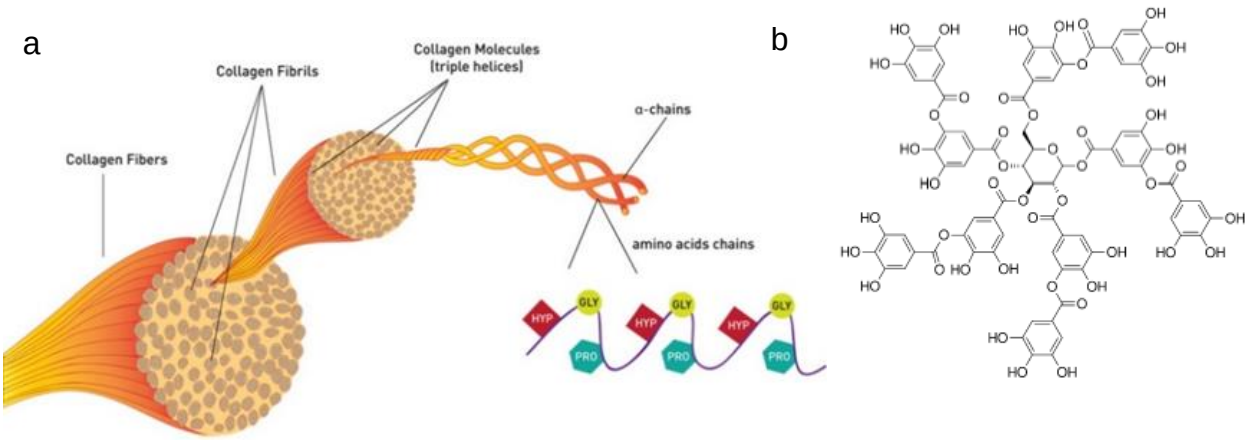


**Figure 2** : (a) Représentation schématique de la structure du collagène : des chaînes d'acides aminés aux fibres et (b) Structure chimique de l'acide tannique.

## 2.2 Résultats

Nous avons ainsi étudié la construction et les propriétés des films COL/TA afin d'obtenir des propriétés antibactériennes. Due à la solubilité limitée du collagène, la construction des films $(COL/TA)_n$ (*n :* le nombre de bicouche déposée), a été réalisée à pH 4 en utilisant deux tampons acétate de sodium et citrate de sodium. La construction du film COL/TA-acétate est meilleure atteignant 7 paires de couches une épaisseur de 300 nm contre 50 nm pour COL/TA-citrate (Figure 3a). La topographie de COL/TA-acétate est fibrillaire et celle de COL/TA-citrate granulaire (Figure 3b). Lorsque les films sont mis au contact d'un milieu à pH physiologique (pH 7.4), ils perdent 10% de leurs épaisseurs avec une libération de TA (Figure 3c). Les films citrates libèrent plus de TA que les films acétates. Ceci a été expliqué par l'incorporation plus élevée de TA dans le cas de la construction réalisée dans le tampon citrate par rapport à l'acétate. TA interagit avec COL via des sites supplémentaires en présence de citrate. Lorsqu'on compare les films $(COL/TA)_6$-COL-citrate et $(COL/TA)_7$-acetate, la quantité de TA libérée dans le milieu est

similaire atteignant 7 µg/mL après 72 h. Cependant, les films construits dans citrate sont antimicrobiens mais pas ceux construit dans l'acide acétique (Figure 3d). Sachant que la concentration minimale inhibitrice de TA en solution est de plus 100 µg/mL, la topographie granulaire des films COL/TA construit dans le tampon citrate permet une libération localisée de TA induisant un effet bactéricide efficace.

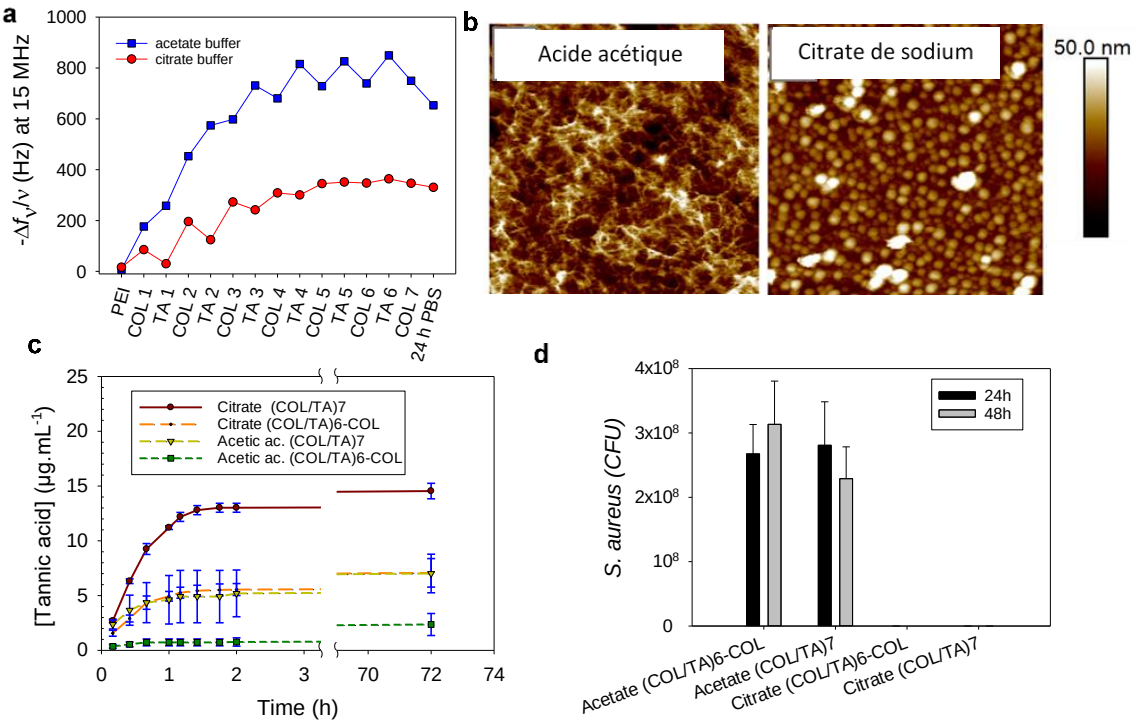


**Figure 3** : Propriétés des films multicouches COL/TA construit à pH 4 dans le tampon acide acétique et citrate, obtenus par la méthode de trempage (a) Evolution de la fréquence, mesurée en QCM, en fonction de la couche adsorbée. En première approximation, la fréquence est proportionnelle à la masse adsorbée (b) Images AFM, obtenues en mode contact et en phase liquide, des films $(COL/TA)_2$, (c) Profil de libération de l'acide tannique au cours du temps des films en milieu physiologique à 37°C et (d) Activité antimicrobienne des films contre *Staphylococcus aureus*.

Les deux types de films LbL n'ont montré aucune cytotoxicité envers les fibroblastes gingivaux humains, ce qui est crucial pour assurer la bio-intégration des biomatériaux implantés. Ce travail a été publié dans *ACS Applied Materials and Interfaces.*

## 3. Films de collagène/acide tannique pour l'orientation de myoblastes

### 3.1 Contexte

Les tissus musculo-squelettiques sont l'un des composants les plus importants du corps humain et représentent environ 40% de la masse corporelle adulte. Contenant des milliers de fibres musculaires regroupées en une organisation parallèle alignée, leur rôle central est d'effectuer la locomotion volontaire en créant des forces qui sont ensuite transmises par le tendon, un autre tissu reliant le muscle squelettique à l'os pour former le squelette. En cas de blessures mineures, les tissus musculaires possèdent une capacité de régénération via l'activation des cellules satellites qui peuvent se différencier en myoblastes. Les myoblastes se différencient ensuite en fibres musculaires pour rejoindre le tissu musculaire. Cependant, cette capacité de régénération est limitée aux blessures légères. En cas de traumatisme grave ou de perte musculaire importante, il est nécessaire de développer des solutions pour la régénération du tissu musculaire.

La régénération du tissu musculaire nécessite l'orientation parallèle et droite des myoblastes afin de favoriser leur différenciation en myotubes, pour finalement former des myofibres alignées afin de compenser la perte musculaire. Les fibres orientées de collagène ont la propriété d'orienter les cellules le long de leur axe en dirigeant les voies de migration. Plusieurs stratégies ont été utilisées pour aligner les fibres de collagène, la lithographie,[7] l'électrospinning,[8] l'impression 3D,[9-10] la microfluidique,[11] le flux de cisaillement,[12] le champ magnétique[13] puissant ou l'étirement.[14] Ces techniques présentent certaines limites, par exemple la nécessité de montage complexe.[15] Il a été

montré (i) qu'*in vivo* la consommation d'extraits de thé vert (riche en polyphénols) permet d'augmenter la surface normale des fibres musculaires de souris Mdx, modèle de souris souffrant de dystrophie musculaire de Duchenne et (ii) qu'*in-vitro* le traitement des myoblastes de souris C2C12 par des extraits de polyphénols augmente leur taille et accélère leur différenciation.

Après avoir exploré les interactions entre le collagène (COL) et l'acide tannique (TA) en présence de différents tampons dans le chapitre précédent, nous avons développé et optimisé l'élaboration de films orientés TA/COL LbL en utilisant une méthode simple et économique d'assemblage à l'aide de pinceau, la méthode de brossage.[3-4] Les interactions entre la surface des films TA/COL orientés et les cellules ont été explorées avec les fibroblastes murins et les myoblastes humains. Les résultats physico-chimiques et biologiques ont été comparés aux multicouches conventionnelles par trempage.

### 3.2 Résultats

Les films COL/TA ont été déposés en utilisant des pinceaux de peintures afin d'orienter les fibres de collagène (Figure 4).

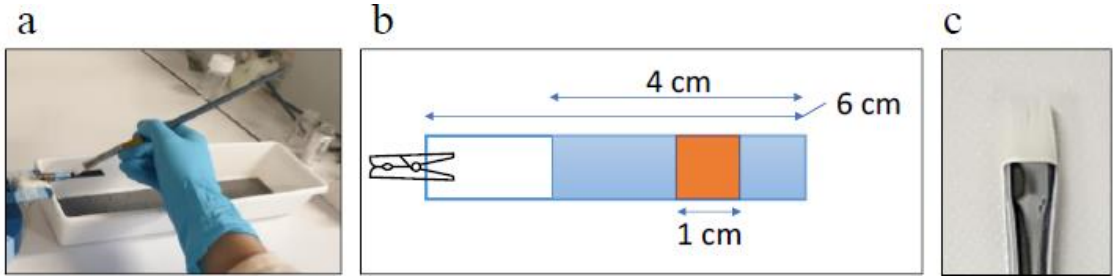


**Figure 4** : (a) Dépôt couche par couche (LbL) utilisant la technique de brossage manuelle. (b) Représentation schématique de la zone bleue sélectionnée sur des lames de verre pour déposer des films multicouches en utilisant la méthode LbL par brossage. La zone orange a été ensuite caractérisée. (c) Pinceau en nylon à poils denses utilisé pour le dépôt de couches.

La topographie des films COL/TA obtenus par brossage, appelés orientés, montre des structures fibrillaires orientées alors qu'aucune orientation n'est obtenue par la méthode de trempage (films non-orientés) (Figure 5).

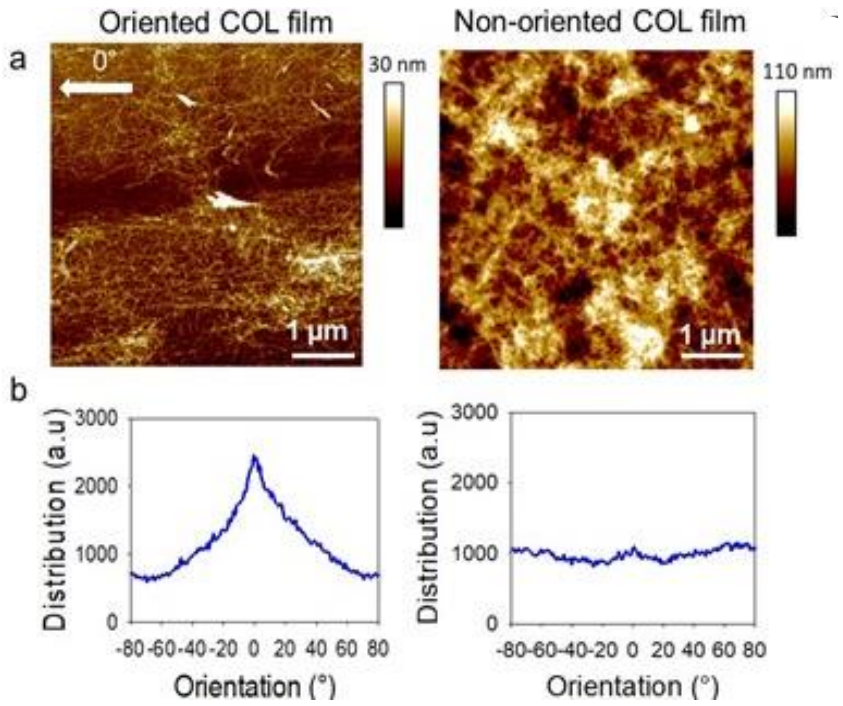


**Figure 5** : (a) Images AFM des films orienté et non-orienté de collagène avec (b) leur distribution d'orientation respective (OrientationJ via Image J).

Les cellules fibroblastes de souris NIH3T3 ont été mises au contact des films COL/TA. Une très bonne orientation cellulaire a été obtenue sur les films COL/TA orientés à contrario des films non-orientés. Les cellules cultivées sur les films brossés semblent se lier les unes aux autres, créant un fuseau de cellules qui migrent ensemble, phénomène similaire lors de la cicatrisation. Par la suite, l'effet de la présence de TA dans le milieu de culture des myoblastses humains a été évalué en fonction de sa concentration. TA devient toxique après 24 h de contact à des concentrations supérieures à 100 µg/mL. À des concentrations plus faibles en TA (10 et 25 µg/mL), après

seulement 24 h d'incubation, les myoblastes présentent une morphologie allongée et un allongement des filaments d'actine, également connu sous le nom de phénotype pro-différenciation, qui est un précurseur essentiel de la fusion cellulaire. En l'absence de TA, les cellules sont bien étalées, sans élongation significative. La libération de TA des films a été évaluée dans un milieu physiologique (PBS). Les films TA/COL non orientés, c'est-à-dire $(TA/COL)_8$, ont libéré 37 ± 3,6 µg/mL de TA, soit environ 9 fois plus que le film orienté avec 4,2 ± 0,5 µg/mL. Les deux valeurs se trouvent sous la concentration de TA toxique envers les myoblastes. Les films orientés de collagène ont permis l'orientation et la fusion des myoblastes sous forme de myotubes au bout de 12 jours (Figure 6).

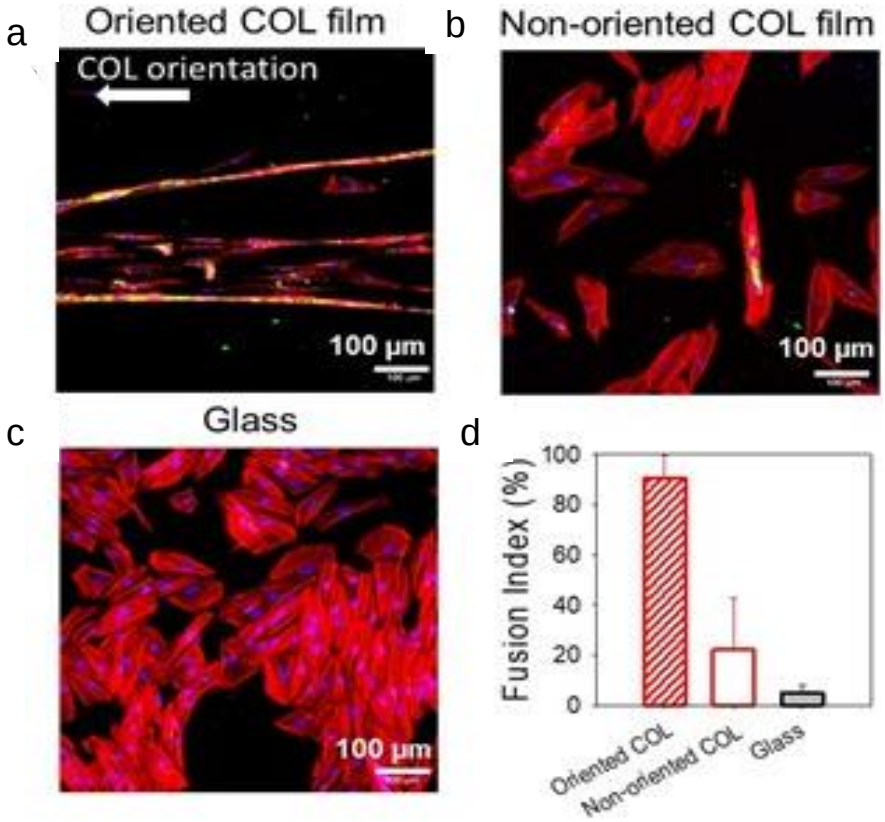


**Figure 6 :** Myoblastes humains (C25 CL48) après 12 jours d'incubation, observés par microscopie optique confocale (noyau en bleu, myosine en vert et filaments d'actine en rouge) sur des films de collagène (a) orienté, (b) non orienté et (c) sur verre nu. (d) Index de fusion des cellules.

La présence de myosine en vert sur les images de microscopie optique confocale est le signe de la formation de myotubes. Aucune orientation n'a été obtenue sur les films non-orientés avec cependant la présence d'un faible signal de myosine. Dans le cas des films TA/COL orientés, 92% des cellules forment les myotubes selon l'index de fusion (Figure 6d). Les films de collagène non-orienté et le verre ne permettent pas l'orientation des cellules avec un faible index de fusion, rapport entre le nombre de noyaux fusionné dans les myocytes sur le nombre total de noyaux. Cet indice est très faible sur le verre et le film non-orienté. Ce revêtement ouvre la voie à l'ingénierie de tissus musculaires de remplacement à partir de myoblastes de patients.

## 4. Films antibactériens de chitine et d'acide tannique

### 4.1 Contexte

Récemment, les surfaces biomimétiques avec des caractéristiques nanotopographiques sont apparues comme une stratégie possible pour contrer l'adhésion des bactéries et la formation de biofilms. Ces surfaces nanostructurées sont inspirées des caractéristiques nanométriques et topographiques naturellement présentes sur les ailes de cigales, les feuilles de lotus, les pattes de gecko, et la peau des requins. Ce type de revêtement serait idéal pour les coques de navires, souvent recouvertes d'une matrice bactérienne visqueuse qui réduit la vitesse, augmente les coûts de carburant et limite la manœuvrabilité, représentant un énorme coût financier pour l'industrie maritime. Bien que les surfaces nanostructurées apparaissent comme une stratégie prometteuse, leur développement implique des instruments coûteux et des processus complexes comme l'ablation au laser, l'électropolissage, et les techniques photolithographiques.

La chitine, le deuxième polysaccharide le plus abondant, est peu coûteux, renouvelable et semi-cristallin. Elle est produite à partir des exosquelettes de crustacés ou de champignons. Les

exosquelettes à base de chitine contiennent naturellement de grandes quantités de fer. Les nanocristaux de chitine cristalline (CNC) et les nanofibres de chitine sont généralement utilisés pour leurs excellentes propriétés mécaniques afin de concevoir des matériaux biodégradables. On s'est beaucoup intéressé à l'orientation des nanostructures anisotropes à base de chitine en utilisant des champs électriques et magnétiques ou encore par cisaillement. Malgré quelques études sur les films à base de chitine, aucune n'a décrit leur propriétés antibacteriennes. En général, les films antibactériens à base de chitine sont obtenus après modification chimique des nanocristaux ou incorporation d'agent antimicrobiens.

Dans ce chapitre, nous avons développé des films à base de nanocristaux de chitine (CNC) obtenus par brossage au pinceau afin d'obtenir des films CNC orientés en les comparants aux films obtenus par trempage, films CNC non-orientés.

### 4.2 Résultats

Les films CNC ont été obtenus en associant l'acide tannique et les ions $Fe^{3+}$ comme suit : PEI-$(TA/Fe^{3+}/CNC/Fe^{3+})_n$ avec *n* le nombre de « quadricouche ». Les films orientés obtenus par brossage ont une épaisseur plus faible que ceux obtenus par trempage atteignant 30 nm après 8 quadricouches (Figure 7a). La topographie de surface des films, caractérisée par l'AFM, montre une topographie orientée des CNC parallèle à la direction de brossage pour les films obtenus par brossage et orienté de manière aléatoire pour ceux obtenus par trempage (Figure 7b-c).

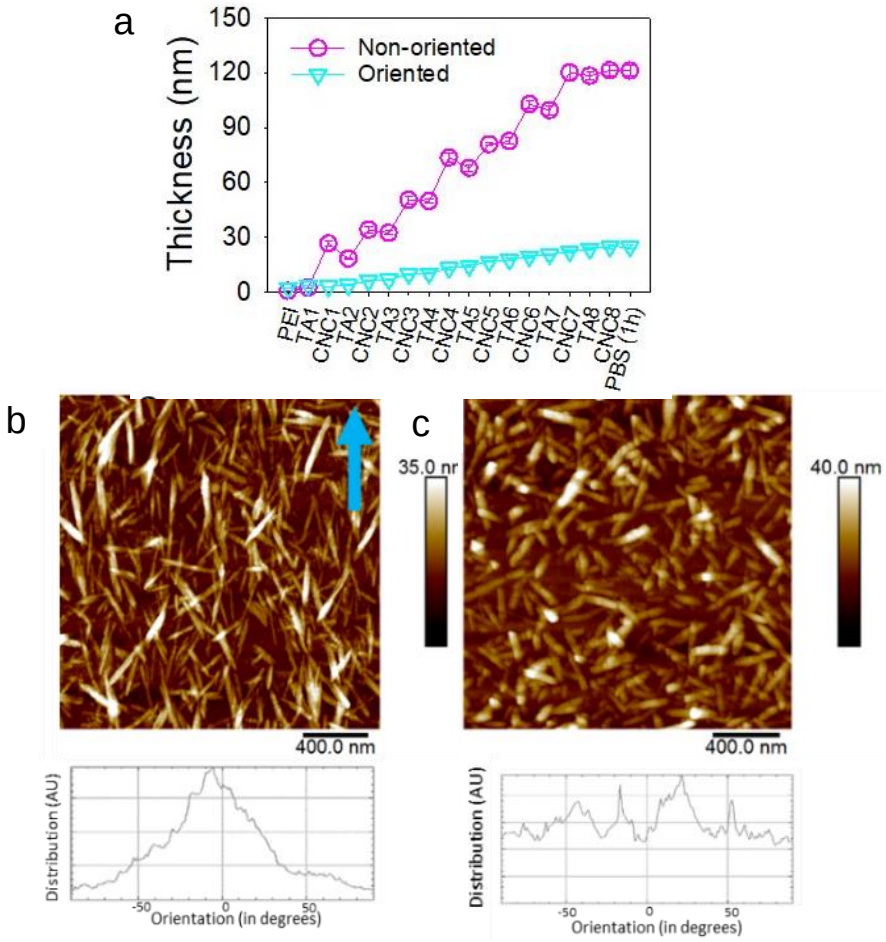


**Figure 7 :** (a) Evolution de l'épaisseur en fonction de la dernière couche adsorbée et images AFM des films PEI-(TA/$Fe^{3+}$/CNC/$Fe^{3+}$)$_n$ obtenus (b) par brossage (film CNC orienté) et (c) par trempage (film CNC non-orienté). La flèche bleue indique la direction du brossage.

L'activité antibactérienne des films CNC orientés et non orientés a été évaluée vis-à-vis de de *Staphylococcus aureus* et *Escherichia coli* en terme d'adhésion, de prolifération et de formation de biofilm. Les expériences ont été menées dans des conditions statiques afin de permettre un dépôt ou un contact maximal des bactéries sur les substrats sous l'effet de la gravité. Un marquage fluorescent LIVE/DEAD a été réalisé sur les bactéries après 1,5 h d'adhésion suivi de 24 h de prolifération afin de différencier les bactéries vivantes (vert) et celles endommagées (rouge). Ce

marquage permet de dénombrer les bactéries sur une surface et d'obtenir le pourcentage de bactéries endommagées par rapport aux nombre de bactéries totales (Figure 8).

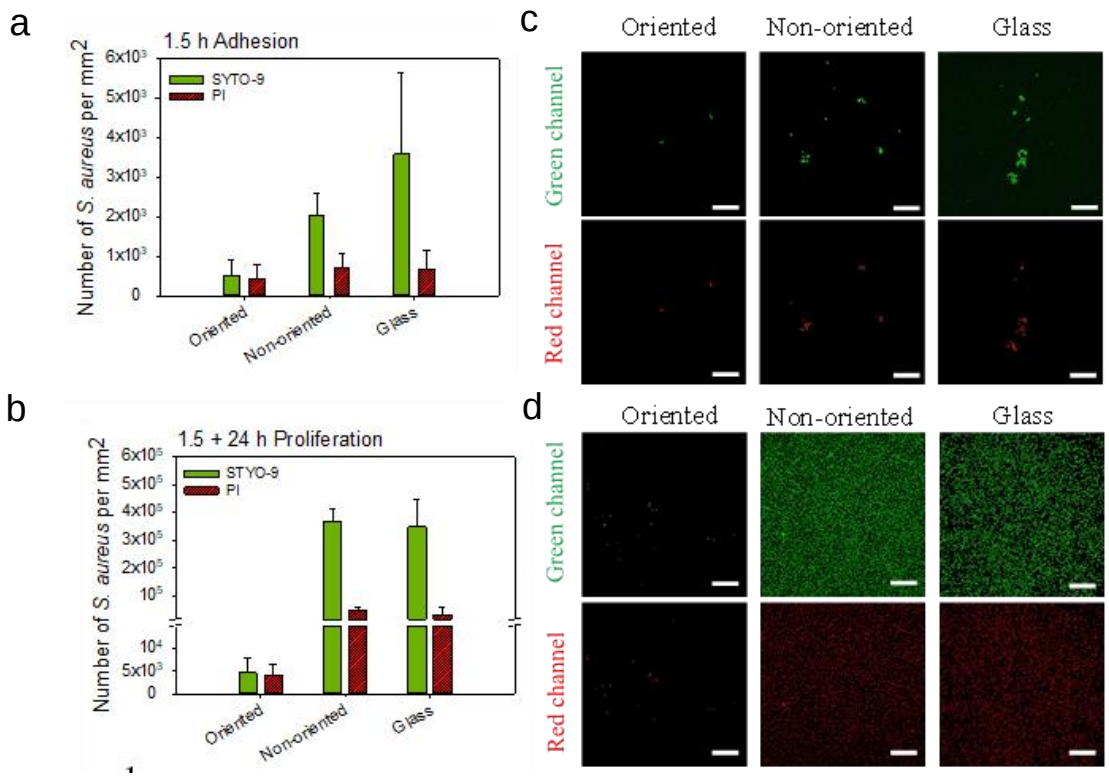


**Figure 8** : Adhésion et prolifération de *Staphylococcus aureus* sur des films CNC orientés et non-orientés, terminés par une couche de CNC. (a, b) Nombre de bactéries ayant adhérées par mm² déterminé à partir (c, d) des images de microscopie optique confocale (barre d'échelle : 20 µm), après marquage des bactéries vivantes en vert (SYTO 9) et endommagées en rouge (PI), obtenues (a, c) après 1,5 h d'incubation (b, d) après 1,5+24 h de prolifération à 37 °C.

Les images de microcopie optique confocale montrent une différence très nette en termes d'adhésion et de prolifération de *Staphylococcus aureus* (Figure 8c-d). Très peu de bactéries sont visibles sur les films CNC orientés par rapport au verre nu avec une réduction du nombre de bactéries vivantes de 86% après 1,5 h d'adhésion et 98.6 % après 24 h de prolifération. En outre,

46 à 48 % des bactéries présentes en ont été endommagées dans les deux cas. Les films CNC non-orientés réduisent l'adhésion des bactéries de 46% mais présentent une prolifération après 24 h similaire au verre avec seulement 10% de bactéries endommagés. Les résultats obtenus avec *Escherichia coli* sont similaires avec un effet bactéricide meilleur pour les films CNC orientés par rapport aux films CNC non-orientés ou au verre. Les images de microscopie électronique à balayage ont permis de vérifier l'intégrité des membranes des bactéries (Figure 9).

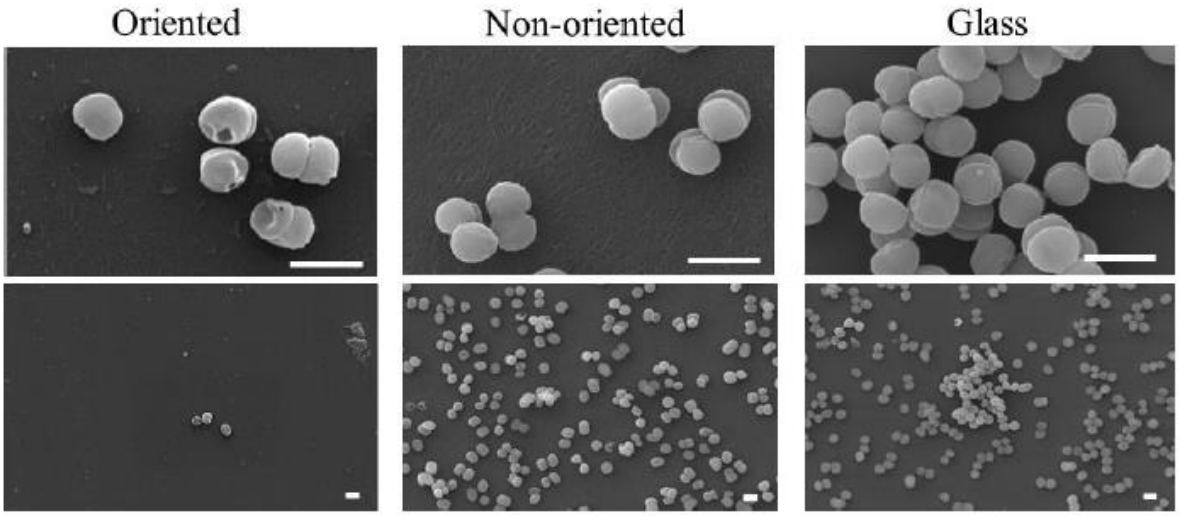


**Figure 9** : Morphologie de *Staphylococcus aureus* observées par microscopie électronique sur des films CNC orientés et non orientés, terminé par une couche de CNC, et le verre nu, après 1,5+24 h de prolifération (barre d'échelle : 1 µm).

Très peu de bactéries étaient fixées sur les films CNC orientés, toutes avec des membranes sévèrement endommagées avec la présence de trous. Au contraire, un grand nombre de bactéries saines ont été observées sur les films CNC non orientés et sur le verre nu. De plus, la formation de biofilm par les bactéries *Staphylococcus aureus* a été évaluée quantitativement en utilisant la coloration à la Safranine. La formation de biofilm est inférieure de 81 % sur les films CNC orientés

par rapport au verre nu (avec une valeur $p \leq 0,01$). Les films CNC non orientés semblent au contraire favoriser la formation du biofilm par rapport au verre nu (avec une valeur $p \leq 0,01$).

L'influence de la dernière couche et de la composition des films CNC orientés a été étudiée. Afin d'assurer les propriétés antibactériennes des films CNC orientés, il faut que la dernière couche soit du CNC. Les propriétés bactéricides sont perdues (i) si la dernière couche est TA ou $Fe^{3+}$, (ii) si les couches de CNC sont remplacées par du chitosane (dérivé soluble de la chitine qui est connu pour ses propriétés antibactériennes) (iii) les couches de TA/$Fe^{3+}$ par l'acide hyaluronique. Des études en microscopie à force atomique en mode imagerie ont permis de mettre en évidence le rôle de la nanotopographie "en piques" des films (Figure 10). Les coupes profilométriques des images AFM des films CNC orientés et non orientés sont présentés dans la figure 10. Le film orienté présente des pics plus fréquents et plus grands (20-30 nm de hauteur) par rapport au film non orienté. L'analyse des paliers est une méthode utilisée pour tracer et analyser la distribution de la hauteur d'une surface en révélant quel pourcentage de la surface (axe des y sur la figure 10c), est inférieur ou supérieur à une hauteur sélectionnée (axe des x sur la figure 10c). L'augmentation de la courbe de la Figure 10c à partir de valeurs de hauteurs plus élevées représente une surface dont la topographie est très rugueuse et en forme de pointe, ce qui est confirmées par le profil de la coupe AFM. Aucune différence de topographie des films n'a été observée selon la dernière couche déposée sur les films CNC orientés. Par contre, la composition du film a un impact sur la nanotopographie. La distribution des hauteurs se décale vers des hauteurs plus faibles lorsque CNC est remplacé par le chitosane, ce qui est attendu mais également lorsque TA/$Fe^{3+}$ est remplacé par HA. Les pointes sont ainsi moins hautes sur la surface de ces films.

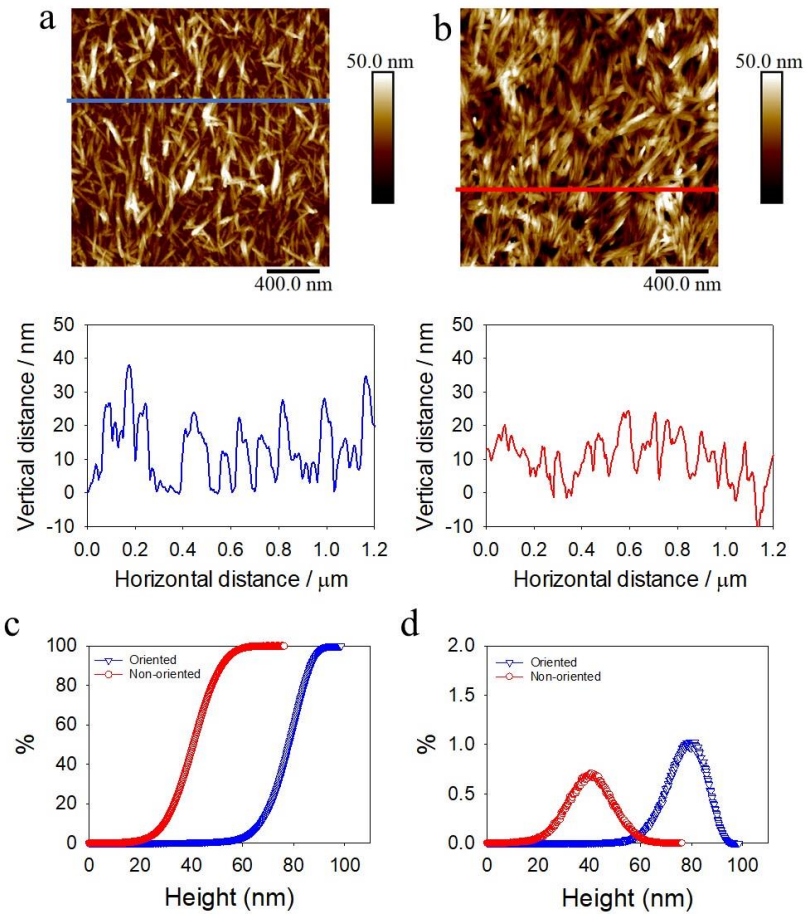


**Figure 10** : Images AFM et coupes profilométriques des films CNC (a) orientés et (b) non orientés. Analyse topographique des images AFM (5×5 μm²) avec (c) le rapport de la surface d'appui et (d) les histogrammes de hauteur.

En collaboration avec Gregory Francius (LCPME, Vandoeuvre), la microscopie à force chimique (CFM) a été utilisée pour caractériser la densité de charge de surface des différents films étudiés. Dans ce but, la CFM utilise des interactions chimiques entre une pointe de microscope à force atomique (AFM) fonctionnalisée et un échantillon. L'interaction chimique est mesurée par la déviation du cantilever AFM pendant l'approche et le retrait de la pointe AFM. Dans notre cas, la charge de surface positive des films a été caractérisée en utilisant une sonde AFM fonctionnalisée

au phosphate, pour mimer les membranes cellulaires des bactéries, dans du PBS à pH 7,2. Les films CNC orienté, terminé par CNC, ont montré une force d'adhésion plus élevée, avec une valeur médiane de 0,35 nN, que le film CNC non orientée, terminé par CNC, révélant probablement une interaction plus forte avec la pointe fonctionnalisée au phosphate et donc de fortes interactions électrostatiques (Figure 11a). Cependant, le test d'analyse de variance ANOVA appliqué aux données enregistrées n'a montré aucune différence significative.

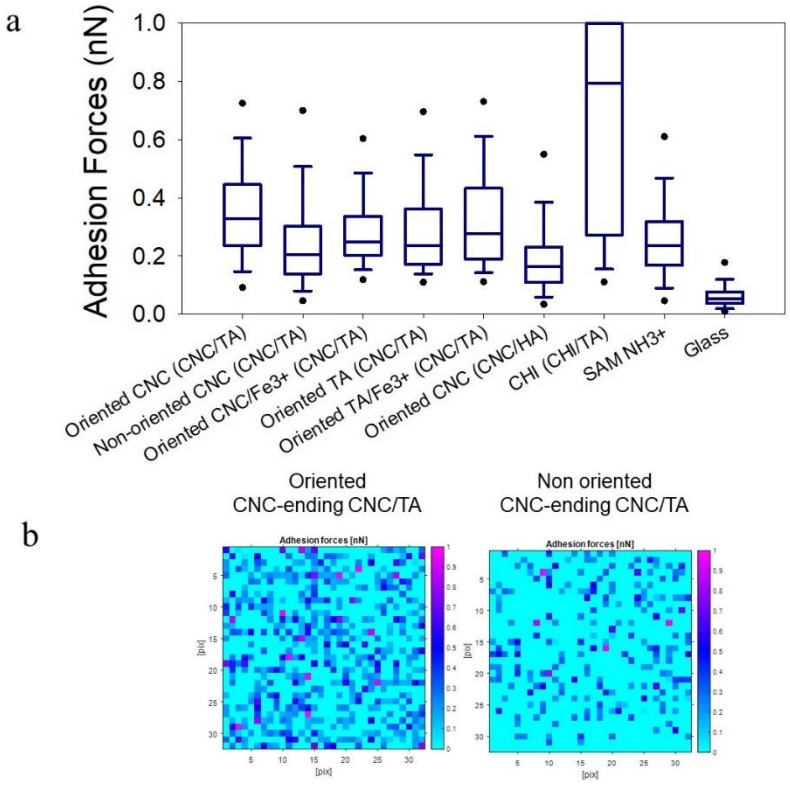


**Figure 11** : Force d'adhésion, mesurée à l'aide d'une pointe AFM fonctionnalisée par un groupement phosphate, (a) Les diagrammes en boîte montrent la médiane (ligne), les quartiles à 5 % et 95 % (valeur $p \leq 0{,}001$ pour tous) et (b) la cartographie sur une zone de $1 \times 1$ µm$^2$ des films CNC orienté et non orienté terminés par une couche de CNC.

Par contre, la cartographie des deux surfaces du film a montré une plus grande densité de charges pour le film orienté (Figure 11b). L'influence de la dernière couche et de la composition du film a également été évaluée montrant des résultats significativement différents. Les films ont des densités de charges de surface plus élevées dans tous les cas.

Ces films ont été testés en culture cellulaire. La prolifération de fibroblastes de souris (NIH3T3) est très bonne et similaire à celle du verre nu. La nanotopographie des films ne perturbe pas les cellules.

En conclusion, les films CNC orientés présentent à la fois des propriétés antiadhésives et de bactéricides par contact sur *Staphylococcus aureus* et *Escherichia coli*. De plus, ce film empêche la formation du biofilm de S. aureus. L'activité antibactérienne des films CNC orientés est associée à l'orientation nanotopographique des CNC en forme de pic avec une densité de charge de surface élevée. En comparaison, les films non orientés présentent une topographie plus lisse avec une moindre densité de charges (Schéma 1).

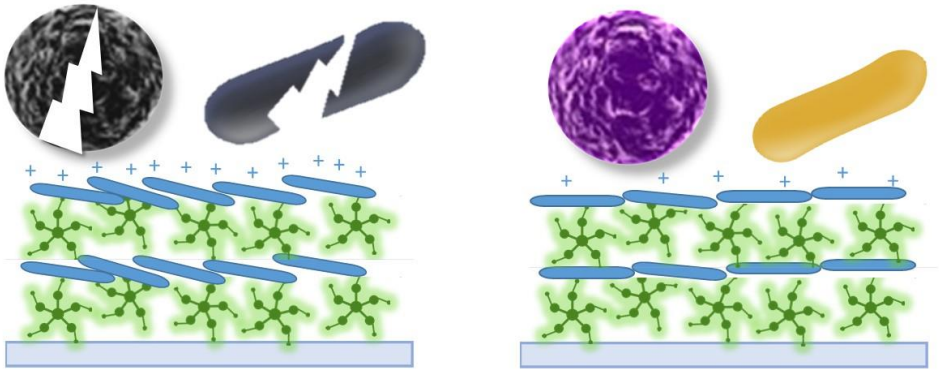

**Schéma 1** : Représentation schématique de l'activité antibactérienne par destruction par contact de (a) les films CNC orientés et (b) les films CNC non orientés en contact avec *Staphylococcus aureus* et *Escherichia coli*.

Les pointes chargées positivement des films CNC orientés appliquent probablement une force de cisaillement sur la membrane cellulaire conduisant à sa perforation. Cette hypothèse doit être approfondie avec la caractérisation des propriétés mécaniques des membranes des bactéries et l'analyse de microscopie électronique à transmission des bactéries en contact avec la surface. Le mode d'action pourrait être similaire à celui des surfaces nanotexturées d'organismes, comme les ailes de cigales ou de libellules, toutes deux composées de chitine et de protéines. Dans le cas des nanopiliers d'ailes de cigale, la rupture de la membrane a été expliquée par le contact direct de la membrane de la cellule bactérienne avec les nanopiliers, qui sont suffisamment forts pour endommager la membrane bactérienne.[16] Dans le cas des ailes de libellule, une combinaison de deux phénomènes a été rapportée : (i) la forte adhérence entre les nanopilliers et la bactérie et la force de cisaillement lorsque la bactérie immobilisée tente de s'éloigner de la topographie défavorable de la surface.[17]

## 5. Perspectives

Ces travaux de thèse ouvrent la voie à deux perspectives de recherche :

- *Le développement de films COL/TA en tant que plateforme pour la délivrance localisée de polyphénols.* Les interactions polyphénol/protéine peuvent être exploitées pour l'administration de médicaments pour le traitement du cancer colorectal. L'épigallocatéchine gallate (EGCG) est un polyphénol issu du thé vert, qui a montré un potentiel anticancéreux contre les tumeurs colorectales à des concentrations de 375 µg/mL. Mais il possède certains inconvénients tels qu'une faible biodisponibilité et une courte demi-vie (hydrolyse à pH neutre et basique), ce qui rend inefficace son utilisation libre en solution. Il est ainsi nécessaire de concevoir des systèmes pour sa délivrance

prolongée. Dans ce but, nos résultats préliminaires montrent qu'il est possible de charger et libérer de l'EGCG à partir d'une plateforme basée sur des films TA/COL. Une libération contrôlée d'EGCG a été obtenu dans un milieu physiologique. Il faudra tester cette plateforme *in-vitro* contre ces cellules cancéreuses et améliorer ses propriétés mécaniques par diverses stratégies de réticulation afin d'assurer la stabilité mécanique des plateformes.

- *L'application de la méthode de brossage pour obtenir des revêtements ou de peintures virucides.*

Les surfaces à forte densité de charge positive ont été décrites comme inactivant les virus en désintégrant leurs enveloppes virales chargées négativement. Par conséquent, nous prévoyons d'analyser l'activité du virus SARS-CoV-2, connu sous le nom de COVID-19, sur les revêtements nanostructurés à base de CNC.

**Bibliographie :**


1. Decher, G., Fuzzy nanoassemblies: Toward layered polymeric multicomposites. *Science* **1997,** *277* (5330), 1232-1237.
2. Schlenoff, J. B.; Dubas, S. T.; Farhat, T., Sprayed polyelectrolyte multilayers. *Langmuir* **2000,** *16* (26), 9968-9969.
3. Park, K.; Choi, D.; Hong, J., Nanostructured Polymer Thin Films Fabricated with Brush-based Layer-by-Layer Self-assembly for Site-selective Construction and Drug release. *Sci Rep* **2018,** *8* (1), 3365.
4. Zhao, X.; Zhou, C.; Lvov, Y.; Liu, M., Clay Nanotubes Aligned with Shear Forces for Mesenchymal Stem Cell Patterning. *Small* **2019,** *15* (21), 1900357.
5. vander Straeten, A.; Lefevre, D.; Demoustier-Champagne, S.; Dupont-Gillain, C., Protein-based polyelectrolyte multilayers. *Adv Colloid Interfac* **2020,** *280*.
6. Hammond, P. T., Building biomedical materials layer-by-layer. *Mater Today* **2012,** *15* (5), 196-206.
7. Wilson, D. L.; Martin, R.; Hong, S.; Cronin-Golomb, M.; Mirkin, C. A.; Kaplan, D. L., Surface organization and nanopatterning of collagen by dip-pen nanolithography. *PNAS* **2001,** *98* (24), 13660-13664.
8. Zhong, S.; Teo, W. E.; Zhu, X.; Beuerman, R. W.; Ramakrishna, S.; Yung, L. Y., An aligned nanofibrous collagen scaffold by electrospinning and its effects on in vitro fibroblast culture. *J. Biomed. Mater. Res. A* **2006,** *79* (3), 456-63.
9. Yang, S.; Shi, X.; Li, X.; Wang, J.; Wang, Y.; Luo, Y., Oriented collagen fiber membranes formed through counter-rotating extrusion and their application in tendon regeneration. *Biomaterials* **2019,** *207*, 61-75.
10. Nocera, A. D.; Comin, R.; Salvatierra, N. A.; Cid, M. P., Development of 3D printed fibrillar collagen scaffold for tissue engineering. *Biomed. Microdevices* **2018,** *20* (2), 26.
11. Lee, P.; Lin, R.; Moon, J.; Lee, L. P., Microfluidic alignment of collagen fibers for in vitro cell culture. *Biomed. Microdevices* **2006,** *8* (1), 35-41.
12. Saeidi, N.; Sander, E. A.; Ruberti, J. W., Dynamic shear-influenced collagen self-assembly. *Biomaterials* **2009,** *30* (34), 6581-92.
13. Guo, C.; Kaufman, L. J., Flow and magnetic field induced collagen alignment. *Biomaterials* **2007,** *28* (6), 1105-1114.
14. Chaubaroux, C.; Perrin-Schmitt, F.; Senger, B.; Vidal, L.; Voegel, J. C.; Schaaf, P.; Haikel, Y.; Boulmedais, F.; Lavalle, P.; Hemmerle, J., Cell Alignment Driven by Mechanically Induced Collagen Fiber Alignment in Collagen/Alginate Coatings. *Tissue eng. C* **2015,** *21* (9), 881-8.
15. Liu, G. Y.; Agarwal, R.; Ko, K. R.; Ruthven, M.; Sarhan, H. T.; Frampton, J. P., Templated Assembly of Collagen Fibers Directs Cell Growth in 2D and 3D. *Sci Rep* **2017,** *7* (1), 9628.
16. Ivanova, E. P.; Hasan, J.; Webb, H. K.; Truong, V. K.; Watson, G. S.; Watson, J. A.; Baulin, V. A.; Pogodin, S.; Wang, J. Y.; Tobin, M. J.; Lobbe, C.; Crawford, R. J., Natural Bactericidal Surfaces: Mechanical Rupture of Pseudomonas aeruginosa Cells by Cicada Wings. *Small* **2012,** *8* (16), 2489-2494.
17. Bandara, C. D.; Singh, S.; Afara, I. O.; Wolff, A.; Tesfamichael, T.; Ostrikov, K.; Oloyede, A., Bactericidal Effects of Natural Nanotopography of Dragonfly Wing on Escherichia coli. *ACS Appl Mater Inter* **2017,** *9* (8), 6746-6760.

## Liste des publications :

**Publiés :**

1. **M. H. Iqbal**, A. Schroder, H. Kerdjoudj, C. Njel, B. Senger, V. Ball, F. Meyer, and F. Boulmedais, "Effect of the Buffer on the Buildup and Stability of Tannic Acid/Collagen Multilayer Films Applied as Antibacterial Coatings", *ACS Applied Materials & Interfaces*, 2020

2. M. Criado-Gonzalez, **M. H. Iqbal**, A. Carvalho, M. Schmutz, L. Jierry, P. Schaaf, F. Boulmedais, "Surface Triggered Self-Assembly of Fmoc-Tripeptide as an Antibacterial Coating" *Frontiers in Bioengineering and Biotechnology*, 2020

3. N. Zydziak, **M. H. Iqbal**, A. Chaumont, A. Combes, E. Wasielewski, M. Legros, L. Jierry, P. Lavalle, F. Boulmedais, D. Chan-Seng, "Unexpected aqueous UCST behavior of a cationic comb polymer with pentaarginine side chains" *European Polymer Journal*, 2020

4. M. Criado-Gonzalez, D. Wagner, **M. H. Iqbal**, A. Ontani, A. Carvalho, M. Schmutz, J. B. Schlenoff, P. Schaaf, L. Jierry, F. Boulmedais, "Supramolecular tripeptide self-assembly initiated at the surface of coacervates by polyelectrolyte exchange" *Journal of Colloid and Interface Science*, 2021

5. A. Seica, **M. H. Iqbal**, A. Carvalho, J. Yong-Choe, F. Boulmedais, P. Hellwig, " Study of Membrane Protein Monolayers Using Surface-Enhanced Infrared Absorption Spectroscopy (SEIRAS): Critical Dependence of Nanostructured Gold Surface Morphology", *ACS Sensors*, 2021

**En cours de soumission :**

1. F. Omeis, Z. B. Fezoua, A. F. S. Seica, **M. H. Iqbal**, F. Boulmedais, D. Moss, P. Hellwig, "Temperature Phase Transition of Thiophospholipid bilayers on Plasmonic Nanoantennas: An Infrared Spectroscopic Study" *ACS Applied Nano Materials*

**En cours de préparation :**

1. **M. H. Iqbal**, E. Pradel, G. Francius, L. Heux, F. Meyer, and F. Boulmedais, "Unexpected Antibacterial Activity of Biobased Nanostructured Multilayer Films", to be submitted in *Advanced Materials*; un Brevet en préparation avec la SATT Conectus

2. **M. H. Iqbal**, V. Gribova, F. J. R. Revana, F. Meyer, F. Boulmedais, "Aligned Collagen/Tannic acid Nanofilms for Tissue Engineering", à soumettre dans *Small*

3. **M. H. Iqbal**, F. Meyer, F. Boulmedais, "Multilayer Films at Biointerfaces", à soumettre dans *Advanced Healthcare Materials*

4. **M. H. Iqbal**, F. Meyer, F. Boulmedais, "Layer-by-layer platforms for localized delivery of bioactive molecules for anticancer treatment", à soumettre dans *ACS Nano*

## Liste des conférences :

### Présentations orales

1. **M. H. Iqbal**, "Effect of the Buffer on the Buildup and Stability of Tannic Acid/Collagen Multilayer Films Applied as Antibacterial Coatings", 6th Annual meeting of MatSan, 20th Annual meeting of IMBL, 14-16 October 2020, webinar

2. **M. H. Iqbal**, "Collagen-based multilayer films for wound healing", 30th Annual Conference of the European Society for Biomaterials (ESB) & 26th Annual Conference of the German Society for Biomaterials (DGBM), Sep 9-13, 2019, Dresden, Germany

3. **M. H. Iqbal**, "Collagen-based multilayer films for wound healing", 3rd BIOMAT Congress, Materials for Health, June 3-7, 2019, Grande Motte, France

### Présentations de posters

1. **M. H. Iqbal**, "Antimicrobial multilayer coatings based on Collagen and Tannic acid", ESAO Winter School on Materials, Surfaces and Cells, February 29-29, 2020, Lutherstadt-Wittenberg, Germany

2. **M. H. Iqbal**, "Collagen-based multilayer films for wound healing", The 5th Stevens Conference on Bacteria-Material Interactions, June 12-13, 2019, Stevens Institute of Technology, New Jersey, USA

# General Introduction

Biomaterials are being extensively used in tissue engineering (TE) to develop constructs that repair, conserve, or promote tissue function or entire organ. Their surface properties act as first line of defense at cell-biomaterial interface to fight infections and promote bio-integration. Hence, the surface modification of biomaterials is of paramount importance to cope nosocomial infections and to allow tissue integration.

Five percent of patients develop nosocomial infections every year during hospitalization time in western countries. The prevention of early bacterial attachment and colonization on medical devices and biomaterials is of vital significance because of increasing bacterial resistance towards antibiotics, increasing hospitalization times, and related financial burden. Since a few decades, an intensive research is being carried out to explore the potential of polyphenols, found in plants as secondary metabolites, as antibacterial and antioxidants agents. Tannic acid (TA) is a polyphenol known to inhibit the growth of several bacterial strains.

The thesis is divided into five chapters.

In **chapter 1**, an overview of coatings different techniques is provided, and more focus is given to the layer-by-layer assembly of proteins and their general biomedical applications.

The **chapter 2** entails the materials and methods used in the entire thesis.

The **chapter 3** provides comprehensive discussion on how the interactions between tannic acid and collagen affects the growth of the LbL buildup, its physico-chemical and biological properties. Thanks to their ability to interact with proteins via hydrogen bonding, we developed tannic acid/collagen (TA/COL) LbL films built in acetate or citrate buffers at pH 4. Surprisingly, the used buffer impacts not only the physicochemical but also the antibacterial properties of the films. When

incubated in physiological conditions, both types of TA/COL films released comparable amount of TA depending on the last layer but showed an antibacterial effect against *Staphylococcus aureus* only for citrate-built films. The topographies of the films are different with a granular and fibrillary structure for citrate and acetate-built films, respectively. The distinct behavior is attributed to the change in nature of complexation between tannic acid and collagen both in solution and LbL films in the presence acetate or citrate buffer. Moreover, the LbL films did not show any cytotoxicity towards human gingival fibroblasts which is crucial to ensure bio-integration of implanted biomaterials.

The **chapter 4** discusses the development of oriented TA/COL LbL films using a fast and economical brush-coating LbL method. In regenerative medicine, surface design has great potential to design cell-surface interface by playing with microenvironment cues, such as bioactive molecules and surface topography. Aligned collagen fibers have the property to orient cells along their axis by contact guidance. Several strategies have been used to align collagen fibers e.g., lithography, electrospinning, 3D printing, microfluidics, shear flow, magnetic field, and mechanical stretching. These techniques have certain limitations such as the need for a complex instrumentation which can denature collagen. Herein, we used the brushing method to deposit oriented collagen layers with nanometric control, and sustained delivery of bioactive compounds to accelerate cell differentiation. These nanofilms are shown to be of particular interest for anisotropic alignment, migration, and the differentiation of human myoblast cells for the muscle tissue engineering.

In **chapter 5**, we explored the possibility of replacing COL fibrillar molecules with highly crystalline and stiff chitin nanocrystals (CNC) to develop TA/CNC LbL films. Besides working with proteins and polyphenols, here, we explored the potential of biobased nanostructures for

functionalized biomaterials. To that aim, we developed nanostructured coatings with different nanoscale orientations using LbL method. Surprisingly, *S. aureus* and *E. coli* does not adhere, proliferate, or form biofilms on the parallel oriented nanofilms, unlike randomly oriented ones. The distinct antibacterial activity was associated with change in overall charge density of different surfaces observed by bacterial membrane mimicking $PO_3^-$ coated AFM tip.

At last, an overall conclusion of the work and some outlooks are given.

# Chapter 1 : Introduction

## Table of Contents

This chapter gives a brief overview of various surface functionalization strategies. Among different coating techniques, the use of layer-by-layer (LbL) method to develop nanofilms for biomedical applications is a goal of the thesis. We will focus on the physico-chemical properties of LbL coatings based on bio-sourced polymers and their biomedical applications.

## 1.1 Coatings: a historical perspective of molecules at interface

Around a thousand years ago, Japanese used a technique namely Sumi Nagashi, to form a monolayer at water-air interface and its transfer on a solid surface to obtain a film.[1] Following the similar principle, a Chinese ink, a mixture of carbon particles and protein, was developed to obtain the first protein monolayer by using lifting method. The mixture distributed on a water-air interface was then lifted by using a paper.[2]

### 1.1.1 Langmuir-Blodgett (LB)

Earlier in 20$^{th}$ century, the study of soap films at air-water interface under compression allowed to conclude on the formation of a monomolecular layer giving the value of surfactant size.[3-4] Following the same principle of forming a monolayer at air-water interface, Langmuir-Blodgett (LB) film deposition introduced by Langmuir[5] and Blodgett[6] became the basis for the development of first single or multi monolayers of amphiphilic molecules (fatty acids) with fine control over their spatial arrangement.[7] The LB deposition on hydrophilic substrate consist in the transfer of a monolayer of amphiphilic molecules from the air-water interface to a solid substrate during its vertical passage through the interface (**Figure 1.1)**. In the case of hydrophobic substrate, the transfer is ensured by contact with the surface of the monolayer. LB deposition is limited to planar surfaces and the type of molecules that can be deposited are restricted to mainly amphiphiles and lipids. However, other components such as 2D metal organic frameworks and DNA origami were also used in LB assembly.[8]

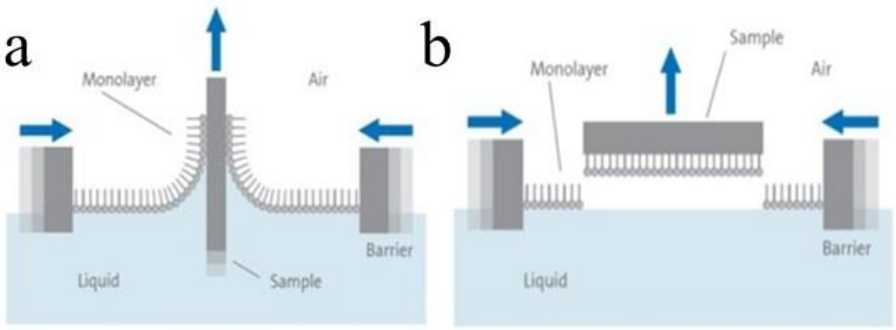


***Figure 1.1:*** *A schematic representation of Langmuir-Blodgett film deposition of amphiphilic molecules on* ***(a)*** *a hydrophilic and* ***(b)*** *a hydrophobic substrate.*[9]

### 1.1.2 Self-assembled monolayers (SAM)

Self-assembled monolayers (SAM) can be developed either by immersing a substrate into an amphiphile solution[10] or via vapor deposition.[11] Thiols and disulfides modified organic species can develop well organized monolayers on gold substrates. The obtained films are homogeneous, stable and densely packed. The method depends on interactions of a surface with thiol groups, thus limited to noble metals and silanes.[10]

### 1.1.3 Polymers at surfaces

Polymer chains adsorb on a surface following a three-step mechanism, (i) transport of chains from the bulk solution to the surface, (ii) attachment to the surface, and (iii) rearrangement of the adsorbed chains on the surface. Jenkel and Rumbach[12] proposed a model of a polymer chain adsorbed on a surface. According to the model, an adsorbed polyelectrolyte chain can have three segments, (i) “trains” which are in contact with the surface, (ii) “tails” which are the non-adsorbed chain ends, and (iii) non-adsorbed “loops” which connect two trains **(Figure 1.2)**.[13]

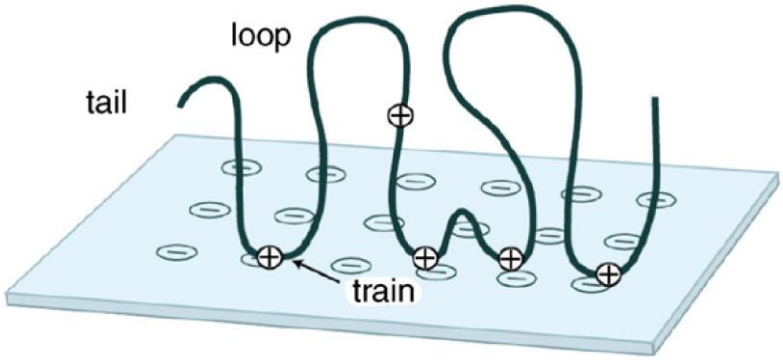


***Figure 1.2:*** *Schematic representation of a polyelectrolyte chain adsorbed on an oppositely charged substrate. Trains, tails, and loops are shown. The charged segments are mostly attached to the surface. The counterions are not considered.*

### 1.1.4 Polyelectrolytes

Polyelectrolytes are negatively or positively charged polymers, called polyanion and polycation, respectively. The charge of the polymer chains appears when they are dissolved in a polar solvent like water. Thanks to the ionic bonds, one type of charges stay linked to the polymer chains whereas the opposite charges dissociate into the solution. Polyelectrolyte charges are compensated by their counterions in solution. In the presence of salt, polyelectrolytes adopt different conformations. At low ionic strength, they present a “flat” or rigid rod like conformation since the charges on the polyelectrolyte repel each other. At high ionic strength, polyelectrolytes adopt a “loopy” conformation by charge screening. Strong polyelectrolytes are fully charged regardless of pH, but the weak polyelectrolytes, mostly containing amine or carboxylic groups, are pH sensitive possessing a pKa. Below the pKa, weak polyanions are protonated with low density of charges with a flat conformation. Above the pKa, their density of charged per chain increases leading to a loopy conformation.

### 1.1.5 Layer-by-layer (LbL) assembly

The layer-by-layer (LbL) assembly involves alternating deposition of polycations and polyanions on usually a negatively charged surface, thus obtaining a polyelectrolyte multilayer **(Figure 1.3)**.

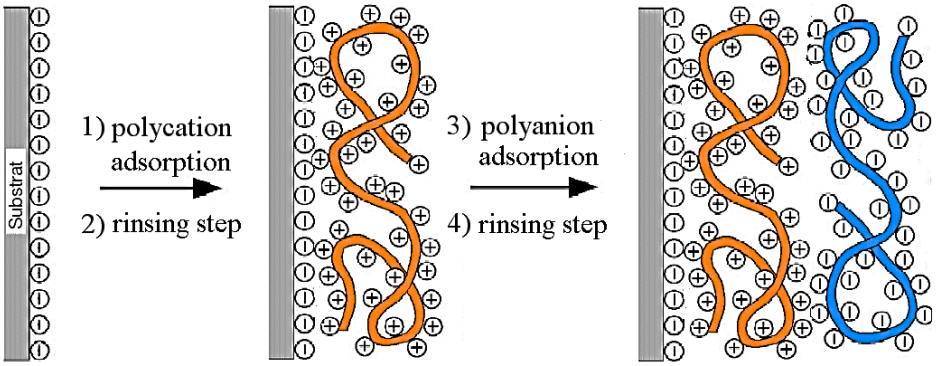


***Figure 1.3:*** *Schematic illustration of polyelectrolyte multilayer film development by alternating depositions of polycationic and polyanionic polyelectrolytes on a negatively charged substrate, followed by a rinsing step, via the dipping method.*[14]

#### *1.1.5.1 Driving force for LbL buildup*

*1.1.5.1.1 Electrostatic assembly*

To build a LbL film, the surface is brought in contact with a polycation solution to allow the electrostatic adsorption of the positively charged polymer chains. Thus, the adsorbed layer of polycation gives a positively charged surface with several excess unpaired charges by overcompensation of charges. With the adsorption of the polyanion layer, a negatively charged surface is obtained reversing the excess charge. Hence, allowing the deposition of next polycation layer.[15] Each adsorption of polycation or polyanion is followed by a rinsing step to remove weakly bound molecules. This process can be repeated to obtain the desired film thickness. Different parameters such as the pH, temperature, solvent, ionic strength, and the type and characteristics of each polyelectrolyte strongly influence the electrostatic assembly.

*Temperature*

The effect of temperature is mainly reported with the LbL films showing linear buildup. PDADMAC/PSS films showed linear buildup at 15°C and 25°C, and an exponential buildup at higher temperatures, 45°C and 55°C. The change in the growth mechanism is attributed to faster polyelectrolyte diffusion at higher temperatures.[16]

*Ionic strength*

The ionic strength of polyelectrolyte solutions strongly impacts the film thickness and growth mechanism. Higher salt concentrations are generally reported to give thicker LbL films.[17-19] For example, PAH/PSS LbL showed an increase in mean bilayer thickness from 10.9 to 22.6 Å for NaCl concentrations of 0 to 2M, respectively.[18] Polyelectrolytes adopt linear or rod-like conformation at low ionic strength due to the charge repulsion on the polymer chains, whereas they adopt a loopy conformation at high ionic strength due to charge screening effect. This loopy conformation is responsible for thicker LbL films at by increasing ionic strength.[18]

*Effect of pH*

The pH of the polyelectrolyte solutions determines the characteristics of the multilayers, especially the LbL based on weak polyelectrolytes. The charge density (ionization degree, $I_D$) of the adsorbing polyelectrolyte is controlled by the pH, which has an impact on the polyelectrolyte conformation in solution, and therefore on the composition and structure of the multilayer system. When highly ionized ($I_D \rightarrow 1$), the polymer chains adopt a flat or rod-like conformation leading to thinner films. For example, for PAH/PAA LbL, the thickness of PAA layer can be modified from 5 to 80 Å over a pH range of 2.5 to 8.5.[20]

*Nature of counterions*

Nature of counterions can strongly affect the LbL growth. Ions can be categorized as kosmotropic (highly hydrated) and chaotropic (weakly hydrated). Regarding hydration, anions

have significant effect on water molecules than the cations. Kosmotropes are known to favor order and stability of water-water interactions. This results in strong and stable interactions between the polyelectrolytes, leading to thinner films. However, the chaotropes favor disorder by destabilizing hydrogen bonding between the water molecules. This results in reduction of interactions between the polyelectrolytes, a phenomenon similar to high ionic strength, leading to thicker films. For instance, PDADMAC/PSS LbL was reported to show different thickness depending on the type of anion, while fixing sodium as cation **(Figure 1.4)**.[21]

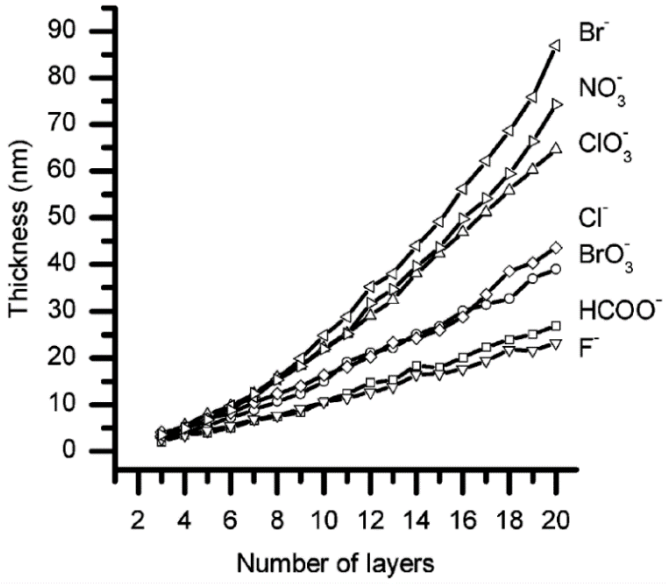


***Figure 1.4:*** *Evolution of the thickness of PDADMAC/PSS LbL films in the presence of different kinds of anions, and 0.1M sodium salt. The LbL growth switches from linear to exponential with anions from kosmotropes to chaotropes.*

*Molecular weight*

The molecular weight of the polyelectrolytes can impact the chain diffusion process. The thickness of exponentially growing CHI/HA films was reported to depend of the molecular weights of both CHI and HA, the diffusing and non-diffusing polyelectrolyte respectively.[22] The short polymer chains favor diffusion compared to long chain which can block the diffusion

process. In the example of Polyarginine (PAR)/HA LbL, the PAR chains with 30 residues were reported to diffuse within the LbL film unlike PAR-200.[23]

*1.1.5.1.2 Other interactions*

LbL films based on other interactions were also reported based on hydrogen bonds,[24] covalent bonds,[25-26] hydrophobic interactions,[27-28] charge transfer,[29] and bio-specific interactions.[30] We will give few examples of each of them.

*Hydrogen-bonding*

Apart from electrostatic interactions, hydrogen bonding is one of the most studied driving forces because it allows the insertion of uncharged molecules that can operate as hydrogen bonding donors and acceptors into multilayer structures. H-bond LbL films are influenced by pH and temperature, not the ionic strength. Rubner's team first reported multilayer buildup of polyaniline (PA) with h-bonding polymers e.g., poly(acrylamide) (PAA), poly(ethylene oxide) (PEO), and poly(vinyl alcohol) (PVA).[31] H-bonded LbL films are highly sensitive to post-buildup treatment. For example, PAA/poly(4-vinylpyridine) (PVP) LbL films disassemble above pH 6.9 due to ionization of carboxylic groups of PAA, thus inducing electrostatic repulsion inside the multilayer.[32] Thanks to the pH responsiveness, H-bonded LbL films or capsules with controlled degradation are extensively used for drug delivery.[33]

*Hydrophobic interactions*

The hydrophobic interactions play a significant role on the adsorption of proteins, polymers, nanostructures, etc. in LbL manner.[27] Hydrophobically anchored monolayer of bovine serum albumin (BSA) on a surface favored the LbL buildup with HEP such that the film bilayer composition remained the same, independent of the increasing layer pairs. Hence, contributing to the buildup of a regular LbL films with uniform thickness.[25]

*Metal-ion coordination*

Copper metal ions were first incorporated into polyelectrolyte LbL films by developing poly(copper styrene 4-sulfonate) (PSS-Cu)/PVP multilayer, thanks to the formation of coordination bonds between the copper ions, sulfonates from the PSS-Cu, and pyridine groups from the PVP.[34] The coordination driven assembly is not limited to polyelectrolytes. Caruso et al., reported the LbL assembly of tannic acid (TA) and iron (III) ions over a broad pH range, from 2 to pH 10. The buildup at high pH resulted in thick films **(Figure 1.5a)**,[35] thanks to the change in complexation state of Fe(III) from mono-complex below pH 2, to tris-complex above pH 7 **(Figure 1.5b)**.[36]

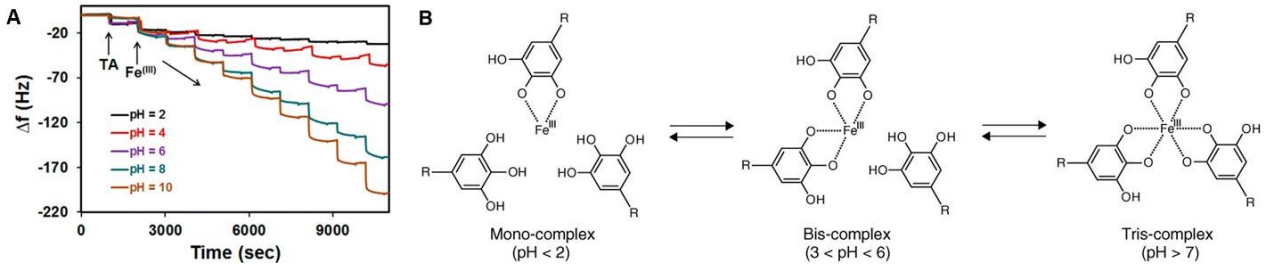


***Figure 1.5: (a)*** *Evolution of multilayer buildup of TA/Fe(III) LbL film at different pH values of TA solution, followed by QCM-D,* ***(b)*** *pH dependent transition of complexation state of TA-Fe(III).*

*Bio-specific interactions:*

Towards protein containing LbL films, bio-specific interactions have been widely explored. Thanks to the bio-specific interactions, the LbL assembly of avidin/poly(vinyl sulfate) (PVS) has been reported to increase avidin loading four times more than monomolecular deposition.[30]

*Covalent interactions*

The film stability and rigidity can be enhanced via chemical interactions to develop the most stable LbL films, contrary to the ones obtained by other interactions. For example, ionic self-assembled poly(sodium styrene sulfonate)/diazo-resins (DAR) LbL films were crosslinked by photocurable diazonium and sulfonate groups via UV exposure. The crosslinked film showed higher stability unlike the non-crosslinked one.[26] Covalent crosslinked films are probably the

most used films in various application like cell-surface interactions, drug delivery, surface patterning, electrooptical devices, catalytic substrates, anti-friction etc.[37]

#### *1.1.5.2 Methods of LbL deposition*

LbL films have been developed using various methods namely, the dipping, the spin-coating, the spray-coating, and more recently via the brushing method **(Figure 1.6)**.

##### *1.1.5.2.1 Dip coating*

The dip coating method was introduced in the 1990s using synthetic polymers to develop poly(allylamine hydrochloride)/poly(styrene sulfonate) (PAH/PSS) multilayer.[14] The substrate is immersed in the different solutions (polycation, polyanion and the rinsing buffer) **(Figure 1.6a)**. This simple technique can be used on various substrates of practically any possible shape, with economical consumption of products *i.e.*, same solutions can be used for several deposition steps. It offers a huge selection of materials, from synthetic to biological molecules, that can be deposited, and fine control on the film structure, thickness, and functionality. However, each deposition steps require prolonged time, generally between 5 to 20 minutes for each deposition or rinsing.

##### *1.1.5.2.2 Spin-coating*

The problem with long deposition time was addressed by using the spin-coating to develop LbL films on planar surfaces. This method involves dispensing a droplet of polyelectrolyte solution in the center of the surface and rotating the surface at controlled speed (rpm). The rotating surface exerts a centrifugal force on the polyelectrolyte solution causing it to spread radially outwards on the surface. Under this motion, the excess material is ejected off the surface, leaving behind a uniformly deposited layer **(Figure 1.6b)**. The required to deposit one layer is typically around 1 min which is extremely fast compared to the dip-coating. Generally, there is no rinsing step required in this method which allows a faster film deposition. The

rotation speed, viscosity or concentration, and type of polyelectrolyte impact the film roughness and thickness. High concentration of polyelectrolytes and low rotation speed led to thicker LbL films.[38] However in the case of anisotropic cellulose nanocrystals/poly(vinyl amine) (PVAm), higher rotation speed led to thicker films due to improved packing of the cellulose nanofibrils.[39] Though, spin-coating allows fast deposition time but it is limited to a planar surface with reasonable size.

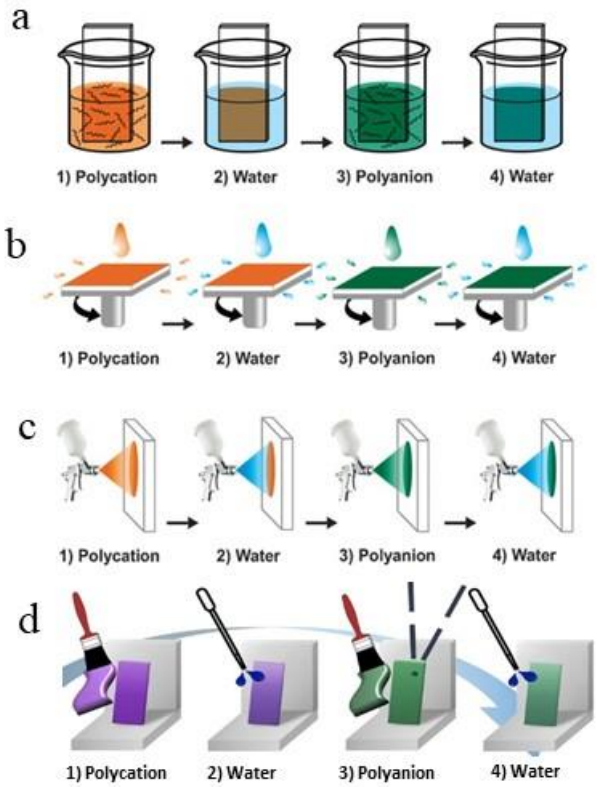


***Figure 1.6:*** *Schematic representation of the deposition methods used for the buildup of layer-by-layer films by (a) the dipping,[14] (b) the spin-coating, (c) the spray-coating,[40] and (d) the brushing[41] of polyelectrolytes solutions.*

*1.1.5.2.3 Spray-coating*

This method was first reported by Schlenoff et al. to develop PSS and poly(diallyl dimethyl ammonium chloride) (PDADMAC) LbL films.[40] Polyelectrolyte solutions and rinsing water were sprayed on the substrate held vertically to allow solution drainage under gravity **(Figure 1.6c)**. Like spin-coating, this is also a fast method which allows to coat larger surface areas,

but this process consumes a high amount of solution. Later, the method was used to develop the "Simultaneous Spray Coating of Interacting Species". First reported by Porcel et al. in 2005[42] and generalized (i) to almost any kind of polycation/polyanion systems, (ii) to polyelectrolyte/small multi-charged molecule systems, (iii) to polyelectrolyte/nanoparticles systems and even (iv) to the simultaneous spraying of two inorganic solutions.[43] This simultaneous spraying method allows reducing the buildup time of polyelectrolyte films since the spraying time can be divided by two, but the films are generally rougher and no longer structured.[44]

*1.1.5.2.4 Brushing coating*

Recently, an attractive and simple method to develop LbL films has been proposed by brushing **(Figure 1.6d)**. Unlike the dip-coating, this method is tremendously fast requiring only a few seconds of deposition time for one layer and does not require specific and expensive material. Indeed, the LbL buildup requires one brush for each polyelectrolyte, that cost less than 2 € each. The brushing process allowed to design chitosan and alginate multilayer films for drug delivery,[41] and to align a monolayer of clay (halloysite) nanotubes in strip patterns, thanks to the shearing effect of the brushing, to align human fibroblasts and bone mesenchymal stem cells along the axis of nanotubes.[45] The concentrations of solutions and the type of brush were reported to impact the film thickness and nanotopography.

## 1.2 Protein based LbL films for biomedical applications

In context of this thesis, we will mainly focus on the LbL films developed using proteins as at least one component. We are not considering the biosensing application or electrochemistry aspects using specific proteins, *i.e.*, enzymes. Synthetic and natural polymers, metal ions or particles, enzymes, peptides etc. have been extensively explored in LbL assembly. Yet, incorporation of proteins in LbL assembly is rare due to the heterogeneity of protein molecules making it hard to build in LbL manner. For instance, collagen type I and fibronectin were reported to show unsuccessful LbL buildup despite using three different buffers, native or denatured collagen, and incorporation of a PEI anchoring first layer.[46] Therefore, the state of the art is limited to successful protein LbL films compared to other polyelectrolytes. The proteins which are mostly used to develop LbL films are collagen type-I[47-54], gelatin,[55-62] fibronectin,[63-64] fibrinogen,[63] elastin,[65] laminin,[66] lysozyme,[67-68] casein,[68] BSA,[66, 69-70] etc.

In 2001, a protein-based LbL film was developed by using collagen type I (COL), a fibrillar protein mostly found in extracellular matrix, to promote cell adhesion on biomaterial surfaces.[71] COL is a triple helix of elongated fibrils containing the repetition of the glycine-proline-hydroxyproline sequence. Only five years later in 2006, the LbL assembly of extracellular matrix proteins gained huge interest to develop multifunctional biomaterials.[72] Since then, proteins in LbL assembly has increased rapidly despite various difficulties associated with their use.

### 1.2.1 Protein based LbL films for antibacterial activity

Antimicrobial surface design has attracted great attention over past few decades. Microbial contamination and infection pose severe health and economic threats. Material surface properties act as first line of defense against microbial contamination. Such contaminations/infections occur and spread via touching commonly used surfaces, food, water, biomedical devices and implants, hospital acquired infections, and so on. Moreover, increasing

resistance of bacteria towards conventional antibiotic treatments is a huge challenge to date. Hence, designing surfaces with sustainable and long-term antimicrobial properties is of vital importance with broad spectrum of applications in health and environment.

Towards antimicrobial surface design, LbL films have been widely developed to achieve mainly three kinds of surfaces, (i) antiadhesive coatings to prevent bacteria attachment, (ii) contact-killing coatings that inactivate bacteria upon contact, and (iii) release-killing coatings that leach out antimicrobial agents **(Figure 1.7)**. A comprehensive description on how to design these coatings using organic and inorganic molecules, antimicrobial peptides, nanoparticles etc. is nicely reviewed elsewhere.[73]

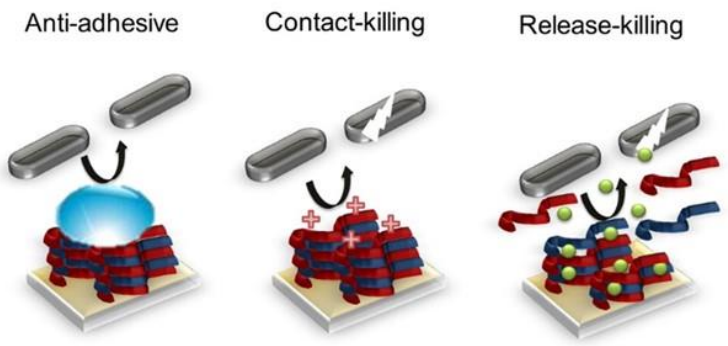


***Figure 1.7:*** *Schematic illustration of three major strategies to develop antimicrobial multilayer films.*[73]

Bilayer of Gelatin (Gel) and chitosan (CHI) LbL film was reported to inhibit the growth of *Escherichia coli* (*E. coli*) upon contact with both CHI and Gel showing antibacterial property against *E. coli* and *Listeria monocytogenes*, in solution.[74] Gel is obtained by the controlled hydrolysis of the fibrous insoluble COL present in the bones and skin generated as waste during animal slaughtering and processing. Antimicrobial activity of the Gel solution was attributed to the presence of oligopeptide chains ($M_w$ < 1000 Da), presenting specific amino-acids sides chains obtained by hydrolysis of the protein.[75-76] CHI, a polysaccharide derived from chitin, is known to be antibacterial against numerous pathogens due to its positive charges able to disturb

the negatively charged bacterial membranes.[77] Upon comparison with Gel/CHI blend films developed by drop casting, the multilayer films showed superior antifungal and antimicrobial properties upon contact for preservation of melons allowing the preservation of fruit texture and weight when used as edible coating.[78] Gel/TA LbL films were developed to incorporate N-diazeniumdiolates, a nitric oxide generating moiety. The developed Gel/TA LbL films were used as a controlled delivery system for nitric oxide gas release to reduce *Staphylococcus aureus* (*S. aureus*) planktonic growth of 35% with no cytotoxicity towards human dermal fibroblasts.[79]

Besides Gel, collagen (COL) was used to develop LbL films with TA,[80] hyaluronic acid (HA),[81] Lysozyme,[82] CHI,[83] and a broad spectrum antimicrobial peptides.[84] Compared to Gel, COL is not antimicrobial then an antibacterial agent is always incorporated to achieve the antibacterial property. Lysozyme is an antimicrobial enzyme produced by animals able to hydrolysis 1,4-beta-linkages between N-acetylmuramic acid and N-acetyl-D-glucosamine residues in peptidoglycan, which is the major component of gram-positive bacterial cell. COL/lysozyme was used to coat silk fibroin and nylon 6 electrospun nanofibrous mats. The functionalized mats were reported to show strain selective antibacterial property with >98% reduction of viable *S. aureus*, compared to *E. coli*.[82] CHI-ending $(COL/CHI)_{10}$ LbL films functionalized on silk fibroin/polycaprolactone nanofibrous mat showed excellent killing efficacy of around 88% and 80% against *S. aureus* and *E. coli*, respectively. The activity was associated to polycationic nature of CHI, around 30-35% killing efficacy comes from one CHI layer.[83] HA-ending COL/HA LbL films, *i.e.* HA-terminating layer, showed anti-adhesive property with 40% less attachment of *E. coli* (strain DH10B).[81] The antibacterial property was improved by incorporating an antimicrobial peptide LL-37 by physical adsorption or chemical modification. In both cases, a strong *E. coli* inhibition was observed on the surface of the film with less than 3% of bacterial adhesion and in the surrounding bacteria culture medium. Both antiadhesive

and contact-killing properties were thus obtained. The incorporation of Tet213, an antimicrobial peptide, in HA/COL IV films was done by its chemical grafting on COL IV (collagen type-IV). The LbL film, built at acidic pH, showed a long lasting release-killing effect against a Gram-positive (*Staphylococcus aureus*) and a Gram-negative bacteria (*Porphyromonas gingivalis*) up to 30 days, thanks to the sustained release of the peptide in physiological medium (pH 7.4).[84] The release is due to the dissolution of HA/COL IV by change of the overall charge of COL IV (pI 7.5-8) at pH 7.4.

### 1.2.2 Protein based LbL films promoting mammalian cell adhesion

A primary function of a biomaterials is to repair, conserve, or promote tissue function or entire organ. The surface properties of the biomaterials are determining factors for their successful implantation. Therefore, a lot of attention has been devoted to design cell-biomaterial interface, where cells come in contact with the biomaterials. Surface design becomes essentially important to favor mammalian cell adhesion and subsequently proliferation and differentiation to ensure successful bio-integration. The LbL films have widely been used to modulate cell response on a surface via increase in stiffness by ionic or covalent cross-linking, introducing positive charge, and cell recognition molecules **(Figure 1.8)**.

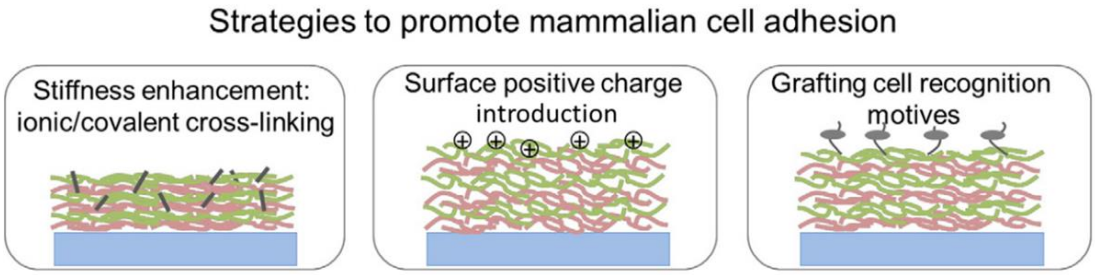


***Figure 1.8:*** *Schematic representation of the LbL strategies to promote cell adhesion.*[85]

LbL films of overall polyelectrolytes to modulate cell-surface interactions have been reviewed elsewhere.[85-86] **Table 1.1** summarizes protein-based LbL films developed to favor cell

adhesion. COL, Gel and Fibronectin (Fn) have been mostly used to promote cell adhesion by recognition of pro-adhesive moieties (Arginine-Glycine-Aspartic, RGD, sequence). RGD sequence makes up an anchoring place for both α and β integrin receptors, which enhances adhesion and proliferation of many kinds of cells. Elastin, a fibrous ECM protein composed of single tropoelastin subunits, presents repeating amino acids sequence VPG (V: valine, P: proline, G: glycine). This protein was also used due to the presence of RGD domain. Moreover, the cell-elastin interactions are also attributed to elastin receptors, G protein-coupled receptors and integrins.[87]

***Table 1.1:*** *A summary of protein based LbL films reported to modulate mammalian cell response.*

*Here DS = dextran sulfate, HA = hyaluronic acid, COL = collagen type 1, HEP = heparin, Gel = gelatin, PS = polystyrene, ELP = elastin, Fn = fibronectin, Ln = laminin, CHI = chitosan, PRM = protamine, PAA = polyacrylic acid, PDDA = poly(dimethyl diallyl ammonium chloride), PDADMAC = Poly(diallyl dimethylammonium chloride), CA = cellulose acetate, PLL = poly L-lysine, PDMS = Polydimethylsiloxane, Ti = titanium, PLLA = Polylactic acid, PEI = poly(ethyleneimine), PCL = polycaprolactone, PSS = poly(styrene sulfonate), NPs = nanoparticles, NFs = nanofibers, AuNPs = gold nanoparticles, TPPA = photosensitizer-coupled polypeptides, PAN = , polyacrylonitrile, PLGA = Poly Lactic-co-Glycolic Acid, Dex = dextran, SiCHA = silicon-carbonated hydroxyapatite, CaP = calcium phosphate, BSA = bovine serum albumin, DNA = deoxyribonucleic acid, HUVECs = Human umbilical vein endothelial cell, MSCs = Mesenchymal stem cells, bFGF = basic fibroblast growth factor*

| LbL system | Substrate | Type of cells | Ref. |
|---|---|---|---|
| **Collagen(COL) based multilayers** | | | |
| COL/PSS | - | C2C12 mouse myoblasts | [71] |
| COL/HA | PLLA | Cell-mat interaction | [88] |
| COL/HA | - | Chondrosarcoma | [89] |
| COL/HA | - | NIH-3T3 mouse fibroblasts | [90] |
| COL/HA | PDMS | Rat model | [91] |
| COL/HA, CHI/HA | Ti | MC3T3-E1 fibroblasts | [92] |
| COL/HA (x RGD peptide) | Ti | MC3T3-E1 fibroblasts | [93] |
| COL/oCS, HA | - | Murine embryonic fibroblasts | [94] |
| COL/HEP | - | HUVECs, shear degradation | [95] |
| COL/bFGF/HEP | - | bFGF growth factor delivery | [96] |
| COL/HEP | - | interferon-γ expression, hMSC | [97] |
| CHI/$(HA/COL\ IV)_n$ + LAMA3 gene | Ti | Implant-gingival epithelium bio-sealing | [98] |
| COL/CHI | PCL/CA NFs | Human dermal fibroblasts | [99] |
| COL/Alg | PLA NFs | Human periodontal ligament cells | [100] |

| | | | |
|---|---|---|---|
| COL/Alg (crosslinking with genipin) | PDMS stretching | NIH-3T3 mouse fibroblasts | [101] |
| COL/ Lumican | - | Hepatic stellate cells, myoblast | [102] |
| (Methylated COL/succinylated COL) | Microfluidic | hepatocyte cultures | [103] |
| COL | PAN, PLGA NFs | L-929 fibroblasts | [104] |
| COL/PAA on NPs | - | C2Cl2 myoblasts | [105] |
| COL/SiCHA | PLA films | MSCs proliferation | [106] |
| AuNPs-COL/TPPAs-PLL | $SiO_2$ glass | NIH-3T3 mouse fibroblasts | [107] |
| PEI-(AuNPs-COL/PLL) | - | NIH-3T3 mouse fibroblasts | [108] |
| COL/CaP enzymatic mineralization | - | L929 fibroblasts | [109] |
| **Gelatin (Gel) based multilayers** | | | |
| Gel/PDADMAC, Gel/CHI | CHI unstable | L-929 mouse fibroblast | [110] |
| Gel/Alg, COL IV/Ln, BSA, DS, PLL | PS | Mouse embryonic stem cells | [111] |
| Gel/Fn LbL lift-off | Micropattern | Rat aorta smooth muscle cells | [112] |
| Gel/Fn | | Smooth muscle cells | [113] |
| Gel/PSS | PLLA | Chondrocyte culture | [114] |
| **Fibronectin (Fn) based multilayers** | | | |
| Fn/PLL | - | Biocompatible | [115] |
| Fn/PLL, Fn/Gel, Fn/ELP, Fn/HEP, Fn/Dex | - | Cell adhesion | [60] |
| $(PDDA/PSS)_3/(PLL/Fn)_3$ | - | Biocompatible coating | [116] |
| PSS/PDDA/Fn, Vitronectin/PEI/antibody | - | Cell-surface interaction | [117] |
| **Elastin based multilayers** | | | |
| $ELP^+/ELP^-$ | - | Biocompatible coating | [118] |
| ELP-PEI/ELP-PAA | - | Cell adhesion | [119] |

### 1.2.3 Protein based LbL films for drug and gene delivery

Sustained and controlled release of drug formulations is essential for higher drug efficiency and lower risks of toxicity. To this aim, the LbL technology offers enormous possibilities and is a far better replacement to conventional drug encapsulation techniques.[120] For instance, the LbL offers nanometric control over the order, location, and concentration or loading of various polymer layers.[121] The LbL films can release the desired compounds via various triggers such as the ionic strength, pH, temperature, photo/electric stimulation, hydrolytic and enzymatic degradation.[72] In **Table 1.2** the protein based LbL films reported for drug and gene delivery

are summarized in terms of the LbL system developed, nature of trigger mechanism used to stimulate the delivery, the type of bioactive species, and the intended application.

***Table 1.2:*** *A summary of protein based LbL drug and gene delivery systems.*

*Here DS = dextran sulfate, HA = hyaluronic acid, COL = collagen type 1, HEP = heparin, Gel = gelatin, CMC = carboxymethyl cellulose, CHI = chitosan, PRM = protamine, PDDA = poly(dimethyl diallyl ammonium chloride), PEI = poly(ethyleneimine), PSS = poly(styrene sulfonate), NPs = nanoparticles, TA = tannic acid, EGCG = Epigallocatechin gallate, Ova = ovalbumin, DMPA = l-α-Dimyristoylphosphatidic Acid, WPI = Whey Protein Isolate, GF = growth factor, BSA = bovine serum albumin, HSA = human serum albumin, Lys = lysozyme, NGF = Neurotrophin growth factor, IgG = immunoglobulin G, DNA = deoxyribonucleic acid, PBS = phosphate-buffered saline, BLG = β-Lactoglobulin, THCP = 3,4,9,10-tetra-(hectoxycarbonyl)-perylene, CpG = Cytosine-phosphate diester-Guanine rich, DOX = doxorubicin hydrochloride, HGF = hepatocyte growth factor, TGF-β1 = Transforming growth factor beta, PDGF = Platelet-derived growth factor.*

| **LbL system** | **Trigger** | **Drug/application** | **Ref.** |
|---|---|---|---|
| **Collagen (COL)based multilayers** | | | |
| COL/HA, capsules | Collagenase degradation | BSA / wound healing | [122] |
| COL/DS, capsules, s-layer protein | - | - | [123] |
| COL or GFs/DS, HEP | Diffusion, erosion | TGF-β1, PDGF-ββ, IGF-1/ *in-vitro* TK173 human renal fibroblast, neonatal rat dermal fibroblasts | [124] |
| COL/Sirolimus | Collagenase degradation | Sirolimus / stents | [125] |
| **Gelatin (Gel) based multilayers** | | | |
| Gel/EGCG | - | Dextran, antioxidant | [126] |
| Gel/CMC, PRM/DS | pH | EGCG, anticancer | [127] |
| Gel/DS | $Ca^{2+}$, pH | Minocycline, medical implants | [128] |
| Gel/Silk fibroin | PBS degradation | trypan blue, inulin, BSA | [129] |
| Gel/DS, HEP | PBS degradation | NGF, Lys / neural prostheses | [130] |
| $SiO_2$NP/Gel/ Phor21-βCG(ala) | Ionic strength | Phor21-βCG(ala) / anticancer | [131] |
| Gel/Alg, G/DS | - | Naproxen / anti-inflammatory | [132] |
| Gel/PSS nanocapsules | PBS degradation | Lornoxicam/anti-inflammatory | [133] |
| Gel/PSS | pH | Furosemide | [134] |
| Gel/PDDA capsules | pH | - | [135] |
| Gel/$SiO_2$ | - | - | [136] |

| | | | |
|---|---|---|---|
| **Albumins based multilayers** | | | |
| BSA/PDADMAC | - | - | [137] |
| BSA/IgG | - | - | [138] |
| Py-BSA, Cu-BSA/CHI | pH | Curcumin, Doxorubicin/ therapeutics | [139] |
| BSA/DNA | proteinase K | DNA | [140] |
| BSA/glutaraldehyde | pH | Dextran | [141] |
| BSA NPs/CHI | pH | Doxorubicin | [142] |
| BSA/PEI | Physiological | Miramistin | [143] |
| Albumin/PEI | - | Albumin / cardiovascular | [144] |
| BSA, pepsin/TA | pH | IgG, BLG/oral delivery | [145] |
| BSA/TA | α-chymotrypsin, trypsin | THCP | [146] |
| BSA/polyphenols | pH | IgG, site-selective bioactive | [147] |
| HSA/DMPA | pH | Ibuprofen | [148] |
| HSA/DMPA | - | - | [149] |
| Ovalbumin/Poly-1 | Hydrolytic | Ova, CpG/ transcutaneous | [150] |
| **Protamine (PRM) based multilayers** | | | |
| PRM/DS | - | - | [151] |
| PRM/Alg | pH | α-chymotrypsin | [152] |
| PRM/Alg | pH | DOX, anticancer | [153] |
| PRM/HA | | Gambogic acid / *in-vivo anticancer* | [154] |
| PRM/HEP | pH, trypsin | Doxorubicin/anticancer | [155] |
| PRM/PSS | pH | Ibuprofen, site-selective | [156] |
| PRM/CMC | Magnetic field | Doxorubicin/anticancer | [157] |
| PRM/HGF-pDNA | | HGF/ transfection | [158] |
| Gel/CMC, PRM/DS | pH | EGCG, anticancer | [127] |
| **Others** | | | |
| WPI/pectin | - | - | [159] |

### 1.2.4 Protein based LbL films for bone tissue engineering

Failure to osseointegration, formation of interfacial fibrous tissue between bone and implant, is a major reason for implant rejection by host. Titanium and its alloys are predominantly utilized as dental and orthopedic implants and related devices. Though titanium provides better mechanical/biological performances and corrosion resistance, but certainly does not directly connect to the bone rather exhibits passive-osseointegration. A brief introduction to bone tissue

engineering including differentiation and the types of cells involved can be found elsewhere.[160] Various studies reported the modifications of titanium surfaces through the LbL technique. Subsequently, different LbL films emerge to address various aspects of bone tissue engineering. They can regulate cell behavior on host tissue/implantable devices' interface by producing osteoinductive or osteoconductive extracellular microenvironment to later induce osteogenesis (*de-novo* bone formation), also by maintaining sterility.

Thanks to the nonimmunogenic properties of Gel and osteoconductive ones of CHI, titanium functionalized by Gel/CHI LbL films showed a better adhesion, proliferation and viability of osteoblasts in comparison to the uncoated substrate.[161] Incorporation and subsequent release of Zn ions, below toxicity concentration (2 ppm), from Gel/CHI coatings showed better proliferation and cell activity up to 7 days than the uncoated titanium substrate. Thanks to Zn ions, such coatings showed also reduced adhesion and growth of *S. aureus* and *E. coli*.[162]

#### *1.2.4.1 Drug delivery*

Drug delivery to the host site via LbL films is a practical option considering the advantages of prolonged bioactivity and controlled release. Surface modification of titanium substrate through drug loaded Gel/CHI based nanoparticles carriers was reported with different drugs, such as vancomycin to inhibit *S. aureus* ,[163] β-estradiol to upregulate osteoblast (proliferation, alkaline phosphatase expression and mineralization) and to reduce osteoclast growth. This makes this coating a favorable candidate in clinical application as bone hemostatic coatings especially for patients with osteoporosis. For this purpose, β-estradiol loaded mesoporous silica nanoparticles modified with Gel/CHI LbL films, were embedded into Gel/CHI LbL coatings. Upon enzymatic degradation of Gel/CHI LbL coating in physiological conditions, the adhered osteoblasts can uptake the drug loaded nanocarriers triggering the release.[164] Besides the delayed degradation in physiological medium, enzymatic degradation can also occur via matrix metalloproteinase secretions triggered by cell/material interactions, specific to gelatin or

collagen. Growth factor loaded Gel/CHI films with fibronectin terminating layer demonstrated sustained release of gelatin and growth factor over 14 days and were put in contact with Mesenchymal stem cells (MSCs). Bone morphogenetic protein (BPM-2) was used as it play an important role in postnatal bone formation. MSCs displayed higher osterix, osteocalcin, osteopontin, alkaline phosphatase, COL type-I, and Runt related transcription factor 2 expressions after 7 and 21 days in comparison to the uncoated substrate. *In-vivo* study suggested the *de-novo* bone formation was pronounced with BMP-2 release.[165] Insulin-like growth factor incorporated Gel/CHI coated titanium implants demonstrated significantly higher osteogenic differentiation (proliferation, ECM maturation and mineralization) of bone marrow MSCs and new bone formation in osteoporotic rat model.[166] Titanium porous scaffold was coated with Gel/CHI LbL film loaded with BMP-2 displaying higher alkaline phosphatase expression (2-fold), mineralization (4-fold), and antibacterial activity against *S. aureus* up to 8-log reduction in planktonic and adherent bacteria in comparison to the uncoated scaffold. *In-vivo* subcutaneous implantation in Fisher rats revealed the connective tissue formation with no foreign body response after 8 weeks.[167]

Icariin is a natural flavonoid from *Epimedium* herbs potent to treat osteoporosis, trigger estrogen receptors and inhibit osteoclast differentiation. Icariin was delivered from titanium nanotubes (TNT) covered by Gel/CHI LbL films. In physiological conditions, the films showed delayed release, due to the diffusion of Icariin through the film, up to 5 days with initial maximum burst release within 24 h. It showed higher osteoblast proliferation, osteopontin, osteoprotegerin, type-I COL, and reduced mRNA expression.[168] Osteogenic and antibacterial properties against *S. aureus* and *E. coli* were also reported Gel/CHI-PANI coated TNT, with the chemical grafting of polyaniline (PANI) onto CHI.[169] pH triggered release of BMP-2, from methacrylate modified-Gel/N-Cl modified poly(N,N′-methylene bis(acrylamide)) LbL coated

TNTs, was found effective for osteogenic and antibacterial properties towards *S. aureus* and *E. coli*.[170]

#### *1.2.4.2 Cell differentiation*

Protein-based LbL films are frequently used to coat titanium (Ti) or related alloys. COL and hyaluronic acid (HA), both components of extracellular matrix (ECM), films dissolved in physiological conditions and lead to higher ALP, osteocalcin and gene expression of preosteoblasts after 14 days.[171] Chemical cross-linking can drastically enhance the stability of COL/HA LbL films. An *in-vivo* comparison between stable *i.e.*, cross-linked, and unstable COL/HA LbL films highlights the importance of film stability in rabbit model. Stable COL/HA films showed better osteointegration with tight *de-novo* bone-implant interfacial contact.[172] Disulfide cross-linked COL/HA can modulate the degradation time to give tunable stability in PBS. *In-vitro,* the association of RGD modified HA exhibited markedly higher adhesion, proliferation, and differentiation of murine pre-osteoblasts than uncoated Ti.[93]

Carbodiimide cross-linked COL/Alg coatings show significantly higher APL activity (12 days) of murine pre-osteoblasts when alginate is the terminating layer.[173] Fibronectin (Fn), a glycoprotein, is known to support cell adhesion, migration, proliferation, and differentiation via transmembrane integrin interactions. Fn/PLL LbL films significantly improved osteoblast adhesion and proliferation in comparison to the uncoated glass[116] and pre-osteoblast cells proliferation in comparison to Fn monolayer.[115] Hydroxyapatite (HAP), a mineral that comprises approximately 70% of the bone mass, is naturally found in bone as nanoneedles and exhibits good resorbability. Several layers of HAP nanofibers were sandwiched in Gel/CHI LbL films to obtain a lamellar stack hybrid film. HAP containing films showed better osteoblast viability, activity (more extended network), cell migration observed after scratching, significant mineralization up to 14 days, differentiation with upregulated osteocalcin and osteopontin expression.[174]

Protein based LbL films are reported to coat various substrates like PLLA, [175] SS, [176] PCL scaffold [177] and fibers, [178] PPC, [179] to name a few as substitute implant materials. Collagen and heparin (COL/HEP) multilayers increased the hydrophilicity of PLLA substrates with contact angle from 80° around 60° and showed good mouse osteoblasts adhesion after 1 day. Later after 2-3 days, the adhesion is less proficient and could be attributed to the film degradation and the nature of COL/HEP complexation. Indeed, HEP can interact with telopeptide regions of COL and block cell-binding sites.

Moreover, higher number of COL/HEP bilayers decreased the cell adhesion. It could be attributed to the change in surface topography with the decrease of the fibrillar structures coming mainly from HEP with the increase of the number of layers. The cell density up to 7 days of human MSCs is low on COL/HEP coatings, alike murine pre-osteoblast behavior. However, a comparable cell density could be observed after 14 and 28 days. Higher ALP activity and mineralization of human MSCs could be observed on COL/HEP LbL coated PLLA after 28 days.[175] By decreasing the contact angle from 70° to 58° of poly(propylene carbonate), Gel/PEI LbL films enhanced fibroblast proliferation and osteoblast differentiation.[179] A comparative study of COL was assembled with native or oxidized HA or chondroitin sulfate (CS) showed that the molecular composition of LbL films only to impact the physicochemical properties but the human adipose derived stem cells (hADSCs) adhesion and spreading. A favorable microenvironment was obtained with COL/CS films with a higher COL remodeling by the stem cells.[180] This was attributed to the higher amount of COL deposition in COL/CS films. Protamine sulfate, a polypeptide approved by FDA for treating heparin overdose or excessive bleeding disorder, gives rise to hydrophilic coatings on silicon (Si) substrates with poly(styrene sulfonate) as polyanionic counterpart. The increase in layer pair number from 20 to 240 directly impacts the surface roughness and young's modulus in hydrated state. Such

mechanical properties of the coated surfaces appear to significantly influence murine pre-osteoblasts spreading, proliferation, and differentiation (ALP activity and mineralization).[181] Polyethylene terephthalate (PET) artificial ligament grafts, coated with cationized Gel/HA LbL films, significantly suppressed the inflammatory response with superior COL type-I formation, in rabbit model for anterior cruciate ligament reconstruction.[182]

### 1.2.5 Blood contacting surfaces

Vascular tissue engineering ensures least immunogenicity and rejection of biomaterial constructs by host tissues. During hemostasis, initial wound healing cascade, aggregation of platelets and red blood cells occur, resulting in the formation of blood clots known as thrombosis. Besides being a healthy response by the body, it can block blood flow in health blood vessels. Endothelial cells that form inner layer of blood vessels, besides many other important functions, endothelial cells can modulate antithrombotic factors. Therefore, vascular tissue engineering evaluates the attachment and proliferation of endothelial cells on blood contacting biomaterial constructs.

Unfavorable host response towards blood contacting biomedical devices is being targeted by numerous surface modification strategies. Besides other methods, to cope thrombogenesis and related complications, layer-by-layer technique offered various routes over the past few decades. Unique chemical composition and concentration play important role here. For example, incorporating albumins into LbL films, plasma proteins famous for anti-thrombogenic potential by reducing non-specific adhesion. Jian Ji et al. electrostatically assembled Bovine serum albumin/poly(ethylene imine) (BSA/PEI) LbL films on poly(vinyl chloride) (PVC)[183] and stainless steel (SS)[184] surfaces. Such films, built at around physiological pH, were stable for up to 45 days in physiological medium (PBS) under static conditions with less than 10% BSA release. On multilayer coated PVC surfaces, platelet adhesion is reduced with the increase of the number of BSA/PEI bilayers, with around 0% platelet adhesion at 4

bilayers. Whereas the buildup of BSA/PEI on SS was heterogeneous. The granular structures, lateral size <100 nm, were observed for 1 bilayer and the homogeneous surface coverage was obtained after 8 bilayers which reduced the platelet adhesion by 90%, thanks to albumin.

Similarly, sulfated polysaccharide heparin (HEP), a commercially known anticoagulant drug, was incorporated into LbL films with BSA, [185-187] streptavidin, [188] Fn, [189-190] and COL. BSA/HEP LbL films were used to functionalize PVC[185], ELISA polystyrene (PS) surfaces [186] and poly(ether sulfone) (PES) foils.[187] Built at pH 3.9 on PVC sheets, BSA/HEP films are unstable in PBS and were compared to cross-linked BSA/HEP films. The effect of the cross-linking by glutaraldehyde (GA) and the ending layer was investigated on platelet attachment and clot formation. HEP-ending BSA/HEP films showed no clotting up to 20 min irrespective of the cross-linking. While cross-linked BSA-ending BSA/HEP films prevented the clot formation for only 6 min. Higher anticoagulant efficiency of uncross-linked films was attributed to the release of HEP.[185] On PS substrates, BSA/HEP films built at pH 4 and cross-linked by GA showed a reduced platelet adhesion with the increase of bilayers. This result was similar with only BSA crosslinked LbL films. Dried and reswollen $(BSA/HEP)_3$ coatings showed insignificant increase in platelet attachment. HEP once incorporated into LbL films loss its thrombin inhibition by less than 10%, perhaps due to HEP interactions within LbL assembly. Thrombin inhibition efficacy was also improved by increasing number of bilayers.[186] BSA/HEP multilayers with two kind of HEP (standard, and high anticoagulant fraction) were built at pH 4 on PES foils. Interestingly, the type of HEP solely affected the biological properties of LbL films. Platelet adhesion was roughly comparable on BSA/HEP and BSA control coatings. But the coagulation activation was pronounced with high anticoagulant fraction HEP. Such coatings could be used in blood purification systems.[187] Heparinylated multilayers were constructed using streptavidin/biotin bio-specific interaction on Ti. The films showed reduced platelet adhesion and enhanced clotting time.[188]

Collagen (COL), a major part of mammalian body protein content, is known to promote cell adhesion, proliferation, and differentiation through cell receptor-amino acid sequence interactions. Titanium was modified by COL/HEP using electrostatic LbL assembly. The coated surfaces shows decreased platelet adhesion and activation, and increment in the clotting time.[191-192] Oxidized dopamine (oDOP) used as precursor layer on Ti allowed to obtain COL/HEP LbL films with higher thickness, prolonged thromboplastin activation time, lower hemolysis ratios and platelet coverage.[193] COL/HEP coatings were compared with DOP/HEP on Ti substrates. Though DOP/HEP showed a better adhesion of the coating and stability of the film, COL/HEP is better at maintaining the anti-coagulant efficiency.[194] Yet film's stability over prolonged time remains a challenge. COL can provide favorable environment for the endothelialization of implants.

Endothelial cells (ECs) form inner layer of blood and lymphatic vessels. ECs possess antithrombogenic potential by maintaining a physiological barrier between outer host tissue and circulating blood. Thrombosis or incomplete endothelialization can cause other damages like restenosis that leads to blood vessel narrowing by increased neointimal formation and host tissue remodeling. Rapid endothelialization is considered as a better and long-lasting solution for blood contacting surfaces. [195-197] Combining the benefits of COL biocompatibility and HEP anticoagulant capacity, COL/HEP coatings on SS intravascular stents showed antithrombic properties with good adhesion and proliferation towards human umbilical vein ECs. [195] *In-vivo* assessments were performed to better elucidate the vascularization potential of multilayer films. A better angiogenesis was obtained with COL/HEP coated porous hydroxyapatite scaffolds with enhanced mechanical properties using the chicken chorioallantois membrane (CAM) *in-vivo* model. [196] COL IV/HEP modified Ti surfaces exhibited new angiogenesis, new blood vessels formation, after 15 days in dog femoral artery model. [197]

Another perspective within vascularization approach is to develop multifunctional coatings with selectivity towards ECs to support early and fast endothelialization. For this, COL/HEP LbL films were immobilized with EC sensitive REDV peptide. Hydrophobic, Teflon (ePTFE) films were coated with COL/HEP films and showed weak platelet activation and adhesion, prolonged coagulation time and reduced hemolysis. REDV containing films showed enhanced early cell attachment, proliferation (cell density after 72 h) and cell activity. [198] The delivery of growth factor to the host site can potentially enhance endothelialization and angiogenesis. However, their controlled delivery is challenging due to extremely small half-life of growth factors (less than 1 hour) and susceptibility to degradation in physiological environment or under the action of enzymes.[194] Their embedding into LbL films could overcome this issue.[199] Prolonged release (above 35 days) of basic fibroblast growth factor from COL/HEP LbL films showed enhanced angiogenesis of subcutaneous tissue of rat model, i.e. high blood vessels' density and diameter. [194] Antibodies can improve EC specificity by their cell-surface antigen interactions. LbL assembly provides a platform for antibody (Ab) immobilization to selectively capture EC from the circulating blood for vascular tissue engineering. CD34 is one kind of cell surface antigen, which is specifically presented on vascular ECs, EPCs, and hematopoietic progenitor cells. Few examples are reported here. Endothelial progenitor cells (EPCs) are more selective for endothelial layer formation. Electrostatically immobilized CD34 Ab into COL/HEP LbL films on Ti surface formed compact EC lining just after 2 days, [200] compared to 3 days reported for COL/HEP films without the antibody. [201] Stable under static and flow conditions, COL/HEP LbL films loaded with CD34 Ab immobilized on SS stents showed enhanced *in-vitro* early attachment (1 h) of ECs and significantly reduced neointimal formation in rabbit femoral artery model *in-vivo*. However, SMCs showed comparable early adhesion on COL/HEP LbL with or without CD34.[202]

Commercially available ePTFE grafts were functionalized with COL/HEP LbL loaded with anti-CD 133 Ab. CD133 is more specific than CD34 as a surface marker for endothelial progenitor cells. Antibodies functionalized grafts showed enhanced EC adhesion and *in-situ* rapid early endothelialization in a porcine carotid artery transplantation model. However, further investigations with smaller diameters (< 6mm) of the grafts and host relevant antibodies are essential.[203] Yet, with human mesenchymal stem cells (hMSCs), the films exhibit higher ALP, h-COL1, h-ALP mRNA, h-OPN mRNA, h-OC mRNA expressions compared to unmodified Ti.[203] Our group investigated the effect of chemical cross-linking on endothelialization of COL/ALG LbL films. Genipin, a natural plant derived agent, crosslinked coatings showed rapid attachment of HUVECs within 1 h, leading to a confluent layer in 5 days.[204]

Fibronectin (Fn), a glycoprotein, is important based on its interaction with white blood cells. The effect of surface chemistry of PU (its ionic nature and hydrophobicity) on Fn/PLL LbL deposition was studied regarding Fn conformation within the multilayers and the response of monocytes. Fn interacts with PLL in LbL assembly such that its N-terminal domains are abundantly available on the functionalized PU surface. Polycationic PLL interacts with negatively charged cell binding domain and can also react with negatively charged sub-domains with C-terminal, rendering their low availability. Because monocytes are activated via VLA-5 (RGD domain) and VLA-4 (C-terminal) of Fn, their unavailability results in suppressing monocyte activation. Opposite results were observed on high ionic and high hydrophobic PU substrate due to relatively lower availability of N-domain. A strong Fn unfolding could render some Fn domains available for the antibodies to recognize.[190]

### 1.2.6 Neural applications

Protein based LbL films can provide physicochemical as well as bio-specific cues for attachment, proliferation, and differentiation of neural cells.

Laminin (Ln) is known to favor neuron adhesion, proliferation, and differentiation by integrin specific interactions. Fn and laminin (Ln), a tri-peptide glycoprotein, were used with poly(D-lysine) to build Fn/PDL or Ln/PDL on silicon rubber functionalized by $(PSS/PEI)_3$ precursor layer. Stable in PBS for 30 days, both films showed comparable neuron attachment, differentiation and neurite outgrowth with elongated shape (lactate dehydrogenase and fluorescence cellular metabolism assays).[205] Silicon microelectrode arrays (Si MEAs) can detect neural activity *in-vivo*. But their long-term performance, in terms of impedance, is compromised by fibrous encapsulation and scar tissue development. Si MEAs were coated with Ln/PEI, Gel/PEI, and Gel/CHI LbL films. Ln LbL films showed the highest attached neuron density (4 h) and neurite outgrowth with clearly observable growth cones and network connections. Comparing Ln and Gel based films, the cell spreading is better on Ln based films with least aggregation. Moreover, neurites are longer and thicker. Gel/CHI showed least attached neuron density in 4 h in comparison to Gel/PEI. The authors suggested that the interpenetration of underlying bulky CHI chains renders fewer gelatin sites available for neuron attachment, in comparison linear PEI chains. Nevertheless, the neurite outgrowth was comparable to Gel/PEI after 24 and 48 h.[206] Similar results were reported for Gel/CHI LbL films coated on PLLA electrospun fibers. Where the cell viability decreased considerably with CHI as terminating layer. Moreover, the number and length of dendrites (a differentiated form of neurons responsible for signal transfer) were higher with Gel/CHI multilayers irrespective of the ending layer compared to control monolayers of gelatin or chitosan. Gelatin, denatured collagen, can support cell adhesion and differentiation due to the presence of cell binding RGD and various integrin domains.[207] Ln was also assembled with CHI in LbL manner to coat PLLA electrospun fibers. Ln/CHI coatings were stable in PBS at 37°C with less than 10% loss of laminin after 20 days. The neuron adhesion, viability, neurite length, and proliferation improved by increasing the number of Ln/CHI bilayers (from 1 to 5) with DRG neurons and

neuronal stem cells (NSCs). The better performance of Ln/CHI films is associated with the higher amounts of laminin incorporated with each bilayer. [208] Wu et al., demonstrated a decreasing trend for neuron cell density and neurite length with increasing number of bilayers of COL/HA from 4 to 8. The adhesion and outgrowth of hippocampal and cortical neurons showed preference towards HA/PAH and COL/HA LbL films, respectively. HA-ending films also showed attachment and neurite outgrowth even though HA is known as non-adhesive towards neurons. It was explained by higher roughness or heterogeneity of COL/HA films (ending with negatively charged HA) rendering fewer polycationic COL sites exposed on the surface for the neurons to attach.[209]

## 1.3 Conclusion

Despite of tremendously increasing interest in protein LbL research (two thousand publications per year and exponentially growing),[210] the literature on the use of therapeutic proteins is limited (a few hundred publications only) and most data is reported with enzymes. The reason might be the involvement of more complications such as molecular nature of protein, ions and counterions, substrate properties, buffers, etc., involved in using proteins, unlike conventional polyelectrolytes. This makes the analysis and understanding of the system more challenging. The right choice of the proteins-polyelectrolyte couple, LbL buildup conditions and the analysis methodologies can help in translation of the developed LbL to the desired application.

## 1.4 Bibliography


1. Kuhn, H., Present status and future prospects of Langmuir-Blodgett film research. *Thin Solid Films* **1989,** *178* (1), 1-16.
2. T. Terada, R. Y. a. T. W., Experimental studies on colloid nature of Chinese black ink. Part I. *Scientific papers of the Institute of Physical and Chemical Research* **1934,** *23* (482), 173-184.
3. Rayleigh, Surface Tension. *Nature* **1891,** *43* (1115), 437-439.
4. Rayleigh, XXXVI. Investigations in Capillarity:—The size of drops.—The liberation of gas from supersaturated solutions.—Colliding jets.—The tension of contaminated water-surfaces. *The London, Edinburgh, and Dublin Philosophical Magazine and Journal of Science* **1899,** *48* (293), 321-337.
5. Langmuir, I.; Schaefer, V. J., Monolayers and Multilayers of Chlorophyll. *Journal of the American Chemical Society* **1937,** *59* (10), 2075-2076.
6. Blodgett, K. B., Films Built by Depositing Successive Monomolecular Layers on a Solid Surface. *Journal of the American Chemical Society* **1935,** *57* (6), 1007-1022.
7. Blodgett, K. B.; Langmuir, I., Built-Up Films of Barium Stearate and Their Optical Properties. *Physical Review* **1937,** *51* (11), 964-982.
8. Ariga, K., Don't Forget Langmuir–Blodgett Films 2020: Interfacial Nanoarchitectonics with Molecules, Materials, and Living Objects. *Langmuir* **2020,** *36* (26), 7158-7180.
9. Langmuir Films. https://www.nanoscience.com/techniques/langmuir-films/
10. Ulman, A., Formation and Structure of Self-Assembled Monolayers. *Chemical reviews* **1996,** *96* (4), 1533-1554.
11. Jung, G.-Y.; Li, Z.; Wu, W.; Chen, Y.; Olynick, D. L.; Wang, S.-Y.; Tong, W. M.; Williams, R. S., Vapor-Phase Self-Assembled Monolayer for Improved Mold Release in Nanoimprint Lithography. *Langmuir* **2005,** *21* (4), 1158-1161.
12. Jenckel, E.; Rumbach, B., Über die Adsorption von hochmolekularen Stoffen aus der Lösung. *Zeitschrift für Elektrochemie und angewandte physikalische Chemie* **1951,** *55* (7), 612-618.
13. Nylander, T.; Samoshina, Y.; Lindman, B., Formation of polyelectrolyte–surfactant complexes on surfaces. *Advances in colloid and interface science* **2006,** *123-126*, 105-123.
14. Decher, G., Fuzzy Nanoassemblies: Toward Layered Polymeric Multicomposites. *Science* **1997,** *277* (5330), 1232-1237.
15. Schlenoff, J. B.; Ly, H.; Li, M., Charge and Mass Balance in Polyelectrolyte Multilayers. *Journal of the American Chemical Society* **1998,** *120* (30), 7626-7634.
16. Salomäki, M.; Vinokurov, I. A.; Kankare, J., Effect of temperature on the buildup of polyelectrolyte multilayers. *Langmuir* **2005,** *21* (24), 11232-40.
17. Lvov, Y.; Decher, G.; Moehwald, H., Assembly, structural characterization, and thermal behavior of layer-by-layer deposited ultrathin films of poly(vinyl sulfate) and poly(allylamine). *Langmuir* **1993,** *9* (2), 481-486.
18. Decher, G.; Schmitt, J. In *Fine-Tuning of the film thickness of ultrathin multilayer films composed of consecutively alternating layers of anionic and cationic polyelectrolytes*, Trends in Colloid and Interface Science VI, Darmstadt, 1992//; Helm, C.; Lösche, M.; Möhwald, H., Eds. Steinkopff: Darmstadt, 1992; pp 160-164.
19. Ladam, G.; Schaad, P.; Voegel, J. C.; Schaaf, P.; Decher, G.; Cuisinier, F., In Situ Determination of the Structural Properties of Initially Deposited Polyelectrolyte Multilayers. *Langmuir* **2000,** *16* (3), 1249-1255.
20. Shiratori, S. S.; Rubner, M. F., pH-Dependent Thickness Behavior of Sequentially Adsorbed Layers of Weak Polyelectrolytes. *Macromolecules* **2000,** *33* (11), 4213-4219.

21. Salomäki, M.; Tervasmäki, P.; Areva, S.; Kankare, J., The Hofmeister Anion Effect and the Growth of Polyelectrolyte Multilayers. *Langmuir* **2004,** *20* (9), 3679-3683.
22. Kujawa, P.; Moraille, P.; Sanchez, J.; Badia, A.; Winnik, F. M., Effect of Molecular Weight on the Exponential Growth and Morphology of Hyaluronan/Chitosan Multilayers: A Surface Plasmon Resonance Spectroscopy and Atomic Force Microscopy Investigation. *Journal of the American Chemical Society* **2005,** *127* (25), 9224-9234.
23. Mutschler, A.; Tallet, L.; Rabineau, M.; Dollinger, C.; Metz-Boutigue, M.-H.; Schneider, F.; Senger, B.; Vrana, N. E.; Schaaf, P.; Lavalle, P., Unexpected Bactericidal Activity of Poly(arginine)/Hyaluronan Nanolayered Coatings. *Chemistry of Materials* **2016,** *28* (23), 8700-8709.
24. Stockton, W. B.; Rubner, M. F., Molecular Layer Processing of Polyaniline via the Use of Hydrogen Bonding Interactions. *MRS Proceedings* **2011,** *369*, 587.
25. Houska, M.; Brynda, E., Interactions of Proteins with Polyelectrolytes at Solid/Liquid Interfaces: Sequential Adsorption of Albumin and Heparin. *Journal of Colloid and Interface Science* **1997,** *188* (2), 243-250.
26. Sun, J.; Wu, T.; Sun, Y.; Wang, Z.; Zhang* Jiacong Shen, X.; Sun, J.; Cao, W., Fabrication of a covalently attached multilayer via photolysis of layer-by-layer self-assembled films containing diazo-resins. *Chemical Communications* **1998,** (17), 1853-1854.
27. Kotov, N. A., Layer-by-layer self-assembly: The contribution of hydrophobic interactions. *Nanostructured Materials* **1999,** *12* (5), 789-796.
28. Lojou, É.; Bianco, P., Buildup of Polyelectrolyte−Protein Multilayer Assemblies on Gold Electrodes. Role of the Hydrophobic Effect. *Langmuir* **2004,** *20* (3), 748-755.
29. Shimazaki, Y.; Mitsuishi, M.; Ito, S.; Yamamoto, M., Preparation of the Layer-by-Layer Deposited Ultrathin Film Based on the Charge-Transfer Interaction. *Langmuir* **1997,** *13* (6), 1385-1387.
30. Anzai, J.-i.; Nakamura, N., Preparation of active avidin films by a layer-by-layer deposition of poly(vinyl sulfate) and avidin on a solid surface. *Journal of the Chemical Society, Perkin Transactions 2* **1999,** (11), 2413-2414.
31. Stockton, W. B.; Rubner, M. F., Molecular-Level Processing of Conjugated Polymers. 4. Layer-by-Layer Manipulation of Polyaniline via Hydrogen-Bonding Interactions. *Macromolecules* **1997,** *30* (9), 2717-2725.
32. Sukhishvili, S. A.; Granick, S., Layered, Erasable Polymer Multilayers Formed by Hydrogen-Bonded Sequential Self-Assembly. *Macromolecules* **2002,** *35* (1), 301-310.
33. Quinn, J. F.; Johnston, A. P. R.; Such, G. K.; Zelikin, A. N.; Caruso, F., Next generation, sequentially assembled ultrathin films: beyond electrostatics. *Chemical Society Reviews* **2007,** *36* (5), 707-718.
34. Xiong, H.; Cheng, M.; Zhou, Z.; Zhang, X.; Shen, J., A New Approach to the Fabrication of a Self-Organizing Film of Heterostructured Polymer/Cu2S Nanoparticles. *Advanced Materials* **1998,** *10* (7), 529-532.
35. Rahim, M. A.; Ejima, H.; Cho, K. L.; Kempe, K.; Müllner, M.; Best, J. P.; Caruso, F., Coordination-Driven Multistep Assembly of Metal–Polyphenol Films and Capsules. *Chemistry of Materials* **2014,** *26* (4), 1645-1653.
36. Ejima, H.; Richardson, J. J.; Liang, K.; Best, J. P.; van Koeverden, M. P.; Such, G. K.; Cui, J.; Caruso, F., One-Step Assembly of Coordination Complexes for Versatile Film and Particle Engineering. *Science* **2013,** *341* (6142), 154-157.
37. An, Q.; Huang, T.; Shi, F., Covalent layer-by-layer films: chemistry, design, and multidisciplinary applications. *Chemical Society Reviews* **2018,** *47* (13), 5061-5098.
38. Lee, S.-S.; Hong, J.-D.; Kim, C. H.; Kim, K.; Koo, J. P.; Lee, K.-B., Layer-by-Layer Deposited Multilayer Assemblies of Ionene-Type Polyelectrolytes Based on the Spin-Coating Method. *Macromolecules* **2001,** *34* (16), 5358-5360.

39. Merindol, R.; Diabang, S.; Mujica, R.; Le Houerou, V.; Roland, T.; Gauthier, C.; Decher, G.; Felix, O., Assembly of Anisotropic Nanocellulose Films Stronger than the Original Tree. *ACS Nano* **2020,** *14* (12), 16525-16534.
40. Schlenoff, J. B.; Dubas, S. T.; Farhat, T., Sprayed Polyelectrolyte Multilayers. *Langmuir* **2000,** *16* (26), 9968-9969.
41. Park, K.; Choi, D.; Hong, J., Nanostructured Polymer Thin Films Fabricated with Brush-based Layer-by-Layer Self-assembly for Site-selective Construction and Drug release. *Scientific Reports* **2018,** *8* (1), 3365.
42. Porcel, C. H.; Izquierdo, A.; Ball, V.; Decher, G.; Voegel, J. C.; Schaaf, P., Ultrathin Coatings and (Poly(glutamic acid)/Polyallylamine) Films Deposited by Continuous and Simultaneous Spraying. *Langmuir* **2005,** *21* (2), 800-802.
43. Lefort, M.; Popa, G.; Seyrek, E.; Szamocki, R.; Felix, O.; Hemmerlé, J.; Vidal, L.; Voegel, J. C.; Boulmedais, F.; Decher, G.; Schaaf, P., Spray-on organic/inorganic films: a general method for the formation of functional nano- to microscale coatings. *Angewandte Chemie International Edition* **2010,** *49* (52), 10110-3.
44. Cado, G.; Kerdjoudj, H.; Chassepot, A.; Lefort, M.; Benmlih, K.; Hemmerlé, J.; Voegel, J. C.; Jierry, L.; Schaaf, P.; Frère, Y.; Boulmedais, F., Polysaccharide Films Built by Simultaneous or Alternate Spray: A Rapid Way to Engineer Biomaterial Surfaces. *Langmuir* **2012,** *28* (22), 8470-8478.
45. Zhao, X.; Zhou, C.; Lvov, Y.; Liu, M., Clay Nanotubes Aligned with Shear Forces for Mesenchymal Stem Cell Patterning. *Small* **2019,** *15* (21), 1900357.
46. Mauquoy, S.; Dupont-Gillain, C., Combination of collagen and fibronectin to design biomimetic interfaces: Do these proteins form layer-by-layer assemblies? *Colloids and Surfaces B: Biointerfaces* **2016,** *147*, 54-64.
47. Johansson, J. Å.; Halthur, T.; Herranen, M.; Söderberg, L.; Elofsson, U.; Hilborn, J., Build-up of Collagen and Hyaluronic Acid Polyelectrolyte Multilayers. *Biomacromolecules* **2005,** *6* (3), 1353-1359.
48. Wang, Y.; Chang, D.; Dai, C.; Jiang, W.; Hou, X.; Yao, K. In *Synthesis and characterization of elastin coated with hyaluronic acid/collagen multilayer films*, 2010 3rd International Conference on Biomedical Engineering and Informatics, 16-18 Oct. 2010; 2010; pp 1736-1738.
49. Castilla-Casadiego, D. A.; Pinzon-Herrera, L.; Perez-Perez, M.; Quiñones-Colón, B. A.; Suleiman, D.; Almodovar, J., Simultaneous characterization of physical, chemical, and thermal properties of polymeric multilayers using infrared spectroscopic ellipsometry. *Colloids and Surfaces A: Physicochemical and Engineering Aspects* **2018,** *553*, 155-168.
50. Cherng, W.-J.; Dong, Z.-S.; Chou, C.-C.; Yeh, C.-H.; Pan, Y.-H., Hydrodynamic Simulation of an Orbital Shaking Test for the Degradation Assessment of Blood-Contact Biomedical Coatings. *Micromachines* **2017,** *8* (4), 132.
51. Mauquoy, S.; Dupont-Gillain, C., Combination of collagen and fibronectin to design biomimetic interfaces: Do these proteins form layer-by-layer assemblies? *Colloids and surfaces. B, Biointerfaces* **2016,** *147*, 54-64.
52. Landoulsi, J.; Demoustier-Champagne, S.; Dupont-Gillain, C., Self-assembled multilayers based on native or denatured collagen: mechanism and synthesis of size-controlled nanotubes. *Soft Matter* **2011,** *7* (7), 3337-3347.
53. de Mesquita, J. P.; Patrício, P. S.; Donnici, C. L.; Petri, D. F. S.; de Oliveira, L. C. A.; Pereira, F. V., Hybrid layer-by-layer assembly based on animal and vegetable structural materials: multilayered films of collagen and cellulose nanowhiskers. *Soft Matter* **2011,** *7* (9), 4405-4413.
54. Pinto, T. d. S.; Rodrigues, P. N. S.; Marinho, L. E. S.; Verly, R. M.; Bretas Roa, J. P.; de Oliveira, L. C. A.; Pereira, F. V.; de Magalhães, M. T. Q.; de Mesquita, J. P., Self-assembled

hybrid nanocomposite films of carbon dots and hydrolyzed collagen. *Materials Chemistry and Physics* **2019,** *230*, 44-53.
55. Ringwald, C.; Ball, V., Step-by-step deposition of type B gelatin and tannic acid displays a peculiar ionic strength dependence at pH 5. *RSC Advances* **2016,** *6* (6), 4730-4738.
56. Bahmanzadeh, S.; Ruzgas, T.; Sotres, J., Proteolytic degradation of gelatin-tannic acid multilayers. *Journal of Colloid and Interface Science* **2018,** *526*, 244-252.
57. Criado, M.; Rey, J. M.; Mijangos, C.; Hernández, R., Double-membrane thermoresponsive hydrogels from gelatin and chondroitin sulphate with enhanced mechanical properties. *RSC Advances* **2016,** *6* (107), 105821-105826.
58. Westwood, M.; Gunning, A. P.; Parker, R., Temperature-Dependent Growth of Gelatin−Poly(galacturonic acid) Multilayer Films and Their Responsiveness to Temperature, pH, and NaCl. *Macromolecules* **2010,** *43* (24), 10582-10593.
59. Rivero, S.; García, M. A.; Pinotti, A., Composite and bi-layer films based on gelatin and chitosan. *Journal of Food Engineering* **2009,** *90* (4), 531-539.
60. Nakahara, Y.; Matsusaki, M.; Akashi, M., Fabrication and enzymatic degradation of fibronectin-based ultrathin films. *Journal of Biomaterials Science, Polymer Edition* **2007,** *18* (12), 1565-1573.
61. Mengyan, L.; Kondabatni, K. K.; Tianhong, C.; McShane, M. J., Fabrication of 3-D gelatin-patterned glass substrates with layer-by-layer and lift-off (LbL-LO) technology. *IEEE Transactions on Nanotechnology* **2004,** *3* (1), 115-123.
62. Lin, Y.; Su, Z., Layer-by-layer assembly of gelatin. *Journal of Polymer Science Part B: Polymer Physics* **2008,** *46* (12), 1252-1257.
63. Berlind, T.; Poksinski, M.; Tengvall, P.; Arwin, H., Formation and cross-linking of fibrinogen layers monitored with in situ spectroscopic ellipsometry. *Colloids and Surfaces B: Biointerfaces* **2010,** *75* (2), 410-417.
64. Lehnert, M.; Rosin, C.; Knoll, W.; Veith, M., Layer-by-Layer Assembly of a Streptavidin–Fibronectin Multilayer on Biotinylated TiOX. *Langmuir* **2013,** *29* (6), 1732-1737.
65. Costa, R. R.; Ribeiro, A. J.; Rodríguez-Cabello, J. C.; Mano, J. F., Nanostructured Thin Coatings from Chitosan and an Elastin-Like Recombinamer with Acute Stimuli-Responsive Behavior. *Materials Science Forum* **2013,** *730-732*, 32-37.
66. Malmström, J.; Agheli, H.; Kingshott, P.; Sutherland, D. S., Viscoelastic Modeling of Highly Hydrated Laminin Layers at Homogeneous and Nanostructured Surfaces: Quantification of Protein Layer Properties Using QCM-D and SPR. *Langmuir* **2007,** *23* (19), 9760-9768.
67. Izumrudov, V. A.; Kharlampieva, E.; Sukhishvili, S. A., Multilayers of a Globular Protein and a Weak Polyacid: Role of Polyacid Ionization in Growth and Decomposition in Salt Solutions. *Biomacromolecules* **2005,** *6* (3), 1782-1788.
68. Lundin, M.; Elofsson, U. M.; Blomberg, E.; Rutland, M. W., Adsorption of lysozyme, β-casein and their layer-by-layer formation on hydrophilic surfaces: Effect of ionic strength. *Colloids and Surfaces B: Biointerfaces* **2010,** *77* (1), 1-11.
69. Lu, C.; Luo, C.; Cao, W., Fabrication of ultrathin films based on chitosan and bovine serum albumin and their stability studied with the radio-labeled method. *Colloids and Surfaces B: Biointerfaces* **2002,** *25* (1), 19-27.
70. Lazzara, T. D.; Lau, K. H. A.; Knoll, W.; Janshoff, A.; Steinem, C., Macromolecular shape and interactions in layer-by-layer assemblies within cylindrical nanopores. *Beilstein Journal of Nanotechnology* **2012,** *3*, 475-484.
71. Grant, G. G. S.; Koktysh, D. S.; Yun, B.; Matts, R. L.; Kotov, N. A., Layer-By-Layer Assembly of Collagen Thin Films: Controlled Thickness and Biocompatibility. *Biomedical Microdevices* **2001,** *3* (4), 301-306.

72. Tang, Z.; Wang, Y.; Podsiadlo, P.; Kotov, N. A., Biomedical Applications of Layer-by-Layer Assembly: From Biomimetics to Tissue Engineering. *Advanced Materials* **2006,** *18* (24), 3203-3224.
73. Séon, L.; Lavalle, P.; Schaaf, P.; Boulmedais, F., Polyelectrolyte Multilayers: A Versatile Tool for Preparing Antimicrobial Coatings. *Langmuir* **2015,** *31* (47), 12856-12872.
74. Pereda, M.; Ponce, A. G.; Marcovich, N. E.; Ruseckaite, R. A.; Martucci, J. F., Chitosan-gelatin composites and bi-layer films with potential antimicrobial activity. *Food Hydrocolloids* **2011,** *25* (5), 1372-1381.
75. Mosquera, M.; Giménez, B.; Ramos, S.; López-Caballero, M. E.; Gómez-Guillén, M. d. C.; Montero, P., Antioxidant, ACE-Inhibitory, and Antimicrobial Activities of Peptide Fractions Obtained From Dried Giant Squid Tunics. *Journal of Aquatic Food Product Technology* **2016,** *25* (3), 444-455.
76. Di Bernardini, R.; Harnedy, P.; Bolton, D.; Kerry, J.; O'Neill, E.; Mullen, A. M.; Hayes, M., Antioxidant and antimicrobial peptidic hydrolysates from muscle protein sources and by-products. *Food Chemistry* **2011,** *124* (4), 1296-1307.
77. Sudarshan, N. R.; Hoover, D. G.; Knorr, D., Antibacterial action of chitosan. *Food Biotechnology* **1992,** *6* (3), 257-272.
78. Poverenov, E.; Rutenberg, R.; Danino, S.; Horev, B.; Rodov, V., Gelatin-Chitosan Composite Films and Edible Coatings to Enhance the Quality of Food Products: Layer-by-Layer vs. Blended Formulations. *Food and Bioprocess Technology* **2014,** *7* (11), 3319-3327.
79. Park, K.; Jeong, H.; Tanum, J.; Yoo, J.-c.; Hong, J., Developing regulatory property of gelatin-tannic acid multilayer films for coating-based nitric oxide gas delivery system. *Scientific Reports* **2019,** *9* (1), 8308.
80. Iqbal, M. H.; Schroder, A.; Kerdjoudj, H.; Njel, C.; Senger, B.; Ball, V.; Meyer, F.; Boulmedais, F., Effect of the Buffer on the Buildup and Stability of Tannic Acid/Collagen Multilayer Films Applied as Antibacterial Coatings. *ACS Applied Materials & Interfaces* **2020,** *12* (20), 22601-22612.
81. Cassin, M. E.; Ford, A. J.; Orbach, S. M.; Saverot, S. E.; Rajagopalan, P., The design of antimicrobial LL37-modified collagen-hyaluronic acid detachable multilayers. *Acta Biomaterialia* **2016,** *40*, 119-129.
82. Yuan, M.; Dai, F.; Li, D.; Fan, Y.; Xiang, W.; Tao, F.; Cheng, Y.; Deng, H., Lysozyme/collagen multilayers layer-by-layer deposited nanofibers with enhanced biocompatibility and antibacterial activity. *Materials Science and Engineering: C* **2020**, 110868.
83. Wu, G.; Ma, X.; Fan, L.; Gao, Y.; Deng, H.; Wang, Y., Accelerating dermal wound healing and mitigating excessive scar formation using LBL modified nanofibrous mats. *Materials & Design* **2020,** *185*, 108265.
84. Shi, J.; Liu, Y.; Wang, Y.; Zhang, J.; Zhao, S.; Yang, G., Biological and immunotoxicity evaluation of antimicrobial peptide-loaded coatings using a layer-by-layer process on titanium. *Scientific Reports* **2015,** *5* (1), 16336.
85. Guo, S.; Zhu, X.; Loh, X. J., Controlling cell adhesion using layer-by-layer approaches for biomedical applications. *Materials Science and Engineering: C* **2017,** *70* (Pt 2), 1163-1175.
86. Ren, K.-f.; Hu, M.; Zhang, H.; Li, B.-c.; Lei, W.-x.; Chen, J.-y.; Chang, H.; Wang, L.-m.; Ji, J., Layer-by-layer assembly as a robust method to construct extracellular matrix mimic surfaces to modulate cell behavior. *Progress in Polymer Science* **2019,** *92*, 1-34.
87. Rodgers, U. R.; Weiss, A. S., Cellular interactions with elastin. *Pathologie-biologie* **2005,** *53* (7), 390-8.
88. Zhao, M. Y.; Li, L. H.; Li, B.; Zhou, C. R., LBL coating of type I collagen and hyaluronic acid on aminolyzed PLLA to enhance the cell-material interaction. *Express Polymer Letters* **2014,** *8*, 322-335.

89. Zhang, J.; Senger, B.; Vautier, D.; Picart, C.; Schaaf, P.; Voegel, J. C.; Lavalle, P., Natural polyelectrolyte films based on layer-by layer deposition of collagen and hyaluronic acid. *Biomaterials* **2005,** *26* (16), 3353-61.
90. Fujie, T.; Furutate, S.; Niwa, D.; Takeoka, S., A nano-fibrous assembly of collagen–hyaluronic acid for controlling cell-adhesive properties. *Soft Matter* **2010,** *6* (19), 4672-4676.
91. Hsieh, C. Y. C.; Hu, F.-W.; Chen, W.-S.; Tsai, W.-B., - Reducing the Foreign Body Reaction by Surface Modification with Collagen/Hyaluronic Acid Multilayered Films. **2014**.
92. Zhan, J.; Luo, Q.-j.; Huang, Y.; Li, X.-d., Cellular response to titanium discs coated with polyelectrolyte multilayer films. *International Journal of Minerals, Metallurgy, and Materials* **2014,** *21* (9), 925-933.
93. Huang, Y.; Luo, Q.; Li, X.; Zhang, F.; Zhao, S., Fabrication and in vitro evaluation of the collagen/hyaluronic acid PEM coating crosslinked with functionalized RGD peptide on titanium. *Acta Biomaterialia* **2012,** *8* (2), 866-877.
94. Zhao, M.; Li, L.; Zhou, C.; Heyroth, F.; Fuhrmann, B.; Maeder, K.; Groth, T., Improved Stability and Cell Response by Intrinsic Cross-Linking of Multilayers from Collagen I and Oxidized Glycosaminoglycans. *Biomacromolecules* **2014,** *15* (11), 4272-4280.
95. Chen, J.; Huang, N.; Li, Q.; Chu, C. H.; Li, J.; Maitz, M. F., The effect of electrostatic heparin/collagen layer-by-layer coating degradation on the biocompatibility. *Applied Surface Science* **2016,** *362*, 281-289.
96. Han, U.; Hong, J., Structure of a Multilayer Nanofilm To Increase the Encapsulation Efficiency of Basic Fibroblast Growth Factor. *Molecular Pharmaceutics* **2018,** *15* (3), 1277-1283.
97. Castilla-Casadiego, D. A.; García, J. R.; García, A. J.; Almodovar, J., Heparin/Collagen Coatings Improve Human Mesenchymal Stromal Cell Response to Interferon Gamma. *ACS Biomaterials Science & Engineering* **2019,** *5* (6), 2793-2803.
98. Zhang, J.; Wang, H.; Wang, Y.; Dong, W.; Jiang, Z.; Yang, G., Substrate-mediated gene transduction of LAMA3 for promoting biological sealing between titanium surface and gingival epithelium. *Colloids and Surfaces B: Biointerfaces* **2018,** *161*, 314-323.
99. Huang, R.; Li, W.; Lv, X.; Lei, Z.; Bian, Y.; Deng, H.; Wang, H.; Li, J.; Li, X., Biomimetic LBL structured nanofibrous matrices assembled by chitosan/collagen for promoting wound healing. *Biomaterials* **2015,** *53*, 58-75.
100. Li, W.; Zhao, P.; Lin, C.; Wen, X.; Katsanevakis, E.; Gero, D.; Félix, O.; Liu, Y., Natural Polyelectrolyte Self-Assembled Multilayers Based on Collagen and Alginate: Stability and Cytocompatibility. *Biomacromolecules* **2013,** *14* (8), 2647-2656.
101. Chaubaroux, C.; Perrin-Schmitt, F.; Senger, B.; Vidal, L.; Voegel, J. C.; Schaaf, P.; Haikel, Y.; Boulmedais, F.; Lavalle, P.; Hemmerle, J., Cell Alignment Driven by Mechanically Induced Collagen Fiber Alignment in Collagen/Alginate Coatings. *Tissue engineering. Part C, Methods* **2015,** *21* (9), 881-8.
102. Saums, M. K.; Wang, W.; Han, B.; Madhavan, L.; Han, L.; Lee, D.; Wells, R. G., Mechanically and Chemically Tunable Cell Culture System for Studying the Myofibroblast Phenotype. *Langmuir* **2014,** *30* (19), 5481-5487.
103. McCarty, W. J.; Usta, O. B.; Luitje, M.; Bale, S. S.; Bhushan, A.; Hegde, M.; Golberg, I.; Jindal, R.; Yarmush, M. L., A novel ultrathin collagen nanolayer assembly for 3-D microtissue engineering: Layer-by-layer collagen deposition for long-term stable microfluidic hepatocyte culture. *Technology* **2014,** *2* (1), 67-74.
104. Truong, Y. B.; Glattauer, V.; Briggs, K. L.; Zappe, S.; Ramshaw, J. A. M., Collagen-based layer-by-layer coating on electrospun polymer scaffolds. *Biomaterials* **2012,** *33* (36), 9198-9204.

105. Sinani, V. A.; Koktysh, D. S.; Yun, B.-G.; Matts, R. L.; Pappas, T. C.; Motamedi, M.; Thomas, S. N.; Kotov, N. A., Collagen Coating Promotes Biocompatibility of Semiconductor Nanoparticles in Stratified LBL Films. *Nano Letters* **2003,** *3* (9), 1177-1182.
106. Baba Ismail, Y. M.; Ferreira, A. M.; Bretcanu, O.; Dalgarno, K.; El Haj, A. J., Polyelectrolyte multi-layers assembly of SiCHA nanopowders and collagen type I on aminolysed PLA films to enhance cell-material interactions. *Colloids and Surfaces B: Biointerfaces* **2017,** *159*, 445-453.
107. Xing, R.; Jiao, T.; Ma, K.; Ma, G.; Möhwald, H.; Yan, X., Regulating Cell Apoptosis on Layer-by-Layer Assembled Multilayers of Photosensitizer-Coupled Polypeptides and Gold Nanoparticles. *Scientific Reports* **2016,** *6* (1), 26506.
108. Xing, R.; Jiao, T.; Yan, L.; Ma, G.; Liu, L.; Dai, L.; Li, J.; Möhwald, H.; Yan, X., Colloidal Gold–Collagen Protein Core–Shell Nanoconjugate: One-Step Biomimetic Synthesis, Layer-by-Layer Assembled Film, and Controlled Cell Growth. *ACS Applied Materials & Interfaces* **2015,** *7* (44), 24733-24740.
109. Yamauchi, K.; Goda, T.; Takeuchi, N.; Einaga, H.; Tanabe, T., Preparation of collagen/calcium phosphate multilayer sheet using enzymatic mineralization. *Biomaterials* **2004,** *25* (24), 5481-5489.
110. Kittitheeranun, P.; Potiyaraj, P.; Bunaprasert, T.; Sanchavanakit, N.; Dubas, S. T., Improved L-929 cell growth from self assembled PDADMAC/gelatin thin films. *Journal of Metals, Materials and Minerals* **2017,** *18* (1).
111. Brynda, E.; Pacherník, J.; Houska, M.; Pientka, Z.; Dvořák, P., Surface Immobilized Protein Multilayers for Cell Seeding. *Langmuir* **2005,** *21* (17), 7877-7883.
112. Li, M.; Cui, T.; Mills, D. K.; Lvov, Y. M.; McShane, M. J., Comparison of selective attachment and growth of smooth muscle cells on gelatin- and fibronectin-coated micropatterns. *Journal of nanoscience and nanotechnology* **2005,** *5* (11), 1809-15.
113. Mengyan, L.; Mills, D. K.; Tianhong, C.; McShane, M. J., Cellular response to gelatin- and fibronectin-coated multilayer polyelectrolyte nanofilms. *IEEE Transactions on NanoBioscience* **2005,** *4* (2), 170-179.
114. Lin, Y.; Chen, X.; Jing, X.; Jiang, Y.; Su, Z., Gelatin multilayers assembled on poly(L-lactic acid) surface for better cytocompatibility. *Journal of Applied Polymer Science* **2008,** *109* (1), 530-536.
115. Gand, A.; Tabuteau, M.; Chat, C.; Ladam, G.; Atmani, H.; Van Tassel, P. R.; Pauthe, E., Fibronectin-based multilayer thin films. *Colloids and Surfaces B: Biointerfaces* **2017,** *156*, 313-319.
116. Soumetz, F. C.; Pastorino, L.; Ruggiero, C. In *Osteoblast-like cells response to layer by layer self assembled biomimetic coatings*, 2007 7th IEEE Conference on Nanotechnology (IEEE NANO), 2-5 Aug. 2007; 2007; pp 566-569.
117. Shaik, J.; Mills, D. K., Micropatterned antibody-terminated nanocomposites (MANs) fabricated using layer-by-layer lift-off (LBL-LO) technique. *Journal of Biomedical Materials Research Part B: Applied Biomaterials* **2012,** *100B* (5), 1411-1415.
118. Golonka, M.; Bulwan, M.; Nowakowska, M.; Testera, A. M.; Rodríguez-Cabello, J. C.; Zapotoczny, S., Thermoresponsive multilayer films based on ionic elastin-like recombinamers. *Soft Matter* **2011,** *7* (19), 9402-9409.
119. Swierczewska, M.; Hajicharalambous, C. S.; Janorkar, A. V.; Megeed, Z.; Yarmush, M. L.; Rajagopalan, P., Cellular response to nanoscale elastin-like polypeptide polyelectrolyte multilayers. *Acta Biomaterialia* **2008,** *4* (4), 827-837.
120. Uhrich, K. E.; Cannizzaro, S. M.; Langer, R. S.; Shakesheff, K. M., Polymeric systems for controlled drug release. *Chemical reviews* **1999,** *99* (11), 3181-98.

121. Bertrand, P.; Jonas, A.; Laschewsky, A.; Legras, R., Ultrathin polymer coatings by complexation of polyelectrolytes at interfaces: suitable materials, structure and properties. *Macromolecular Rapid Communications* **2000,** *21* (7), 319-348.
122. Sousa, F.; Kreft, O.; Sukhorukov, G. B.; Möhwald, H.; Kokol, V., Biocatalytic response of multi-layer assembled collagen/hyaluronic acid nanoengineered capsules. *Journal of Microencapsulation* **2014,** *31* (3), 270-276.
123. Habibi, N.; Pastorino, L.; Ruggiero, C., Functionalized biocompatible polyelectrolyte multilayers for drug delivery: In situ investigation of mechanical properties by dissipative quartz crystal microbalance. *Materials Science and Engineering: C* **2014,** *35*, 15-20.
124. Damanik, F. F. R.; Brunelli, M.; Pastorino, L.; Ruggiero, C.; van Blitterswijk, C.; Rotmans, J.; Moroni, L., Sustained delivery of growth factors with high loading efficiency in a layer by layer assembly. *Biomaterials Science* **2020,** *8* (1), 174-188.
125. Chen, M. C.; Liang, H. F.; Chiu, Y. L.; Chang, Y.; Wei, H. J.; Sung, H. W., A novel drug-eluting stent spray-coated with multi-layers of collagen and sirolimus. *Journal of controlled release : official journal of the Controlled Release Society* **2005,** *108* (1), 178-89.
126. Shutava, T. G.; Balkundi, S. S.; Lvov, Y. M., (−)-Epigallocatechin gallate/gelatin layer-by-layer assembled films and microcapsules. *Journal of Colloid and Interface Science* **2009,** *330* (2), 276-283.
127. Shutava, T. G.; Balkundi, S. S.; Vangala, P.; Steffan, J. J.; Bigelow, R. L.; Cardelli, J. A.; O'Neal, D. P.; Lvov, Y. M., Layer-by-Layer-Coated Gelatin Nanoparticles as a Vehicle for Delivery of Natural Polyphenols. *ACS Nano* **2009,** *3* (7), 1877-1885.
128. Zhang, Z.; Nix, C. A.; Ercan, U. K.; Gerstenhaber, J. A.; Joshi, S. G.; Zhong, Y., Calcium Binding-Mediated Sustained Release of Minocycline from Hydrophilic Multilayer Coatings Targeting Infection and Inflammation. *PLOS ONE* **2014,** *9* (1), e84360.
129. Mandal, B. B.; Mann, J. K.; Kundu, S. C., Silk fibroin/gelatin multilayered films as a model system for controlled drug release. *European Journal of Pharmaceutical Sciences* **2009,** *37* (2), 160-171.
130. Zhang, Z.; Li, Q.; Han, L.; Zhong, Y., Layer-by-layer films assembled from natural polymers for sustained release of neurotrophin. *Biomedical Materials* **2015,** *10* (5), 055006.
131. Prouty, M.; Lu, Z.; Leuschner, C.; Lvov, Y., Layer-by-Layer Engineered Nanoparticles for Sustained Release of Phor21-・CG(ala) Anticancer Peptide. *Journal of Biomedical Nanotechnology* **2007,** *3*, 184-189.
132. Shenoy, D. B.; Sukhorukov, G. B., Engineered microcrystals for direct surface modification with layer-by-layer technique for optimized dissolution. *European Journal of Pharmaceutics and Biopharmaceutics* **2004,** *58* (3), 521-527.
133. Pandey, A. P.; Singh, S. S.; Patil, G. B.; Patil, P. O.; Bhavsar, C. J.; Deshmukh, P. K., Sonication-assisted drug encapsulation in layer-by-layer self-assembled gelatin-poly (styrenesulfonate) polyelectrolyte nanocapsules: process optimization. *Artificial Cells, Nanomedicine, and Biotechnology* **2015,** *43* (6), 413-424.
134. Ai, H.; Jones, S. A.; de Villiers, M. M.; Lvov, Y. M., Nano-encapsulation of furosemide microcrystals for controlled drug release. *Journal of Controlled Release* **2003,** *86* (1), 59-68.
135. Ai, H.; Gao, J., Size-controlled polyelectrolyte nanocapsules via layer-by-layer self-assembly. *Journal of materials science* **2004,** *39* (4), 1429-1432.
136. Guan, G.; Liu, R.; Wu, M.; Li, Z.; Liu, B.; Wang, Z.; Gao, D.; Zhang, Z., Protein-building molecular recognition sites by layer-by-layer molecular imprinting on colloidal particles. *Analyst* **2009,** *134* (9), 1880-1886.
137. Sukhorukov, G. B.; Donath, E.; Davis, S.; Lichtenfeld, H.; Caruso, F.; Popov, V. I.; Möhwald, H., Stepwise polyelectrolyte assembly on particle surfaces: a novel approach to colloid design. *Polymers for Advanced Technologies* **1998,** *9* (10-11), 759-767.

138. Caruso, F.; Möhwald, H., Protein Multilayer Formation on Colloids through a Stepwise Self-Assembly Technique. *Journal of the American Chemical Society* **1999,** *121* (25), 6039-6046.
139. Mohanta, V.; Madras, G.; Patil, S., Albumin-mediated incorporation of water-insoluble therapeutics in layer-by-layer assembled thin films and microcapsules. *Journal of Materials Chemistry B* **2013,** *1* (37), 4819-4827.
140. Lu, Z.; Li, C. M.; Zhou, Q.; Bao, Q.-L.; Cui, X., Covalently linked DNA/protein multilayered film for controlled DNA release. *Journal of Colloid and Interface Science* **2007,** *314* (1), 80-88.
141. Tong, W.; Gao, C.; Möhwald, H., pH-responsive protein microcapsules fabricated via glutaraldehyde mediated covalent layer-by-layer assembly. *Colloid and Polymer Science* **2008,** *286* (10), 1103.
142. Mohanta, V.; Madras, G.; Patil, S., Layer-by-Layer Assembled Thin Film of Albumin Nanoparticles for Delivery of Doxorubicin. *The Journal of Physical Chemistry C* **2012,** *116* (9), 5333-5341.
143. Kulikouskaya, V. I.; Lazouskaya, M. E.; Kraskouski, A. N.; Agabekov, V. E., Formation and Properties of Multilayer Films Based on Polyethyleneimine and Bovine Serum Albumin. *Russian Journal of Physical Chemistry A* **2018,** *92* (1), 146-152.
144. Ren, K. F.; Ji, J.; Shen, J. C., Construction of Biodegradable Multilayer Films via Layer-by-Layer Self-Assembly as Gene Delivery System. *Key Engineering Materials* **2005,** *288-289*, 101-104.
145. Lau, H. H.; Murney, R.; Yakovlev, N. L.; Novoselova, M. V.; Lim, S. H.; Roy, N.; Singh, H.; Sukhorukov, G. B.; Haigh, B.; Kiryukhin, M. V., Protein-tannic acid multilayer films: A multifunctional material for microencapsulation of food-derived bioactives. *Journal of Colloid and Interface Science* **2017,** *505*, 332-340.
146. Lomova, M. V.; Brichkina, A. I.; Kiryukhin, M. V.; Vasina, E. N.; Pavlov, A. M.; Gorin, D. A.; Sukhorukov, G. B.; Antipina, M. N., Multilayer Capsules of Bovine Serum Albumin and Tannic Acid for Controlled Release by Enzymatic Degradation. *ACS Applied Materials & Interfaces* **2015,** *7* (22), 11732-11740.
147. Chen, C.; Chen, G.; Wan, P.; Chen, D.; Zhu, T.; Hu, B.; Sun, Y.; Zeng, X., Characterization of Bovine Serum Albumin and (−)-Epigallocatechin Gallate/3,4-O-Dicaffeoylquinic Acid/Tannic Acid Layer by Layer Assembled Microcapsule for Protecting Immunoglobulin G in Stomach Digestion and Release in Small Intestinal Tract. *Journal of Agricultural and Food Chemistry* **2018,** *66* (42), 11141-11150.
148. An, Z.; Lu, G.; Möhwald, H.; Li, J., Self-Assembly of Human Serum Albumin (HSA) and l-α-Dimyristoylphosphatidic Acid (DMPA) Microcapsules for Controlled Drug Release. *Chemistry – A European Journal* **2004,** *10* (22), 5848-5852.
149. An, Z.; Tao, C.; Lu, G.; Möhwald, H.; Zheng, S.; Cui, Y.; Li, J., Fabrication and Characterization of Human Serum Albumin and l-α-Dimyristoylphosphatidic Acid Microcapsules Based on Template Technique. *Chemistry of Materials* **2005,** *17* (10), 2514-2519.
150. Su, X.; Kim, B.-S.; Kim, S. R.; Hammond, P. T.; Irvine, D. J., Layer-by-Layer-Assembled Multilayer Films for Transcutaneous Drug and Vaccine Delivery. *ACS Nano* **2009,** *3* (11), 3719-3729.
151. Jin, Y.; Liu, W.; Wang, J.; Fang, J.; Gao, H., (Protamine/dextran sulfate)6 microcapules templated on biocompatible calcium carbonate microspheres. *Colloids and Surfaces A: Physicochemical and Engineering Aspects* **2009,** *342* (1), 40-45.
152. Tiourina, O. P.; Sukhorukov, G. B., Multilayer alginate/protamine microsized capsules: encapsulation of α-chymotrypsin and controlled release study. *International Journal of Pharmaceutics* **2002,** *242* (1), 155-161.

153. Xie, M.; Zhang, F.; Liu, L.; Zhang, Y.; Li, Y.; Li, H.; Xie, J., Surface modification of graphene oxide nanosheets by protamine sulfate/sodium alginate for anti-cancer drug delivery application. *Applied Surface Science* **2018,** *440*, 853-860.
154. Ke, Z.; Yang, L.; Wu, H.; Li, Z.; Jia, X.; Zhang, Z., Evaluation of in vitro and in vivo antitumor effects of gambogic acid-loaded layer-by-layer self-assembled micelles. *International Journal of Pharmaceutics* **2018,** *545* (1), 306-317.
155. Radhakrishnan, K.; Thomas, M. B.; Pulakkat, S.; Gnanadhas, D. P.; Chakravortty, D.; Raichur, A. M., Stimuli-responsive protamine-based biodegradable nanocapsules for enhanced bioavailability and intracellular delivery of anticancer agents. *Journal of Nanoparticle Research* **2015,** *17* (8), 341.
156. Wang, C.; He, C.; Tong, Z.; Liu, X.; Ren, B.; Zeng, F., Combination of adsorption by porous CaCO3 microparticles and encapsulation by polyelectrolyte multilayer films for sustained drug delivery. *International Journal of Pharmaceutics* **2006,** *308* (1), 160-167.
157. Elumalai, R.; Patil, S.; Maliyakkal, N.; Rangarajan, A.; Kondaiah, P.; Raichur, A. M., Protamine-carboxymethyl cellulose magnetic nanocapsules for enhanced delivery of anticancer drugs against drug resistant cancers. *Nanomedicine: Nanotechnology, Biology and Medicine* **2015,** *11* (4), 969-981.
158. Chang, H.; Ren, K.-f.; Wang, J.-l.; Zhang, H.; Wang, B.-l.; Zheng, S.-m.; Zhou, Y.-y.; Ji, J., Surface-mediated functional gene delivery: An effective strategy for enhancing competitiveness of endothelial cells over smooth muscle cells. *Biomaterials* **2013,** *34* (13), 3345-3354.
159. Rossier-Miranda, F. J.; Schroën, K.; Boom, R., Microcapsule production by an hybrid colloidosome-layer-by-layer technique. *Food Hydrocolloids* **2012,** *27* (1), 119-125.
160. Brown, J. L.; Kumbar, S. G.; Laurencin, C. T., Chapter II.6.7 - Bone Tissue Engineering. In *Biomaterials Science (Third Edition)*, Ratner, B. D.; Hoffman, A. S.; Schoen, F. J.; Lemons, J. E., Eds. Academic Press: 2013; pp 1194-1214.
161. Cai, K.; Rechtenbach, A.; Hao, J.; Bossert, J.; Jandt, K. D., Polysaccharide-protein surface modification of titanium via a layer-by-layer technique: Characterization and cell behaviour aspects. *Biomaterials* **2005,** *26* (30), 5960-5971.
162. Liu, P.; Zhao, Y.; Yuan, Z.; Ding, H.; Hu, Y.; Yang, W.; Cai, K., Construction of Zn-incorporated multilayer films to promote osteoblasts growth and reduce bacterial adhesion. *Materials Science and Engineering: C* **2017,** *75*, 998-1005.
163. Sangfai, T.; Dong, F.; Tantishaiyakul, V.; Jandt, K.; Lüdecke, C.; Boonrat, O.; Hirun, N., Layer-by-layer gelatin/chitosan polyelectrolyte coated nanoparticles on Ti implants for prevention of implant-associated infections. *Express Polym. Lett.* **2017,** *11* (1), 73.
164. Hu, Y.; Cai, K.; Luo, Z.; Jandt, K. D., Layer-By-Layer Assembly of β-Estradiol Loaded Mesoporous Silica Nanoparticles on Titanium Substrates and Its Implication for Bone Homeostasis. *Advanced Materials* **2010,** *22* (37), 4146-4150.
165. Hu, Y.; Cai, K.; Luo, Z.; Zhang, Y.; Li, L.; Lai, M.; Hou, Y.; Huang, Y.; Li, J.; Ding, X.; Zhang, B.; Paul Sung, K. L., Regulation of the differentiation of mesenchymal stem cells in vitro and osteogenesis in vivo by microenvironmental modification of titanium alloy surfaces. *Biomaterials* **2012,** *33* (13), 3515-3528.
166. Xing, H.; Wang, X.; Xiao, S.; Zhang, G.; Li, M.; Wang, P.; Shi, Q.; Qiao, P.; E, L.; Liu, H., Osseointegration of layer-by-layer polyelectrolyte multilayers loaded with IGF1 and coated on titanium implant under osteoporotic condition. *International journal of nanomedicine* **2017,** *12*, 7709-7720.
167. Amin Yavari, S.; Croes, M.; Akhavan, B.; Jahanmard, F.; Eigenhuis, C. C.; Dadbakhsh, S.; Vogely, H. C.; Bilek, M. M.; Fluit, A. C.; Boel, C. H. E.; van der Wal, B. C. H.; Vermonden, T.; Weinans, H.; Zadpoor, A. A., Layer by layer coating for bio-functionalization of additively manufactured meta-biomaterials. *Additive Manufacturing* **2020,** *32*, 100991.

168. Zhang, Y.; Chen, L.; Liu, C.; Feng, X.; Wei, L.; Shao, L., Self-assembly chitosan/gelatin composite coating on icariin-modified TiO2 nanotubes for the regulation of osteoblast bioactivity. *Materials & Design* **2016,** *92*, 471-479.
169. Yu, Y.; Tao, B.; Sun, J.; Liu, L.; Zheng, H., Fabrication of chitosan-graft-polyaniline-based multilayers on Ti substrates for enhancing antibacterial property and improving osteogenic activity. *Materials Letters* **2020,** *268*, 127420.
170. Jiao, Y.; Liu, Q.; Chen, J., Construction of N-halamine biocompatible multilayers onto BMP2 loaded titanium nanotubes for bacterial infection inhibition and osteogenic effect improvement. *Materials Letters* **2020,** *267*, 127526.
171. Li, X.; Luo, Q.; Huang, Y.; Li, X.; Zhang, F.; Zhao, S., The responses of preosteoblasts to collagen/hyaluronic acid polyelectrolyte multilayer coating on titanium. *Polymers for Advanced Technologies* **2012,** *23* (4), 756-764.
172. Ao, H.; Zong, J.; Nie, Y.; Wan, Y.; Zheng, X., An in vivo study on the effect of coating stability on osteointegration performance of collagen/hyaluronic acid multilayer modified titanium implants. *Bioactive Materials* **2018,** *3* (1), 97-101.
173. Gregurec, D.; Wang, G.; Pires, R. H.; Kosutic, M.; Lüdtke, T.; Delcea, M.; Moya, S. E., Bioinspired titanium coatings: self-assembly of collagen–alginate films for enhanced osseointegration. *Journal of Materials Chemistry B* **2016,** *4* (11), 1978-1986.
174. Yang, W.; Xi, X.; Si, Y.; Huang, S.; Wang, J.; Cai, K., Surface engineering of titanium alloy substrates with multilayered biomimetic hierarchical films to regulate the growth behaviors of osteoblasts. *Acta Biomaterialia* **2014,** *10* (10), 4525-4536.
175. Ferreira, A. M.; Gentile, P.; Toumpaniari, S.; Ciardelli, G.; Birch, M. A., Impact of Collagen/Heparin Multilayers for Regulating Bone Cellular Functions. *ACS Applied Materials & Interfaces* **2016,** *8* (44), 29923-29932.
176. Liu, W. C.; Lin, Y.-C.; Xu, M.; Nabilla, S. C.; Lin, Y.-L.; Chen, L.-C.; Chung, R.-J., Study of collagen/γ-PGA polyelectrolyte multilayers coating on plasma treated 316 L stainless steel substrates. *Surface and Coatings Technology* **2018**.
177. Kim, T. G.; Park, S.-H.; Chung, H. J.; Yang, D.-Y.; Park, T. G., Microstructured scaffold coated with hydroxyapatite/collagen nanocomposite multilayer for enhanced osteogenic induction of human mesenchymal stem cells. *Journal of Materials Chemistry* **2010,** *20* (40), 8927-8933.
178. Li, X.; Xie, J.; Yuan, X.; Xia, Y., Coating Electrospun Poly(ε-caprolactone) Fibers with Gelatin and Calcium Phosphate and Their Use as Biomimetic Scaffolds for Bone Tissue Engineering. *Langmuir* **2008,** *24* (24), 14145-14150.
179. Zhong, X.; Lu, Z.; Valtchev, P.; Wei, H.; Zreiqat, H.; Dehghani, F., Surface modification of poly(propylene carbonate) by aminolysis and layer-by-layer assembly for enhanced cytocompatibility. *Colloids and Surfaces B: Biointerfaces* **2012,** *93*, 75-84.
180. Zhao, M.; Altankov, G.; Grabiec, U.; Bennett, M.; Salmeron-Sanchez, M.; Dehghani, F.; Groth, T., Molecular composition of GAG-collagen I multilayers affects remodeling of terminal layers and osteogenic differentiation of adipose-derived stem cells. *Acta Biomaterialia* **2016,** *41*, 86-99.
181. Samuel, R. E.; Shukla, A.; Paik, D. H.; Wang, M. X.; Fang, J. C.; Schmidt, D. J.; Hammond, P. T., Osteoconductive protamine-based polyelectrolyte multilayer functionalized surfaces. *Biomaterials* **2011,** *32* (30), 7491-7502.
182. Li, H.; Chen, C.; Zhang, S.; Jiang, J.; Tao, H.; Xu, J.; Sun, J.; Zhong, W.; Chen, S., The use of layer by layer self-assembled coatings of hyaluronic acid and cationized gelatin to improve the biocompatibility of poly(ethylene terephthalate) artificial ligaments for reconstruction of the anterior cruciate ligament. *Acta Biomaterialia* **2012,** *8* (11), 4007-4019.

183. Ji, J.; Tan, Q.; Shen, J., Construction of albumin multilayer coating onto plasma treated poly(vinyl chloride) via electrostatic self-assembly. *Polymers for Advanced Technologies* **2004,** *15* (8), 490-494.
184. Ji, J.; Tan, Q.; Fan, D.-Z.; Sun, F.-Y.; Barbosa, M. A.; Shen, J., Fabrication of alternating polycation and albumin multilayer coating onto stainless steel by electrostatic layer-by-layer adsorption. *Colloids and Surfaces B: Biointerfaces* **2004,** *34* (3), 185-190.
185. Tan, Q.; Ji, J.; Zhao, F.; Fan, D.-Z.; Sun, F.-Y.; Shen, J.-C., Fabrication of thromboresistant multilayer thin film on plasma treated poly (vinyl chloride) surface. *Journal of Materials Science: Materials in Medicine* **2005,** *16* (7), 687-692.
186. Houska, M.; Brynda, E.; Solovyev, A.; Broučková, A.; Křížová, P.; Vaníčková, M.; Dyr, J. E., Hemocompatible albumin-heparin coatings prepared by the layer-by-layer technique. The effect of layer ordering on thrombin inhibition and platelet adhesion. *Journal of Biomedical Materials Research Part A* **2008,** *86A* (3), 769-778.
187. Sperling, C.; Houska, M.; Brynda, E.; Streller, U.; Werner, C., In vitro hemocompatibility of albumin–heparin multilayer coatings on polyethersulfone prepared by the layer-by-layer technique. *Journal of Biomedical Materials Research Part A* **2006,** *76A* (4), 681-689.
188. Weng, Y. J.; Jing, F. J.; Chen, J. Y.; Huang, N., Construction of heparinylated multilayer films on TiO via streptavidin/biotin interaction. *Applied Surface Science* **2012,** *258* (16), 5947-5954.
189. Li, G.; Yang, P.; Huang, N., Layer-by-layer construction of the heparin/fibronectin coatings on titanium surface:stability and functionality. *Physics Procedia* **2011,** *18*, 112-121.
190. Gossart, A.; Battiston, K. G.; Gand, A.; Pauthe, E.; Santerre, J. P., Mono vs multilayer fibronectin coatings on polar/hydrophobic/ionic polyurethanes: Altering surface interactions with human monocytes. *Acta Biomaterialia* **2018,** *66*, 129-140.
191. Chen, J. L.; Li, Q. L.; Chen, J. Y.; Chen, C.; Huang, N., Improving blood-compatibility of titanium by coating collagen–heparin multilayers. *Applied Surface Science* **2009,** *255* (15), 6894-6900.
192. Chou, C.-C.; Zeng, H.-J.; Yeh, C.-H., Blood compatibility and adhesion of collagen/heparin multilayers coated on two titanium surfaces by a layer-by-layer technique. *Thin Solid Films* **2013**, 117-122.
193. Chou, C.-C.; Hsin, S.-W.; Lin, H.-C.; Yeh, C.-H.; Wu, R.; Cherng, W.-J., Oxidized dopamine as the interlayer between heparin/collagen polyelectrolyte multilayers and titanium substrate: An investigation of the coating's adhesion and hemocompatibility. *Surface and Coatings Technology* **2016,** *303*, 277-282.
194. Hao, W.; Han, J.; Chu, Y.; Huang, L.; Zhuang, Y.; Sun, J.; Li, X.; Zhao, Y.; Chen, Y.; Dai, J., Collagen/Heparin Bi-Affinity Multilayer Modified Collagen Scaffolds for Controlled bFGF Release to Improve Angiogenesis In Vivo. *Macromolecular Bioscience* **2018,** *18* (11), 1800086.
195. Lin, Q.; Yan, J.; Qiu, F.; Song, X.; Fu, G.; Ji, J., Heparin/collagen multilayer as a thromboresistant and endothelial favorable coating for intravascular stent. *Journal of biomedical materials research. Part A* **2011,** *96* (1), 132-41.
196. Jin, K.; Ye, X.; Li, S.; Li, B.; Zhang, C.; Gao, C.; Ye, J., A biomimetic collagen/heparin multi-layered porous hydroxyapatite orbital implant for in vivo vascularization studies on the chicken chorioallantoic membrane. *Graefe's archive for clinical and experimental ophthalmology = Albrecht von Graefes Archiv fur klinische und experimentelle Ophthalmologie* **2016,** *254* (1), 83-9.
197. Zhang, K.; Chen, J.-y.; Qin, W.; Li, J.-a.; Guan, F.-x.; Huang, N., Constructing bio-layer of heparin and type IV collagen on titanium surface for improving its endothelialization and blood compatibility. *Journal of Materials Science: Materials in Medicine* **2016,** *27* (4), 81.

198. Yaping, S.; Bing, J.; Ming, Y.; Hua, S.; Weicheng, C.; Huifeng, Z., Application of Heparin/Collagen-REDV Selective Active Interface on ePTFE Films to Enhance Endothelialization and Anticoagulation. *Artificial Organs 0* (0).
199. Liu, P.; Zhao, Y.; Yan, Y.; Hu, Y.; Yang, W.; Cai, K., Construction of extracellular microenvironment to improve surface endothelialization of NiTi alloy substrate. *Materials Science and Engineering: C* **2015,** *55*, 1-7.
200. Chen, J. L.; Li, Q. L.; Chen, J. Y.; Huang, N., Adsoption CD34 Antibody onto the Col/Hep Coating Film on Titanium to Improve Cytocompatibility of Titanium. *Advanced Materials Research* **2008,** *47-50*, 1411-1414.
201. Chen, J.; Chen, C.; Chen, Z.; Chen, J.; Li, Q.; Huang, N., Collagen/heparin coating on titanium surface improves the biocompatibility of titanium applied as a blood-contacting biomaterial. *Journal of biomedical materials research. Part A* **2010,** *95* (2), 341-9.
202. Lin, Q.; Ding, X.; Qiu, F.; Song, X.; Fu, G.; Ji, J., In situ endothelialization of intravascular stents coated with an anti-CD34 antibody functionalized heparin-collagen multilayer. *Biomaterials* **2010,** *31* (14), 4017-25.
203. Lu, S.; Zhang, P.; Sun, X.; Gong, F.; Yang, S.; Shen, L.; Huang, Z.; Wang, C., Synthetic ePTFE Grafts Coated with an Anti-CD133 Antibody-Functionalized Heparin/Collagen Multilayer with Rapid in vivo Endothelialization Properties. *ACS Applied Materials & Interfaces* **2013,** *5* (15), 7360-7369.
204. Chaubaroux, C.; Vrana, E.; Debry, C.; Schaaf, P.; Senger, B.; Voegel, J. C.; Haikel, Y.; Ringwald, C.; Hemmerle, J.; Lavalle, P.; Boulmedais, F., Collagen-based fibrillar multilayer films cross-linked by a natural agent. *Biomacromolecules* **2012,** *13* (7), 2128-35.
205. Ai, H.; Meng, H.; Ichinose, I.; Jones, S. A.; Mills, D. K.; Lvov, Y. M.; Qiao, X., Biocompatibility of layer-by-layer self-assembled nanofilm on silicone rubber for neurons. *Journal of Neuroscience Methods* **2003,** *128* (1), 1-8.
206. He, W.; Bellamkonda, R. V., Nanoscale neuro-integrative coatings for neural implants. *Biomaterials* **2005,** *26* (16), 2983-2990.
207. He, L.; Shi, Y.; Han, Q.; Zuo, Q.; Ramakrishna, S.; Xue, W.; Zhou, L., Surface modification of electrospun nanofibrous scaffolds via polysaccharide–protein assembly multilayer for neurite outgrowth. *Journal of Materials Chemistry* **2012,** *22* (26), 13187-13196.
208. He, L.; Tang, S.; Prabhakaran, M. P.; Liao, S.; Tian, L.; Zhang, Y.; Xue, W.; Ramakrishna, S., Surface Modification of PLLA Nano-scaffolds with Laminin Multilayer by LbL Assembly for Enhancing Neurite Outgrowth. *Macromolecular Bioscience* **2013,** *13* (11), 1601-1609.
209. Wu, Z.-R.; Ma, J.; Liu, B.-F.; Xu, Q.-Y.; Cui, F.-Z., Layer-by-layer assembly of polyelectrolyte films improving cytocompatibility to neural cells. *Journal of Biomedical Materials Research Part A* **2007,** *81A* (2), 355-362.
210. vander Straeten, A.; Lefèvre, D.; Demoustier-Champagne, S.; Dupont-Gillain, C., Protein-based polyelectrolyte multilayers. *Advances in colloid and interface science* **2020,** *280*, 102161.

# Chapter 2 : Materials and Methods

# Table of Contents

This chapter describes the materials and methods used in this thesis. All polymers, chemicals and reagents are listed with product reference, supplier information, and the intended use. Different physico-chemical characterization performed in the thesis work are reported here.

## 2.1 Materials

Most of the products and chemicals used in this work are gathered in the **Table 2.1**. They were all used as received, without further purifications.

***Table 2.1:*** *List of all chemicals and products used.*

| Product | Provider | Reference | Use in the project |
|---|---|---|---|
| **Collagen (COL) type-I** | Symatese, France | - | LbL component: cell recognition |
| **Tannic acid (TA)** | Sigma Aldrich | 403040 | LbL component: protein interaction |
| **Chitin nanocrystals (CNC)** | CERMAV (Grenoble) | - | LbL component: bio-based nanocomposite |
| **Acetic acid** | Sigma Aldrich | A6283 | Buffer solution |
| **Citric acid monohydrate** | Sigma Aldrich | C1909 | Buffer solution |
| **Sodium citrate tribasic dihydrate** | Sigma Aldrich | C8532 | Buffer solution |
| **Polyethyleneimine (PEI)** | Alfa Aesar | 45024 | Precursor layer |
| **Iron chloro-hexahydrate** | Sigma Aldrich | 3132 | LbL component |
| **Dulbecco's Modified Eagle Medium (DMEM)** | Dominique Dutscher | L0103 | Culture medium |
| **Dulbecco's phosphate buffered saline (PBS)** | Dominique Dutscher | L0615 | Rinsing medium |
| **Triton X-100** | Fisher Scientific | BP151 | Cytoplasmic and nuclear membrane permeabilization agent |

| | | | |
|---|---|---|---|
| **NIH3T3 mouse fibroblast** | ATCC | - | Mammalian cells |
| **C25 CL48 human myoblast** | Institut de Myologie (Paris) | - | Mammalian cells |
| **Trypsin/EDTA in PBS** | Dominique Dutscher | L0940 | Cells detach enzyme |
| **Paraformaldehyde (PFA)** | Electron Microscopy Sciences | 15170 | Fixing agent |
| **Fetal Bovine Serum (FBS)** | Dominique Dutscher | P04-96650 | Blocking buffer for immunofluorescence, and serum to add in the culture medium (contains several factors such as proteins, hormones, ions) conducive to cell growth |
| **Horse Bovine Serum** | Dominique Dutscher | P30-0702 | Serum to add in the DMEM culture medium for myoblasts differentiation |
| **Alexa Fluor 568 conjugated-Phalloidin** | Invitrogen | A12380 | Actin filament staining agent |
| **Mounting medium (with or without DAPI)** | VECTASHIELD | H-1000 | Mounting medium<br>DAPI: nucleus staining agent |
| **ProLong™ Diamond Antifade Mountant** | Invitrogen | P36965 | Cross-linkable mounting medium for enhanced image quality |
| **Sodium dodecyl sulfate (SDS)** | Sigma Aldrich | 71725 | Glass substrate cleaning agent |
| **Sodium hydroxide (NaOH)** | Sigma Aldrich | S0899 | pH adjustment agent |
| **Hydrochloric acid (HCl)** | Sigma Aldrich | 320331 | pH adjustment agent and class substrate cleaning agent |
| **Nylon paint brushes** | Soserene Grene, Denmark | - | Brush for the LBL manufacturing |
| **5-Cyano-2,3-ditolyl tetrazolium chloride (CTC)/ SYTO 24®** | Invitrogen | B34956 | Alive bacteria staining agent |

| | | | |
|---|---|---|---|
| **Propidium iodide / SYTO®-9** | Thermo Fisher | L7012 | Live/Dead bacteria staining |
| **Safranin** | Alfa Aesar | B21674 | Bacterial biofilm staining agent |
| ***S. aureus*** | ATCC 25923 | - | Gram positive bacterium |
| ***E. coli*** | ATCC 25922 | Biomerieux | Gram negative bacterium |
| **Lysogeny broth (LB)** | Difco™, Fisher scientific | 244620 | Bacterial growth medium |
| **Mueller-Hinton (MH) broth** | Difco™, Fisher scientific | 275730 | Bacterial growth medium |
| **Roswell Park Memorial Institute (RPMI)** | Dominique Dutscher | L0498 | Bacterial growth medium that enhances bacteria adhesion |
| **p-Nitrophenyl phosphate (pNPP)** | Sigma Aldrich | P7998 | Acid phosphatase cell viability assay |
| **Hoechst 33342** | Invitrogen | B2261 | Stains cell nuclei by binding to DNA |

### 2.1.1 Poly(ethylenimine) (PEI)

PEI is a branched polycation that is made up of repeated units of amine groups and two aliphatic carbons. It's a key polymer in medicinal chemistry, and it's been employed in gene therapy, DNA complexation, and transfection in a variety of cell lines and tissues. It is, however, cytotoxic. PEI is employed as an adhesion promoter anchoring layer in the LbL assembly, resulting in a positively charged substrate, minimizing the influence of the underlying surface on the growth of subsequent layers. The chemical structure of PEI is shown in the **Figure 2.1**.

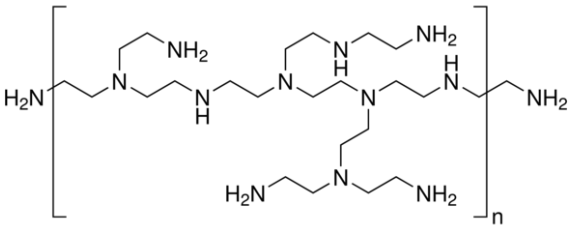


***Figure 2.1:*** *Chemical structure of Poly(ethylenimine) (PEI)*

### 2.1.2 Proteins

#### *2.1.2.1 Collagen*

To enhance the integration of the biomaterials into the body, the LbL films must be biocompatible, biodegradable, and non-immunogenic. Collagen (COL) is a fibrous protein present in all connective tissues and is the most abundant protein in the extracellular matrix (25-30%). Collagen is involved in the mechanical support of tissue, responsible for the strength of the extracellular matrix and forming high tensile strength fibres in tendons or ligaments. To this day, 29 distinct collagen types have been characterized and all display a typical triple helix structure. COL molecules are obtained by cleavage of telopeptide regions of procollagen. The COL molecule is composed of three α chains that assemble into a tripe helix due to their molecular interactions **(Figure 2.2)**.

The α chains are composed of thousands amino acids based on the repetition of the sequence Gly-X-Y, where X and Y are mostly filled by proline and 4-hydroxyproline. The presence of glycine is essential at every third amino acid position to allow the formation of tropocollagen from the three α-chains. Then the tropocollagen molecules assemble into a 10 to 300 nm sized collagen fibril which aggregates to form the collagen fibre, with a diameter ranging from 0.5 to 3 μm.[1]

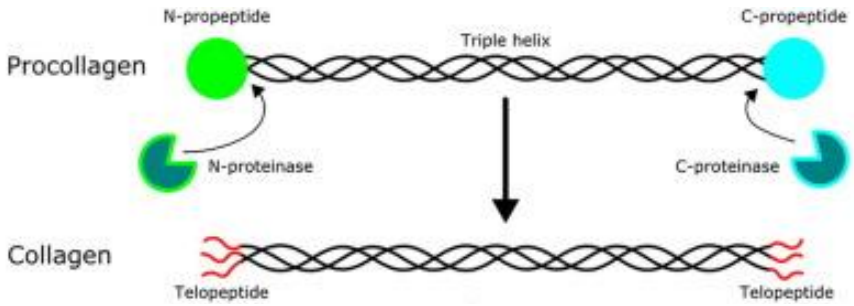


***Figure 2.2:*** *Schematic insight into structure of collagen: N- and C- propeptides of procollagen are cleaved by respective proteinase to obtain triple helical collagen molecules.*[2]

### 2.1.3 Polyphenols

Polyphenols are secondary plant metabolites abundantly found in fruits, tea, coffee, wines, chocolate etc. Their primary function is to protect the plants from external factors such as UV light from sun and bacteria invasion. They are known to have astringent effect. For instance, upon oral intake, they make complexations with and precipitate the saliva proteins causing sudden dryness in the mouth. Around 8000 polyphenolic compounds are identified and characterized into four main classes; including phenolic acids, flavonoids, stilbenes and lignans.[3] Polyphenols are known for their antioxidant, anticancer, and antimicrobial properties. Moreover, they were generally observed to form films on walls of their storage containers. In this thesis, we are interested in tannic acid (TA) which is a hydrolysable polyphenols, *i.e.* galloyl esters of glucose, mainly due to its antibacterial properties and ability to bind with proteins via hydrogen bonding and hydrophobic interactions.[4]

#### *2.1.3.1 Tannic acid*

Tannic acid (TA) is a hydrolysable polyphenol consisting of a pentagalloyl glucose core containing five galloyl moieties attached to the core via ester linkages **(Figure 2.3)**. It is a weak acid with pKa around 6. It is the best-known polyphenol for its ability to precipitate proteins which is attributed to its highest molecular weight (1701.2 g/mol) among other polyphenols. It has been explored for the LbL buildup with enzymes, proteins, and metal ions.[4] We are interested to use TA due to its antibacterial properties and the ability to interact with proteins.

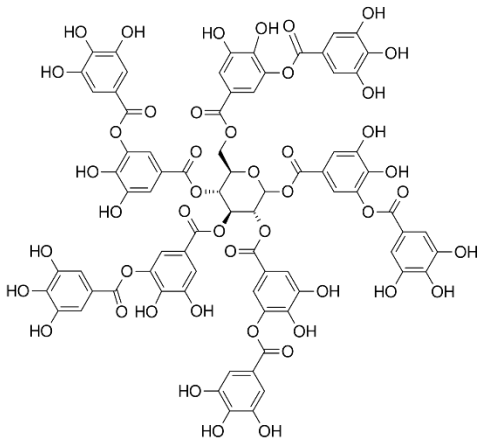

***Figure 2.3:*** *Chemical structure of tannic acid (TA).*

### 2.1.4 Polysaccharides

Polysaccharides, also known as polycarbohydrates or glycans, are the most abundant carbohydrates present in food. Chemically, they are composed on monosaccharides joined together by glycosidic linkages. In this thesis, we are interested in chitin, a structural polysaccharide.

#### *2.1.4.1 Chitin*

Chitin[5] is the second most abundant natural polymer after cellulose; extracted from crustaceans shell **(Figure 2.4)**. Chitin is a semi crystalline biopolymer and submitted to a strong acid hydrolysis treatment, nano whiskers can be isolated. Chitin is known for its biocompatibility, biodegradability and for its antibacterial properties. Chitin has been shown to be primarily antibacterial against gram-positive bacteria.[6] It targets the cytoplasmic membranes of bacteria and the mode of action could be summarized as: the adsorption onto the bacteria cell surface, the diffusion through the cell wall, the binding to the cytoplasmic membrane, disruption of the cytoplasmic membrane and release of cytoplasmic constituents such as K+ ions, DNA and RNA with induce bacteria death.[7] Chitin, is never fully acetylated, and some amino groups are present randomly distributed on the surface. It can interact with polyanion to create LBLs films . Chitin nanofiber have been used to develop micropatterned flexible substrate to induce fibroblasts orientation via contact guidance.[8-

[9] This LBL can be very interesting in the field of biomaterials where there is a growing interest in developing new coatings and materials to prevent bacterial adhesion and biofilm formation.

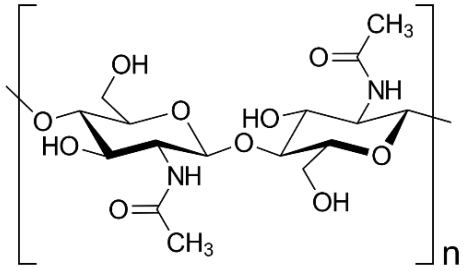


***Figure 2.4:*** *Molecular structure of chitin.*[10]

## 2.2 Solutions and substrates

All solutions were prepared freshly prior to use except COL. Deionized water (Milli-Q, 18.2 MΩ·cm at 25 °C) supplied by Advantage A10 (MERCK) was used in the entire study. The pH values were adjusted by using 0.1 M HCl or 0.1 M NaOH solution prepared in deionized water. Prior to thin film buildup, all the solutions were filtered using a 0.20 µm filter (Sarstedt, no. 831826001) to remove any impurity or undissolved substances.

Silicon wafers or microscopic glass slides were cut using a sharp diamond pen to obtain 1 × 6 $cm^2$ rectangular substrates. Silicon wafers were cleaned with ethanol/water (50% v/v) solution for 15 min prior to their use. Glass substrates were cleaned by immersing in the solutions of 10 mM SDS and 0.1 M HCl at 70°C for 10 min each, followed by extensive rinsing with deionized water. Prior the film buildup, the substrates were plasma etched for 2.5 min with air using Harrick PDC-002-HP at high RF level to remove particles and to render the surface negatively charged and hydrophilic.

The relevant details are provided in the corresponding chapters.

## 2.3 Characterization techniques

### 2.3.1 Quartz crystal microbalance with dissipation (QCM-D)

Quartz crystal microbalance (QCM) was developed by Sauerbrey in the early 1960s. It is a technique that allows to follow the deposition of mass on a surface with a sensitivity of around 17.7 ng.cm$^{-2}$ corresponding to 1 Hz change in the resonance frequency. Based on the nature of the deposited material, *i.e.*, metal, polymer, etc. and the environment, *i.e.*, air and water, the mathematical models allow to calculate the mass and the thickness of the material deposited. It should be noted that the thickness calculated is valid for homogenous deposits and not for heterogeneous ones.

The working of the QCM uses the piezoelectric properties of a quartz crystal resonator. When an electrical field is applied to a quartz crystal, it is mechanically deformed **(Figure 2.5)** and vice versa. The quartz crystal is sandwiched by two conducting gold layers to apply an electric potential.

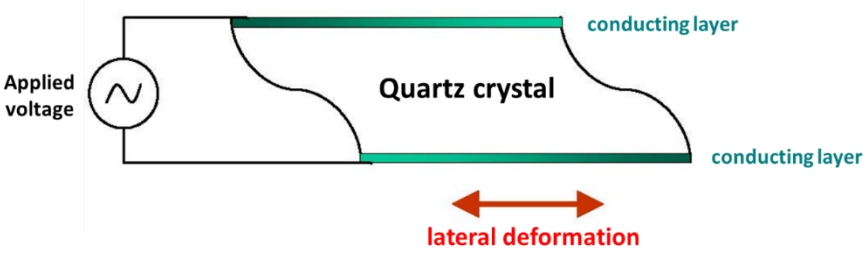


***Figure 2.5:*** *Schematic representation of a sandwiched quartz crystal submitted to an electric field and vibrating in the lateral direction.*

Upon connecting to the electric potential, the system acts as a harmonic oscillator with an associated resonance frequency $f_r$ described as below:

$$f_r = \frac{1}{2\pi}\sqrt{\frac{k}{M}}$$

where *k* is the stiffness constant of the quartz crystal in N/m and *M* is its mass in kg. Therefore, it is shown that if the mass of the crystal is increased by depositing material on it, inevitably its resonance frequency will decrease (**Figure 2.6**). Hence, the evolution of the mass deposition on the crystal can be followed be the change in the resonance frequency.

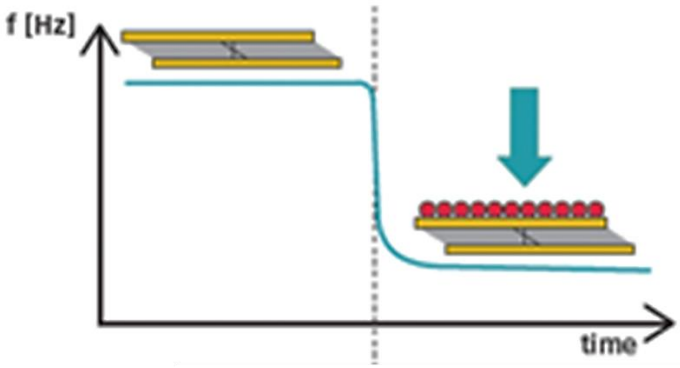


***Figure 2.6:*** *Schematic representation frequency shift measured by QCM-D of the adsorption of material on the crystal.*[11]

In the case of a small amount of material deposited on top of the crystal of a mass *m* with *m*<<*M* , the resonance frequency can be written:

$$f = \frac{1}{2\pi}\sqrt{\frac{k}{m+M}} \approx f_r\left(1 - \frac{m}{2M}\right)$$

Hence, the difference of frequency *Δf* can be written as:

$$\Delta f = f - f_r = -\frac{f_r m}{2M} = -\frac{m}{C}$$

where C is a characteristic constant of the crystal also known as “Sauerbrey’s constant” and can be written as:

$$C = \frac{2M}{f_r}$$

By measuring the resonance frequency shift of the system during an experiment, QCM with dissipation (QCM-D) allows to determine the mass deposited on the crystal with a precision of ng.cm$^{-2}$. It is also possible to measure the frequency shifts of the odd harmonics during an experiment. The Sauerbrey equation can thus be written as:

$$m = -C\frac{\Delta f_v}{v}$$

with *v* the number of the considered harmonic. This equation is valid in the case where uniform and rigid layers are deposited in air or in aqueous medium. The validity of Sauerbrey's equation can be estimated from the fact that the normalized frequency shift $\frac{\Delta f_v}{v}$ measured is independent of the l harmonics. However, it cannot be applied for viscous layers which is the case in this thesis.[12]

The QCM-D also allows the determination of a viscous dissipation factor D which relates to the sum of all the losses in the system. This parameter is defined by the proportion of dissipated energy at each oscillation with respect to the total stored energy:

$$D = \frac{E_{dissipated\ at\ each\ oscillation}}{2\pi E_{stored}}$$

This dissipation factor is measured by exciting the quartz crystal at its fundamental frequency and the odd harmonics and then by measuring the time needed by the crystal to relax while its energy is dissipated in the crystal, in the deposit and in the medium in contact with the crystal surface **(Figure 2.7)**.

The D factor gives an indication about the viscoelastic character of a coating. If it is superior to a few tens, the viscous modulus of the deposit cannot be neglected and the Sauerbrey relation is not valid anymore.[13-14]

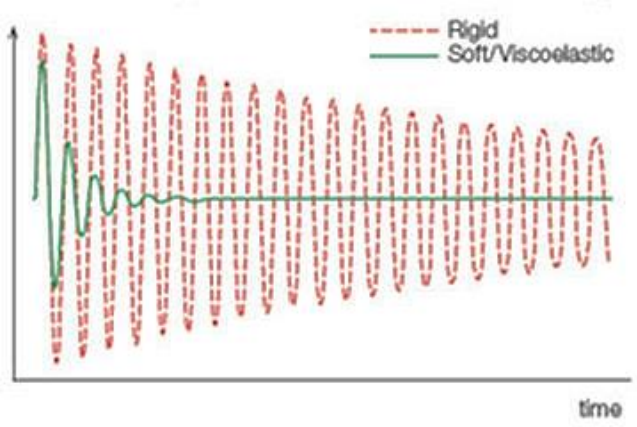


***Figure 2.7:*** *Schematic representation of the time evolution of the potential difference at a quartz crystal in the case of a rigid and viscoelastic coating. The damping observed for a rigid film is low while the damping corresponding to the adsorption of a viscoelastic layer is high due to the dissipative nature of the viscoelastic film towards the acoustic wave generated by the resonator. The dissipation factor D higher for a viscoelastic substrate deposited on the quartz crystal than for a rigid one.*

### 2.3.2 Optical characterization

Light can be considered as an electromagnetic wave that travels through space. The electric field behavior of waves in space and time is defined as polarization. A wave's electric field is always orthogonal to its direction of propagation. As a result, the x- and y-components of a wave traveling in the z-direction can be used to characterize it. Unpolarized light is described to have a completely random direction and phase. The different light polarizations are explained below.

*Linear polarization:* When the outcome of two orthogonal light waves is confined to a single plane along the propagation direction, it is called linearly polarized.

*Circular polarization:* If the two orthogonal waves are out of phase by 90°, but equal in amplitude, light is referred to as circularly polarized.

*Elliptical polarization:* Light is called elliptically polarized when the orthogonal waves have arbitrary phase and amplitudes.

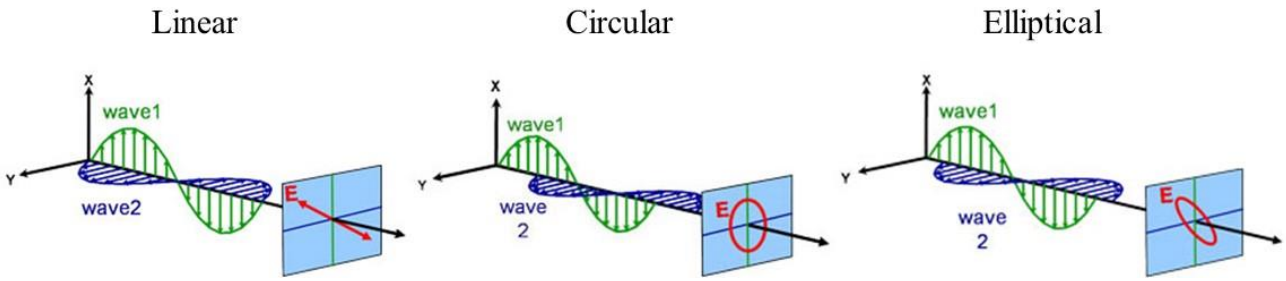


***Figure 2.8:*** *Schematic illustration of orthogonal waves to show light polarization.*[15]

Various optical characterizations used in this thesis are described below.

#### *2.3.2.1 Ellipsometry*

Ellipsometry, a non-destructive optical technique, is used to measure mainly the thin film thickness. At an incidence angle of 45° to the normal a linearly polarized light beam, with p-polarized and s-polarized components, falls on a sample. In general, the reflected wave is elliptically polarized **(Figure 2.9)**. This change in the polarized light after reflection from the sample surface is measured. The ellipsometer analyzes this information in terms of film optical properties such as roughness, thickness, and refractive index. A monochromatic light source, often a laser in the visible spectral area with a wavelength of 632.8 nm, is used in single wavelength ellipsometry to focus the beam on a small spot size. The ellipsometry is strictly limited to the samples with lower surface roughness values usually <30% and the deposited material should permit light reflection. Surfaces with high roughness scatter a large portion of the incident laser making the measurements difficult.

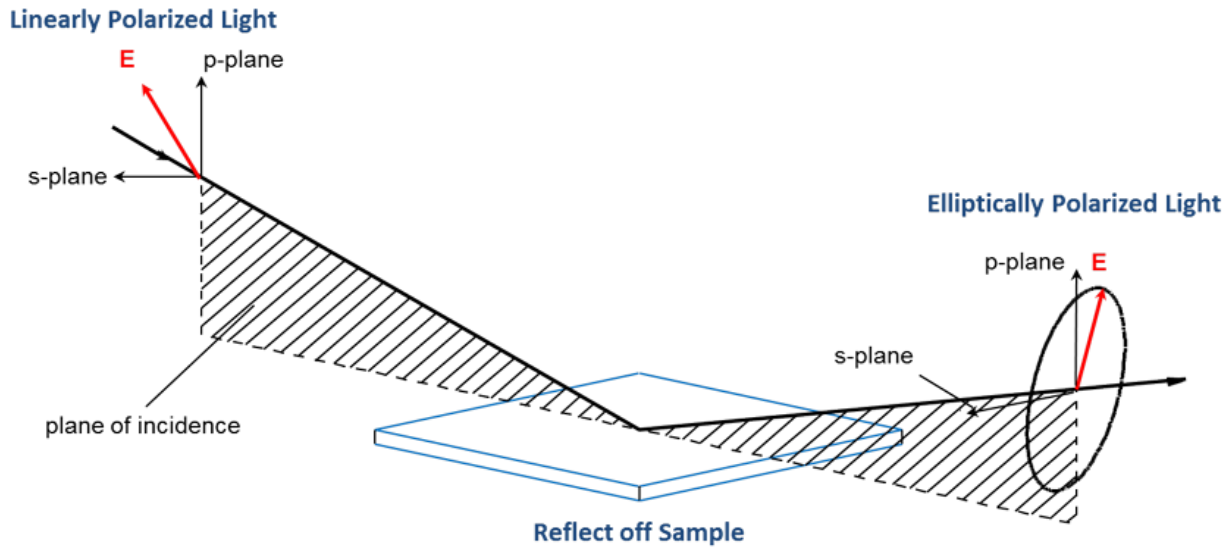


***Figure 2.9:*** *Schematic illustration of an ellipsometry measurement with the change of polarization state of light from linear to elliptical after reflecting off of the sample.*[15]

For the LbL films, the reflected wave is made of the light reflected from all the interfaces **(Figure 2.10)**. First, the incident light encounters the air-polymer interface where a part of the light is reflected and the rest of the light is transmitted through the polymer layer thickness, until it encounters the next polymer-substrate interface where it undergoes a phase difference "β" which is related to the layer thickness by the equation below:

$$\beta = 2\pi \left(\frac{d}{\lambda}\right) N_2 \cos\alpha_2$$

where d is the thickness of the polymer layer, λ is the wavelength of the incident light, $\alpha_2$ is the incidence angle, and $N_2$ is the complex refraction index of the polymer layer.[16-17]

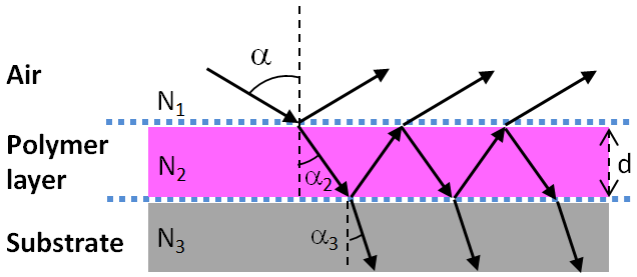


***Figure 2.10:*** *Schematic illustration of light reflection from the two phases; the polymer-air and polymer substrate interface, upon contact with a polymer film deposited on a substrate.*

*2.3.2.1.1 Experimental setup*

In this thesis, the film thickness was measured, after rinsing with water and drying by compressed air, using an Ellipsometer (SD2300, PLASMOS) with an incident laser beam (632.8 nm) and a constant angle of 45°. Refractive index was assumed to be constant and $n$ = 1.465 for all the measurements. The dry thickness values reported here are the average of ten measurements observed at random areas on each multilayer sample surface. Such ellipsometry measurements show insignificant differences in absolute dry thickness.

### *2.3.2.2 Dynamic Light Scattering*

Dynamic Light Scattering (DLS), Zetasizer® from Malvern, was used to determine the average size and zeta potential of the nanocrystals in solution. This technique measures, at a fixed angle, the mean particle size in a limited size range. The sample is illuminated by a laser beam and the fluctuations of the scattered light are detected at an angle of 90° by a photon detector. The signal is used to determine the diffusion coefficient and the particle size by the Stokes-Einstein equation.

### *2.3.2.3 Circular dichroism*

Circular dichroism (CD) spectroscopy is quite sensitive to determine the secondary structure of polypeptides and proteins. The difference in absorbance of right- and left-circularly polarized light

is measured and generally presented as a spectrum in the far UV range from 180 nm to 300 nm (or even higher). The obtained spectra can be analyzed for various secondary structures such as, β-sheets, α-helix, random coil etc. As we are using COL to develop LbL films, it is important to get insight into the secondary structure of the triple helix. Specific experimental details are provided in the chapters when required.

#### *2.3.2.4 Fourier transform infrared spectroscopy*

Infrared (IR) spectroscopy works on the principles of light-matter interactions, *i.e.,* the matter absorbs light. Fourier transform infrared spectroscopy (FTIR) uses mid infrared region (4500 $cm^{-1}$ to 400 $cm^{-1}$). When infrared light travels through a sample, characteristic frequencies related to chemical bonds are absorbed by the substance's, causing molecular vibrations. Upon absorption, the resulting molecular vibrations can be presented as a function of wavenumber in the IR spectrum with molecular fingerprints unique to a certain compound. The intensities and the frequencies of absorbed IR light depend on the specific bond strengths. The wavelength at which maximal absorption occurs is defined as an absorption band. Because the intensity of this band is proportional to the number of molecules in the substance, the IR spectrum can provide both qualitative and quantitative data. Thanks to the correlation between intensities and the mass, the FTIR spectroscopy can be used to follow the layer-by-layer deposition process by recording the FTIR spectra after the deposition of each deposited polymer layer. The absorbance of one or more distinctive bands of the polymers that are being deposited for LbL buildup determines the growth process. The growth of the LbL film occurs when the absorbance of these bands rises in intensity with the number of deposited layers.[18-20]

Hence, we can follow the LbL buildup *in-situ* using the FTIR technique. The specific experimental details are provided in the chapters when required.

### 2.3.3 Morphological characterizations

#### *2.3.3.1 Atomic Force Microscopy*

The topography of LbL films was observed to check if the brush-based layer-by-layer method enables to create the aligned nanotopography surfaces. To analyze the sample's surface topography, we used the Atomic Force Microscopy (AFM), a scanning probe microscopy technique. There are two main modes for AFM imaging, contact mode and tapping mode. In contact mode, the tip is in contact with the sample and go throw the surface. In tapping mode, the tip oscillates at its frequency close to the sample surface without making contact. The interaction between the tip and the sample can be attractive or repulsive that modifies then the oscillation frequency. AFM detects the interatomic forces (electrostatic force, Van der Waals force, ionic repulsion force, etc.) that exist between a tip and the sample surface. The tip has a fixed spring constant and enable to detect forces in the piconewton range providing high resolution images (of the order of fractions of a nanometer).[21-22]

#### *2.3.3.2 Scanning electron microscopy (SEM)*

Scanning electron microscopy (SEM) is a technique for examining and analyzing sample surface morphology. SEM uses electrons, instead of light, that are bombarded on the sample. To Condenser lenses intensify an electron beam, from an electron gun, into a tiny spot as small as 1 nm in diameter which is used to scan desired sample areas. When the electron beam interacts with the sample, it produces secondary electrons, backscattered electrons, and characteristic X-rays. Detectors gather the generated signals, which are then stored in computer memory and mapped as brightness variations to create an image. The commonly utilized signal, generated by the interaction of the electron beam with the sample, is the secondary electron signal which fluctuates

with the morphology of the sample surface and the scanned image appears as dark for recesses and bright for edges.[23-24] In this thesis, we used SEM mostly to determine the morphology of bacteria.

## 2.4 Bibliography


1. Parenteau-Bareil, R.; Gauvin, R.; Berthod, F., Collagen-Based Biomaterials for Tissue Engineering Applications. *Materials* **2010,** *3* (3), 1863-1887.
2. Revell, C. K.; Jensen, O. E.; Shearer, T.; Lu, Y.; Holmes, D. F.; Kadler, K. E., Collagen fibril assembly: New approaches to unanswered questions. *Matrix Biology Plus* **2021,** *12*, 100079.
3. Xu, L. Q.; Neoh, K.-G.; Kang, E.-T., Natural polyphenols as versatile platforms for material engineering and surface functionalization. *Progress in Polymer Science* **2018,** *87*, 165-196.
4. Reitzer, F.; Allais, M.; Ball, V.; Meyer, F., Polyphenols at interfaces. *Advances in colloid and interface science* **2018,** *257*, 31-41.
5. Stef - Mincea, M.; Negrulescu, A.; Ostafe, V., Preparation, modification, and applications of chitin nanowhiskers: A review. *Reviews on Advanced Materials Science* **2012,** *30*, 225-242.
6. Qin, Y.; Zhang, S.; Yu, J.; Yang, J.; Xiong, L.; Sun, Q., Effects of chitin nano-whiskers on the antibacterial and physicochemical properties of maize starch films. *Carbohydrate Polymers* **2016,** *147*, 372-378.
7. Kim, C.-H.; Kim, S.-Y.; Choi, K.-S., Synthesis and Antibacterial Activity of Water-soluble Chitin Derivatives. *Polymers for Advanced Technologies* **1997,** *8* (5), 319-325.
8. Qi, Z.-D.; Saito, T.; Fan, Y.; Isogai, A., Multifunctional Coating Films by Layer-by-Layer Deposition of Cellulose and Chitin Nanofibrils. *Biomacromolecules* **2012,** *13* (2), 553-558.
9. Taniguchi, T.; Kyung, K.-H.; Shiratori, S., Layer-by-layer self-assembled thin films of chitin fibers and heparin with anti-thrombus characteristics. *RSC Advances* **2015,** *5* (130), 107488-107496.
10. Berezina, N., Production and application of chitin. *Physical Sciences Reviews* **2016,** *1* (9).
11. QCM-D. https://www.3t-analytik.de/technologies/qcm-d/what-qcm-d.
12. Sauerbrey, G., Verwendung von Schwingquarzen zur Wägung dünner Schichten und zur Mikrowägung. *Zeitschrift für Physik* **1959,** *155* (2), 206-222.
13. Dixon, M. C., Quartz crystal microbalance with dissipation monitoring: enabling real-time characterization of biological materials and their interactions. *J Biomol Tech* **2008,** *19* (3), 151-158.
14. Alves, N. M.; Picart, C.; Mano, J. F., Self Assembling and Crosslinking of Polyelectrolyte Multilayer Films of Chitosan and Alginate Studied by QCM and IR Spectroscopy. *Macromolecular Bioscience* **2009,** *9* (8), 776-785.
15. Light Polarization and Ellipsometry
16. Woollam, J. A.; Snyder, P. G., Fundamentals and applications of variable angle spectroscopic ellipsometry. *Materials Science and Engineering: B* **1990,** *5* (2), 279-283.
17. Introduction to Spectroscopic Ellipsometry. In *Spectroscopic Ellipsometry*, 2007; pp 1-11.
18. Wallrabe, U.; Korvink, J.; Mohr, J., 1.13 - LIGA. In *Comprehensive Microsystems*, Gianchandani, Y. B.; Tabata, O.; Zappe, H., Eds. Elsevier: Oxford, 2008; pp 293-340.
19. Colthup, N. B., Infrared Spectroscopy. In *Encyclopedia of Physical Science and Technology (Third Edition)*, Meyers, R. A., Ed. Academic Press: New York, 2003; pp 793-816.
20. Nan, C.; Yue, W.; Tao, L.; Yang, X., Fourier transform infrared nano-spectroscopy: Mechanism and applications. *Applied Spectroscopy Reviews* **2020**, 1-22.
21. Fundamentals of Atomic Force Microscopy—Part I *MRS Bulletin* **2016,** *41* (4), 341-341.

22. Garcia, R.; Herruzo, E. T., The emergence of multifrequency force microscopy. *Nature Nanotechnology* **2012,** *7* (4), 217-226.
23. Vernon-Parry, K. D., Scanning electron microscopy: an introduction. *III-Vs Review* **2000,** *13* (4), 40-44.
24. Aharinejad, S. H.; Lametschwandtner, A., Fundamentals of Scanning Electron Microscopy. In *Microvascular Corrosion Casting in Scanning Electron Microscopy: Techniques and Applications*, Aharinejad, S. H.; Lametschwandtner, A., Eds. Springer Vienna: Vienna, 1992; pp 44-51.

# Chapter 3 : Antibacterial Tannic acid/Collagen coatings

## Effect of the Buffer on the Buildup and Stability of Tannic acid/Collagen Multilayer Films applied as antibacterial coatings

The following chapter was published in ACS Applied Materials and Interfaces 2020, 12, 22601

# Table of Contents

The deposition of polyelectrolyte multilayers, obtained by the Layer-by-layer (LbL) method, is a well-established technology to design biocompatible and antibacterial coatings aimed at preventing implant-associated infections. In this chapter, we explored the interactions between tannic acid (TA) and collagen (COL) to develop the LbL films using acetate and citrate buffers at pH 4. Surprisingly, the used buffer impacts not only the physico-chemical but also the antibacterial properties of the films. An emphasis is placed on a comprehensive evaluation of the physico-chemical parameters driving the buildup and the antibacterial property of TA/COL films.

## 3.1 Introduction

Development of multifunctional coatings has drawn a great attention in the last few decades because of their broad spectrum of applications. In biomedical related fields, surface properties like antimicrobial activity and biocompatibility are highly desired. Such surfaces can be used to improve host tissue-material interaction and subsequent tissue integration of biomedical implants.[1] Medical devices are most likely to undergo nosocomial infections because of local contamination during the surgery. Such infections are triggered by bacterial adhesion on the surface of the implant followed by their proliferation and matrix synthesis leading to the formation of a biofilm. Prevention of the early attachment and proliferation of bacteria has created huge interest and led to the development of antibacterial coatings.[2-3] Among the surface modification techniques, the Layer-by-Layer (LbL) method is a versatile way to functionalize surfaces by the alternated deposition of oppositely charged polyelectrolytes generally by dip coating.[4] It is an attractive method as it can be applied to any type of substrate, even neutral polymers.[5] The coherence of these films is usually due to the electrostatic interactions between the chains. Hydrogen bonded LbL films were also reported.[6-7] The adhesion strength between the LbL films and the substrate can be improved by grafting of the first deposited layer. The growth of LbL films is either linear

or exponential with the number of deposition steps. Performed at room temperature using aqueous solutions, the LbL method allows the development of biocompatible and bioactive thin films, in particular with antimicrobial property.[8-9] Several types of LbL films have been reported to exhibit anti-adhesive and/or antimicrobial (contact-killing or release killing) properties governed not only by the incorporated compounds but also by the buildup conditions or post-buildup treatments. Adhesion-resistant LbL films are either highly hydrophilic preventing the close contact of bacteria[10] or have specific stiffnesses to prevent bacterial adhesion.[11-12] The hydrophilicity[13] of the films as well as their rigidity[11, 14] can be tuned by the adjustment of physico-chemical parameters of the film buildup, such as pH and/or ionic strength. Knowing that bacterial membranes are negatively charged, most of contact-killing LbL films were developed ending with positively charged polyelectrolytes, such as chitosan,[15] poly(allylamine),[16] poly(L-arginine),[17], poly(L-Lysine)[18] or quaternary ammonium containing polymers.[19-20] Various factors or properties govern the bactericidal effect of these films, such as surface composition[13] or diffusion of polycations in exponentially growing films.[17-18, 21] Diffusion ability of polycations in exponentially growing LbL films is a crucial property to obtain a contact-killing effect on several strains of bacteria. The antibacterial property was explained by mobile polycation chains diffusion out of the film toward the negatively charged bacterial membranes leading to their destabilization.[17-18, 21] Release-killing LbL films leach out antibacterial agents, by direct diffusion[22-23] or by film degradation due to hydrolysis,[24-25] pH,[26] or enzymes.[27] In last few decades, an intensive research is being carried out to explore the potential of polyphenols, found in plants as secondary metabolites, as antibacterial and antioxidants agents. Tannic acid (TA) is a polyphenol **(Section 2.1.3.1)** known to inhibit the growth of bacteria.[28] TA based LbL films were mainly developed to obtain antifouling,[29] self-healing[30] and hemostatic[31] properties. With the exception of one study,[32] antibacterial properties

of TA based LbL films were always obtained with the incorporation of antibacterial compounds, such as antibiotics,[33] peptides[34] or chitosan.[35] Park et al.[32] developed sprayed TA/Fe(III) films as an antifungal coating for shoe insoles.

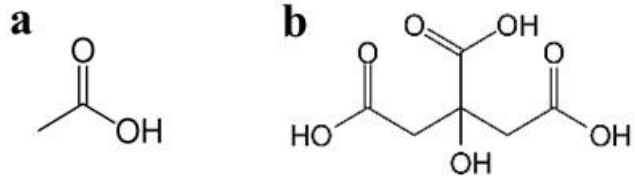


***Scheme 3.1:*** *Chemical formulae of the buffers used in this study* ***(a)*** *acetic acid and* ***(b)*** *citric acid.*

In this study, we report buffer dependent antibacterial property of LbL films based on TA and collagen type I (COL). COL is the most abundant extracellular matrix protein present in the mammalian body and can be assembled in LbL manner with different polyanions.[36-40] Because of solubility issues of COL, TA/COL films were built at pH 4 using either acetate buffer or citrate buffer **(Scheme 3.1b and c)** to prepare TA and COL solutions. Acetic acid is a monoprotic acid with a pKa at 4.7. Citric acid is a triprotic acid with three different pKa at 3.1, 4.8, and 6.4 leading to only one deprotonated and two protonated carboxylic acids at pH 4. In this form, citric acid is thus able to form hydrogen bonds and electrostatic interactions. Surprisingly, the used buffer impacts not only the physicochemical properties but also the antibacterial effect of TA/COL films. Emphasis is given on a comprehensive evaluation of the physicochemical parameters driving the buildup and the antibacterial property of the films. Specifically, complexation strengths between TA and COL are different in the presence of acetate or citrate affecting the LbL deposition.

## 3.2 Experimental section

### 3.2.1 Materials

Collagen (COL, purified type I from calf, Symatese, France), tannic acid (TA, Mw = 1701.2 g/mol, Sigma-Aldrich, France), poly(ethylene imine) (PEI, branched, 30% w/w aq. solution, Mw = 50 000–100 000 g/mol, Alfa Aesar, Germany), acetic acid (Mw = 60.05 g/mol, Sigma-Aldrich), citric acid monohydrate (Mw = 210.14 g/mol, Sigma-Aldrich), sodium citrate tribasic dihydrate (Mw = 294.10 g/mol, Sigma-Aldrich), Dulbecco's phosphate buffer saline (PBS, L0615, Dominique Dutscher, France), sodium dodecyl sulfate (Prolabo, Poland), HEPES sodium salt (Mw = 260.29 g/mol, Sigma-Aldrich), NaCl (VWR), HCl, and NaOH (Sigma-Aldrich) were used as received.

### 3.2.2 TA/COL layer-by-layer buildup

TA/COL films were built on a PEI precursor layer. The PEI solution was prepared at 0.1 mg/mL in 0.15 M NaCl without pH adjustment. Acetate buffer was prepared at pH 4 with 0.1 M acetic acid. Citrate buffer was prepared at pH 4 by mixing 59 mL 0.1 M of citric acid and 41 mL of 0.1 M sodium citrate solutions. TA and COL were prepared at 0.1 mg/mL using either acetate or citrate buffer. TA solutions were prepared freshly, and COL solutions were prepared and left under stirring overnight before use. One hundred microliters of compound (respectively buffer) were deposited on the substrate at each deposition (respectively rinsing) steps. PEI was used as a first layer with 5 min of deposition step followed by two rinsing steps (5 min) with 0.15 M NaCl and acetate or citrate buffer. TA deposition time was 5 min and COL deposition time was 15 min with a rinsing step of 5 min with the same solution used to dissolve the compounds. The obtained PEI-(COL/TA)n were denoted (COL/TA)n acetate (respectively citrate) films when built with compound solutions prepared in acetate (respectively citrate) buffer.

### 3.2.3 Quartz crystal microbalance with dissipation (QCM-D)

TA/COL film buildup was followed by quartz crystal microbalance with dissipation (QCM-D) using QCM-D E1 (Q-Sense, Goteborg, Sweden) with the QCM open cell allowing the pipetting of the solutions. $SiO_2$ coated quartz crystal (Microvacuum, Budapest, Hungary) was excited at its fundamental frequency (about 5 MHz), as well as at the third, fifth, seventh, and ninth overtones (denoted by $\nu = 3, 5, 7$ and 9) corresponding to 15, 25, 35, and 45 MHz, respectively. The results corresponding to changes in the frequency shifts ($\Delta f_\nu/\nu$) and dissipation ($\Delta D_\nu$), obtained from QCM-D experiments, were analyzed using the Voigt-Voinova model to determine the film thickness.[41] The mass density of the film was fixed at 1 g/cm$^3$, the mass density of the solutions was fixed at 1.009 g/cm$^3$, and their viscosity was at 0.91 mPa·s. $SiO_2$-coated QCM crystals were treated by UV/ozone treatment for 15 min prior to experiment to ensure negatively charged hydrophilic surface. One hundred microliters of compound solution (respectively buffer) were deposited on the crystal at each deposition (respectively rinsing). PEI was used as a first layer with 5 min of deposition step and 5 min of rinsing step with 0.15 M NaCl. TA deposition time was 5 min and COL deposition was 15 min to reach a stability of the QCM signal with a rinsing step of 5 min with the same solution used to dissolve the compounds. To test the stability of the films in physiological conditions, $(COL/TA)_6$-COL acetate and citrate films were put in contact with 350 µL of PBS at pH 7.4 overnight, followed by a rinsing step with the buffer.

### 3.2.4 Atomic force microscopy (AFM)

AFM Multimode Nanoscope IV from Bruker (Palaiseau, France) was used to image TA/COL films in the liquid state using silicon nitride coated tips on a gold-covered cantilever (Model ScanAsyst-Fluid from Bruker with force constant $k$ = 0.7 N/m and frequency $f_o$ = 150 kHz) in the peak force tapping (ScanAsyst Fluid) mode. The images were obtained at a scan rate of 1 Hz with a resolution

of 256 × 256 pixels. The data analysis was performed using NanoScope Analysis Software (version 1.7). After dipping into ethanol/water (50:50 v/v) for 15 min followed by plasma cleaner treatment for 3 min, silicon wafers were used as substrates for TA/COL buildup. The samples were stored in the buffer before observation. Different areas of the samples were scanned to obtain typical topography images. The roughness of the film was determined using the RMS value given by the Nanoscope software on at least three AFM images (10 × 10 $\mu m^2$). The film thickness was measured by imaging film scratches, obtained using a sharp tweezer, on three different areas perpendicular to the fast scan axis. We define the film thickness as the minimal *z*-distance between the bare substrate and the surface of the film, which covers the whole substrate.

### 3.2.5 Isothermal titration calorimetry (ITC)

Nano ITC standard volume (TA Instruments, U.S.A.) was used to record interaction isotherms during the titration of COL by TA in both acetate and citrate buffers at pH 4. The sample and reference cell volumes were 1 mL, and the syringe volume was 250 μL. The reference cell was filled with ultrapure water (Milli-Q) and the sample cell with a COL solution at 0.62 mM. A 1.645mM TA solution (titrant) was placed in a-motor driven syringe, which was set on rotation (300 rpm) to ensure proper mixing of the reactants. Two-hundred fifty microliters of the titrant was added in the sample cell in 25 injection steps of 10 μL each with a stabilization time of 1200 s between two consecutive injections. Different controls were performed, that is, buffer in buffer, titrant dilution in buffer, and buffer in COL. The latter did not show a significant difference with the buffer in buffer experiment. The heat associated with the titrant-in-buffer control was subtracted from the heat of the COL/TA association. TA/COL mixture solutions, at 0.28 TA/COL molar ratio in citrate and acetate buffers, were observed by AFM in the peak force tapping (ScanAsyst Air) mode in dry state. The samples were diluted 8-fold in their respective buffer. Fifty

microliters of the diluted solution were put in contact on the muscovite mica substrates followed by two steps of rinsing with water at pH 4 and a drying step at room temperature.

### 3.2.6 Circular dichroism (CD) spectroscopy

CD spectra were collected using a JASCO J-810 spectropolarimeter. The spectra were recorded between 190 and 400 nm with a bandwidth of 1 nm, NIR bandwidth of 20 nm, number of accumulations 3, and the scanning speed of 100 nm/min. After UV/ozone treatment for 15 min, quartz lamellae were used as substrates to build TA/COL films. The background was measured with uncoated quartz lamella. CD spectra were recorded in the dry state with data pitch of 1 nm on the light wavelength.

### 3.2.7 Attenuated total reflection – Fourier transform infrared spectroscopy (ATR - FTIR)

FTIR experiments were performed on a Vertex 70 spectrometer (Bruker, Germany) using a DTGS detector. Spectra were recorded in the attenuated total reflection (ATR) mode using a ZnSe crystal (45° trapezoidal, six reflections, dimensions of 72 × 10 × 6 $mm^3$) by averaging 128 interferograms between 800 and 4000 $cm^{-1}$ at 2 $cm^{-1}$ resolution, using Blackman-Harris three-term apodization and Bruker OPUS/IR software (version 7.5). FTIR spectra of TA/COL films were recorded after each polyelectrolyte deposition step followed by the rinsing step. After buildup, FTIR spectra were recorded during the contact with PBS buffer for 24 h. All the solutions were prepared in deuterated buffer to avoid the interference of the water peak in the amide I region of collagen. The background spectrum was taken with a bare ZnSe crystal in contact with the buffer used for the film buildup.

### 3.2.8 X-ray Photoelectron Spectroscopy

A Thermo Scientific K-alpha+ spectrometer was used to acquire the XPS spectra. The monochromatic Al Kα line was used as X-ray excitation (1486.6 eV) with pass energy of 50 eV to

obtain high resolution spectra. The samples were analyzed using a microfocused, monochromated AlKα X-ray source (400 μm spot size). XPS spectra were fit with one or more Voigt profiles (binding energy uncertainty: ±0.2 eV) and Scofield sensitivity factors were applied for quantification.[42] All spectra were referenced to the C 1s peak (C—C, C—H) at 285.0 eV binding energy controlled by means of the photoelectron peaks of metallic Cu, Ag, and Au, respectively. Carbon (C 1s) spectra were recorded at the beginning and after each resolution analysis to check the absence of any sample degradation under irradiation. XPS analyses were performed on $(COL/TA)_7$ films in comparison to COL and TA monolayers, obtained by dipping. All the samples were rinsed with water at pH 4 before the drying step to avoid salt deposition from the supernatant. The COL/TA molar ratio of the films was calculated using the amount of oxidized carbon (named $C_{ox}$), corresponding to the 286, 288, and 289 eV peaks, present on all compounds and the total amount of nitrogen, present only for COL.

#### *3.2.8.1 Determination of the proportion of TA and COL by XPS*

XPS investigation allowed the determination of both atomic and chemical functions composition of the samples. Determined by curve fitting, the atomic concentration (%) of a peak represents the ratio of the peak intensity to the total intensity of electrons in the measurement. COL/TA molar ratio was determined by the atomic ratio given by:

$$\text{COL/TA} = \text{quantity of COL / quantity of TA} = X\text{COL} / (X\text{TA/COL films} - X\text{COL})$$

where $X = C\text{ox}/N\text{total}$, $C$ox being the total atomic concentrations of oxidized carbon (named $C$ox), corresponding to the 286, 288 and 289 eV peaks (present for all compounds) and $N$total the total amount of nitrogen present only on COL. In the case of TA/COL citrate films, there are also oxidized carbon peaks originating from citrate. Then, $C$ox is given by :

$$Cox\ (\text{TA/COL citrate films}) = Cox\ (\text{total}) - Cox\ (\text{citrate})$$

$$\text{with } Cox\ (\text{citrate}) = Na \times (4/3)$$

where *Na* being the total atomic concentration of sodium and (4/3) the value obtained by calculation of *C*ox/*Na* of citrate powder.

### 3.2.9 TA release in physiological media

TA release from TA/COL films in PBS buffer was followed by measuring the absorbance intensity at 277 nm using a spectrofluorometer (SAFAS Xenius XC). COL used in the study showed no absorption at this wavelength. First, a calibration curve of TA was obtained by measuring the absorbance intensity at 277 nm for different concentrations of TA in PBS buffer. TA/COL films were prepared on 12 mm Ø glass slides and stored in the buffer used for their buildup. Five hundred microliters of PBS buffer at pH 7.4 at room temperature was put in contact with the films. One hundred microliters of the supernatant was withdrawn and put in an UV-Star 96-well plate (Greiner bio-one) to measure the absorbance at 277 nm. The remaining 400 µL of supernatant was replaced by 500 µL of PBS buffer. Similar experiments were performed using HEPES 10 mM pH 7.4 at 37 °C, without and with an additional 150 mM NaCl, to mimic the medium used in microbiology and in cell culture, respectively.

### 3.2.10 Antimicrobial assay

The antibacterial activity of $(COL/TA)_6$-COL and $(COL/TA)_7$ films, prepared on 12 mm Ø glass substrates using acetate and citrate buffers, were determined towards *Staphylococcus aureus* (*S. aureus*, ATCC® 25923™), a gram-positive strain, and *Escherichia coli* (*E. coli*, ATCC® 25922™). One colony of *bacteria* was pre-cultured aerobically in Mueller-Hinton (MH) broth and lysogeny broth (LB) (pH 7.2-7.6, Merck, Darmstadt, Germany), for *S. aureus* and *E. coli*

respectively, in an incubator under agitation for 24 h at 37°C. The pre-culture was diluted to an optical density at 620 nm ($OD_{620}$) of 0.001 corresponding to approximately $8 \times 10^5$ CFU/mL just before use. Before the test the TA/COL films were exposed 20 min to UV radiation. TA/COL films were incubated with 400 µL of bacterial solution ($OD_{620}$ = 0.001) in an incubator at 37°C. For *S. aureus*, the quantification of the bacteria in their planktonic state after contact with film samples for 24 and 48 h, was performed by using a serial dilution and counting method. Bacterial suspensions in contact with the samples were diluted, by serial dilution, between $10^2$ to $10^5$ times. 100 µL of each dilution were spread uniformly on nutrient agar plates and the number of colonies forming units (CFU) were counted after 24 h incubation. Quantification was performed on the first plate showing formation of isolated CFUs. For *E. coli*, the normalized growth (%) was calculated as the following equation, using the optical density ($OD_{620}$), measured at 620 nm of the inoculation in contact with the films:

$$\text{Normalized Growth (\%)} = \frac{OD_{620}(\text{film with bacteria}) - OD_{620}(\text{film without bacteria})}{OD_{620}\ (\text{uncoated glass coverslips with bacteria}) - OD_{620}(\text{film without bacteria})} \times 100$$

### 3.2.11 Scanning electron microscopy (SEM)

SEM (FEI Quanta 250 FEG) was used to image TA/COL films after 24 h of contact with MH medium with and without bacterial inoculation. After a rinsing step in PBS, TA/COL samples were dipped in 400 µL of paraformaldehyde 4% (PFA) for 15 min to fix the bacterial cells on the film surface, followed by three PBS rinsing steps, three water rinsing steps, and water/ethanol rinsing steps using 70%, 95%, and 100% ethanol. The samples were treated with hexamethyldisilazane (HMDS)/ethanol mixture (50:50 v/v) for 5 min followed by two rinsing steps with pure HMDS (5 min each). After removal of the HMDS solution, the samples were dried under a laminar flow fume hood and metalized with gold using a sputter coater.

### 3.2.12 Cytotoxicity analysis

The cytotoxic effect of $(COL/TA)_6$-COL and $(COL/TA)_7$ films, prepared on 14 mm Ø glass slides using acetate and citrate buffers, was determined toward fibroblasts derived from human gingiva (HGFs). Human gingiva harvesting was approved ethically and methodologically by our local Research Institution and was conducted with informed patients (written consent) in accordance with the usual ethical legal regulations (Article R 1243-57). All procedures were done in accordance with our authorization and registration number DC-2014–2262 given by the National ‘‘Cellule de Bioéthique”. HGFs were seeded on the top of substrates at $10^4$ cells/cm$^2$ and maintained in complete culture medium (DMEM, supplemented with 10% decomplemented fetal bovine serum (FBS), 1% penicillin/streptomycin/amphotericin B and 1% glutamax (v/v, Gibco)] for 9 days. WST-1 cell proliferation assay (Roche Diagnostics, France) was performed after 2, 5, and 9 days of culture. Absorbance was measured at 490 nm using a FLUOstar Omega microplate reader (BMG Labtech) against a background control as a blank with a reference wavelength of 750 nm. After 2, 5, and 9 days of culture, DNA was extracted using the MasterPureTMDNA Purification Kit (EpicenterBiotechnologies) in accordance with the manufacturer protocol. Extracted DNA was assessed by measuring the absorbance at 260 and 280 nm (Nanodrop, Thermo Scientific) with a 260/280 nm absorbance ratio for all measured samples comprised between 1.8 and 2. Cytoskeleton staining was accomplished with Alexa Fluor-488 conjugated-Phalloidin. After 15 days of culture, fibroblasts were fixed with 4% (w/v) paraformaldehyde for 15 min at room temperature, permeabilized with 0.5% (v/v) Triton X-100 for 15 min, and finally stained with Alexa Fluor-488 conjugated-Phalloidin (Invitrogen, 1/100) for 30 min. Nuclei were counterstained with 4,6-diamidino-2-phenylindole (DAPI, 100 ng/mL, 1:10,000 dilution) for 5 min. The stained cells were then mounted and imaged by fluorescence microscopy (Zeiss microscopy, ×20).

## 3.3 Results and discussion

### 3.3.1 TA/COL film buildup in acetate and citrate buffers

The buildup of TA/COL LbL films was monitored *in situ* by QCM-D using TA and COL solutions prepared at pH 4 in acetate or citrate buffers. The film thickness was calculated by fitting the QCM-D data using the Voigt–Voinova model **(Figure 3.1a)**. In contrast to the normalized frequency shift **(Figure 3.2a, b)**, the evolution of the film thickness as a function of adsorbed layer showed no level off but rather a change in the slope of the growth. $(COL/TA)_6$-COL films acetate and citrate films reached 333 and 150 nm in thickness, respectively.

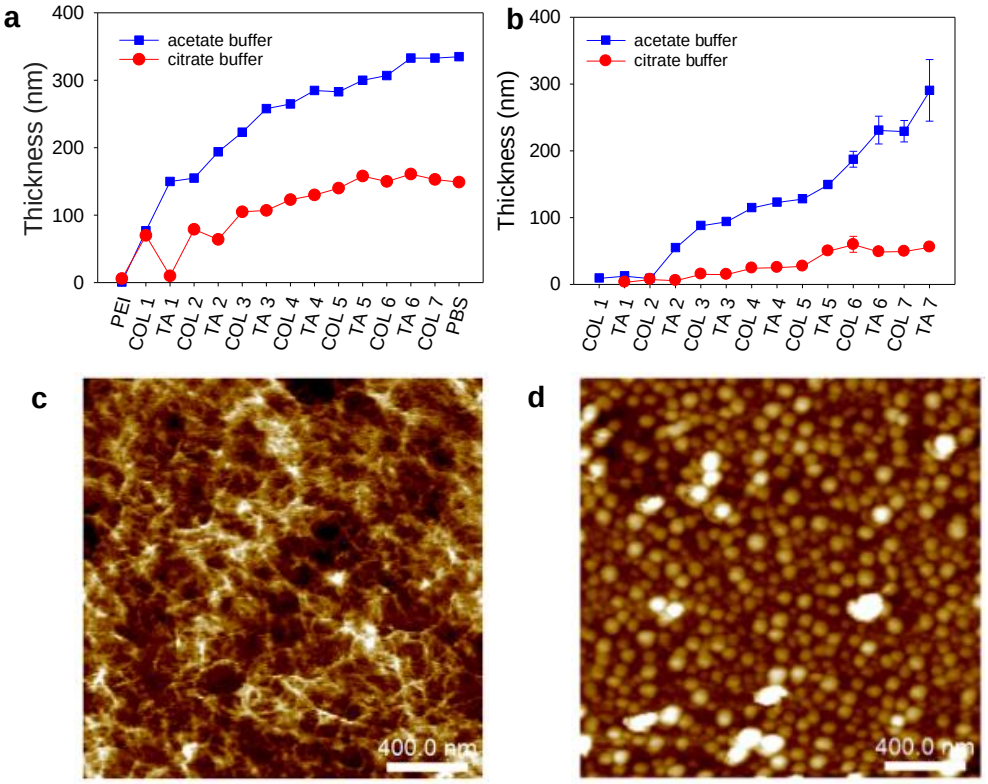


***Figure 3.1:*** *Evolution of the thickness of TA/COL films built in acetate (■) and citrate (●) buffers at pH 4 as a function of each deposited layer* ***(a)*** *determined with the Voigt-Voinova model using the QCM-D data, at the last step, PBS buffer was put in contact for 14 h,* ***(b)*** *determined by AFM in liquid state. Typical AFM images (z scale 50 nm), obtained in Peak Force Tapping mode (ScanAsyst) and in the liquid state, $(COL/TA)_2$ films built at pH 4 in acetate* ***(c)*** *and citrate* ***(d)*** *buffers.*

The normalized frequency shift ($\Delta f_v/v$) measures the contributions from adsorbed material and bound water molecules whereas the dissipation change ($\Delta D_v$) represents the rigidity of the coatings, related to the hydration and conformations of adsorbed material.[43] When $\Delta D_v$ versus $\Delta f_v/v$ are plotted, two phases are displayed with significantly different slopes **(Figure 3.3c, d)**. The first phase with the highest slope corresponds to loosely bound (macro)molecules with a large amount of hydrodynamically coupled water. In the second phase, $\Delta D_v$ slightly increases with the adsorbed material. The amount of hydrodynamically trapped water is reduced creating a denser coating.[44]

Bound water loss of TA/COL films is compensated by adsorbed materials leading to stabilization of the frequency shift. AFM was used to investigate the thickness and the topography of TA/COL films in liquid state. The cross-section of TA/COL scratched films allowed one to determine the film thickness in liquid state. The film thickness was defined as the minimal *z*-distance between the bare substrate and the surface of the film that covers the whole substrate **(Figure 3.4)**. In wet state, TA/COL acetate films have a higher thickness than citrate films reaching (291 ± 46) nm and (56 ± 5) nm after seven bilayers, respectively **(Figure 3.1b)**. The water uptake of TA/COL film was determined by comparing the film thickness in dry state and in wet state. In the case of $(COL/TA)_6$-COL LbL, acetate films swell by 388% with an increase in thickness from (59 ± 4) to (229 ± 16) nm from dry to wet. Citrate films swell by 294% with an increase in thickness from (17 ± 2) to (50 ± 4) nm. A strong difference in water uptake is observed between both types of film in accordance with the difference in dissipation values measured by QCM-D. The high water adsorption is explained by the ability of TA to form hydrogen bonds with water molecules.[45] This ability is probably compromised by the presence of citrate interacting with TA which leads to less hydrated films. **Figure 3.1c,d** shows the typical topography of TA/COL films. Fibrillary structures

were observed for acetate films and granular structures for citrate films throughout the film buildup **(Figure 3.5)**. In citrate buffer, the size of the granular structures increases with the number of bilayers. In acetate buffer, the fibrillary structures are progressively hidden with an increase in the film thickness rendering their observation more and more difficult.

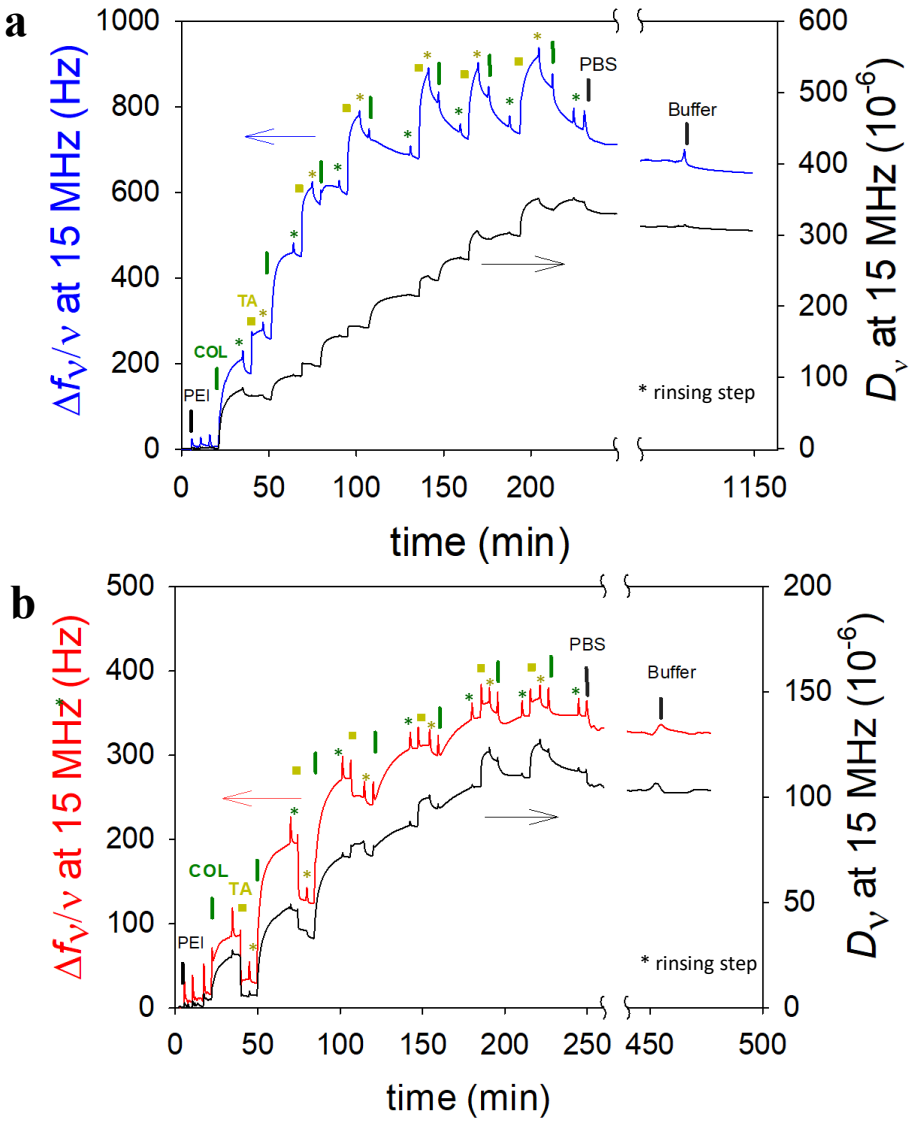


***Figure 3.2:*** *Evolution of the normalized frequency shift, measured by QCM-D using the open cell, as a function of time during the buildup of PEI-(COL/TA)6-COL films in* ***(a)*** *acetate and* ***(b)*** *citrate buffers at pH 4. The stability of the films was evaluated in contact with PBS at pH 7.4 and room temperature. Small perturbations of the signal appeared at each deposition and rinsing steps due to pipetting of the solution on the crystal mounted in the open cell.*

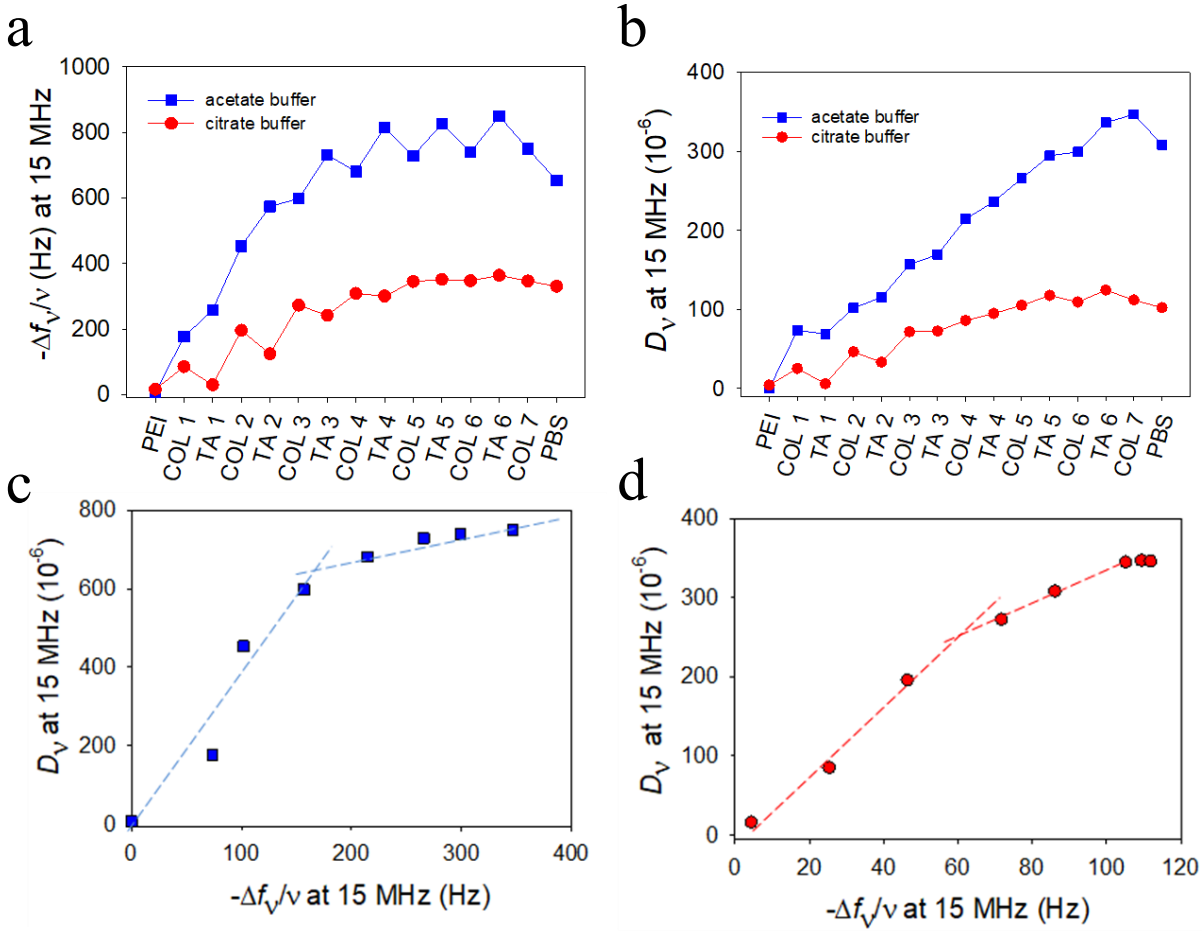


***Figure 3.3:*** *Evolution of the **(a)** frequency shift and **(b)** the dissipation value, measured by QCM-D at 15 MHz as function of each deposited layer and **(c, d)** of the dissipation value as function of the normalized frequency shift during the buildup of a TA/COL film in acetate **(c)** and citrate **(d)** buffers. The plot shows the change in slope during the buildup related to a change from loosely bound (macro)molecules with hydrodynamically trapped water to the deposition of a compact film.*

TA/COL acetate films show a roughness between 10 and 25 nm all along the buildup, representing not more than 10% of the film thickness **(Figure 3.6)**. The roughness of TA/COL citrate film increases reaching around 50 nm after seven bilayers. The thicknesses of TA/COL acetate films are similar when determined by QCM-D and AFM. In contrast, the high roughness of citrate films increased the hydrodynamic thickness determined by QCM-D in comparison to the core thickness determined by AFM (compare **Figure 3.1a** and **b**).

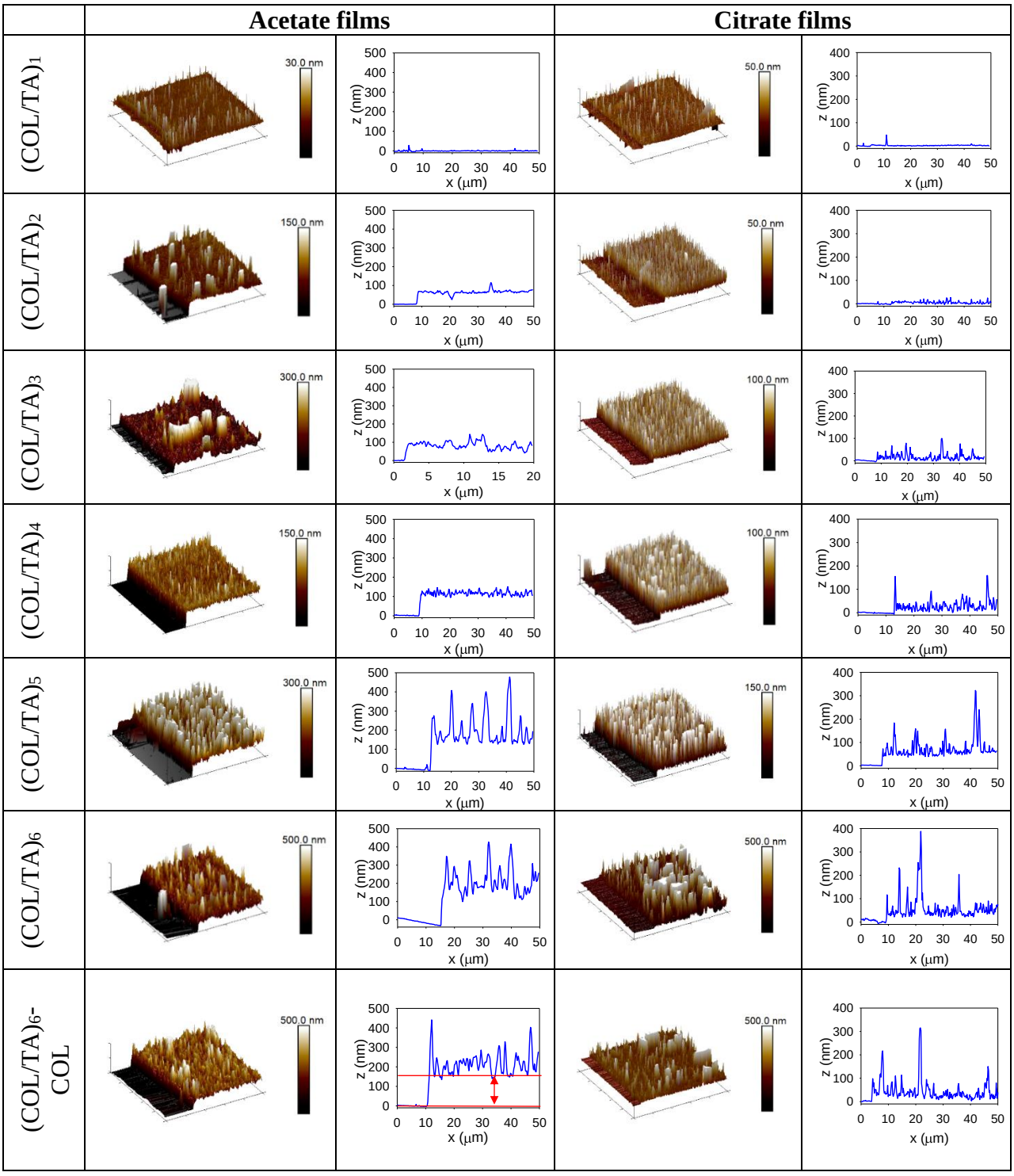


***Figure 3.4:*** *AFM images, obtained in PeakForce Tapping mode (ScanAsyst) and liquid state, and respective cross-sectional profiles of scratched $(COL/TA)_n$ films built in acetate and citrate buffers at pH 4, as a function of number of bilayers. The thickness was analyzed on a scan size of 50 × 50 μm². It was defined as the minimal z distance between the bare substrate and the surface of the film that covers the whole substrate, as represented by the arrow on the cross-section profile of $(COL/TA)_6$-COL acetate.*

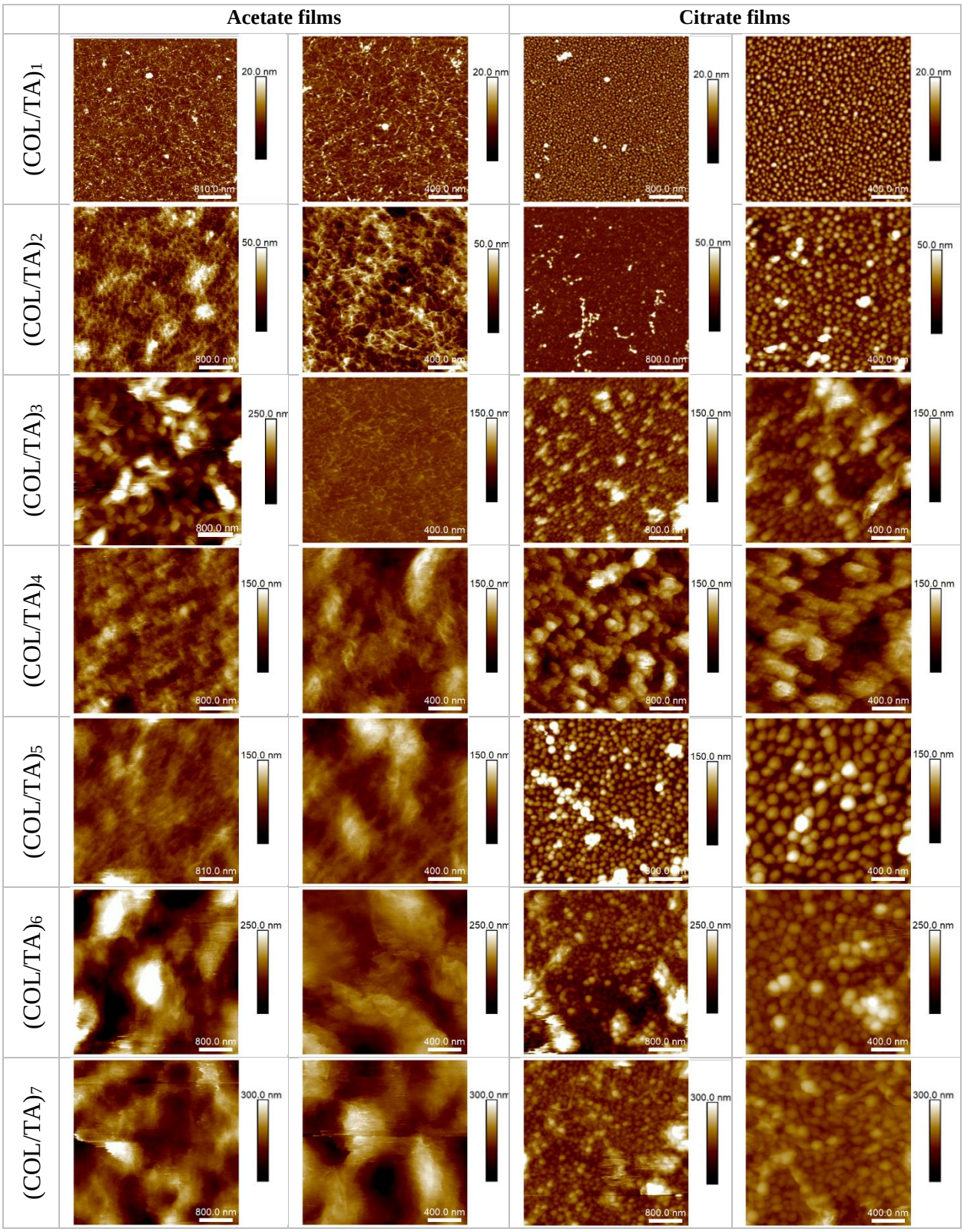


***Figure 3.5:*** *AFM images, obtained in PeakForce Tapping mode (ScanAsyst) in liquid state, of (COL/TA)n films built in acetate and citrate buffers at pH 4, as a function of the number of bilayers.*

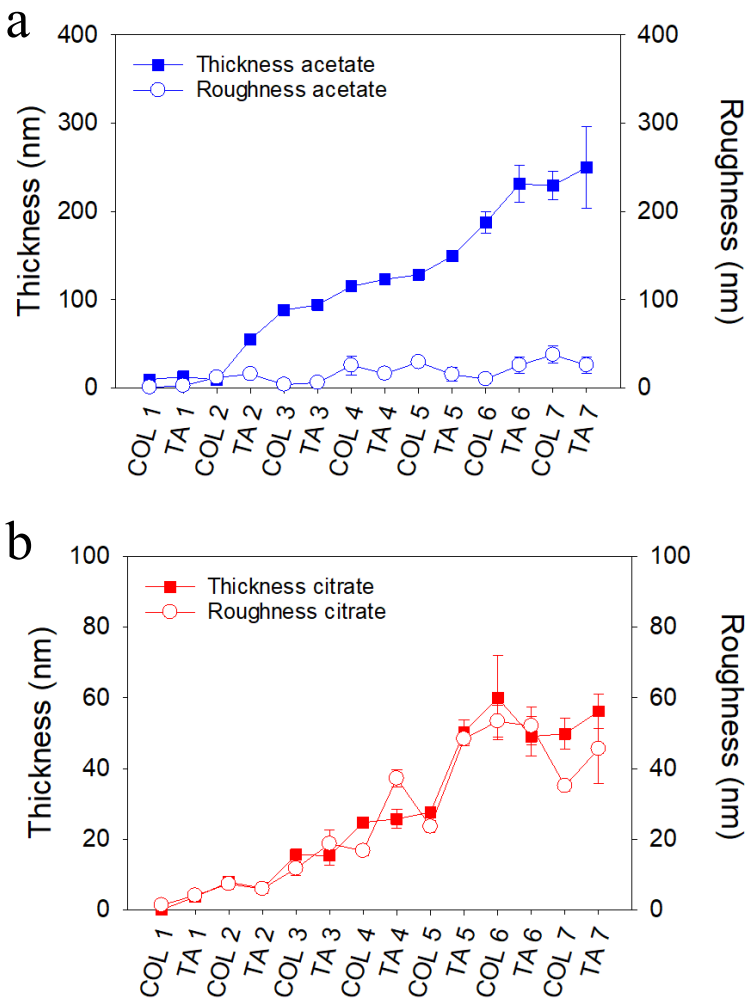


***Figure 3.6:*** *Evolution of the thickness and roughness, determined by AFM in Peak Force Tapping mode and in liquid state, of TA/COL films built in* ***(a)*** *acetate buffer and* ***(b)*** *citrate buffer. The mean and standard deviation of the values were calculated on at least three different areas.*

### 3.3.2 Insight into the nature of TA/COL complexation.

The buffers used to dissolve COL and TA give rise to TA/COL films with two different buildup regimes and topographies. This effect might originate from the modification in the interactions between COL and TA dissolved in these two different buffers. Polyphenols can have multiple interactions with proteins depending on their physicochemical parameters, such as molecular weight, hydrophobicity and isoelectric point.[46] Tannins are known to interact with collagen[47] and

other proline-rich proteins[48] through both hydrogen bonding and hydrophobic interactions. To better elucidate the distinct physicochemical properties of TA/COL films in the two buffers, we performed ITC experiments to investigate COL and TA interactions. The heat of complexation was measured by adding aliquots of TA solution into a cell containing COL solution. The molar enthalpy change ($\Delta H_{obs}$) was calculated from the heat measured at each step of the titration subtracting the heat of the control experiments, that is, buffer in buffer and titrant dilution in buffer **(Figure 3.7)**. For both buffers, the titration plots of $\Delta H_{obs}$ are not a typical sigmoidal curve specific to antigen–antibody interactions. This precludes the fitting of the curves by stoichiometric binding models. As the heat measured was quite small, we performed at least three experiments for each condition **(Figure 3.8a,b)** and control experiments.

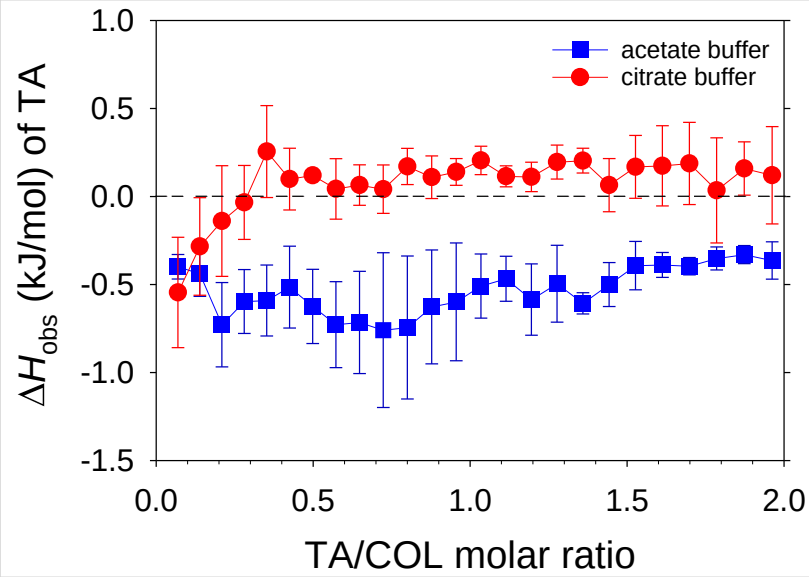


***Figure 3.7:*** *Molar enthalpy change ($\Delta H_{obs}$), measured by ITC, during the titration of COL by TA at 22°C. The data represents the mean and standard deviation of at least three experiments.*

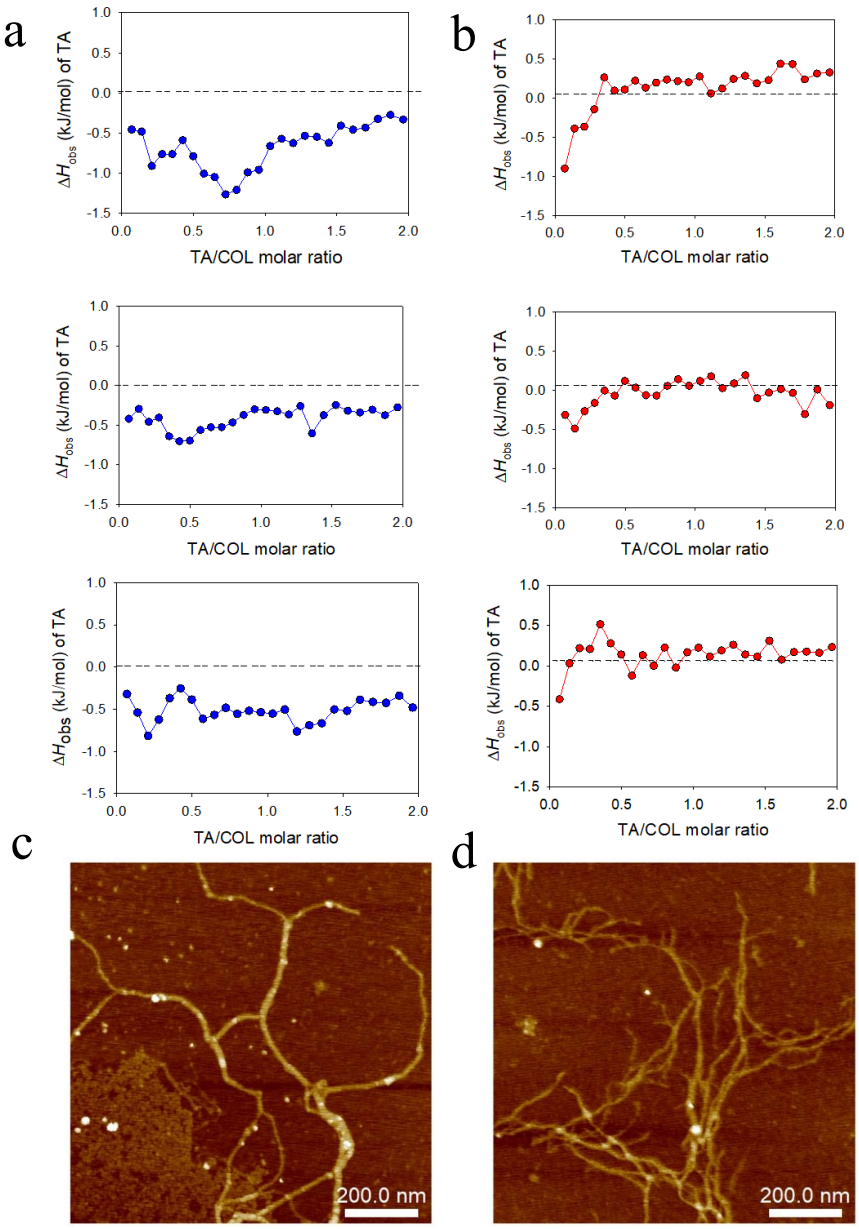


***Figure 3.8: (a-b)*** *Molar enthalpy change ($\Delta H_{obs}$), measured by ITC, during the titration of COL by TA at 22°C in acetate* ***(a)*** *and citrate* ***(b)*** *buffers. The data represent the three experiments used for Figure 5 of the manuscript. The molar enthalpy change ($\Delta H_{obs}$) was calculated from the heat measured at each step of the titration subtracting the heat of the control experiments, i.e., buffer in buffer and titrant dilution in buffer.* ***(c, d)*** *Typical AFM images (z scale = 5 nm), obtained in Peak Force Tapping mode (ScanAsyst) and in the dry state, of TA/COL complexes formed at 0.28. TA/COL molar ratio in acetate* ***(c)*** *and citrate* ***(d)*** *buffers following the ITC titration procedure.*

Two different behaviors were observed depending on the used buffer. In the case of acetate buffer,

TA/COL complexation exhibits an exothermic behavior (*i.e.*, heat is released) all along the titration

by TA up to 2 TA/COL molar ratio. This could be related to the formation of hydrogen bonds between amino groups and peptide bond H-acceptor sites of COL and galloyl or hydroxyphenyl moieties of TA. In the case of citrate buffer, the change in enthalpy reaches zero at 0.28 TA/COL molar ratio, where saturation conditions seem to be reached. At this point, we observed COL aggregation in citrate but not in acetate buffer **(Figure 3.8c,d)**. ITC results suggest that TA/COL binding is stronger in citrate buffer in comparison to acetate buffer.

To determine the proportion of TA and COL in the films, XPS analyses were performed on $(COL/TA)_7$ films in comparison to COL and TA monolayers obtained by dipping. XPS survey spectra revealed that carbon, oxygen, sodium, and nitrogen are present in TA/COL films **(Figure 3.10a,b** and **Table 3.1)**. **Figure 3.9** presents C 1s high-resolution XPS spectra of the different.

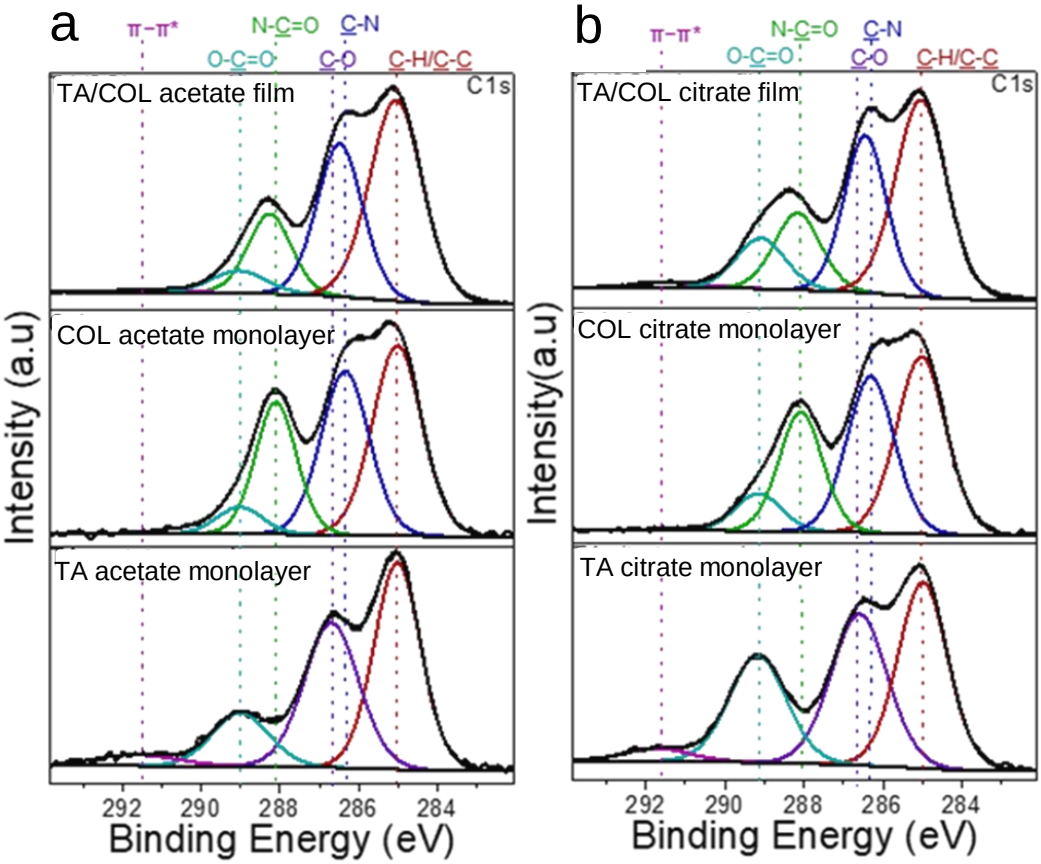


***Figure 3.9:*** *C1s XPS spectra of (COL/TA)7 films, TA and COL monolayers obtained by using TA and COL solutions prepared in* ***(a)*** *acetate and* ***(b)*** *citrate buffers at pH 4.*

The COL/TA molar ratio of the films was calculated using the amount of oxidized carbon, corresponding to the 286, 288, and 289 eV peaks, present on all compounds and the total amount of nitrogen, present only for COL. The details on the calculations can be found in the section **3.2.8.1**.

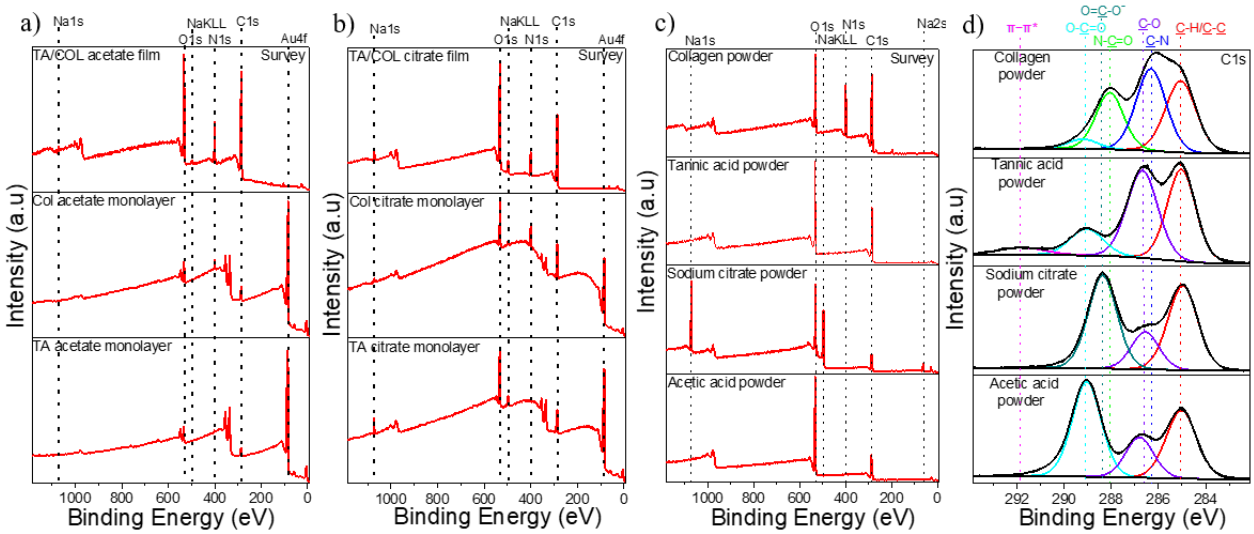


***Figure 3.10: (a, b)*** *Survey XPS spectra of TA/COL films, TA and COL monolayers obtained by using TA and COL solutions prepared in* ***(a)*** *acetate and* ***(b)*** *citrate buffers at pH 4. TA and COL monolayers were obtained by dipping on gold substrate and TA/COL films were built on $SiO_2$ coated QCM crystals.* ***(c)*** *Survey and* ***(d)*** *C1s XPS spectra of TA, COL, acetic acid, and sodium citrate powders.*

***Table 3.1:*** *Elemental composition, in atomic percentage, of TA/COL films and COL monolayers obtained from TA and COL solutions prepared in acetate and citrate buffers.*

| | **COL acetate monolayer** | **COL citrate monolayer** | **TA/COL acetate film** | **TA/COL citrate film** |
|---|---|---|---|---|
| *Cox* (total) (%) | 29 | 36 | 32 | 33 |
| $C_{ox}$ (citrate) (%) | - | 2.7 | - | 1.9 |
| $N_{total}$ (%) | 13 | 15 | 12 | 8.2 |
| Cox/$N_{total}$ (*X*) | 2.2 | 2.2 | 2.7 | 3.8 |
| **COL/TA molar ratio** | - | - | **4.4** | **1.4** |

The COL/TA molar ratio was found at 1.4 for citrate films and 4.4 for acetate ones. A higher quantity of TA is incorporated for each adsorbed COL when citrate is used as a buffer, which is probably related to the strong affinity between both compounds. Besides the presence of the Na 1s peak, a higher contribution of the O–C═O peak (289.1 eV) is observed for TA and COL citrate monolayers in comparison to TA and COL powders or acetate monolayers. Citrate molecules can interact through hydrogen bonds with TA molecules[49] and through both hydrogen bonds[50] and electrostatic interactions[51] with COL. When TA/COL LbL are built in citrate buffer, the incorporated citrate molecules interacting with COL through electrostatic interactions lead probably to supplementary H-bond sites for TA immobilization **(Scheme 3.2)**.

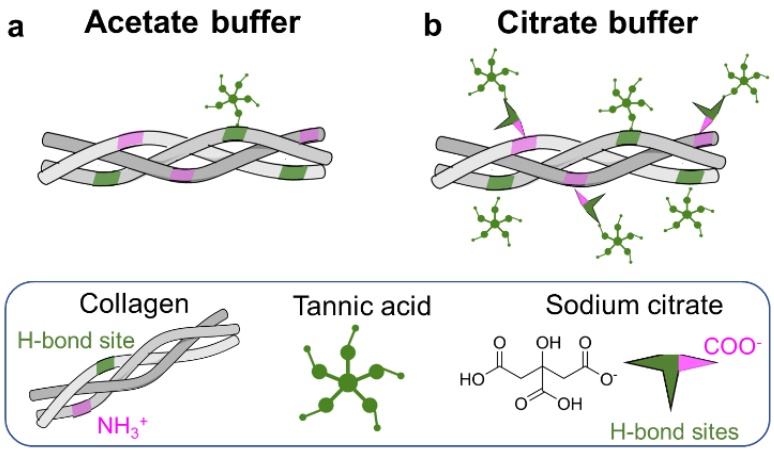


***Scheme 3.2:*** *Schematic illustration of TA/COL interactions in* ***(a)*** *acetate and* ***(b)*** *citrate buffers. At pH 4, citric acid has one deprotonated carboxylic acid. Some elements were produced using Servier Medical Art image bank (https://smart.servier.com). Servier Medical Art by Servier is licensed under a Creative Commons Attribution 3.0 Unported License.*

During the LbL buildup in acetate buffer followed by QCM-D, each deposition of TA and COL induced an increment in the frequency shift **(Figure 3.2a)** but the rinsing steps removed a non-negligible amount of the previous deposited layer suggesting a low binding between TA and COL **(Scheme 3.3)**. The fibrillary structure of COL is maintained all over the buildup.

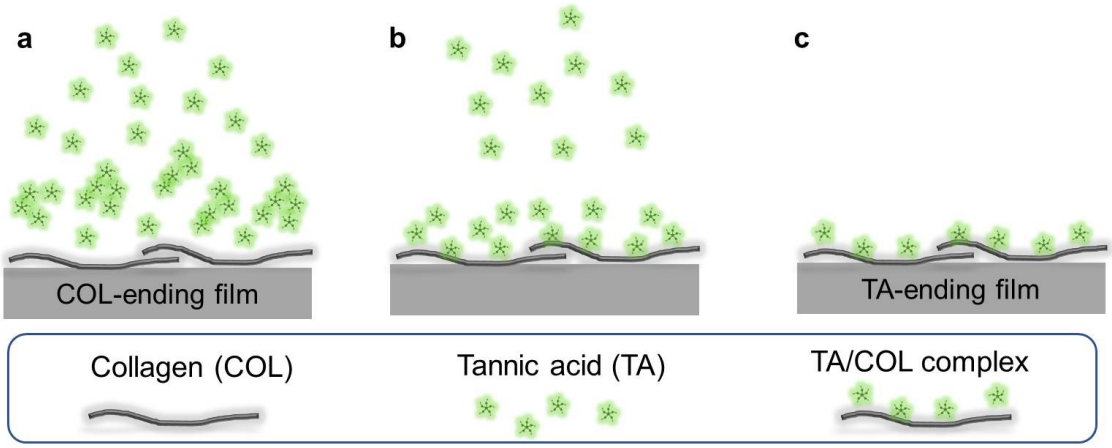


***Scheme 3.3:*** *Schematic illustration of TA/COL LbL buildup in acetate buffer.* ***(a)*** *When TA is put in contact with a COL-ending film,* ***(b)*** *TA molecules adsorbed on COL leading to TA/COL complexes.* ***(c)*** *The rinsing step removes the loosely bound TA molecules leading to TA-ending film. The fibrillary structure of COL is maintained during the buildup.*

In the case of citrate buffer, the buildup is irregular with an increase in the frequency shift for COL and a decrease for TA **(Figure 3.2b)**. An increase in thickness was observed for each TA/COL bilayer suggesting the adsorption of TA/COL complexes on the surface. The rinsing steps do not induce a supplementary loss of material, confirming the strong binding of TA/COL on the surface. A molecular model describing the formation of polyphenol/protein complexes, proposed by Williamson and co-workers,[52] could explain this behavior and the granular topography of TA/COL citrate films. Upon addition of TA solution on COL-ending film, TA binds strongly to several sites of the adsorbed COL forming TA/COL compact complex inducing COL desorption and decrease in frequency shift **(Scheme 3.4a)**. The presence of high concentration of TA in the supernatant leads to the dimerization **(Scheme 3.4b)** and then aggregation of TA/COL complexes **(Scheme 3.4c)** into larger particles that precipitate **(Scheme 3.4d)** on the surface of the LbL film. The TA/COL complex precipitation step thus allows the deposition of the next layer of COL. The deposition of TA/COL precipitates on the surface was obtained because the film buildup was done

by pipetting the solutions on and from the QCM cell as performed in 24-well plates used for microbiology tests.

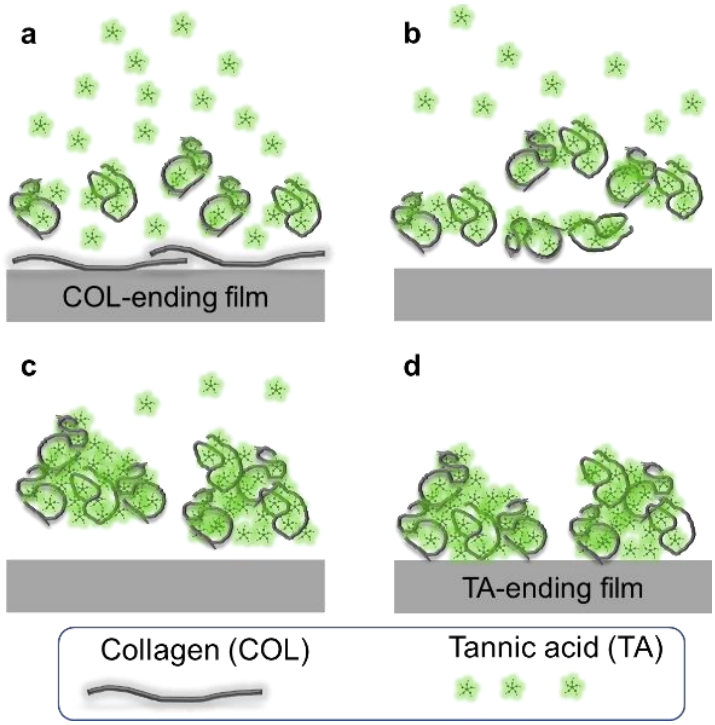


***Scheme 3.4:*** *Schematic illustration of TA/COL LbL buildup in citrate buffer. When TA is put in contact with a COL-ending film, there are* ***(a)*** *desorption of COL by TA leading to TA/COL complexes,* ***(b)*** *dimerization and* ***(c)*** *aggregation of TA/COL complexes followed by* ***(d)*** *their precipitation on the surface leading to the granular topography of TA/COL citrate films.*

### 3.3.3 Chemical characterization of TA/COL films

CD and FTIR spectroscopies were used to characterize TA/COL films. COL in solution displays characteristic optical activity in the far UV spectrum with a small positive peak near 220 nm and a large negative peak about 197 nm. At each deposition of COL, the CD spectra of TA/COL films show an intensity increase in the negative band at 197 nm indicating an effective adsorption of COL **(Figure 3.11)**. In the case of citrate films, the positive peak at 220 nm is increasing too, showing no COL denaturation. In the case of acetate films, no peak at 220 nm is visible. This peak is related to the triple helix structure of COL. Denaturation of COL is generally accompanied not

only by the disappearance of the peak at 220 nm but also by a red-shift of the negative band, which is not the case here.[53] The triple helix structure of COL seems to be impacted when adsorbed in alternated manner with TA in acetate buffer, which is in contrast to a reported study of COL/TA complexes in solution.[45]

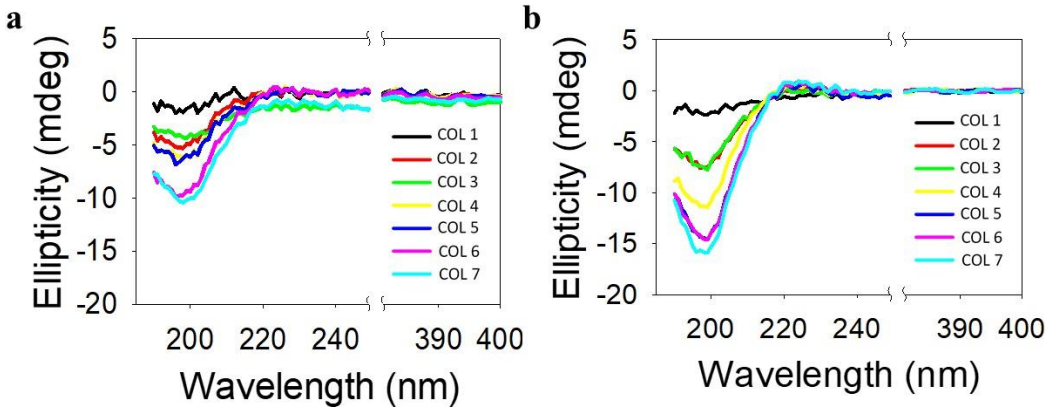


***Figure 3.11:*** *CD spectra of TA/COL films built in acetate* ***(a)*** *and citrate* ***(b)*** *buffers at pH 4. The data represent the mean of three different measurements after COL deposition.*

The ATR-FTIR spectra of TA/COL films were acquired in deuterated buffers after each COL/TA deposition cycle **(Figure 3.12)**. For both buffers, the peaks at 1655, 1565 and about 1200 $cm^{-1}$ were attributed to the characteristic amide I, II and III bands of COL, respectively.[37, 54] TA characteristic bands are also present at 1100 and between 1400 and 1500 $cm^{-1}$, corresponding to C-O vibration and C-C bonds in the phenolic rings.[55] The carbonyl (C=O) stretching and C-O vibrations of TA can be found for the acetate film at 1706 and 1610 $cm^{-1}$, respectively and for the citrate film at 1718 $cm^{-1}$ and 1605 $cm^{-1}$, respectively. The position of these latter bands can be slightly changed by their environment.[56] Intensities of all these representative bands increase after each deposition cycle which demonstrates the layer-by-layer buildup of TA/COL.

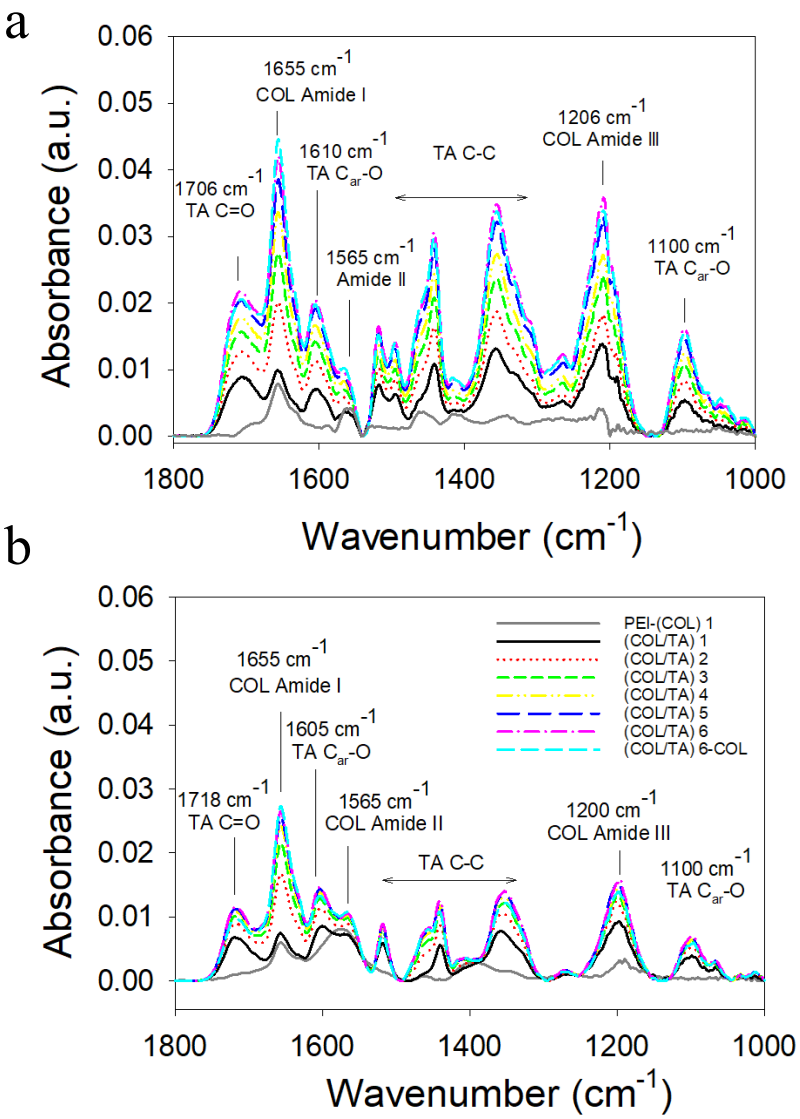


***Figure 3.12:*** *FTIR spectra of TA/COL films as a function of the deposited layers built in acetate* ***(a)*** *and citrate* ***(b)*** *buffers at pH 4. Each spectrum was monitored at room temperature after each rinsing step.*

### 3.3.4 Film stability and TA release in physiological conditions

To evaluate the stability of the films in physiological conditions, TA/COL acetate and citrate films were incubated in PBS at pH 7.4 at room temperature overnight. A decrease in intensity of the C═O stretching band of TA was observed while the amide I band of COL was unaffected **(Figure 3.13a,b)**. The same experiment was performed by QCM-D. An immediate and small decrease in frequency shifts for both films was observed which stabilized within the first 30 min **(Figure 3.2)**.

The majority of the TA/COL films was stable with a loss in the total frequency shift of about 13% for both films. It should be emphasized that most of the COL-based LbL films reported in the literature required an additional cross-linking step to maintain their stability under physiological conditions.[37, 40, 57-59]

The stability of the films toward pH and salt changes can be explained by the fact that (i) TA/COL LbL films are mainly based on hydrogen bonds and (ii) a sufficient amount of TA remains in the films to interact with COL after contact with PBS **(Figure 3.13a,b)**. High stability of hydrogen-bonded neutral polymer/polyphenol LbL films toward pH and salt changes is explained by the p$K_a$ value of TA, reported at 8.5.[60] Recently, gelatin (denatured COL)/TA complexes were reported to possess two kinds of TA species: one strongly bound to the protein matrix (responsible for its stability in physiological conditions) and other loosely bound TA molecules.[61] Weakly bound TA molecules can dissolve from the film's surface into physiological media and strongly bound TA can prevent COL from removing. The amount of TA released was determined by following the intensity of the absorbance measured at 277 nm **(Figure 3.13c)**. TA/COL films were put in contact with PBS at room temperature similar to the FTIR and QCM-D experiments. The rate of release is highest in the first hour and stabilizes afterward. TA ending films induced more TA release. After 72 h of contact, TA-ended citrate films released twice as much TA than acetate films, (13.2 ± 1.3) and (5.9 ± 1.2) μg/mL, respectively **(Figure 3.13c)**. Granular citrate films released a higher amount of TA than acetate films, because of supplementary TA molecules immobilized by electrostatic interactions thanks to citrate **(Scheme 3.5)**.

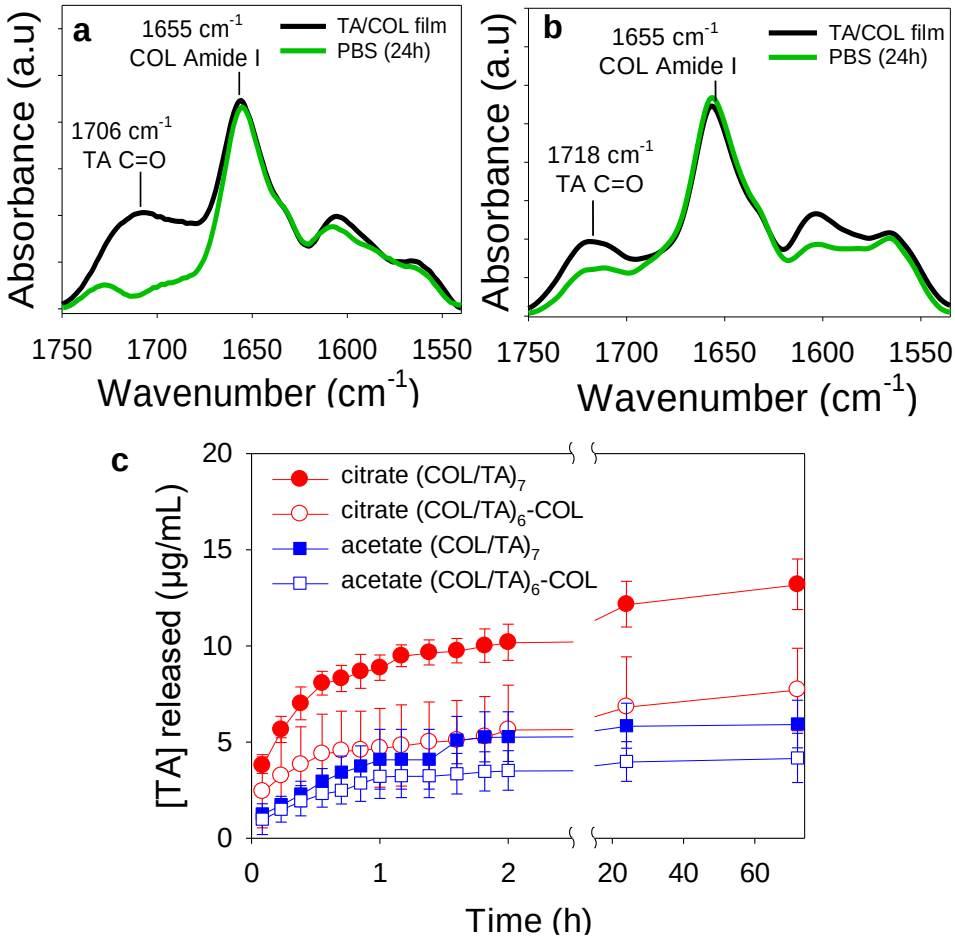


***Figure 3.13:*** *ATR-FTIR spectra of (COL/TA)6-COL films built at pH 4 in deuterated acetate* ***(a)*** *and citrate* ***(b)*** *buffers before and after the contact with deuterated PBS pH 7.4.* ***(c)*** *Cumulative release profile of TA, from TA/COL films in contact with PBS pH 7.4 at room temperature.*

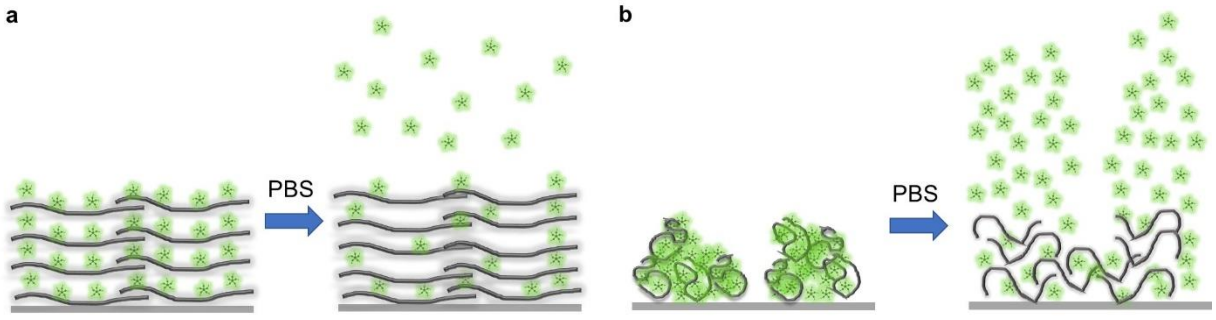


***Scheme 3.5:*** *Schematic representation of TA release obtained from TA/COL* ***(a)*** *acetate and* ***(b)*** *citrate films when put in contact with PBS. Citrate films release a higher amount of TA than acetate films because of supplementary TA molecules immobilized by electrostatic interactions thanks to citrate.*

To mimic biological conditions of bacteria and cell culture, the release kinetics of TA was also followed at 37 °C in HEPES and HEPES/NaCl buffers at pH 7.4, respectively **(Figure 3.14)**. Similar results were obtained with a higher release in the presence of 150 mM NaCl in the case of citrate films, which confirms the contribution of ionic interactions in these films.[46] No compensation of charges are necessary in the case of acetate films. But in the case of citrate films, citrate molecules, interacting through electrostatic interactions with COL, are also released and the charge compensation is obtained thanks to counterions present in the PBS or the culture medium.

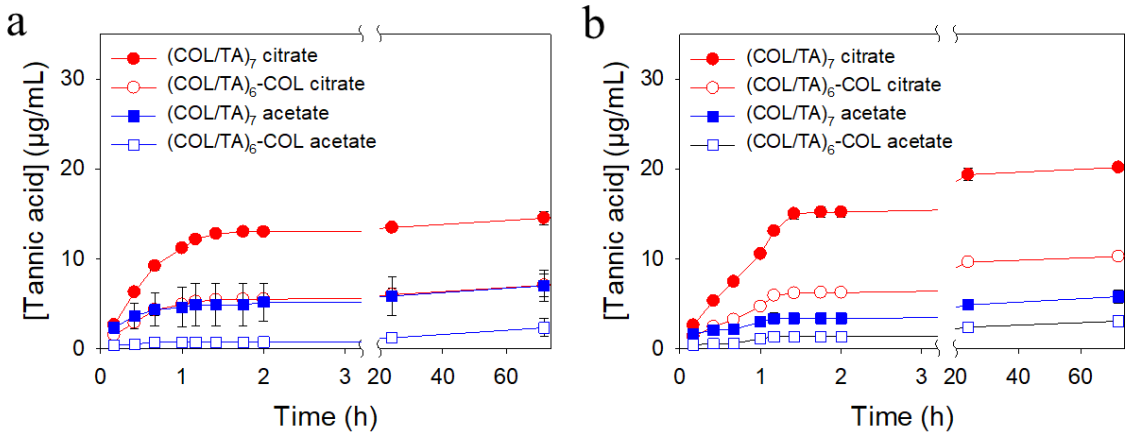


***Figure 3.14:*** *Cumulative release profile of TA from TA/COL films at 37°C in* ***(a)*** *10 mM HEPES buffer, mimicking the bacteria medium and* ***(b)*** *10 mM HEPES – 150 mM NaCl buffer both at pH 7.4, mimicking the cell culture medium.*

### 3.3.5 Antibacterial assays and human cell viability.

With TA being well-known to kill planktonic bacteria,[62] the antibacterial activity of TA/COL multilayer films was assessed against *Staphylococcus aureus* (*S. aureus*), a Gram-positive strain which is one of the most virulent bacteria leading to high rates of device-related systemic infections and mortality,[63] and *Escherichia coli* (*E. coli*), a Gram-negative strain mainly found on the surface of catheters.[64] The viability of bacteria was determined in MH broth after 24 and 48 h of contact with TA/COL acetate and citrate films. For this purpose, the supernatant was plated on agar Petri

dishes to enumerate the colony forming units (CFU) present in their planktonic state. A high antibacterial effect against *S. aureus* is observed for TA/COL citrate films and not for TA/COL acetate ones **(Figure 3.15)**.

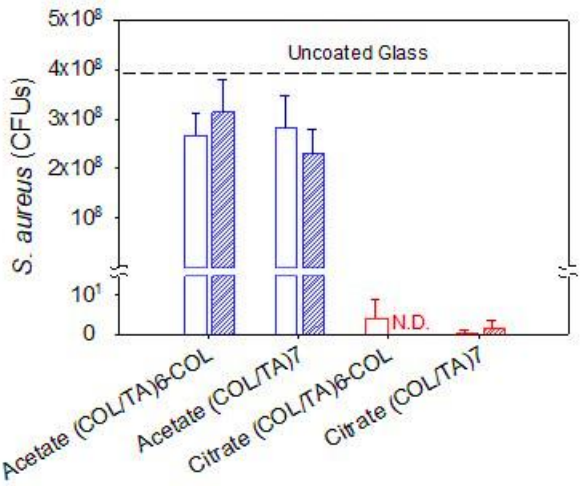


***Figure 3.15:*** *CFU of S. aureus from the supernatant of TA/COL films after 24 h and 48 h of contact. N.D. means not detected: no CFU were observed. The dashed line represents the CFU obtained from the bacterial supernatant in contact with an uncoated glass.*

In HEPES buffer at 37 °C medium mimicking MH broth, no significant difference in TA release was observed between $(COL/TA)_6$-COL citrate and $(COL/TA)_7$ acetate films with (6.0 ± 0.7) and (5.9 ± 2.2) µg/mL after 24 h, respectively **(Figure 3.14)**. However, a dramatic difference in bacterial viability after 24 h of contact is observed with only (4 ± 4) CFU counted on the citrate films against (2.8 ± 0.7) × $10^8$ CFU on the acetate ones. Thus, the antibacterial property of TA/COL citrate films is not linked to the total amount of TA released, which is by far lower than the minimal inhibitory concentration of TA against *S. aureus* (around 100 µg/mL).[28, 61]

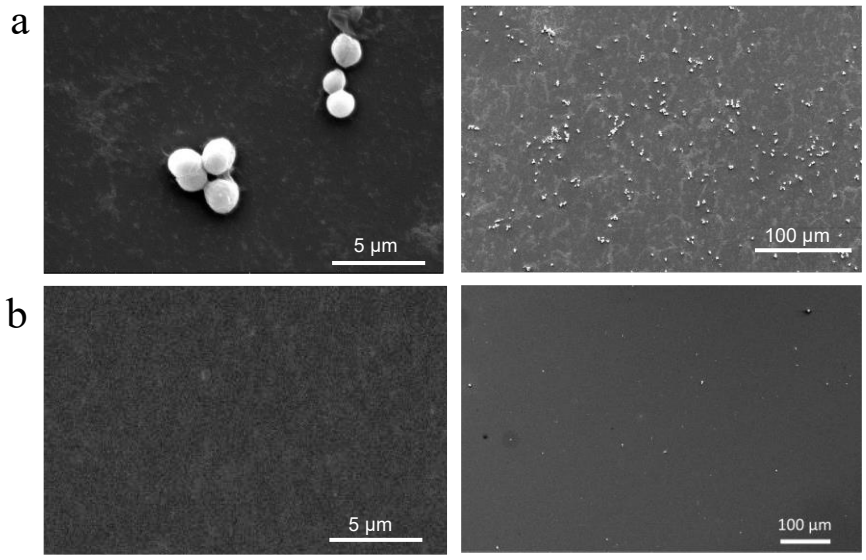


***Figure 3.16:*** *SEM images, at different magnifications, of (COL/TA)6-COL acetate* ***(a)*** *and citrate films* ***(b)*** *after 24 h contact with S. aureus. The samples were fixed using PFA followed by HMDS treatment.*

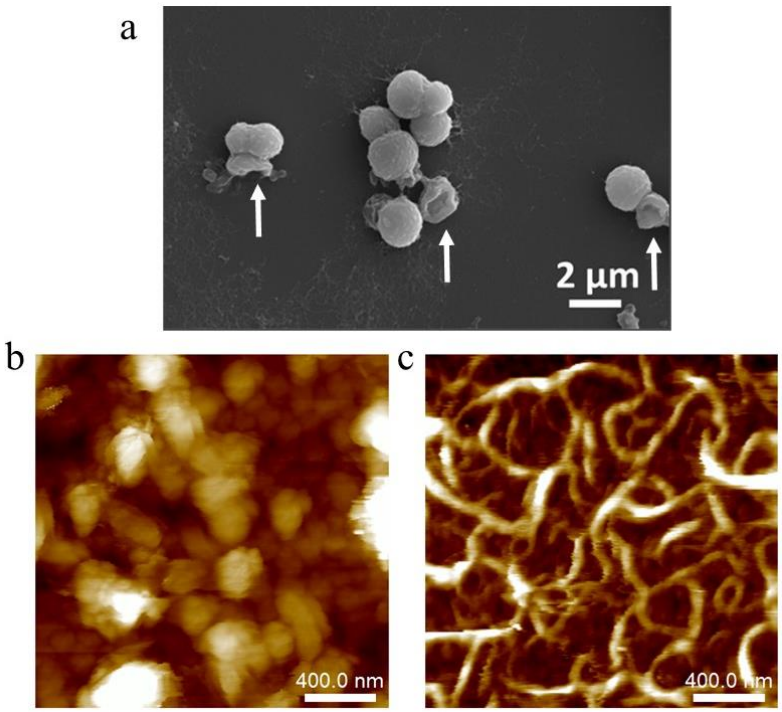


***Figure 3.17: (a)*** *SEM image, magnification 10 000×, of $(COL/TA)_6$-COL citrate film after 4 h contact with S. aureus. White arrows indicate disrupted bacteria cell. The sample were fixed using PFA followed by HMDS treatment. AFM images, obtained in Peak Force Tapping mode (ScanAsyst) and in the liquid state, of $(COL/TA)_6$-COL citrate film* ***(b)*** *before and* ***(c)*** *after 24 h contact with PBS at room temperature (z scale 50 nm). These images show the disappearance of TA granules revealing the fibrillary structure of TA/COL citrate films after TA release.*

TA/COL acetate films present several colonies after 24 h of contact. In contrast, no bacteria were observed on the surface of TA/COL citrate films after 24 h of contact **(Figure 3.16)**. After 4 h of contact with TA/COL citrate films, bacteria with cell membrane disruption are observed **(Figure 3.17a)**. TA molecules were reported to destroy the integrity of the *S. aureus* cell wall, by interacting with the peptidoglycans of the bacterial membrane.[28] The absence of bacteria after 24 h of contact is probably due to the severe damage of cell membrane leading to cell death and detachment from TA/COL films. It could also be explained by the protocol applied on the samples which includes a smooth PBS rinsing before fixation. However, some bacterial debris are visible at low-magnification image **(Figure 3.16)**. TA/COL citrate films exhibit a granular topography rich in TA in contrast to acetate ones. After 24 h of contact with PBS, this granular topography disappeared because of TA release, showing fibrillary structure of COL **(Figure 3.17b,c)**. The dissolution of TA/COL granular aggregates leads probably to a concentration of TA released near the surface of the films higher than the MIC **(Scheme 3.6)**. Incubated without agitation during the assay, bacteria were deposited on the surface of the films by sedimentation. A local release-killing effect is thus observed for TA/COL citrate films in contrast to acetate ones.

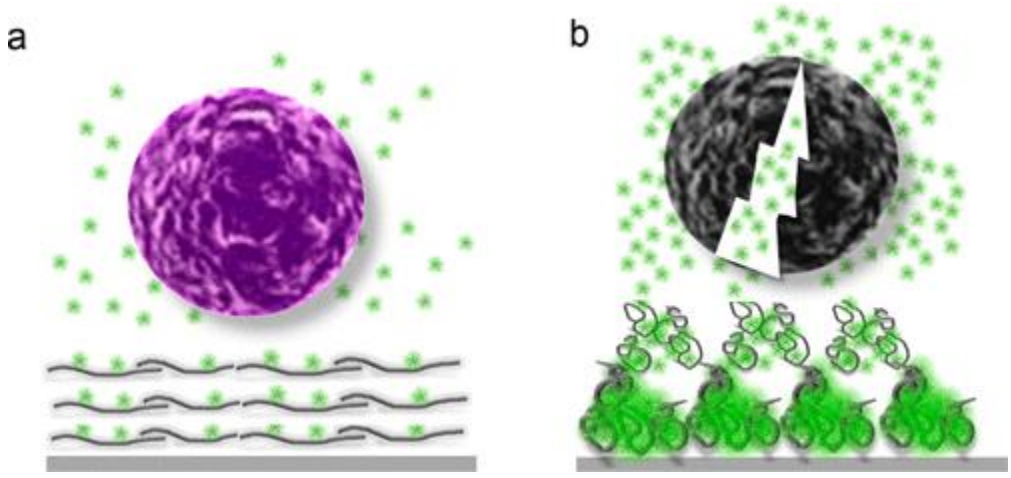


***Scheme 3.6:*** *Schematic representation of TA release from TA/COL films in contact S. aureus for acetate films* ***(a)*** *and citrate films* ***(b)****. A local release-killing effect toward bacteria is observed only for citrate films. Granular aggregates of TA/COL dissolution induce the local release of TA in a concentration above its MIC.*

Concerning *E. coli*, a decrease in the normalized growth of 45% was observed after 24 h of contact with $(COL/TA)_7$ citrate films **(Figure 3.18)**. It is known that the bactericidal activity of tannins is lower against Gram-negative bacteria than against Gram-positive bacteria. This is due to the presence of the lipopolysaccharide on the outer membrane of Gram-negative bacteria.[28]

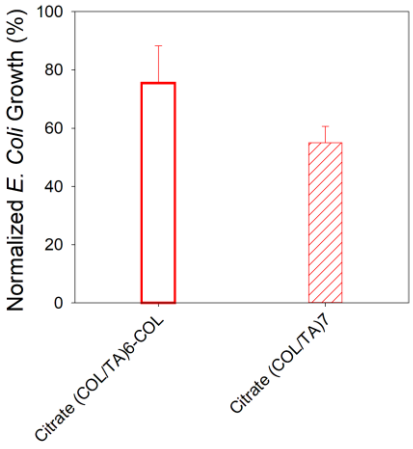


***Figure 3.18:*** *Normalized growth of E. coli incubated for 24 h in contact with TA/COL citrate films.*

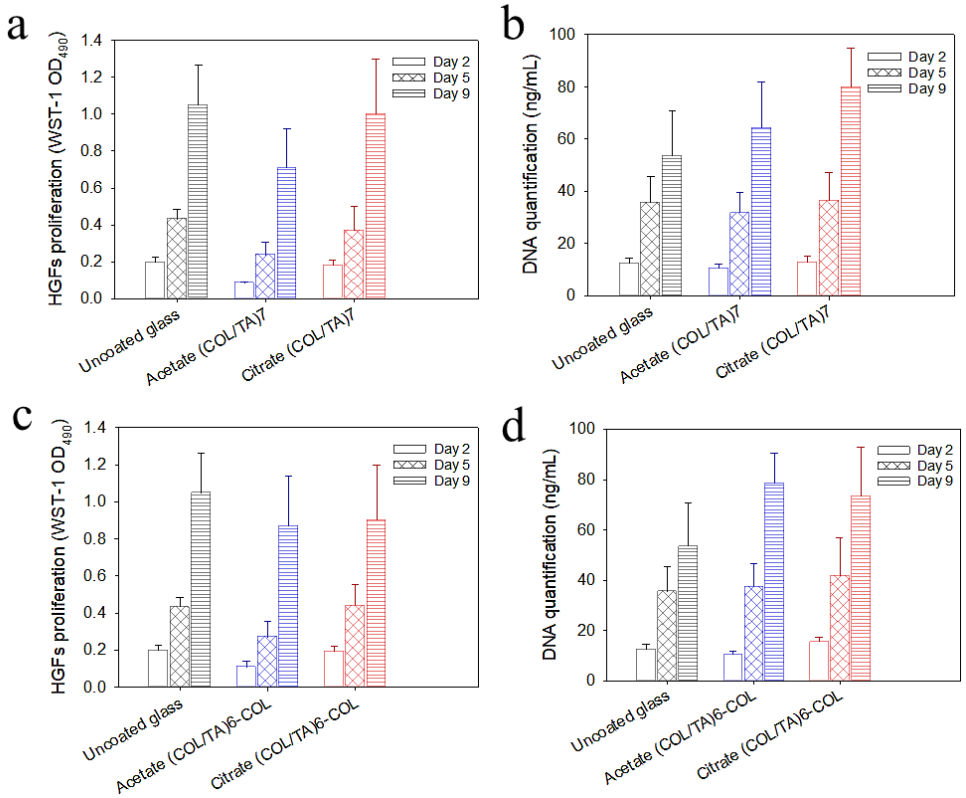


***Figure 3.19:*** *HGFs viability on TA/COL films ended by TA* ***(a, b)*** *and COL* ***(c, d)*** *in comparison to uncoated glass determined* ***(a, c)*** *by WST-1 assay and* ***(b, d)*** *by DNA quantification for films.*

Finally, it is important to ensure that the films are not cytotoxic toward mammalian cells. The behavior of human gingival fibroblasts (HGFs) cultivated on TA/COL acetate and citrate films were compared to an uncoated glass substrate. Proliferation assay and DNA quantification show no significant differences in HGFs proliferation for 9 days whatever the studied conditions, that is, TA or COL ended films **(Figure 3.19)**. Cell integrity of HGFs was evaluated by cytoskeleton labeling. After 15 days of culture, a confluent layer was obtained on all the tested TA/COL films **(Figure 3.20)**. A typical fibroblastic cell shape is observed with polymerized F-actin fibers lying parallel to each other. These results demonstrate the absence of TA/COL cytotoxic effect in both buffers.

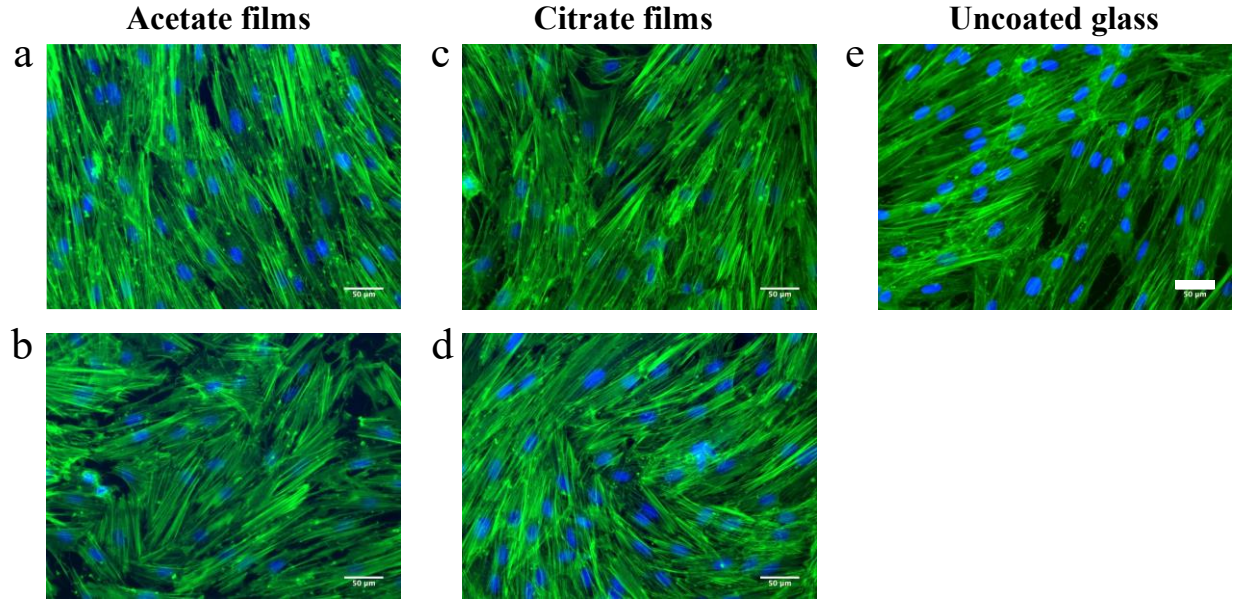


***Figure 3.20:*** *Fluorescent microscopy images of cytoskeleton labeling of HGFs seeded for 15 days on TA/COL films:* ***(a)*** *acetate (COL/TA)$_6$-COL,* ***(b)*** *acetate (COL/TA)$_7$,* ***(c)*** *citrate (COL/TA)$_6$-COL,* ***(d)*** *citrate (COL/TA)$_7$ and* ***(e)*** *uncoated glass. (Scale bars = 50 µm, green = F-actin and blue = nuclei).*

## 3.4 Conclusion

In this study, we reported buffer-dependent antibacterial property of TA/COL films. Because of the solubility issue of COL, acetate and citrate buffers at pH 4 were used to build the LbL films, affecting their physicochemical as well as the antibacterial properties. Specifically, complexation strengths between TA and COL are different in the presence of acetate or citrate affecting the LbL deposition. In comparison to acetate buffer, TA/COL binding is stronger in citrate buffer leading to a higher immobilization of TA and to the granular topography of TA/COL citrate films, providing higher specific surface. A local release-killing effect toward S. aureus was obtained for TA/COL citrate films thanks to their granular topography. The developed LbL films revealed no cytotoxic effect toward human gingival derived fibroblasts. This work constitutes an important step toward the use of polyphenols as antimicrobial agent when incorporated in LbL films.

## 3.5 Bibliography

1. Zhao, L.; Chu, P. K.; Zhang, Y.; Wu, Z., Antibacterial coatings on titanium implants. *Journal of Biomedical Materials Research Part B: Applied Biomaterials* **2009,** *91B* (1), 470-480.
2. Carmona-Ribeiro, A. M., Self-Assembled Antimicrobial Nanomaterials. *International Journal of Environmental Research and Public Health* **2018,** *15* (7), 1408.
3. Wang, M. Q.; Tang, T. T., Surface treatment strategies to combat implant-related infection from the beginning. *Journal of orthopaedic translation* **2019,** *17*, 42-54.
4. Decher, G., Fuzzy Nanoassemblies: Toward Layered Polymeric Multicomposites. *Science* **1997,** *277* (5330), 1232-1237.
5. Bertrand, P.; Jonas, A.; Laschewsky, A.; Legras, R., Ultrathin polymer coatings by complexation of polyelectrolytes at interfaces : suitable materials, structure and properties. *Macromolecules Rapid Communication* **2000,** *21*, 319-348.
6. Kharlampieva, E.; Kozlovskaya, V.; Sukhishvili, S. A., Layer-by-Layer Hydrogen-Bonded Polymer Films: From Fundamentals to Applications. *Advanced Materials* **2009,** *21* (30), 3053-3065.
7. Kharlampieva, E.; Sukhishvili, S. A., Hydrogen-bonded layer-by-layer polymer films. *Journal of Macromolecular Science, Part C* **2006,** *46* (4), 377-395.
8. Séon, L.; Lavalle, P.; Schaaf, P.; Boulmedais, F., Polyelectrolyte Multilayers: A Versatile Tool for Preparing Antimicrobial Coatings. *Langmuir* **2015,** *31* (47), 12856-12872.
9. Pahal, S.; Gakhar, R.; Raichur, A. M.; Varma, M. M., Polyelectrolyte multilayers for bio-applications: recent advancements. *IET Nanobiotechnology* **2017,** *11* (8), 903-908.
10. Schmolke, H.; Demming, S.; Edlich, A.; Magdanz, V.; Buttgenbach, S.; Franco-Lara, E.; Krull, R.; Klages, C. P., Polyelectrolyte multilayer surface functionalization of poly(dimethylsiloxane) (PDMS) for reduction of yeast cell adhesion in microfluidic devices. *Biomicrofluidics* **2010,** *4* (4), 12.
11. Lichter, J. A.; Thompson, M. T.; Delgadillo, M.; Nishikawa, T.; Rubner, M. F.; Van Vliet, K. J., Substrata mechanical stiffness can regulate adhesion of viable bacteria. *Biomacromolecules* **2008,** *9* (6), 1571-1578.
12. Saha, N.; Monge, C.; Dulong, V.; Picart, C.; Glinel, K., Influence of Polyelectrolyte Film Stiffness on Bacterial Growth. *Biomacromolecules* **2013,** *14* (2), 520-528.
13. Fu, J.; Ji, J.; Yuan, W.; Shen, J., Construction of anti-adhesive and antibacterial multilayer films via layer-by-layer assembly of heparin and chitosan. *Biomaterials* **2005,** *26* (33), 6684-6692.
14. Richert, L.; Lavalle, P.; Payan, E.; Shu, X. Z.; Prestwich, G. D.; Stoltz, J. F.; Schaaf, P.; Voegel, J. C.; Picart, C., Layer by layer buildup of polysaccharide films: Physical chemistry and cellular adhesion aspects. *Langmuir* **2004,** *20* (2), 448-458.
15. Bratskaya, S.; Marinin, D.; Simon, F.; Synytska, A.; Zschoche, S.; Busscher, H. J.; Jager, D.; van der Mei, H. C., Adhesion and viability of two enterococcal strains on covalently grafted chitosan and chitosan/kappa-carrageenan multilayers. *Biomacromolecules* **2007,** *8* (9), 2960-2968.
16. Lichter, J. A.; Rubner, M. F., Polyelectrolyte Multilayers with Intrinsic Antimicrobial Functionality: The Importance of Mobile Polycations. *Langmuir* **2009,** *25* (13), 7686-7694.
17. Mutschler, A.; Tallet, L.; Rabineau, M.; Dollinger, C.; Metz-Boutigue, M.-H.; Schneider, F.; Senger, B.; Vrana, N. E.; Schaaf, P.; Lavalle, P., Unexpected Bactericidal Activity of Poly(arginine)/Hyaluronan Nanolayered Coatings. *Chemistry of Materials* **2016,** *28* (23), 8700-8709.

18. Alkekhia, D.; Shukla, A., Influence of poly-l-lysine molecular weight on antibacterial efficacy in polymer multilayer films. *Journal of Biomedical Materials Research Part A* **2019,** *107* (6), 1324-1339.
19. Cui, D.; Szarpak, A.; Pignot-Paintrand, I.; Varrot, A.; Boudou, T.; Detrembleur, C.; Jerome, C.; Picart, C.; Auzely-Velty, R., Contact-Killing Polyelectrolyte Microcapsules Based on Chitosan Derivatives. *Advanced Functional Materials* **2010,** *20* (19), 3303-3312.
20. Yang, W. J.; Pranantyo, D.; Neoh, K. G.; Kang, E. T.; Teo, S. L. M.; Rittschof, D., Layer-by-Layer Click Deposition of Functional Polymer Coatings for Combating Marine Biofouling. *Biomacromolecules* **2012,** *13* (9), 2769-2780.
21. Mutschler, A.; Betscha, C.; Ball, V.; Senger, B.; Vrana, N. E.; Boulmedais, F.; Schroder, A.; Schaaf, P.; Lavalle, P., Nature of the Polyanion Governs the Antimicrobial Properties of Poly(arginine)/Polyanion Multilayer Films. *Chem Mater.* **2017,** *29* (7), 3195-3201.
22. Malcher, M.; Volodkin, D.; Heurtault, B.; Andre, P.; Schaaf, P.; Möhwald, H.; Voegel, J.-C.; Sokolowski, A.; Ball, V.; Boulmedais, F.; Frisch, B., Embedded silver ions-containing liposomes in polyelectrolyte multilayers: Cargos films for antibacterial agents. *Langmuir* **2008,** *24* (18), 10209-10215.
23. Shi, Z.; Neoh, K. G.; Zhong, S. P.; Yung, L. Y. L.; Kang, E. T.; Wang, W., In vitro antibacterial and cytotoxicity assay of multilayered polyelectrolyte-functionalized stainless steel. *Journal of Biomedical Materials Research Part A* **2006,** *76A* (4), 826-834.
24. Moskowitz, J. S.; Blaisse, M. R.; Samuel, R. E.; Hsu, H. P.; Harris, M. B.; Martin, S. D.; Lee, J. C.; Spector, M.; Hammond, P. T., The effectiveness of the controlled release of gentamicin from polyelectrolyte multilayers in the treatment of Staphylococcus aureus infection in a rabbit bone model. *Biomaterials* **2010,** *31* (23), 6019-6030.
25. Shukla, A.; Avadhany, S. N.; Fang, J. C.; Hammond, P. T., Tunable Vancomycin Releasing Surfaces for Biomedical Applications. *Small* **2010,** *6* (21), 2392-2404.
26. Pavlukhina, S.; Lu, Y. M.; Patimetha, A.; Libera, M.; Sukhishvili, S., Polymer Multilayers with pH-Triggered Release of Antibacterial Agents. *Biomacromolecules* **2010,** *11* (12), 3448-3456.
27. Cado, G.; Aslam, R.; Séon, L.; Garnier, T.; Fabre, R.; Parat, A.; Chassepot, A.; Voegel, J.-C.; Senger, B.; Schneider, F.; Frère, Y.; Jierry, L.; Schaaf, P.; Kerdjoudj, H.; Metz-Boutigue, M.-H.; Boulmedais, F., Self-defensive biomaterial coating against bacteria and yeasts: polysaccharide multilayer film with embedded antimicrobial peptide. *Advanced Functional Materials* **2013,** *23* (38), 4801–4809.
28. Dong, G.; Liu, H.; Yu, X.; Zhang, X.; Lu, H.; Zhou, T.; Cao, J., Antimicrobial and anti-biofilm activity of tannic acid against Staphylococcus aureus. *Natural product research* **2018,** *32* (18), 2225-2228.
29. Ren, P.-F.; Yang, H.-C.; Liang, H.-Q.; Xu, X.-L.; Wan, L.-S.; Xu, Z.-K., Highly Stable, Protein-Resistant Surfaces via the Layer-by-Layer Assembly of Poly(sulfobetaine methacrylate) and Tannic Acid. *Langmuir* **2015,** *31* (21), 5851-5858.
30. Qi, X.; Zhang, D.; Ma, Z.; Cao, W.; Hou, Y.; Zhu, J.; Gan, Y.; Yang, M., An Epidermis-like Hierarchical Smart Coating with a Hardness of Tooth Enamel. *ACS Nano* **2018,** *12* (2), 1062-1073.
31. Shukla, A.; Fang, J. C.; Puranam, S.; Jensen, F. R.; Hammond, P. T., Hemostatic Multilayer Coatings. *Advanced Materials* **2012,** *24* (4), 492-496.
32. Park, J. H.; Choi, S.; Moon, H. C.; Seo, H.; Kim, J. Y.; Hong, S. P.; Lee, B. S.; Kang, E.; Lee, J.; Ryu, D. H.; Choi, I. S., Antimicrobial spray nanocoating of supramolecular Fe(III)-tannic

acid metal-organic coordination complex: applications to shoe insoles and fruits. *Scientific Reports* **2017,** *7*.
33. Zhuk, I.; Jariwala, F.; Attygalle, A. B.; Wu, Y.; Libera, M. R.; Sukhishvili, S. A., Self-Defensive Layer-by-Layer Films with Bacteria-Triggered Antibiotic Release. *ACS Nano* **2014,** *8* (8), 7733-7745.
34. Xu, G.; Pranantyo, D.; Zhang, B.; Xu, L.; Neoh, K.-G.; Kang, E.-T., Tannic acid anchored layer-by-layer covalent deposition of parasin I peptide for antifouling and antimicrobial coatings. *RSC Advances* **2016,** *6* (18), 14809-14818.
35. Kumorek, M.; Minisy, I. M.; Krunclová, T.; Voršiláková, M.; Venclíková, K.; Mázl Chánová, E.; Janoušková, O.; Kubies, D., pH-responsive and antibacterial properties of self-assembled multilayer films based on chitosan and tannic acid. *Materials Science and Engineering: C* **2020,** *109*, 110493.
36. Grant, G. G. S.; Koktysh, D. S.; Yun, B.; Matts, R. L.; Kotov, N. A., Layer-By-Layer Assembly of Collagen Thin Films: Controlled Thickness and Biocompatibility. *Biomedical Microdevices* **2001,** *3* (4), 301-306.
37. Chaubaroux, C.; Vrana, E.; Debry, C.; Schaaf, P.; Senger, B.; Voegel, J. C.; Haikel, Y.; Ringwald, C.; Hemmerle, J.; Lavalle, P.; Boulmedais, F., Collagen-based fibrillar multilayer films cross-linked by a natural agent. *Biomacromolecules* **2012,** *13* (7), 2128-35.
38. Chen, J. L.; Li, Q. L.; Chen, J. Y.; Chen, C.; Huang, N., Improving blood-compatibility of titanium by coating collagen–heparin multilayers. *Applied Surface Science* **2009,** *255* (15), 6894-6900.
39. Gong, Y.; Zhu, Y.; Liu, Y.; Ma, Z.; Gao, C.; Shen, J., Layer-by-layer assembly of chondroitin sulfate and collagen on aminolyzed poly(l-lactic acid) porous scaffolds to enhance their chondrogenesis. *Acta Biomaterialia* **2007,** *3* (5), 677-685.
40. Johansson, J. Å.; Halthur, T.; Herranen, M.; Söderberg, L.; Elofsson, U.; Hilborn, J., Build-up of Collagen and Hyaluronic Acid Polyelectrolyte Multilayers. *Biomacromolecules* **2005,** *6* (3), 1353-1359.
41. Voinova, M. V.; Rodahl, M.; Jonson, M.; Kasemo, B., Viscoelastic acoustic response of layered polymer films at fluid-solid interfaces: Continuum mechanics approach. *Physica Scripta* **1999,** *59* (5), 391-396.
42. Scofield, J. H., Hartree-Slater Subshell Photoionization Cross-Sections at 1254 and 1487ev. *Journal of Electron Spectroscopy and Related Phenomena* **1976,** *8* (2), 129-137.
43. Hook, F.; Rodahl, M.; Kasemo, B.; Brzezinski, P., Structural changes in hemoglobin during adsorption to solid surfaces: effects of pH, ionic strength, and ligand binding. *Proceedings of the National Academy of Sciences of the United States of America* **1998,** *95* (21), 12271-6.
44. Belegrinou, S.; Mannelli, I.; Lisboa, P.; Bretagnol, F.; Valsesia, A.; Ceccone, G.; Colpo, P.; Rauscher, H.; Rossi, F., pH-dependent immobilization of proteins on surfaces functionalized by plasma-enhanced chemical vapor deposition of poly(acrylic acid)- and poly(ethylene oxide)-like films. *Langmuir* **2008,** *24* (14), 7251-61.
45. Velmurugan, P.; Singam, E. R.; Jonnalagadda, R. R.; Subramanian, V., Investigation on interaction of tannic acid with type I collagen and its effect on thermal, enzymatic, and conformational stability for tissue engineering applications. *Biopolymers* **2014,** *101* (5), 471-83.
46. Han, Y.; Lin, Z.; Zhou, J.; Yun, G.; Guo, R.; Richardson, J. J.; Caruso, F., Polyphenol-Mediated Assembly of Proteins for Engineering Functional Materials. *Angewandte Chemie International Edition* **2020**, DOI: 10.1002/anie.202002089.

47. Heijmen, F. H.; du Pont, J. S.; Middelkoop, E.; Kreis, R. W.; Hoekstra, M. J., Cross-linking of dermal sheep collagen with tannic acid. *Biomaterials* **1997,** *18* (10), 749-754.
48. Frazier, R. A.; Papadopoulou, A.; Mueller-Harvey, I.; Kissoon, D.; Green, R. J., Probing Protein−Tannin Interactions by Isothermal Titration Microcalorimetry. *Journal of Agricultural and Food Chemistry* **2003,** *51* (18), 5189-5195.
49. Ranoszek-Soliwoda, K.; Tomaszewska, E.; Socha, E.; Krzyczmonik, P.; Ignaczak, A.; Orlowski, P.; Krzyzowska, M.; Celichowski, G.; Grobelny, J., The role of tannic acid and sodium citrate in the synthesis of silver nanoparticles. *Journal of Nanoparticle Research* **2017,** *19* (8), 273.
50. Shao, C.; Zhao, R.; Jiang, S.; Yao, S.; Wu, Z.; Jin, B.; Yang, Y.; Pan, H.; Tang, R., Citrate Improves Collagen Mineralization via Interface Wetting: A Physicochemical Understanding of Biomineralization Control. *Advanced Materials* **2018,** *30* (8), 1704876.
51. Delgado-Lopez, J. M.; Bertolotti, F.; Lyngso, J.; Pedersen, J. S.; Cervellino, A.; Masciocchi, N.; Guagliardi, A., The synergic role of collagen and citrate in stabilizing amorphous calcium phosphate precursors with platy morphology. *Acta Biomaterialia* **2017,** *49*, 555-562.
52. Jobstl, E.; O'Connell, J.; Fairclough, J. P. A.; Williamson, M. P., Molecular model for astringency produced by polyphenol/protein interactions. *Biomacromolecules* **2004,** *5* (3), 942-949.
53. Tiffany, M. L.; Krimm, S., Circular dichroism of the ‘‘random’’ polypeptide chain. *Biopolymers* **1969,** *8*, 347–359.
54. Belbachir, K.; Noreen, R.; Gouspillou, G.; Petibois, C., Collagen types analysis and differentiation by FTIR spectroscopy. *Analytical and Bioanalytical Chemistry* **2009,** *395*, 829-837.
55. Pantoja-Castroa, M. A.; González-Rodríguez, H., Study by infrared spectroscopy and thermogravimetric analysis of tannins and tannic acid. *Revista Latinoamericana de Química* **2011,** *39*, 107-112.
56. Jastrzebska, M.; Zalewska-Rejdak, J.; Wrzalik, R.; Kocot, A.; Mroz, I.; Barwinski, B.; Turek, A.; Cwalina, B., Tannic acid-stabilized pericardium tissue: IR spectroscopy, atomic force microscopy, and dielectric spectroscopy investigations. *Journal of Biomedical Materials Research Part A* **2006,** *78A* (1), 148-156.
57. Chaubaroux, C.; Perrin-Schmitt, F.; Senger, B.; Vidal, L.; Voegel, J. C.; Schaaf, P.; Haikel, Y.; Boulmedais, F.; Lavalle, P.; Hemmerle, J., Cell Alignment Driven by Mechanically Induced Collagen Fiber Alignment in Collagen/Alginate Coatings. *Tissue Engineering, Part C: Methods* **2015,** *21* (9), 881-8.
58. Ao, H.; Zong, J.; Nie, Y.; Wan, Y.; Zheng, X., An in vivo study on the effect of coating stability on osteointegration performance of collagen/hyaluronic acid multilayer modified titanium implants. *Bioactive Materials* **2018,** *3* (1), 97-101.
59. Ao, H.; Xie, Y.; Tan, H.; Yang, S.; Li, K.; Wu, X.; Zheng, X.; Tang, T., Fabrication and in vitro evaluation of stable collagen/hyaluronic acid biomimetic multilayer on titanium coatings. *Journal of The Royal Society Interface* **2013,** *10* (84).
60. Erel-Unal, I.; Sukhishvili, S. A., Hydrogen-Bonded Multilayers of a Neutral Polymer and a Polyphenol. *Macromolecules* **2008,** *41*, 3962-3970.
61. Reitzer, F.; Berber, E.; Halgand, J.; Ball, V.; Meyer, F., Use of Gelatin as Tannic Acid Carrier for Its Sustained Local Delivery. *Pharm. Front.* **2020,** (2), e200002.
62. Payne, D. E.; Martin, N. R.; Parzych, K. R.; Rickard, A. H.; Underwood, A.; Boles, B. R., Tannic acid inhibits Staphylococcus aureus surface colonization in an IsaA-dependent manner. *Infection and immunity* **2013,** *81* (2), 496-504.

63. Katneni, R.; Hedayati, S. S., Central venous catheter-related bacteremia in chronic hemodialysis patients: epidemiology and evidence-based management. *Nature Clinical Practice Nephrology* **2007,** *3* (5), 256-266.
64. Jacobsen, S. M.; Stickler, D. J.; Mobley, H. L. T.; Shirtliff, M. E., Complicated catheter-associated urinary tract infections due to Escherichia coli and Proteus mirabilis. *Clin Microbiol Rev* **2008,** *21* (1), 26-59.

# Chapter 4 : Oriented Collagen Nanocoatings

## Aligned Tannic acid/Collagen Nanofilms for Tissue Engineering Applications

## Table of Contents

After exploiting the interactions between collagen (COL) and tannic acid (TA) in the presence of different buffers in the previous chapter, we developed and optimized the buildup of oriented TA/COL LbL films using the brushing method. The oriented TA/COL film surface-cell interactions are explored towards murine fibroblasts and human myoblasts. Particularly, the orientation of cells and their differentiation on oriented COL surfaces is our main interest here. The physicochemical and biological results are compared with conventional dip-assisted LbL films.

## 4.1 Introduction

Musculoskeletal tissues are one of the most important components of human body which represent around 40% of adult body mass. Containing thousands of muscle fibers bundled together into aligned parallel organization, their pivotal role is to perform routine voluntary locomotion by creating forces which are then transmitted by tendon, another tissue joining skeletal muscle with bone towards skeleton.[1] Upon minor injuries, muscle tissues possess inherent ability to regenerate via activation of satellite cells which can differentiate into myoblasts. Myoblasts further differentiate into muscle fibers to join the muscle tissue.[2-3] However, the inherent regeneration is limited to mild injuries and ceases to occur in case of severe trauma or large muscle loss, due to formation of scar tissue.[4] Musculoskeletal trauma and disorders are the most common and significant causes of disability worldwide, rendering poorer work/social life quality. Loss of normal muscle activity is unavoidable due to muscle injuries, commonly caused by contusions during sports, accidental trauma, or age related wear *etc*.[5] According to World Health Organization, approximately 1.71 billion people suffer from the musculoskeletal conditions causing huge direct (healthcare) or indirect (inability to work) costs.[6] Hence, there is a need to develop solutions for muscle tissue regeneration.

Since the development of first collagen-coated substrate to culture avian myotubes,[7] extensive research has been carried out to develop skeletal muscle tissue engineering approaches. A lot of attention has been centered to develop biomaterial scaffolds mimicking the extracellular matrix (ECM) structure, composition, mechanical properties *etc.*[8] Muscle development involves differentiation of myoblasts into myotubes with parallel and straight orientation, to ultimately form aligned myofibers to compensate the muscle loss.[9] Therefore, the ideal engineered scaffold must provide a close ECM microenvironment for cell-biomaterial interactions to regenerate hierarchically organized tissues.[10] Ignoring ECM-biomaterial interface can lead to failure of implanted medical device. Superseding the bulk properties, interface plays a crucial role in cell-biomaterial interactions. To that aim, the interface can be designed to mimic native ECM by playing with biochemical and structural cues.[11]

Biochemical cues involve the presence of various bioactive molecules like growth factors, which can trigger, support or even accelerate the regeneration process.[1] Over the past two decades, polyphenols have gained increasing interest to develop multifunctional materials with enhanced biological activity, thanks to their ability to interact with bioactive compounds and macromolecules. Polyphenols are essential nutrients for muscle health due to their antioxidant and anti-inflammatory properties. The oral supplementation of proanthocyanidolic oligomer was reported to accelerate *in-vivo* the muscle regeneration of rats by reducing neutrophil infiltration by 10-fold, helping satellite cells migration in the injury site.[12] The antioxidant potential of green tea extracts, rich in polyphenols, may be beneficial in treating dystrophic muscle, because oxidative stress is believed to contribute substantially to muscle pathology.[13] *In vivo*, green tea extracts consumption allowed increasing normal muscle fiber area of mdx mice, Duchenne muscular dystrophy mouse model, by decreasing serum creatine kinase, responsible for muscle damage.[14] It

was shown *in vitro* that polyphenol rich plum extract treatment enhances the size of C2C12 mouse myoblasts and accelerated their differentiation.[15] Moreover, polyphenols such as resveratrol, quercetin, epigallocatechin gallate, and epicatechin were proved to be antiaging agents for C2C12 mouse myoblasts with significant upregulation of mitochondrial enzymes.[16] More recently, tannic acid (TA) and its complexes with proteins (collagen, elastin) and peptides (substance P) were reported to be internalized by myoblasts for targeted drug administration.[17]

The other aspect of interface design involves the development of micro-nano topographical surface features. Indeed, cells are reported to sense and respond to surface topography.[18-19] Biomaterial nanostructures, nanofibers, or nanoparticles, are gaining a huge attention. Among various nanostructured materials,[20] fibrillar proteins such as fibronectin and collagen are famous to create native ECM cues. Collagens, most abundantly available structural proteins, are integral component of ECM. Among 26 other types, collagen type I (COL) is most commonly found in connective and muscle tissues. It is widely used in muscle tissue engineering since muscle fibers are protected by COL based sheets or coatings. Henceforth, the use of COL based constructs are often used to mimic natural ECM niche.[1]

In the context of regenerative medicine, primary goal of a biomaterial is to facilitate healing or to supplement or replace failing tissues and organs. However, optimal function of many tissues substitutes requires anisotropic architecture. For example, in tendons, ligaments, bones, muscles, and conjunctive tissue, an appropriate organization of collagen fibers is essential to maintain the mechanical integrity and normal function of the tissue.[21] Since the early use of COL to functionalize biomaterial surfaces,[7, 22-23] to guide fibroblasts[24] and differentiate myoblasts[25], various approaches involved the deposition of aligned COL molecules with nanometric control.[26] For instance, alignment of COL fibers was achieved via lithography,[27] microgroove substrates,[28]

microfluidic,[29] electrospinning,[30] magnetic field,[31-32] flow,[33] stretching,[34] and by rubbing.[35-36] However, these techniques possess certain limitations such as requirement for specialized instrumentations, mechanical assemblies, and strong electric or magnetic fields.

Herein, we report a simple brushing method to develop oriented TA/COL multilayer films with nanometric control. This method appears as the simplest way to prepare aligned COL-based surfaces without the use of electric or magnetic field that could damage the COL structure[30, 32] and surpasses the need of sophisticated surface nano structuring method[37] or microfluidics[29]. After confirmation of COL orientation and characterization of TA release, TA/COL films were analyzed towards murine fibroblasts and human myoblasts. The cell-surface interactions were characterized in terms of cell orientation, proliferation, migration, and differentiation

## 4.2 Experimental section

### 4.2.1 Polyelectrolyte solutions

All solutions were prepared freshly prior to use except COL. Deionized water (Milli-Q, 18.2 MΩ·cm at 25 °C) supplied by Advantage A10 (MERCK) was used in the entire study. The pH values were adjusted by using 0.1 M HCl or 0.1 M NaOH solution prepared in deionized water. Prior to thin film buildup, all the solutions were filtered using a 0.20 µm filter (Sarstedt, no. 831826001) to remove any impurity or undissolved substances. The citrate buffer used in this study was prepared at pH 4 by mixing 41 mL of 0.1 M sodium citrate tribasic dihydrate solution and 59 mL of 0.1M citric acid monohydrate solution. PEI solution was prepared at 0.1 mg/mL in 0.15 M sodium chloride (NaCl) aqueous solution (no pH adjustment). TA solution was prepared at 0.5 mg/mL in citrate buffer at pH 4 and kept in dark to avoid its photooxidation. COL solution was prepared at 1 mg/mL in citrate buffer at pH 4 by overnight agitation using a magnetic stirrer at 4 °C. Silicon wafers or microscopic glass slides were cut using a sharp diamond pen to obtain 1

× 6 cm² rectangular substrates. Silicon wafers were cleaned with ethanol/water (50% v/v) solution for 15 min prior to their use. Glass substrates were cleaned by immersing in the solutions of 10 mM SDS and 0.1 M HCl at 70°C for 10 min each, followed by extensive rinsing with deionized water. Prior to the film buildup, the substrates were plasma etched for 2.5 min with air using Harrick PDC-002-HP at high RF level to remove particles and to render the surface negatively charged and hydrophilic.

### 4.2.2 LbL Deposition by dipping and brushing techniques

PEI, a branched polycation, was used as precursor layer on each substrate before LbL buildup. Immediately after plasma cleaning, the substrate was dipped in PEI solution for 10 s, rinsed twice with ultrapure water for 5 s and dried with filtered compressed air. The substrate is then a positively charged surface ensuring a good anchoring of the films. Oriented TA/COL based films were obtained by the brushing method. The PEI-functionalized substrate was clipped with a support in a horizontal direction facing upwards to brush the solutions always in the same direction in the area highlighted in blue **(Figure 4.1a-b).** The used brush (Søstrene Grenes, Aarhus, Denmark) is a nylon paintbrush with dense bristles **(Figure 4.1c)**.

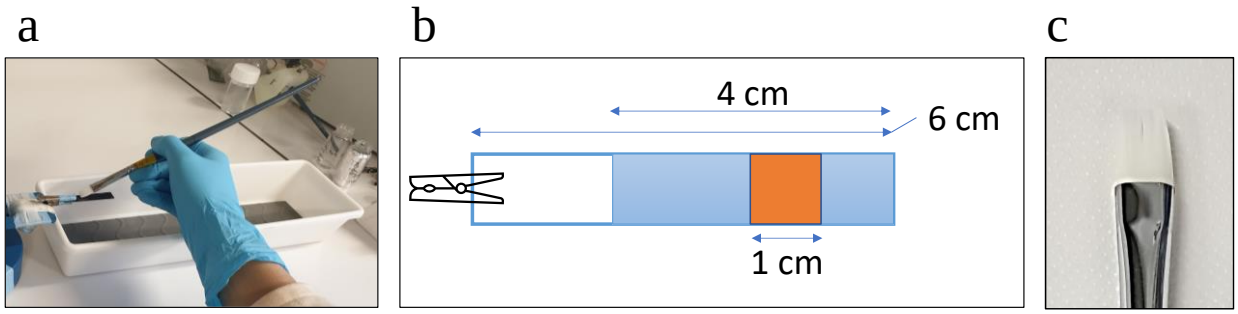


***Figure 4.1:*** ***(a)*** *Layer-by-layer buildup using manual brushing technique.* ***(b)*** *Schematic representation of the area (blue + orange) selected on glass slides to deposit multilayer films using bushing LbL method.* ***(c)*** *Locally available nylon paint brush with dense bristles used for multilayer buildup.*

TA and COL solutions were brushed manually on the substrate and left to dry for 10 s, followed by two rinsing steps with ultrapure water in a vertical direction using a disposable pipette and dried

with filtered compressed air (**Figure 4.2**). With *n* the number of bilayer deposition, the following brushed PEI-$(TA/COL)_n$ films were studied and named oriented TA/COL film with $n = 8$.

Non-oriented TA/COL films were obtained by the dipping method. The PEI-functionalized substrate was immersed in TA solution for 10 s, followed by two rinsing steps by dipping in ultrapure water for 5 s and dried by filtered compressed air. The same process was followed to deposit COL adlayer, to obtain one bilayer. The process was repeated *n* times to obtain PEI-$(TA/COL)_n$ named non-oriented TA/COL film with $n = 8$. Once the desired film architecture is achieved, the homogeneous part, highlighted in orange color, of the sample is selected and cut to obtain 1×1 $cm^2$ area samples as shown in **Figure 4.1b** to characterize the film properties.

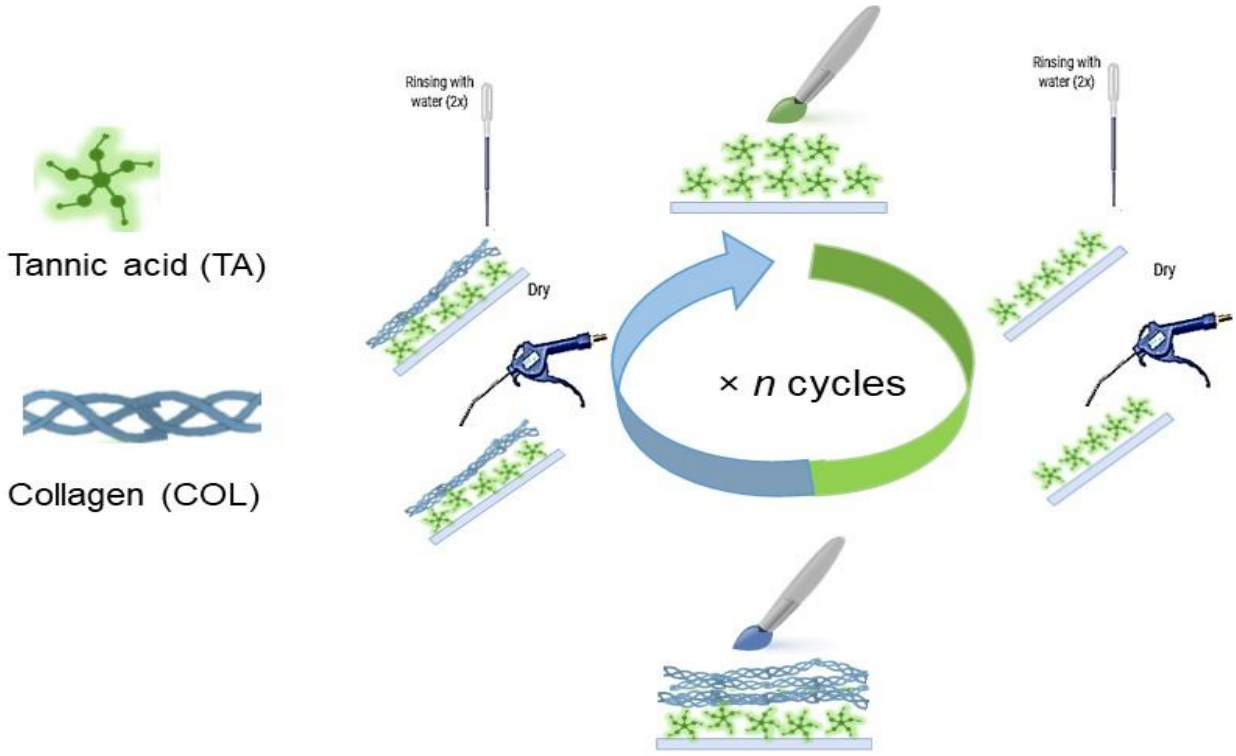


***Figure 4.2:*** *A schematic representation of oriented TA/COL films buildup by the brushing method. After deposition of TA or COL by the nylon painting brush and rest of 10 s, the substrate is rinsed with ultrapure water using a disposable pipette and dried by compressed air.*

### 4.2.3 Ellipsometry

The film thickness was measured, after rinsing with water and drying by compressed air, using an Ellipsometer (SD2300, PLASMOS) with an incident laser beam (632.8nm) and a constant angle of 45°. Refractive index was assumed to be constant and n = 1.465 for all the measurements. The dry thickness values reported here are the average values with standard deviation of three individual LbL buildup experiments. Ten measurements were performed at random areas on each one of the multilayer sample surfaces. The routine ellipsometry measurements might show insignificant differences in absolute dry thickness and a more advanced ellipsometry equipment would be required for accurate measurements. However, the thickness readings are satisfactorily accurate to compare the buildup of different LbL films reported here.

### 4.2.4 Atomic Force Microscopy (AFM) and analysis of COL orientation

AFM Multimode Nanoscope IV from Bruker was used to image both oriented and non-oriented COL/TA films, in dry state using nitride coated silicon tips on a nitride cantilever (Model ScanAsyst-Air, with force constant $k$ = 0.4 N/m and frequency $f_n$ =70 kHz) and Peak Force Tapping (ScanAsyst) mode. The images were obtained at a scan rate of 1 Hz with a resolution of 512 × 512 pixels. The data analysis was performed using NanoScope Analysis software version 1.7. Random areas of the samples were scanned to obtain typical topography images. Open-source software Image J was used to determine the orientation of COL fibers using plugin "Orientation J" developed at the *École Polytechnique Fédérale de Lausanne* (EPFL).[38] Firstly, AFM images were converted into gray scale (8-bit) and then the program computes the local orientation properties. From this software, a visual directional analysis is obtained in which the orientation is encoded in color following the color-coding reference image **(Figure 4.3a)**.

An orientation histogram can be calculated by taking into consideration few parameters such as a Gaussian window of 1 pixel to account for the smallest possible nanostructure, and a minimum coherency and energy of 1% to eliminate the effect of isotropic areas. The distribution of orientation for TA/COL multilayers was adjusted to 0°. The same method was applied on fluorescence microscopy images to determine the orientation of cells seeded the different substrates. An example of human myoblast for color coding orientation analysis via ImageJ is also shown **(Figure 4.3b-c)**.

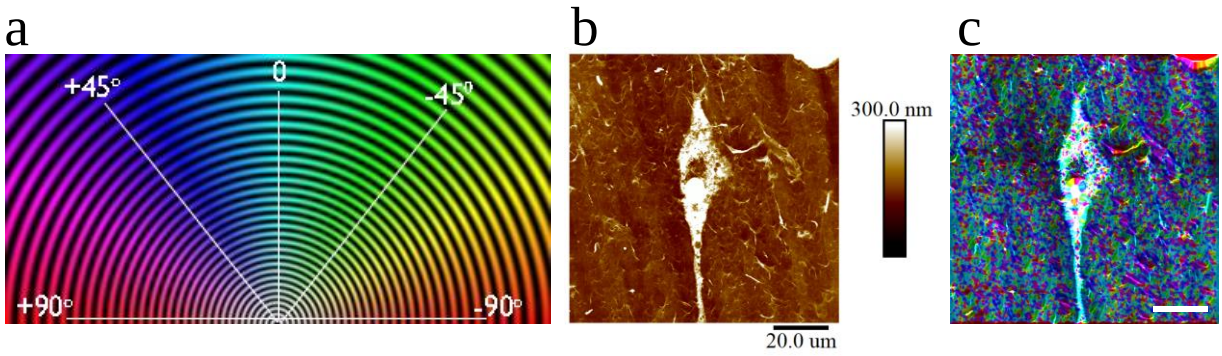


***Figure 4.3:*** ***(a)*** *OrientationJ color coding reference image to characterize the orientation distribution.* ***(b)*** *Example of human myoblast cultured on the oriented TA/COL film for 3 days observed by AFM analysis, after fixation using paraformaldehyde 4%.* ***(c)*** *Typical example of the spatial organization of actin filaments of myoblast and the underlying TA/COL film, which are color-coded according to OrientationJ reference image (Scale bar: 20µm).*

### 4.2.5 TA Release in Physiological Conditions

TA release from the oriented and the non-oriented TA/COL films in contact with PBS buffer at room temperature was followed by measuring the absorbance intensity at 277 nm using a spectrofluorometer (SAFAS Xenius XC). The samples were prepared on glass slides with final dimensions of 1x1 $cm^2$. More details can be found in the experimental section of **Chapter 3**.

### 4.2.6 Cell-surface interactions

#### *4.2.6.1 Mouse fibroblasts (NIH3T3) culture*

Cell culture experiments were performed in a biosafety level 2 laboratory. Cells were cultured in complete medium *i.e.,* Dulbecco's Modified Eagle Medium (DMEM) + 4.5 g/L glucose supplemented with 10% fetal bovine serum, and 1% penicillin and streptomycin, and in a humidified 5% $CO_2$ incubator at 37°C. The samples with final dimensions 1×1 $cm^2$ were placed in a 24-well plate and sterilized using UV light for 30 min. The cells were seeded at a density of 10,000 cells/sample for an initial adhesion of 24 h, followed by rinsing with PBS, and replacing with fresh supplemented medium to follow cell proliferation for additional 48 h.

*Immunostaining*

The immunostaining on proliferated cells was performed using various steps. After 24h of adhesion and 48 h of proliferation, the samples were rinsed twice with 1 mL of PBS, followed by a fixation step using 500 µL of 4% paraformaldehyde solution in PBS for 15 min at room temperature. After thoroughly rinsing with PBS (3 x 500 µL), the cells were permeabilized with 500 µL of 0.1% (v/v) Triton X-100 for 15 min in PBS, and finally stained with 500 µL of Alexa Fluor 568 conjugated-Phalloidin (Invitrogen A12380, 1/400) for 30 min in PBS at room temperature. The focal adhesion points were stained via vinculin using primary mouse anti-vinculin (1/50 dilution in PBS, 1.5 h incubation in dark, US Biological, V2122) and secondary anti-mouse IgG antibody (1/500 dilution in PBS, 30 min incubation in dark, Invitrogen, A11001). The samples were mounted on clear glass slides using a mounting medium containing DAPI (to stain nuclei) to observe under fluorescence microscopy. The results are representative of three individual experiments performed with samples in triplicate. Cell's orientation was determined using Orientation J via ImageJ **(Section 4.2.4)**.

*Cell migration*

Mesenchymal migration is a common mode of cell migration in fibroblasts shown in Figure 4.4. It depends on the interactions between integrins and the extracellular matrix and is characterized by a cell morphological change during its journey. Indeed, during their movement, cells have an asymmetric and polarized morphology. At the front of the cell migration front, membrane protrusions are formed via actin polymerization, to recognize and adhere to the matrix via the formation of focal contacts **(Figure 4.4)**.

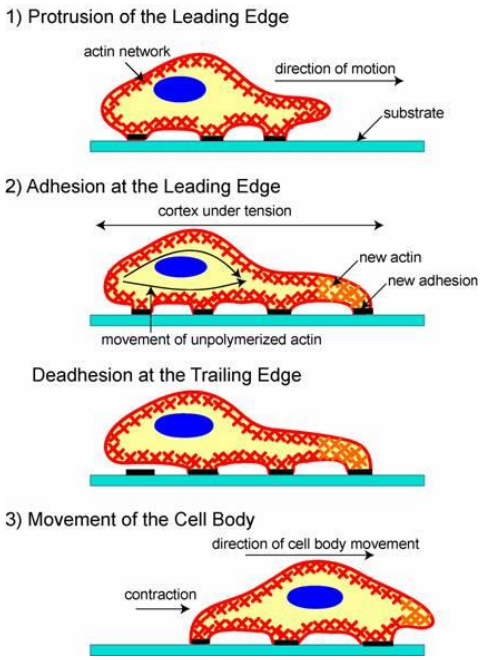


***Figure 4.4:*** *Schematic representation of various steps involved during cell migration.*[39]

The direction of protrusions' formation determined the migration axis. Those protrusions are cytoplasmic extensions whose structure is maintained thanks to different filaments of the intracellular actin cytoskeleton. Their formation is dictated by chemoattraction, the topography of the surface and the localization of certain proteins. The cells backside formed by the actin contraction is involved in the upholding of the direction of the migration.[40]

### 4.2.7 Human myoblasts (C25 CL48) culture

Human myoblasts (kindly provided by the Myology Institute, UMR_S 974 Sorbonne Université - INSERM) were maintained in TCPS flasks in a humidified 5% $CO_2$ incubator at 37°C. The experiments were conducted from cell passage 5-9. The cells were cultured in Dulbecco's Modified Eagle Medium (DMEM) + 4.5 g/L glucose supplemented with 20% fetal bovine serum, and 1% penicillin and streptomycin, named as "growth medium (GM)". The cells were pre-cultured to reach around 70% confluence.

*Human myoblasts' viability: effect of TA concentration*

The cell (3000/well) were seeded in a TCPS 96-well plate and allowed to proliferate for 24 h. The cells were rinsed with PBS, and 100 µL of TA solutions at different concentrations prepared in the growth medium was dispensed in the wells. After 24 h of contact with the TA, followed by a PBS rinsing step, 100 µL of the CellTiter-Glo 2.0 assay reagent (Promega, G9242) was added and incubated in a shaker for 15 min at room temperature. Finally, luminescence was recorded using a spectrofluorometer (SAFAS Xenius XC). The cell area was calculated using Freehand tool in the ImageJ software, and presented as a mean value of 40 cells on five individual images (200 cells in total).

*Differentiation experiment*

The cells (20,000 cells/mL) were seeded on each tested sample and allowed to proliferate for 24 h. Then, the growth medium was switched to differentiation medium (DM) (DMEM high glucose supplemented with 2% horse serum and 1% penicillin and streptomycin). Cell differentiation was followed for 12 days. DM was replaced with fresh DM after every 3-4 days.

*Immunostaining*

After 12 days of differentiation, cells were fixed with 500 µL of 4% PFA for 15 min at room temperature, followed by two rinsing steps using 1mL PBS, 5 min each. The cells were permeabilized by incubating in 1 ml of 0.5% Triton X-100 in PBS for 4 min, followed by three rinsing steps using 1mL PBS, 5 min each. The cells were incubated in 1% BSA solution in PBS for 1h at room temperature to block unnecessary sites to minimize background noise. To stain heavy chain myosin, 500 µL of the primary antibody (MF-20, AB_2147781, 0.039 µg/mL, 1/564 dilution in 0.1% BSA in PBS) was added for 2h at room temperature, in dark. After rinsing with PBS, cells were incubated in 500 µL of Abcam 150113 Goat Anti-Mouse IgG H&L (Alexa Fluor® 488) 1/500 diluted in 0.1 % BSA in PBS for 1 h at room temperature, in dark followed by two rinsing steps with PBS (2 x 1000 µL). Then, the cells were incubated in 500 µL of phalloidin-TRITC solution (dilution 1/800) in PBS for 30 min at room temperature, in dark followed by PBS (1000 µL) rinsing step. Finally, 500 µL of Hoechst 33342 (Invitrogen, B2261, dilution 1/1000) at 5 µg/ml in PBS were added at room temperature for 10 min to stain nuclei. Finally, the samples were mounted in clear glass slides to observe under Zeiss LSM 710 confocal microscopy.

For cell viability in contact with different concentrations of TA solutions, only actin filament (phalloidin-TRITC) and nuclei (Hoechst 33342) were stained following a similar protocol as above.

## 4.3 Results and Discussion

### 4.3.1 Multilayer development and characterization

In the previous chapter, TA/COL films obtained by the dipping method were built at pH 4 with citrate and acetate buffer showing a drastic difference for their antibacterial properties. The oriented COL/TA films buildup conditions were optimized regarding several parameters, such as the choice of paintbrush, COL and TA concentrations, choice of buffer and the rinsing protocol (data not presented). Higher concentrations of TA and COL solutions were required to obtain an efficient buildup in comparison to the conditions of the previous chapter. The best orientation of COL was obtained with the nylon paintbrush, in comparison to horse hair paintbrush, ensuring an appropriate shearing effect as reported by Zhao et al.[41] The buildup of citrate or acetate buffer gave similar oriented COL nanotopography. Regarding the results obtained with myoblasts, this chapter will focus only on TA/COL films built in citrate buffer.

**Figure 4.5a** shows the buildup TA/COL films, optimized in citrate at pH 4 and rinsed with water, obtained by the brushing method, named oriented TA/COL film and by the dipping method, named non-oriented TA/COL films. After 8 deposited bilayers, the thickness of the oriented TA/COL films is around 50 ± 1.5 nm which is approximately 70% less compared to the thickness of the non-oriented film (167 ± 19 nm). The buildup using the brushing method follows strictly a linear growth ($R^2$ = 0.999) with TA and COL thickness increments of 1.3 ± 0.7 and 4.6 ± 1 nm, respectively. The greater thickness increment of COL is probably due to its higher molecular weight (300 000 g/mol) compared to TA with only 1 702 g/mol.

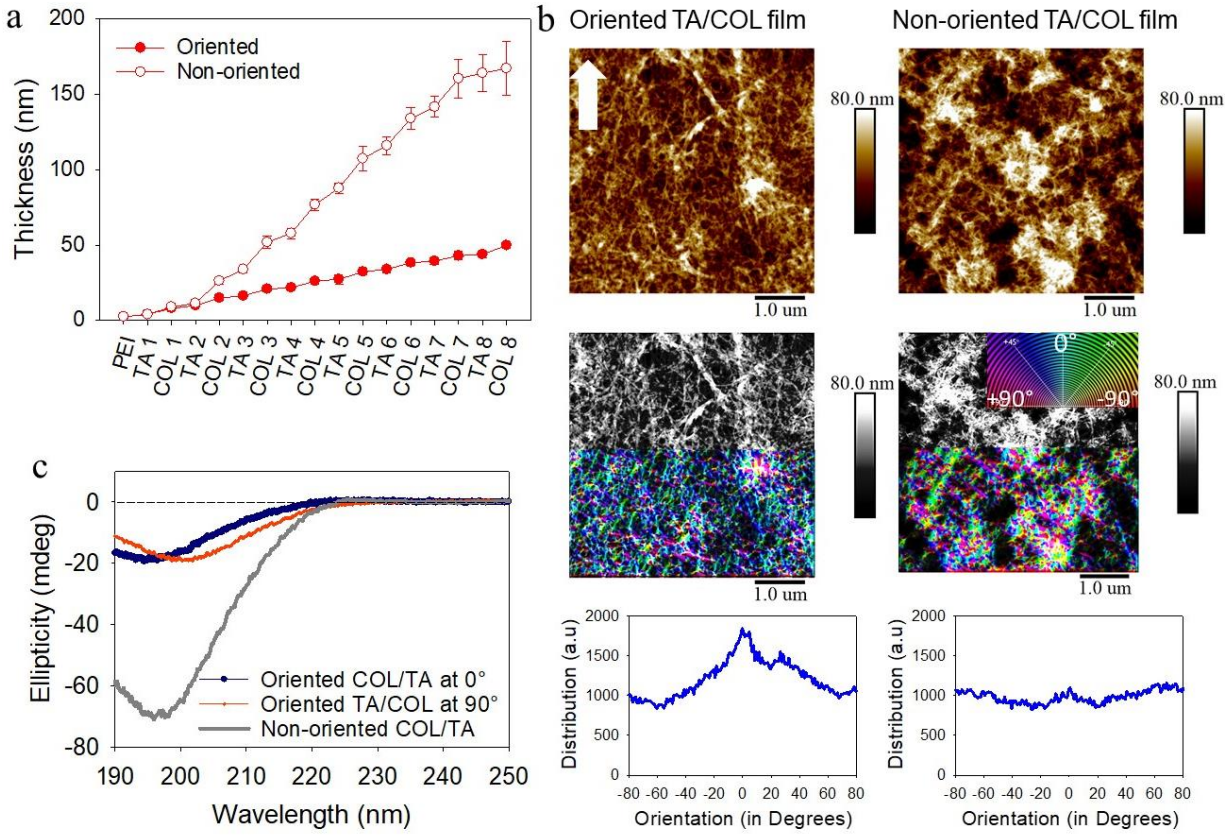


***Figure 4.5:*** *Physico-chemical characterization of the oriented and the non-oriented PEI-(TA/COL)$_8$ films. (a) Evolution of the thickness, followed by ellipsometry. as a function of the last deposited layer (mean and standard deviation from 3 different samples).* ***(b)*** *Typical AFM images with color-coding superimposition of background grayscale image and the orientation distribution graphs calculated by OrientationJ distribution. The brushing direction, visible on the AFM video camera, is indicated by the white arrow.* ***(c)*** *CD spectra obtained by placing the substrates horizontally and vertically with respect to the brushing direction. No influence of the position of the substrate was found for the non-oriented film.*

Isolated COL molecules on mica substrate have a thickness of around 2.8 ± 0.2 nm (**Figure 4.6**). They tend to form large bundles of thickness around 5.7 nm which can justify the higher thickness of COL adlayers. The size of TA molecules is around 1.3 ± 0.1 nm in PBS as determined by dynamic light scattering. TA interacts with COL via hydrogen bonding[42] only on the top of the film leading to a monolayer.

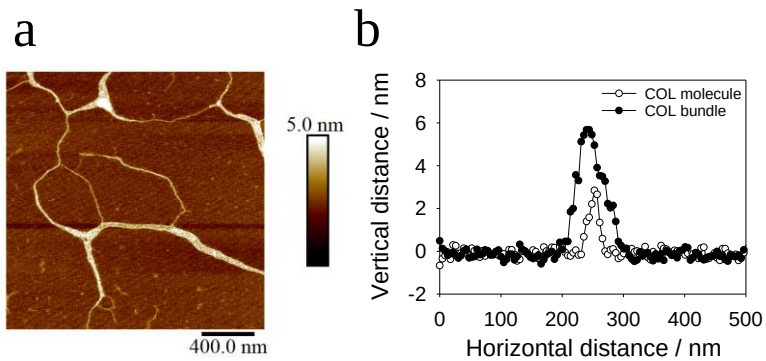


***Figure 4.6: (a)*** *Typical AFM images, obtained in Peak Force Tapping mode (ScanAsyst) in dry state, of COL fibers, dissolved in citrate pH 4, adsorbed on mica substrate for 5 min, rinsed with water and air dried.* ***(b)*** *The corresponding cross-section thickness profile of COL single molecule (empty circles) and aggregated bundle (filled circles).*

The surface topography of TA/COL films was characterized by AFM in dry state by scanning random areas of various sizes, from 20×20 to 2×2 µm², on the sample surface. Large scale images (20 × 20 µm²) of the oriented TA/COL films showed some heterogeneity due to the removal or accumulation of material, due to the shear of brushing. Therefore, only small-scale size images and their orientation evaluation are presented in the chapter. Fibrillary structures were observed for both studied films **(Figure 4.5b)**. In the case of oriented TA/COL film, the alignment of COL fibers is visible on the AFM topography image and also from the color-coded superimposed image (obtained by ImageJ) with prominent overall turquoise color, oscillating between blue and green, which correspond to 0° (*i.e.,* the direction of brushing). The orientation distribution graph shows a broad peak at 0° indicating that some COL fibers are oriented between -45° and +45° unlike the non-oriented TA/COL films showing randomly distributed COL fibers with a flat distribution. The degree of orientation of oriented TA/COL films decreases by increasing the numbers of layer pairs with a loss of orientation at 16 bilayers (data not shown). This might be due to loss of effective shear of the brushing by increasing thickness of underlying multilayer.

Circular dichroism (CD) allows to check the secondary structure of proteins. In CD, COL in solution displays characteristic optical activity in the far UV spectrum with a small positive peak around 220-225 nm and a large negative peak in the range 197-200 nm. In the previous chapter when TA/COL film is built in citrate buffer by the dipping method, we showed an effective deposition of COL with no denaturation with the intensity of both peaks increasing with the number of TA/COL bilayers **(Figure 3.11)**. The CD spectrum of non-oriented TA/COL films, studied in this chapter, shows a broad negative peak around 197 nm and no significant positive peak at 225 nm (**Figure 4.5c)**. In comparison to the conditions of the previous chapter, the dipping method was performed with higher concentration of TA and COL and a rinsing step with water, instead of citrate buffer, followed by a drying step. The CD spectrum of oriented TA/COL films is affected by the direction in which the measurement is recorded. As shown in **Figure 4.5c**, the spectrum recorded at 0° to the brushing direction shows a negative peak at 195.5 nm, with a small negative shift in comparison to the non-oriented film. Whereas for the spectrum recorded at 90° to the brushing direction, the negative peak is located at 199 nm, a random coil like behavior also observed for RGD like peptides.[43-44] The intensity of the negative peak of oriented TA/COL films is lower than non-oriented film which could be explained by the difference in thickness of both films. A diminished or insignificant positive peak at 225 nm is observed in both cases as for non-oriented film. Generally, the absence of positive peak at 225 nm, associated with triple helix, is an indication of partial to full denaturation of COL.[45] However, COL hydrogels crosslinked by TA are reported to sustain COL native conformation with similar CD spectra with a shift for the negative peak (197 nm) and no positive peak (225 nm).[46] The positive peak disappears by decreasing concentration of collagen too.[47] Hence, ruling out the possibility of COL denaturation.

Perhaps, the brushing method renders oriented COL molecules on the surface such that a specific conformation is obtained expressing distinct optical activity in cross directions.

The brushing method generates significant orientation of COL fibrils in comparison to the traditional dipping method. This method is already effective at low number of layer pairs and up to 8 bilayers. The results are representative of overall surface nanotopography because we have characterized random areas of the surface, nevertheless, to have more macroscopic overview, the orientation should be deduced by other microscopic techniques.

### 4.3.2 TA release in physiological medium

Thanks to hydrogen bond interactions between TA and COL, TA/COL LbL films are mainly stable with a part of TA released in physiological medium **(Figure 3.13)**.[48-49] Upon incubation in PBS at room temperature, the non-oriented TA/COL films, *i.e.* $(TA/COL)_8$, released 37 ± 3.6 µg/mL of TA which is approximately 9 times more than the oriented film with 4.2 ± 0.5 µg/mL **(Figure 4.7)**. TA release follows initial burst release trend with roughly 86% of release within the first 4 h, which then stabilized over 1-4 days of PBS incubation. The difference in the amount of TA released can be explained by the initial thickness of the multilayers. In comparison to the results obtained in chapter 3, non-oriented TA/COL films released 7.7 ± 2 µg/mL for $(TA/COL)_6$-COL film obtained with a rinsing step with citrate buffer and no drying step. The high amount of TA released is due to the use of water instead of the buffer at the rinsing step (data not shown).

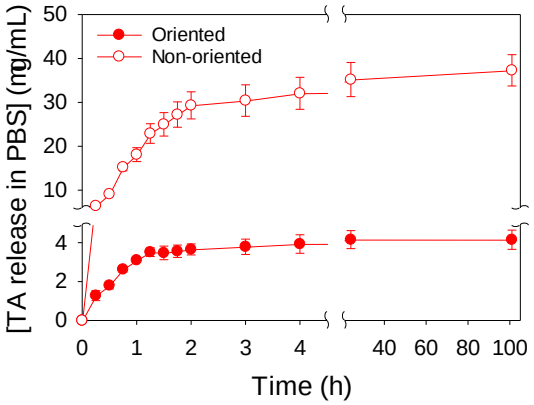


***Figure 4.7:*** *Cumulative release profiles of TA (µg/mL) from the oriented and the non-oriented TA/COL films in contact with PBS pH 7.4 at room temperature.*

### 4.3.3 Cell response on TA/COL films

The cell response of TA/COL films were first studied on murine fibroblasts before to study it on human myoblasts.

#### *4.3.3.1 Multilayer response towards murine fibroblasts (NIH3T3)*

In response to tissue injury, fibroblasts migrate into the wound, where they undergo proliferation and differentiation into myofibroblasts to produce large amounts of collagenous matrix to repair the damaged tissue. TA, in solution, is reported to show cytotoxicity towards murine fibroblasts (NIH3T3) above 100 µM concentration.[48] Pattarayan et al. identified that TA (from 1 to 10 µM) suppresses in dose-dependent manner the differentiation of fibroblasts, preventing the accumulation of ECM. They point out that TA could be an effective therapy to control fibrosis i.e., scar formation, and preserve organ function in the case of the pathogenesis of fibrosis.[50]

TA/COL films present a maximum amount of released TA, around 23 µM, for the non-oriented TA/COL films (8 bilayers) which is 4 times less than the minimal cytotoxicity concentration reported but could impact the differentiation of fibroblasts. The NIH3T3-surface interactions were analyzed in terms of cell adhesion, orientation, and proliferation on the oriented and the non-oriented TA/COL films. The topography of the oriented TA/COL films was characterized after 3

days of incubation in cell culture medium with NIH3T3 cells, to investigate the impact on COL orientation **(Figure 4.8)**. The fibroblast culture after 3 days does not significantly impact the COL orientation as confirmed by AFM topography image and the respective orientation distribution graph.

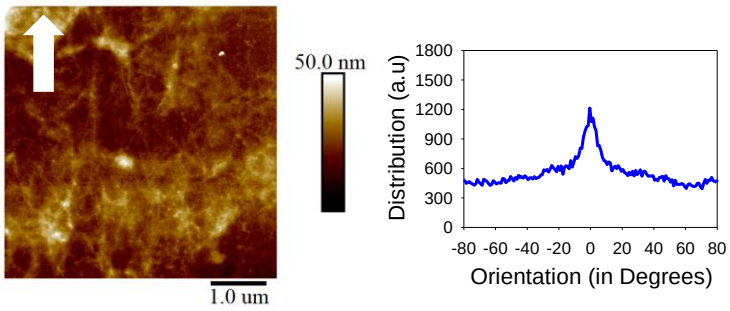


***Figure 4.8:*** *Typical AFM image, using Peak Force Tapping mode (ScanAsyst) in dry state, of the oriented TA/COL film after 3 days of incubation in complete DMEM medium in the presence of NIH T3 cells with the orientation distribution graph. The white arrow shows brushing direction.*

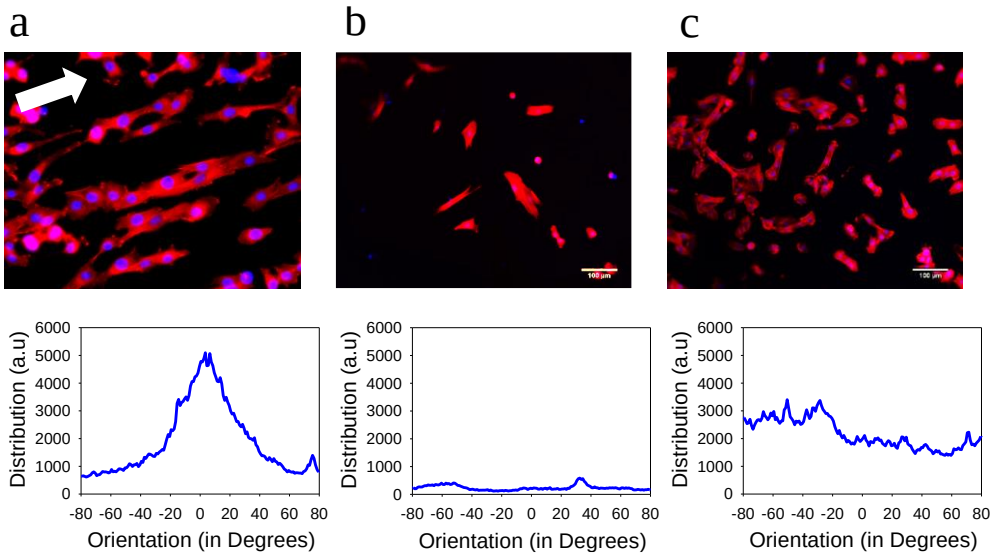


***Figure 4.9:*** *Fluorescence microscopy images of NIH3T3 fibroblasts, seeded for 3 days, on* ***(a)*** *oriented and* ***(b)*** *non-oriented TA/COL films and* ***(c)*** *uncoated glass substrate with immunostaining actin cytoskeleton (phalloidin in red) and nuclei (DAPI in blue) with the respective orientation distribution obtained by using OrientationJ via Image J. The brushing direction is indicated by the white arrow.*

The cells seeded for 3 days on the oriented TA/COL film adhere, spread, and proliferate with a preferential alignment along the brushing direction, *i.e.*, COL fibers orientation direction. The

orientation distribution graph indicated a peak at 0° (set of the brushing direction for the image treatment) (**Figure 4.9a**).

The oriented TA/COL films have no cytotoxicity towards NIH3T3 cells on the contrary to the non-oriented TA/COL film where round shaped cells and some without actin filament can be observed **(Figure 4.9b)**. It can be attributed to the localized TA release, near the multilayer-cell interface, being high enough to cause cytotoxicity effect as we reported it in the previous chapter against bacteria. Indeed, in **Figure 3.13**, the local release of TA by citrate TA/COL films, obtained by the dipping method, induced a dramatic antibacterial effect against *S. aureus* even if the total amount released in the supernatant is far below the minimal inhibitory concentration value. On the uncoated glass substrates, the well spread cells are observed with no preferential orientation. It is a well-established fact that cells sense and respond to micro-nano surface topography. Migration of cells is of vital importance due to its relevance in tissue repair and healing. During migration, cells are reported to have an asymmetric and polarized morphology on oriented topographies, whereas round shapes are observed on random topographies.[51-52] A detailed cell migration mechanism is explained in **Figure 4.4**. The morphology of isolated fibroblasts seeded on the oriented TA/COL films was compared to uncoated glass **(Figure 4.10)**. A well spread cell with randomly distributed focal adhesion points is observed on glass. Whereas an elongated cell with polarized morphology and focal points essentially along the brushing direction, with nucleus on right (direction of moving) were observed on the oriented TA/COL films, this is a typical morphology of a migrating cell.

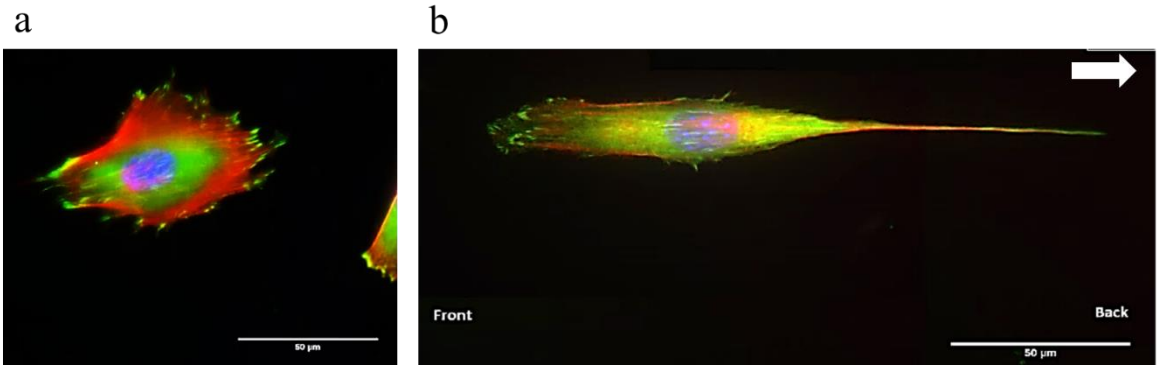


***Figure 4.10:*** *Fluorescence microscopy images of NIH3T3 cell seeded for 3 days on* ***(a)*** *glass substrate and* ***(b)*** *on oriented TA/COL film with immunostaining actin cytoskeleton (phalloidin in red), focal adhesion vinculin (in green) and nuclei (DAPI in blue). The brushing direction is indicated by the white arrow.*

#### *4.3.3.2 Multilayer response towards Human Myoblasts (C25 CL48)*

*Effect of the presence of TA in solution on human myoblasts*

Before to study the effect of TA/COL films on the proliferation and orientation of human myoblasts, we first analyzed the effect of TA in solution towards these cells. Polyphenols are known to protect plants from external microbial attack, thanks to the presence of toxic phenolic moieties.[53] Hence, it becomes essential to assess minimal cytotoxic concentration towards the cell lines under consideration. **Figure 4.11**a shows that TA becomes toxic to human myoblasts after 24 h of contact at concentrations above 33 µg/mL. For instance, human myoblasts were dead above 375 µg/mL of TA with approximately no alive cell, equivalent to the luminescent value of the control (no cells) and worse than DMSO 20%. Nevertheless, the oriented and the non-oriented TA/COL films release a quantity of TA below the cytotoxic threshold. Apart from the toxicity at high concentrations, the presence of TA shows an important change on the cell morphology. At lower TA concentrations (10 and 25 µg/mL) after only 24 h of incubation, myoblasts show elongated morphology and lengthening of actin filaments, also known as a pro-differentiation phenotype, which is an essential precursor for cell fusion **(Figure 4.11d, e)**.[54] In the absence of

TA, cells are well spread with no significant elongation **(Figure 4.11c)**. Such an effect is quantitatively reported in terms of cell area using ImageJ freehand tool. Indeed, incubation with TA causes cells to elongate resulting in roughly 20% reduced cell area compared to control cells with no TA treatment **(Figure 4.11b).** Such effects are consistent with the studies related to the effect of polyphenols (green tea extracts and polyphenol-enriched plum extract) [14-15] on muscle pathology and myotubule formation. Resveratrol, a stilbenoid, is known to accelerate differentiation of myoblasts into myotubes, myobundles and ultimately muscle tissue.[55] Kaminski et al. analyzed the effects of resveratrol, another polyphenol, on mouse myoblast differentiation initiation.[56] The results establish that resveratrol (i) is absorbed by myoblasts and myotubes by both a passive and a facilitated mechanism; (ii) induces the fusion of myoblasts, a prerequisite for their differentiation and (iii) their elongation; (iv) induced the expression of muscle-specific transcription factors as well as of myosin heavy chain; (v) increases the transcription factor Srf transcript level, which is a target mRNA of the miRNA-133b downregulated by resveratrol. Until now, no studies on the effect of TA on the differentiation of myoblasts was performed only the uptake of TA by myoblasts was reported so far.[17]

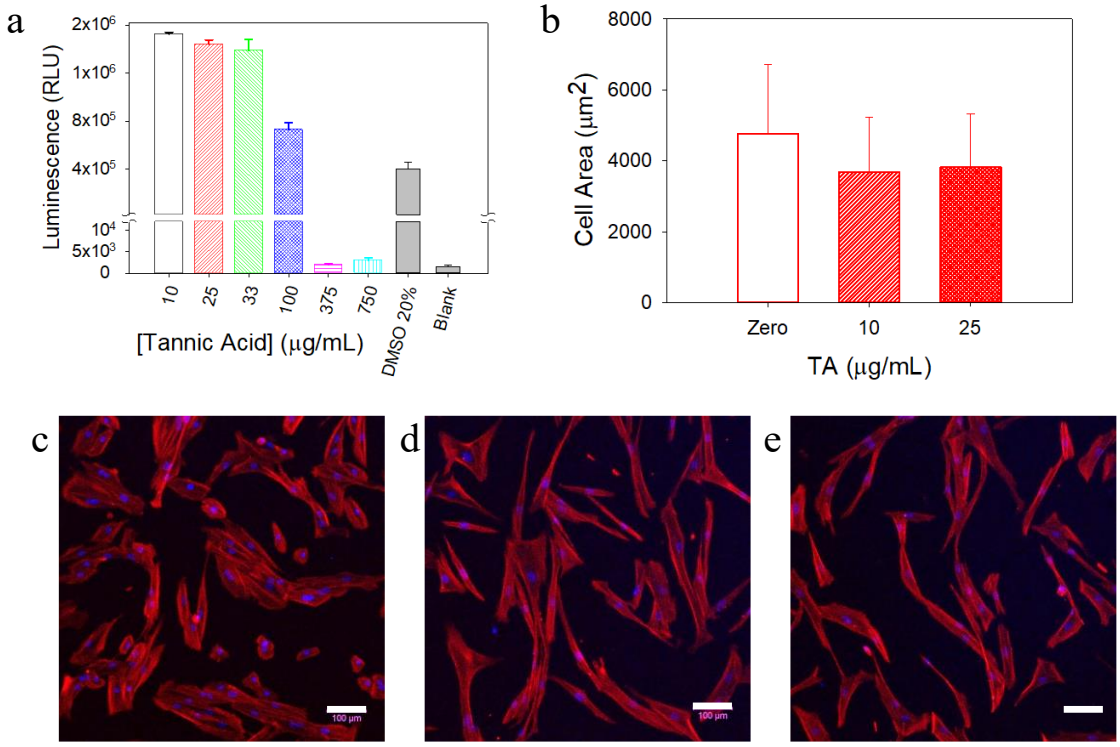


***Figure 4.11:*** *Effect of TA in solution on human myoblasts (C25 CL48) proliferation and morphology.* ***(a)*** *In-vitro cytotoxicity, using CellTitre-Glo 2.0 Reagent, and* ***(b)*** *cell area, calculated using ImageJ freehand tool, after 24 h of contact with different concentrations of TA prepared in complete DMEM growth medium.* ***(c-d)*** *Confocal images of cells after cytoskeleton labeling after 24 h of contact with* ***(c)*** *0,* ***(d)*** *10 and* ***(e)*** *25 µg/mL of TA solutions. (scale bars = 100 µm, red = F-actin, Phalloidin, and blue = nuclei, DAPI). Note: For higher picture quality, refer to electronic version.*

*TA/COL multilayers: orientation and differentiation*

Skeletal muscle development follows a cascade of events from cell adhesion, proliferation, and differentiation into multinucleated myofibers.[57] Noteworthy, as musculoskeletal tissues exhibit highly ordered nanostructured morphology composed of mainly oriented collagen fibers embedded into tissue matrix, a scaffold supporting muscle development should allow hierarchical cell orientation.[58-59] Therefore, the orientation and differentiation of human myoblasts was investigated on TA/COL multilayers via immunocytochemistry to stain heavy chain myosin (MHC) sarcomere protein, typically expressed by mature myotubes after differentiation. Myoblasts (20,000 cells) were seeded on multilayer samples and uncoated glass for 24 h in

complete growth medium. After switching to differentiation medium, confocal microscopy images were recorded at day 12 **(Figure 4.12)**. The response of the myoblasts towards various surfaces is drastically different. On the non-oriented TA/COL films and the uncoated glass surface, randomly distributed, from +90° to -90°, myoblasts and shorter myotubes are observed **(Figure 4.12)**. On the non-oriented TA/COL film, myoblasts were observed to form organoid-like structures that detach from the film surface after 5-7 days of differentiation (data not shown). On oriented TA/COL films, myoblasts follow the orientation of COL expressed as a sharp peak at 0°, *i.e.*, the brushing direction **(Figure 4.12b)**. The alignment of myotubes is of critical importance in muscle regeneration and at first it was achieved by stretching a gel by mechanical tension.[7] In fact, the cells were aligned on the oriented TA/COL films and differentiated into multinucleated long myotubes. Undifferentiated myoblasts appear to move towards and diffuse into the differentiated myotubes. Such myotubes showed an oriented arrangement of myonuclei present at periphery of the myotubes. Moreover, such myotubes were observed to join to form thicker myofibers also known as muscle fibers **(Figure 4.12a)**. At this stage, some myofibers are also observed to neglect the multilayer orientation. Perhaps, their contraction supersedes the surface nanotopography.[54] The differentiation of myoblasts follow a contact-dependent mechanism, where movement or migration to come closer, fuse, and form myotubes is important.[1] In the case of the oriented TA/COL films, cells probably move on oriented COL contact guiding cues to form denser regions which help them to fuse and to differentiate. From translational aspect, 2D nanostructured surfaces are being used to develop monolayers of mature myofibers which are then transplanted directly, or by transferring into a 3D scaffold before transplantation.[1, 60] In the case of critical size defects, 2D surfaces with oriented micro-nano topography can be particularly used for guiding cells to join disconnected tissues.[61-62]

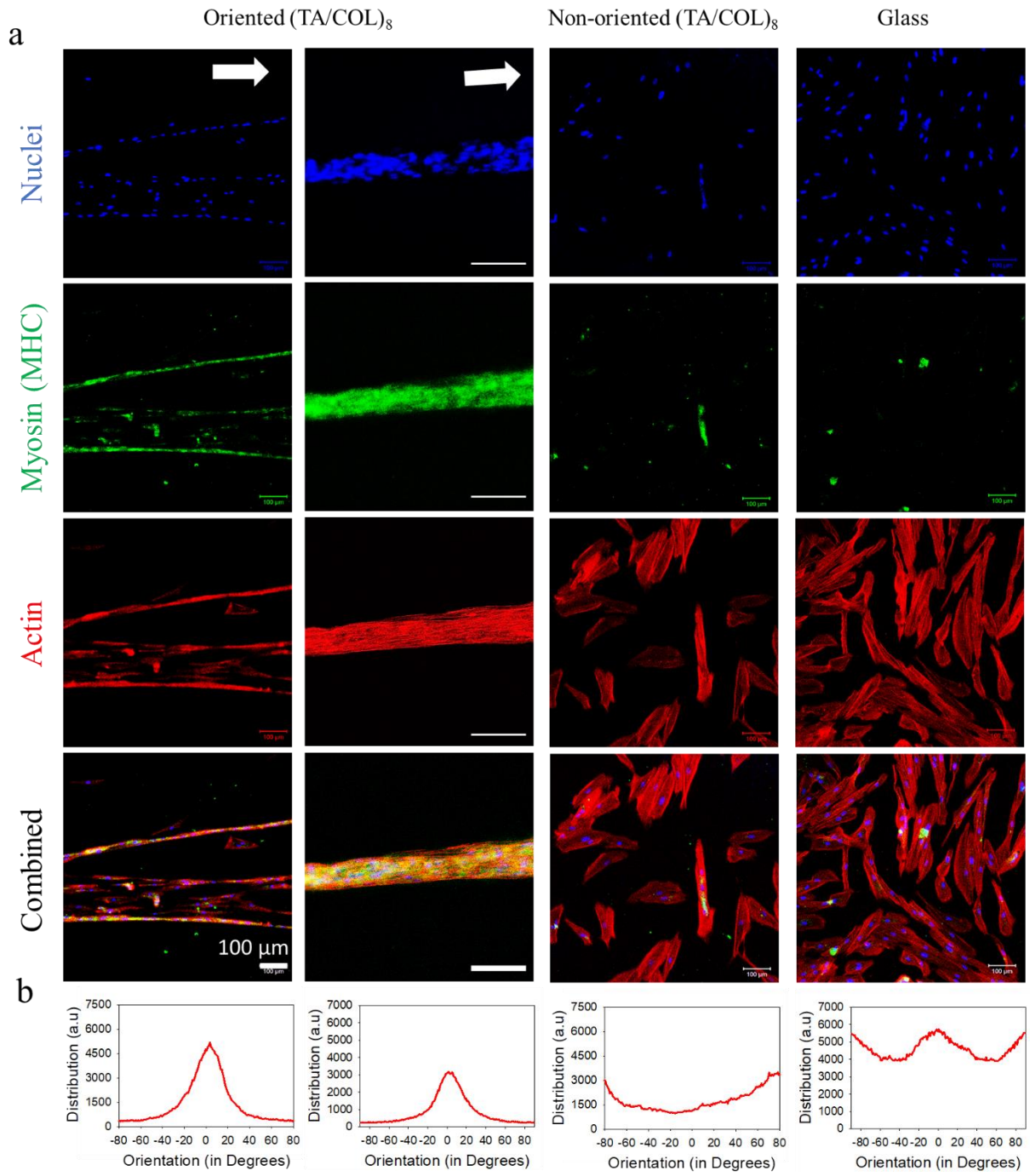


***Figure 4.12:*** *Orientation and differentiation of human myoblasts (C25 CL48) after 12 days of incubation with the oriented and the non-oriented TA/COL films in comparison to uncoated glass.* ***(a)*** *Immunofluorescence confocal microscopy images at different channels with nuclei (stained by Hoechst in blue), myosin heavy chain (stained by MF-20 in green) and actin filament (stained by phalloidin in red). The white arrow represents the brushing direction. Scale bar = 100 µm.* ***(b)*** *The respective orientation distribution graphs calculated from the alignment of actin cytoskeleton (phalloidin) via ImageJ distribution. The images are representative of three experiments (three samples each).*

After 12 days of differentiation, several noteworthy findings were quantified and reported in **Figure 4.13**. Due to the released TA, it is important to assess any possible cytotoxicity. Based on mean values of total nuclei, cell densities are around 80 and 32% on the oriented and the non-oriented TA/COL film, respectively compared to the glass control **(Figure 4.13a)**. It shows that TA/COL films switch significantly from biocompatible to cytotoxic towards human myoblasts depending on the buildup method, which is probably related to the difference in localized amount of TA release by the films. The oriented TA/COL films showed remarkable response for the development of oriented myotubes from human myoblasts. Indeed, the fusion index; defined as myotubes with ≥2 nuclei, calculated on the oriented TA/COL films is around 91% in comparison to 22% for non-oriented films and 5% for the glass control **(Figure 4.13c)**. This indicates that approximately all the attached and proliferated myoblasts differentiated into myotubes after 12 days. This improved differentiation can be explained by the treatment of myoblasts with released TA, as observed in solution previously, and the presence of oriented COL to guide myoblasts throughout their fusion.

Interestingly, the nanotopography of TA/COL films not only impacted the myoblast differentiation but also the morphology of nuclei. Elongated nuclei with aspect ratio of around 2.8 are observed on the oriented TA/COL films. Whereas a broad shape morphology with aspect ratio of approximately 1.5-1.6 is observed on the non-oriented TA/COL film and glass control **(Figure 4.13c)**. Myoblasts were reported to exhibit deformed nuclei morphologies depending on surface nanostructures.[54] Besides fusion index, we observed significant differences in area and dimensions of myotubes formed on the different samples. Myotube area on the oriented TA/COL films is around 3.6 times higher than the one on the non-oriented film and glass control. Consistent with myotube area, the myotubes developed are approximately 4 times longer and 2 times thicker on

the oriented TA/COL films than the non-oriented films or glass substrates **(Figure 4.13e)**. Noteworthy, we calculated myotube dimensions on fluorescence images of given areas only, but the actual length of myotubes might range from hundreds of micrometers to millimeters, depending on the size of the sample. Myotube maturation index shows the number of nuclei present in myotubes (> 2 nuclei) as a percentage of total nuclei **(Figure 4.13f)**.

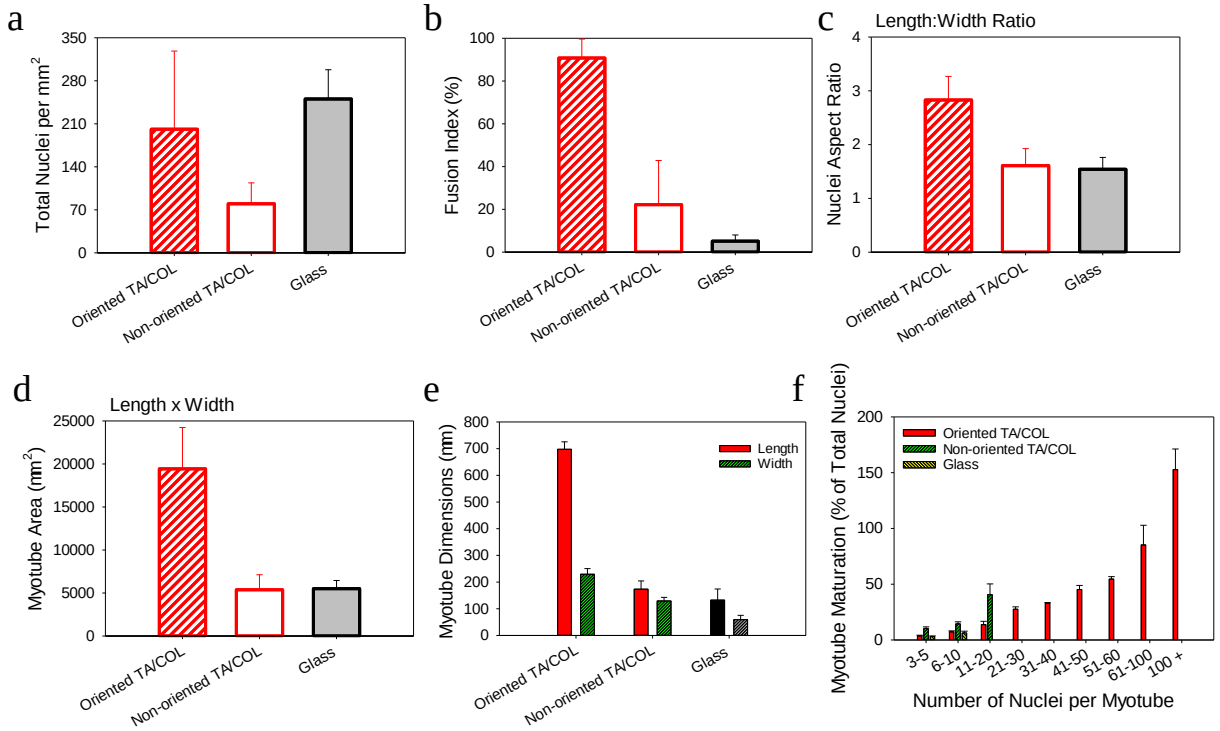


***Figure 4.13:*** *Quantitative information calculated from immunofluorescence images of human myoblast differentiation after 12 days in contact with the oriented and the non-oriented TA/COL films and uncoated glass.* ***(a)*** *cell density presented as number of nuclei per mm², **(b)** fusion index, **(c)** aspect ratio of nuclei, **(d)** area of myotubes and **(e)** their dimensions. **(f)** Myotube maturation index. The informations are calculated on a given surface image of area 691456 µm². Three different fields are measured for each condition and the experiments are conducted in triplicate.*

## 4.4 Conclusion:

The brushing layer-by-layer assembly is a simple and fast method compared to the conventional surface coating by dipping. The biocompatible multilayer coatings developed here possess aligned

nanoscaffolds. COL fibers alignment is demonstrated on LbL films obtained by brushing in comparison to the ones obtained by dipping. For the first time, we demonstrated that the brush-based layer-by-layer assembly appears to be a convenient and simple way to produce surfaces with aligned topography. In comparison to the other methods developed so far, there is no need for sophisticated apparatus, such as for magnetic field or microfluidic methods.

Furthermore, the aligned TA/COL influences the cells behavior, by improving their adhesion to a substrate and influencing their morphology and guiding their migration and proliferation. The differentiation of human myoblasts is obtained in only 12 days of contact with the oriented TA/COL films thanks to two distinct properties: COL orientation which align myoblasts favoring their close contact and TA release which favor the differentiation.

On the TA/COL films, the powerful topography cues and the strong links between cells and the collagen can be used to mimic the complexity of *in vivo* conditions and design new model tissues to regenerate anisotropic tissues.

## 4.5 Bibliography

1. Beldjilali-Labro, M.; Garcia Garcia, A.; Farhat, F.; Bedoui, F.; Grosset, J.-F.; Dufresne, M.; Legallais, C., Biomaterials in Tendon and Skeletal Muscle Tissue Engineering: Current Trends and Challenges. *Materials* **2018,** *11* (7), 1116.
2. Kuang, S.; Gillespie, M. A.; Rudnicki, M. A., Niche regulation of muscle satellite cell self-renewal and differentiation. *Cell stem cell* **2008,** *2* (1), 22-31.
3. Chargé, S. B.; Rudnicki, M. A., Cellular and molecular regulation of muscle regeneration. *Physiological reviews* **2004,** *84* (1), 209-38.
4. Corona, B. T.; Wu, X.; Ward, C. L.; McDaniel, J. S.; Rathbone, C. R.; Walters, T. J., The promotion of a functional fibrosis in skeletal muscle with volumetric muscle loss injury following the transplantation of muscle-ECM. *Biomaterials* **2013,** *34* (13), 3324-3335.
5. Järvinen, M. J.; Lehto, M. U., The effects of early mobilisation and immobilisation on the healing process following muscle injuries. *Sports medicine (Auckland, N.Z.)* **1993,** *15* (2), 78-89.
6. Cieza, A.; Causey, K.; Kamenov, K.; Hanson, S. W.; Chatterji, S.; Vos, T., Global estimates of the need for rehabilitation based on the Global Burden of Disease study 2019: a systematic analysis for the Global Burden of Disease Study 2019. *The Lancet* **2020,** *396* (10267), 2006-2017.
7. Vandenburgh, H. H.; Karlisch, P.; Farr, L., Maintenance of highly contractile tissue-cultured avian skeletal myotubes in collagen gel. *In vitro cellular & developmental biology : journal of the Tissue Culture Association* **1988,** *24* (3), 166-74.
8. Kyburz, K. A.; Anseth, K. S., Synthetic mimics of the extracellular matrix: how simple is complex enough? *Annals of biomedical engineering* **2015,** *43* (3), 489-500.
9. Meyer, G. A.; Lieber, R. L., Elucidation of extracellular matrix mechanics from muscle fibers and fiber bundles. *Journal of biomechanics* **2011,** *44* (4), 771-3.
10. Mano, J. F., Designing biomaterials for tissue engineering based on the deconstruction of the native cellular environment. *Materials Letters* **2015,** *141*, 198-202.
11. Lutolf, M. P.; Hubbell, J. A., Synthetic biomaterials as instructive extracellular microenvironments for morphogenesis in tissue engineering. *Nature Biotechnology* **2005,** *23* (1), 47-55.
12. Myburgh, K. H.; Kruger, M. J.; Smith, C., Accelerated skeletal muscle recovery after in vivo polyphenol administration. *The Journal of Nutritional Biochemistry* **2012,** *23* (9), 1072-1079.
13. Whitehead, N. P.; Yeung, E. W.; Allen, D. G., Muscle damage in mdx (dystrophic) mice: role of calcium and reactive oxygen species. *Clinical and experimental pharmacology & physiology* **2006,** *33* (7), 657-62.
14. Evans, N. P.; Call, J. A.; Bassaganya-Riera, J.; Robertson, J. L.; Grange, R. W., Green tea extract decreases muscle pathology and NF-κB immunostaining in regenerating muscle fibers of mdx mice. *Clinical Nutrition* **2010,** *29* (3), 391-398.
15. Alsolmei, F. A.; Li, H.; Pereira, S. L.; Krishnan, P.; Johns, P. W.; Siddiqui, R. A., Polyphenol-Enriched Plum Extract Enhances Myotubule Formation and Anabolism while Attenuating Colon Cancer-induced Cellular Damage in C2C12 Cells. *Nutrients* **2019,** *11* (5).
16. Chang, W.-T.; Chen, C.-S.; Cheng, M.-C.; Wu, M.-F.; Cheng, F.-T.; Hsu, C.-L., Effects of resveratrol, epigallocatechin gallate, and epicatechin on mitochondrial functions in C2C12 myotubes. *Journal of Functional Foods* **2017,** *35*, 507-512.
17. Shin, M.; Lee, H. A.; Lee, M.; Shin, Y.; Song, J. J.; Kang, S. W.; Nam, D. H.; Jeon, E. J.; Cho, M.; Do, M.; Park, S.; Lee, M. S.; Jang, J. H.; Cho, S. W.; Kim, K. S.; Lee, H., Targeting

protein and peptide therapeutics to the heart via tannic acid modification. *Nature biomedical engineering* **2018,** *2* (5), 304-317.
18. Desai, T. A., Micro- and nanoscale structures for tissue engineering constructs. *Medical engineering & physics* **2000,** *22* (9), 595-606.
19. Dugan, J. M.; Gough, J. E.; Eichhorn, S. J., Directing the Morphology and Differentiation of Skeletal Muscle Cells Using Oriented Cellulose Nanowhiskers. *Biomacromolecules* **2010,** *11* (9), 2498-2504.
20. Sousa, M. P.; Arab-Tehrany, E.; Cleymand, F.; Mano, J. F., Surface Micro- and Nanoengineering: Applications of Layer-by-Layer Technology as a Versatile Tool to Control Cellular Behavior. *Small* **2019,** *15* (30), 1901228.
21. Liu, G. Y.; Agarwal, R.; Ko, K. R.; Ruthven, M.; Sarhan, H. T.; Frampton, J. P., Templated Assembly of Collagen Fibers Directs Cell Growth in 2D and 3D. *Scientific Reports* **2017,** *7* (1), 9628.
22. Morra, M.; Cassinelli, C.; Cascardo, G.; Cahalan, P.; Cahalan, L.; Fini, M.; Giardino, R., Surface engineering of titanium by collagen immobilization. Surface characterization and in vitro and in vivo studies. *Biomaterials* **2003,** *24* (25), 4639-4654.
23. Grant, G. G. S.; Koktysh, D. S.; Yun, B.; Matts, R. L.; Kotov, N. A., Layer-By-Layer Assembly of Collagen Thin Films: Controlled Thickness and Biocompatibility. *Biomedical Microdevices* **2001,** *3* (4), 301-306.
24. Guido, S.; Tranquillo, R. T., A methodology for the systematic and quantitative study of cell contact guidance in oriented collagen gels. Correlation of fibroblast orientation and gel birefringence. *Journal of cell science* **1993,** *105 ( Pt 2)*, 317-31.
25. Bailey, A. J.; Shellswell, G. B.; Duance, V. C., Identification and change of collagen types in differentiating myoblasts and developing chick muscle. *Nature* **1979,** *278* (5699), 67-69.
26. Pastorino, L.; Dellacasa, E.; Scaglione, S.; Giulianelli, M.; Sbrana, F.; Vassalli, M.; Ruggiero, C., Oriented collagen nanocoatings for tissue engineering. *Colloids and surfaces. B, Biointerfaces* **2014,** *114*, 372-8.
27. Xia, Y.; Rogers, J. A.; Paul, K. E.; Whitesides, G. M., Unconventional Methods for Fabricating and Patterning Nanostructures. *Chemical reviews* **1999,** *99* (7), 1823-1848.
28. Vernon, R. B.; Gooden, M. D.; Lara, S. L.; Wight, T. N., Microgrooved fibrillar collagen membranes as scaffolds for cell support and alignment. *Biomaterials* **2005,** *26* (16), 3131-3140.
29. Lee, P.; Lin, R.; Moon, J.; Lee, L. P., Microfluidic alignment of collagen fibers for in vitro cell culture. *Biomedical microdevices* **2006,** *8* (1), 35-41.
30. Zhong, S.; Teo, W. E.; Zhu, X.; Beuerman, R. W.; Ramakrishna, S.; Yung, L. Y., An aligned nanofibrous collagen scaffold by electrospinning and its effects on in vitro fibroblast culture. *Journal of biomedical materials research. Part A* **2006,** *79* (3), 456-63.
31. Dubey, N.; Letourneau, P. C.; Tranquillo, R. T., Guided Neurite Elongation and Schwann Cell Invasion into Magnetically Aligned Collagen in Simulated Peripheral Nerve Regeneration. *Experimental Neurology* **1999,** *158* (2), 338-350.
32. Guo, C.; Kaufman, L. J., Flow and magnetic field induced collagen alignment. *Biomaterials* **2007,** *28* (6), 1105-1114.
33. Lanfer, B.; Freudenberg, U.; Zimmermann, R.; Stamov, D.; Körber, V.; Werner, C., Aligned fibrillar collagen matrices obtained by shear flow deposition. *Biomaterials* **2008,** *29* (28), 3888-3895.
34. Chaubaroux, C.; Perrin-Schmitt, F.; Senger, B.; Vidal, L.; Voegel, J. C.; Schaaf, P.; Haikel, Y.; Boulmedais, F.; Lavalle, P.; Hemmerle, J., Cell Alignment Driven by Mechanically Induced

Collagen Fiber Alignment in Collagen/Alginate Coatings. *Tissue Engineering, Part C: Methods* **2015,** *21* (9), 881-8.
35. Uto, S.; Miki, M.; Kuwata, Y., Orientation of Cultured Myotube on Rubbed Collagen. *Transactions of Japanese Society for Medical and Biological Engineering* **2013,** *51*.
36. Chai, Y.; Okuda, M.; Miyata, M.; Liu, Z.; Tagaya, M., Rubbing-assisted approach for highly-oriented collagen fibril arrays involving calcium phosphate precipitation. *Materials Chemistry Frontiers* **2021,** *5* (10), 3936-3948.
37. Vernon, R. B.; Gooden, M. D.; Lara, S. L.; Wight, T. N., Microgrooved fibrillar collagen membranes as scaffolds for cell support and alignment. *Biomaterials* **2005,** *26* (16), 3131-40.
38. Püspöki, Z.; Storath, M.; Sage, D.; Unser, M., Transforms and Operators for Directional Bioimage Analysis: A Survey. In *Focus on Bio-Image Informatics*, De Vos, W. H.; Munck, S.; Timmermans, J.-P., Eds. Springer International Publishing: Cham, 2016; pp 69-93.
39. Ananthakrishnan, R.; Ehrlicher, A., The Forces Behind Cell Movement. *International journal of biological sciences* **2007,** *3*, 303-17.
40. Fee, T.; Surianarayanan, S.; Downs, C.; Zhou, Y.; Berry, J., Nanofiber Alignment Regulates NIH3T3 Cell Orientation and Cytoskeletal Gene Expression on Electrospun PCL+Gelatin Nanofibers. *PLOS ONE* **2016,** *11* (5), e0154806.
41. Zhao, X.; Zhou, C.; Lvov, Y.; Liu, M., Clay Nanotubes Aligned with Shear Forces for Mesenchymal Stem Cell Patterning. *Small* **2019,** *15* (21), 1900357.
42. Ellis, S. C.; Pankhurst, K. G. A., The interaction of tanning materials with collagen monolayers. *Discussions of the Faraday Society* **1954,** *16* (0), 170-179.
43. Wang, F.; Li, B.; Fu, P.; Li, Q.; Zheng, H.; Lao, X., Effects on tumor growth and immunosuppression of a modified Tα1 peptide along with its circular dichroism spectroscopy data. *Data in Brief* **2018,** *20*, 126-131.
44. He, B.; Ou, Y.; Zhou, A.; Zhu, Y.; Chen, S.; Zhao, W.; Jiang, D.; Zhao, J.; Li, H.; Zhao, Z., Functionalized D-form self-assembling peptide hydrogels for bone regeneration. *Drug Design, Development and Therapy* **2016,** *10*, 1379.
45. Velmurugan, P.; Singam, E. R.; Jonnalagadda, R. R.; Subramanian, V., Investigation on interaction of tannic acid with type I collagen and its effect on thermal, enzymatic, and conformational stability for tissue engineering applications. *Biopolymers* **2014,** *101* (5), 471-83.
46. Brazdaru, L.; Micutz, M.; Staicu, T.; Albu, M.; Sulea, D.; Leca, M., Structural and rheological properties of collagen hydrogels containing tannic acid and chlorhexidine digluconate intended for topical applications. *Comptes Rendus Chimie* **2015,** *18* (2), 160-169.
47. Drzewiecki, K. E.; Grisham, D. R.; Parmar, A. S.; Nanda, V.; Shreiber, D. I., Circular Dichroism Spectroscopy of Collagen Fibrillogenesis: A New Use for an Old Technique. *Biophysical journal* **2016,** *111* (11), 2377-2386.
48. Reitzer, F.; Berber, E.; Halgand, J.; Ball, V.; Meyer, F., Use of Gelatin as Tannic Acid Carrier for Its Sustained Local Delivery. *Pharmaceutical Frontiers* **2020,** *2* (1), e200002.
49. Erel-Unal, I.; Sukhishvili, S. A., Hydrogen-Bonded Multilayers of a Neutral Polymer and a Polyphenol. *Macromolecules* **2008,** *41* (11), 3962-3970.
50. Pattarayan, D.; Sivanantham, A.; Bethunaickan, R.; Palanichamy, R.; Rajasekaran, S., Tannic acid modulates fibroblast proliferation and differentiation in response to pro-fibrotic stimuli. *Journal of Cellular Biochemistry* **2018,** *119* (8), 6732-6742.
51. Parsons, J. T.; Horwitz, A. R.; Schwartz, M. A., Cell adhesion: integrating cytoskeletal dynamics and cellular tension. *Nature Reviews Molecular Cell Biology* **2010,** *11* (9), 633-643.

52. Anselme, K.; Wakhloo, N. T.; Rougerie, P.; Pieuchot, L., Role of the Nucleus as a Sensor of Cell Environment Topography. *Advanced healthcare materials* **2018,** *7* (8), e1701154.
53. Reitzer, F.; Allais, M.; Ball, V.; Meyer, F., Polyphenols at interfaces. *Advances in colloid and interface science* **2018,** *257*, 31-41.
54. Bruyère, C.; Versaevel, M.; Mohammed, D.; Alaimo, L.; Luciano, M.; Vercruysse, E.; Gabriele, S., Actomyosin contractility scales with myoblast elongation and enhances differentiation through YAP nuclear export. *Scientific Reports* **2019,** *9* (1), 15565.
55. Lagouge, M.; Argmann, C.; Gerhart-Hines, Z.; Meziane, H.; Lerin, C.; Daussin, F.; Messadeq, N.; Milne, J.; Lambert, P.; Elliott, P.; Geny, B.; Laakso, M.; Puigserver, P.; Auwerx, J., Resveratrol improves mitochondrial function and protects against metabolic disease by activating SIRT1 and PGC-1alpha. *Cell* **2006,** *127* (6), 1109-22.
56. Kaminski, J.; Lançon, A.; Aires, V.; Limagne, E.; Tili, E.; Michaille, J.-J.; Latruffe, N., Resveratrol initiates differentiation of mouse skeletal muscle-derived C2C12 myoblasts. *Biochemical pharmacology* **2012,** *84* (10), 1251-1259.
57. Andrés, V.; Walsh, K., Myogenin expression, cell cycle withdrawal, and phenotypic differentiation are temporally separable events that precede cell fusion upon myogenesis. *Journal of Cell Biology* **1996,** *132* (4), 657-666.
58. Peng, H.; Liu, X.; Wang, R.; Jia, F.; Dong, L.; Wang, Q., Emerging nanostructured materials for musculoskeletal tissue engineering. *Journal of Materials Chemistry B* **2014,** *2* (38), 6435-6461.
59. Deans, T. L.; Elisseeff, J. H., Stem cells in musculoskeletal engineered tissue. *Current opinion in biotechnology* **2009,** *20* (5), 537-44.
60. Lam, M. T.; Huang, Y. C.; Birla, R. K.; Takayama, S., Microfeature guided skeletal muscle tissue engineering for highly organized 3-dimensional free-standing constructs. *Biomaterials* **2009,** *30* (6), 1150-5.
61. Nauth, A.; Schemitsch, E.; Norris, B.; Nollin, Z.; Watson, J. T., Critical-Size Bone Defects: Is There a Consensus for Diagnosis and Treatment? *Journal of Orthopaedic Trauma* **2018,** *32*, S7-S11.
62. Gentile, P.; Chiono, V.; Tonda-Turo, C.; Ferreira, A. M.; Ciardelli, G., Polymeric membranes for guided bone regeneration. *Biotechnology Journal* **2011,** *6* (10), 1187-1197.

# Chapter 5 : Bio-sourced Antibacterial Nanocoatings

## Unexpected Antibacterial Activity of Aligned Chitin Nanocrystals/Tannic Acid Multilayer Films

# Table of Contents

Besides protein-polyphenolic LbL films herein, we developed multifunctional coatings based on polysaccharides nanostructures using the brushing method. The chapter discusses the development of chitin nanocrystals-based LbL films, their physico-chemical and biological characterizations. It further includes a thorough discussion on how specific orientation of CNCs can govern the antibacterial effect.

## 5.1. Introduction

Nanostructured surface coatings have attracted great attention since the last decade to develop next generation advanced materials. Towards broad horizons of health and environment, multifunctional coatings are particularly applied to design antimicrobial surfaces. Antibacterial surface modification is of paramount importance to cope bacterial infection, a major threat to human health worldwide. Bacteria survive generally by attaching to solid surfaces, proliferate and produce biopolymer matrix embedded colonies called biofilm[1] which can increase bacterial resistance up to thousand times,[2] leading to bacteria survival in harsh environmental conditions. Bacterial infections spread via several pertinent routes such as touching commonly used surfaces,[3] food, fresh and marine water,[4] biomedical implants and devices, hospital-acquired infections, etc.[5] In later case, five percent of patients develop nosocomial infections every year during hospitalization time in western countries, and the situation is even worse for developing countries with above 15% infection rate.[6] According to a WHO report, 0.7 million people die annually because of antimicrobial resistance and the figures are expected to rise up to 10 million by 2050 with approximately $100 trillion economic loss.[4] With progressive development of intrinsic and evolutionary resistance in bacteria towards antibiotics, traditional infection

treatments are becoming ineffective. Multifunctional antibacterial coatings have potential to supersede existing strategies and can certainly have a great impact for research and practical use. Antibacterial coatings are being developed by bottom-up *i.e.,* physico-mechanical surface structuring[7] and top-down approaches that generally involve chemical modification of surfaces.[8] Recently, top-down biomimetic surfaces with nano-topographic features have emerged as a possible strategy to cope bacteria attachment and biofilms.[9] Such nanostructured surfaces are inspired by naturally present nano-micro topographical features on cicada wings,[9] lotus leaves,[10] gecko feet,[11] and shark skin.[12] The later has vital relevance to ship hulls that are often covered with slimy bacterial matrix causing reduced speed, higher fuel costs, and limited maneuverability, and thus putting a huge financial burden on maritime industry.[13] Although nanostructured surfaces are emerging as a promising strategy, however their development involves expensive instrumentation and complex processes like laser ablation,[7] electropolishing,[14] and photolithographic techniques.[15]

The chemical modification involves surface functionalization using nano-objects for instance silver nanoparticles,[16] antimicrobial peptides,[17-18] antibiotics,[19] and synthetic[20] and biobased polymers.[21] Amongst numerous surface functionalization strategies, layer-by-layer (LbL) is one of the simplest and versatile technique that requires alternate deposition of positively and negatively charged polyelectrolytes on a substrate via dip,[22] spin,[23] or spray assembly.[24] Due to its ease of application to practically any shape and size of substrate, and mild fabrication conditions (water soluble solutions, room temperature, pH, and hierarchical control at the nanoscale), it has been widely utilized to develop antiadhesive or bacteriostatic, contact killing, and release killing antimicrobial surfaces.[25] Recently, brush-assisted LbL assembly was

introduced using synthetic polyelectrolytes and soluble polysaccharides.[26] Later, the shearing effect of brushing technique was reported to align monolayer of clay nanotubes.[27]

Chitin is the second most abundant, inexpensive, renewable, and semicrystalline polysaccharide produced from natural origins such as crustacean exoskeletons. Chitin-based exoskeletons naturally contain high amounts of iron,[28] and were reported to act as adsorbents to remove $Fe^{3+}$ from organic wastes[29]. Highly anisotropic nano-objects are usually extracted via acid hydrolysis of chitin macromolecular chains.[30] Crystalline chitin nanocrystals (CNCs) and chitin nanofibers are generally used for their excellent mechanical properties to design biodegradable materials.[31] Since 2000s, chitin and its nanoforms are being increasingly explored to engineer materials like particles,[32] fibers,[33] films,[34-37] aerogels,[38] hydrogels,[39] scaffolds,[40] and so forth. Attention has been given to orient chitin-based anisotropic nanostructures, inspired by naturally existing butterfly wings,[41] using electric[42] and magnetic fields,[43] shear,[44-45] and wet stretching.[46] Mostly, these sophisticated methods are costly as they require expensive equipment. Linearly aligned acetylglucosamine chains are responsible for the presence of primary amines on the surface of chitin[47] with a pKa of around 6.3 that allows stable colloidal suspension in acidic conditions.[48] The amount of primary amines depend on the extraction process parameters and the nature of chitin macromolecules. Chitosan, chitin deacetylated counterpart, has been extensively used to develop antibacterial coatings.[49-51] In contrast, a limited research has been conducted on the antibacterial or antifungal properties of chitin. Few studies reported chitin based membranes with antifungal properties[52-53] for food packaging[37, 54] and antibacterial properties.[53, 55-56] In most of these studies to obtain the fungal or bacterial inhibition, chitin was modified chemically by quaternization,[57] oxidation,[55] or acylation,[37] or was incorporated with chitosan,[53, 56] tannic acid[58]

or copper,[59] or processed into chitin nanofibers using dynamic high pressure homogenization.[52] Chemically modified chitin was also develop to obtain hydrogels for tissue engineering without[60] or with antibacterial properties.[61] Despite few studies on chitin based LbL,[36, 62-65] none of them reported antibacterial properties of the biobased film.

Herein, we report a fully bio-sourced CNC LbL films by using the brushing and dipping methods to develop oriented and non-oriented nanocoatings, respectively. Tannic acid, a naturally occurring polyphenol, can interact with chitin via hydrogen bonding and hydrophobic interactions[58] and $Fe^{3+}$ through coordination bonds.[66] Tannic acid and $Fe^{3+}$ were used during the buildup of CNC films. Composed of only FDA approved materials (FDA: United States Food and Drug Administration),[67-68] only the oriented TA/$Fe^{3+}$/CNC based films exhibit a highly effective anti-adhesive and contact killing properties against *Staphylococcus aureus* (*S. aureus*, a Gram-positive bacteria) and *Escherichia coli* (*E. coli*, a Gram-negative bacteria).

## 5.2. Experimental Section

### 5.2.1. Chitin nanocrystal suspensions

Chitin Nanocrystal Suspensions (CNC) were prepared with a protocol already described elsewhere.[30, 69-70] To prepare the CNC aqueous stock suspension, Chitin powder from shrimp shells with a practical grade was purchased from Aldrich and purified in two steps. All other reagents have been purchased from Aldrich.

*Purification*

First, a NaOH treatment was performed with 5 wt.% sodium hydroxide, with a solid content of about 5% at 80°C for 3 h. Typically, for 42g of chitin, 45g of NaOH is solubilized in 855g of

water. The suspension is then mechanically stirred for 3 h at 80°C, the flask is then cooled in an ice bath and the suspension is filtered on 40µm nylon cloth.

*Bleaching*

The solid residue is then subjected to a second bleaching treatment with sodium chlorite at about 0.3% by weight, at 80°C for 3h. Typically, for the initial 42g of chitin: 2.4g of sodium chlorite are solubilized in 797.6g of water.

Caution: deadly poison by skin contact and releases a deadly gas when in contact with an acid.

After 3 hours of mechanical agitation at 80°C, the flask is cooled for 10 min on an ice bath and the suspension is filtered, under a fume cupboard, on a 40µm nylon cloth. This treatment is also repeated 3 times.

*Hydrolysis*

The chitin pellet is resuspended in 1.2L of distilled water then dialyzed against distilled water and centrifuged at 22000G during 30 min at 4°C. The resulting pellet was put in 5M hydrochloric acid under reflux at 104°C for 90 min. To stop the reaction, the mixture was cooled by diluting with distilled water and ice. The suspensions were washed by repeated centrifugations, dialyzed against distilled water until neutrality and sonicated for 4 min with a Branson B-12 sonifier equipped with a 3 mm microtip. CNC suspensions were diluted with distilled water to 1% (or desired concentrations) by weight and dialyzed against dilute HCl solution (1.0 mM) until stable at pH 3. The suspensions were then filtered through 8 µm and then 1µm cellulose nitrate membranes (Whatman).

### 5.2.2. Materials and solutions

The description of all the materials and reagents used in this work is provided in **Chapter 2**.

CNC suspension was used at a concentration of 1.8% by wt. in water at pH 3. All solutions were prepared freshly prior to use except CNC suspension. Deionized water (Milli-Q, 18.2 MΩ·cm at 25°C) supplied by Advantage A10 (MERCK) was used in the entire study. The pH values were adjusted by using 0.1 M HCl or 0.1 M NaOH solution prepared in deionized water. PEI solution was prepared at 0.1 mg/mL in 0.15 M sodium chloride (NaCl) aqueous solution (no pH adjustment). TA solution was prepared at 0.5 mg/mL in deionized water and adjusted to pH 3 and kept in dark to avoid its photooxidation. Iron chloride solution was prepared at 0.5 mg/mL in water at pH = 2.5. Chitosan (CHI) solution was prepared at 5 mg/mL in ultrapure water at pH 2 and the pH was adjusted to 3 after CHI dissolution. Hyaluronic acid (HA) solution was prepared at 1 mg/mL in water at pH 3 and the final solution pH was around 3.5. Prior to thin film buildup, all the solutions, except CNC suspension, were filtered using a 0.20 µm filter (Sarstedt, no. 831826001) to remove any impurity or undissolved substances.

Silicon wafers or microscopic glass slides were cut using a sharp diamond pen to obtain 1 × 6 $cm^2$ rectangular substrates. Silicon wafers were cleaned with ethanol/water (50% v/v) solution for 15 min prior to their use. Glass substrates were cleaned by immersing in the solutions of 10 mM SDS and 0.1 M HCl at 70°C for 10 min each, followed by extensive rinsing with deionized water. Prior the film buildup, the substrates were plasma etched for 2.5 min with air using Harrick PDC-002-HP at high RF level to remove particles and to render the surface negatively charged and hydrophilic.

### 5.2.3. LbL deposition by dipping and brushing techniques

PEI, a branched polycation, was used as precursor layer on each substrate before LbL buildup. Immediately after plasma cleaning, the substrate was dipped in PEI solution for 10 s, rinsed twice with ultrapure water by dipping for 5 s and dried with filtered compressed air. The substrate is then a positively charged surface ensuring a good anchoring of the films. Oriented CNC/TA based films were obtained by the brushing method. The PEI-functionalized substrate was clipped with a support in a horizontal direction facing upwards to brush the solutions always in the same direction in the area highlighted in blue **(Figure 5.1a-b)**. The used brush (Søstrene Grenes, Aarhus, Denmark) is a nylon paintbrush with dense bristles (**Figure 5.1c**).

Non-oriented CNC/TA films were obtained by the dipping method. The PEI-functionalized substrate was immersed in TA solution for 10 s, followed by two rinsing steps using ultrapure water for 5 s and dried by filtered compressed air. The same process was followed to deposit $Fe^{3+}$, CNC, and again $Fe^{3+}$ adlayer, to obtain ($TA/Fe^{3+}/CNC/Fe^{3+}$) quadrilayer. Once the desired film architecture was achieved, the homogeneous part, highlighted in orange color, of the sample was selected and cut to obtain 1 × 1 $cm^2$ area samples as shown in **Figure 5.1b** to characterize the film properties.

For comparison, oriented PEI-$(HA/CNC)_7$, named HA/CNC, films were prepared by the brushing method and non-oriented $(TA/Fe^{3+}/CHI/Fe^{3+})_n$, named TA/CHI, films were prepared by the dipping method using the same procedure as described above. NB: even if the term “oriented” is not appropriate for CHI based films, we keep the same notation for sake of clarity. It can be noticed $TA/Fe^{3+}$/CHI based films cannot be obtained using the brushing method.

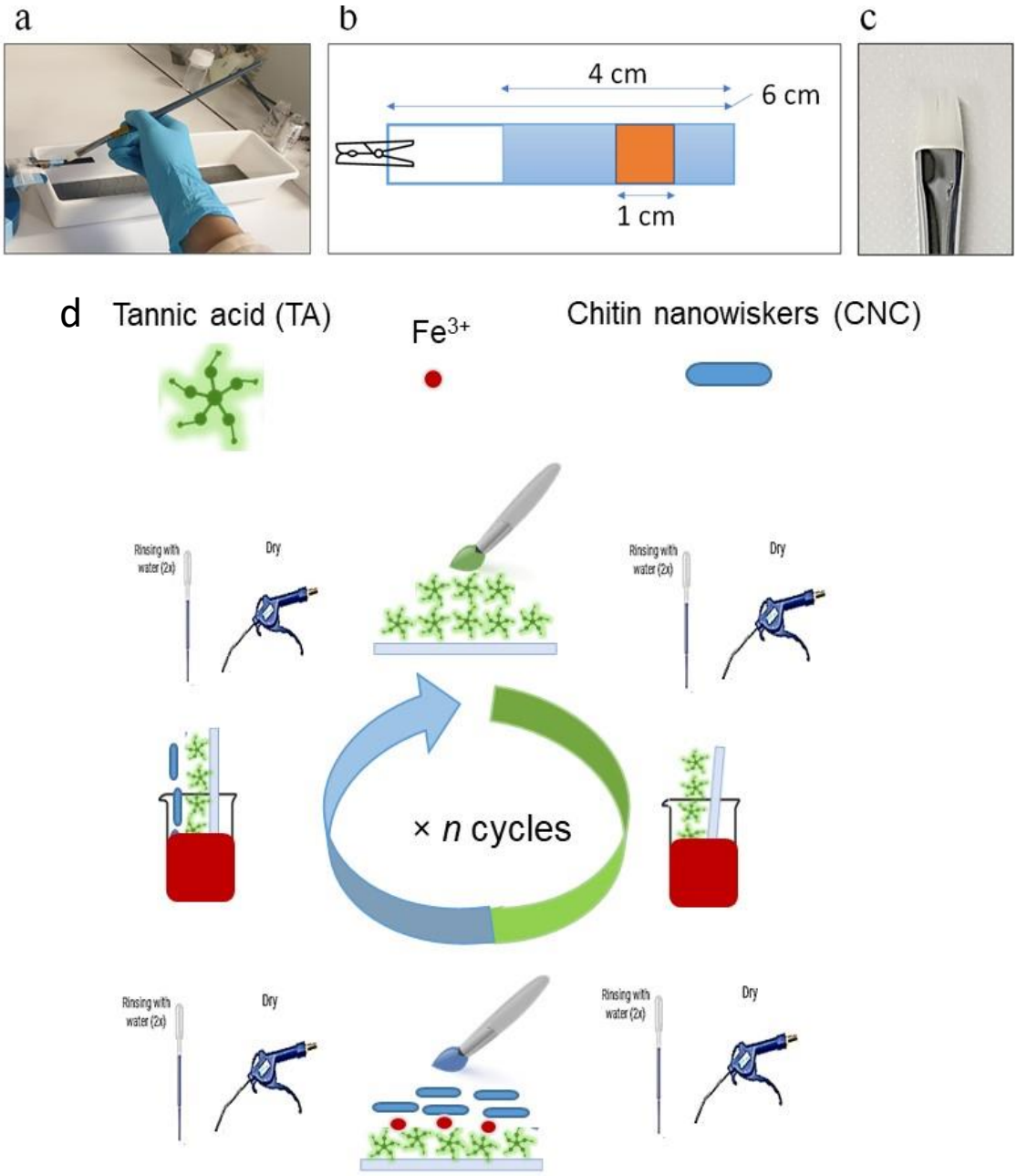


***Figure 5.1:*** *Manual brushing method* ***(a)*** *manual brushing set-up,* ***(b)*** *schematic representation of the area (blue + orange) of the glass slides selected to deposit the films* ***(c)*** *Nylon paintbrush (Søstrene Grenes, Aarhus, Denmark) with dense bristles used.* ***(d)*** *schematic representation of oriented CNC/TA films buildup by the brushing method. After deposition of TA or CNC by the painting brush and rest of 10 s, the substrate is rinsed with ultrapure water using a disposable pipette and dried by compressed air. After each TA or CNC deposition, an adlayer of Iron ($Fe^{3+}$) is deposited by dipping the substrates for 10 s, followed by rinsing with water using a disposable pipette, and dried by compressed air.*

### 5.2.4. Dynamic Light Scattering

Dynamic Light Scattering (DLS), Zetasizer® from Malvern, was used to determine the average size and zeta potential of the nanocrystals in solution. This technique measures, at a fixed angle, the mean particle size in a limited size range. The sample is illuminated by a laser beam and the fluctuations of the scattered light are detected at an angle of 90° by a photon detector. The signal is used to determine the diffusion coefficient and the particle size by the Stokes-Einstein equation.

### 5.2.5. Ellipsometry

The film thickness was measured, after rinsing with water and drying by compressed air, using an Ellipsometer (SD2300, PLASMOS) with an incident laser beam (632.8 nm) and a constant angle of 45°. Refractive index was assumed to be constant and $n$ = 1.465 for all the measurements. The dry thickness values reported here are the average of ten measurements observed at random areas on each multilayer sample surface. Such ellipsometry measurements show insignificant differences in absolute dry thickness.

### 5.2.6. Atomic Force Microscopy

Atomic Force Microscopy (AFM) Multimode Nanoscope IV from Bruker was used to image in dry state a monolayer of CNC, oriented and non-oriented LbL films using nitride coated silicon tips on a nitride cantilever (Model ScanAsyst-Air, with force constant k=0.4 N/m and frequency $f_n$ =70 kHz) and Peak Force Tapping (ScanAsyst) mode. The images were obtained at a scan rate of 1 Hz with a resolution of 512 × 512 pixels. The data analysis was performed using NanoScope Analysis software version 1.7. Random areas of the samples were scanned to obtain typical topography images. The analysis of CNC orientation was performed using an open-source

software ImageJ® with the plugin "Orientation J" developed at the *École Polytechnique Fédérale de Lausanne* (EPFL).[71] Firstly, AFM images were converted into gray scale (8-bit) and then the program computes the local orientation properties. From this software, a visual directional analysis is obtained in which the orientation is encoded in color following the color-coding reference image **(Figure 5.2)**. An orientation histogram can be calculated by taking into consideration few parameters such as a Gaussian window of 1 pixel to account for the smallest possible crystal/nanostructure, and a minimum coherency and energy of 1% to eliminate the effect of isotropic areas. The distribution of orientation for CNC multilayers was adjusted to 0°.

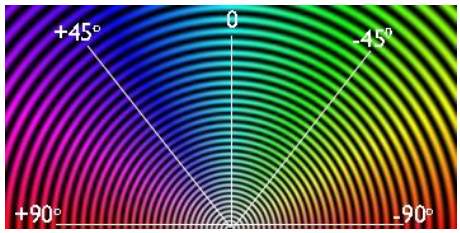


***Figure 5.2:*** *OrientationJ color coding reference image to characterize the orientation distribution.*[71]

The bearing analysis is a method used to analyze the distribution of surface height over a sample by revealing what percentage of the surface i.e., the bearing area ratio, is below or above any selected height. The bearing analysis was performed on the AFM topography images of the oriented and the non-oriented TA/CNC, the oriented HA/CNC, and non-oriented TA/CHI films. AFM images of size 5x5 µm² with a resolution of 512x512 pixels were used. All images were second order plain fitted along XY and flattened to ensure a perfectly horizontal image with no tilt. The bearing analysis was performed using NanoScope Analysis software version 1.7.

#### *5.2.6.1.* ***AFM-probes functionalization and chemical force microscopy (CFM).***

Gold coated cantilevers (NPG-10, Bruker Nano AXS, Palaiseau, France) were functionalized using thiol attachment method with 11-mercaptoundecanoic acid or either with 11-mercaptoundecylphosphonic acid according to the protocol detailed elsewhere[72-74] to obtain $–COO^-$ and $–PO_3^-$ terminated AFM-probes.

CFM experiments were performed in PBS at pH 7.4 and room temperature with a Bioscope Resolve equipment (Bruker AXS, Palaiseau, France). To this end, gold coated cantilevers with spring constants of 0.12 nN/nm previously functionalized were used. Adhesion forces between AFM-probes and sample surface were measured by recording Force-Volume Images (FVI) consisting of a grid of 32 × 32 force curves obtained upon approach and subsequent retraction of the AFM probe at pulling rates of 1 µm/s with a contact time of 100 ms. For each sample, force measurements were performed in triplicate over an area of 5 µm × 5 µm.

AFM images in PBS medium were recorded with a Bioscope Resolve equipment (Bruker AXS, Palaiseau, France) using PeakForce Tapping mode using silicon nitride cantilevers purchased from Bruker (PeakForce HIRSS-SSB, Bruker AXS, Palaiseau, France) with spring constant of 0.10 nN/nm.

### 5.2.7. Antibacterial Activity Assays

The antibacterial activity of the films prepared on glass substrates of 1×1 $cm^2$ final area was evaluated towards *Staphylococcus aureus (S. aureus, ATCC 25923),* a Gram-positive bacterium, and *Escherichia coli (E. coli ATCC 25922)*, a Gram-negative bacterium regarding the adhesion, proliferation, and biofilm formation.

#### *5.2.7.1.* ***Bacteria pre-culture***

To perform antibacterial tests, an isolated colony of *S. aureus* and *E. coli* was pre-cultured aerobically in Mueller-Hinton (MH) and Lysogeny broth (LB) media, respectively, at pH 7.2–7.6 (Merck, Darmstadt, Germany) in an incubator with agitation for 6 h at 37°C to use the inoculation in log phase of bacterial growth. After a pre-dilution in Roswell Park Memorial Institute medium (RPMI 1640) and Lysogeny broth (LB) media of pre-culture bacteria, an optical density at 600 nm ($OD_{600}$ = 0.001) was used to prepare the final inoculation of *S. aureus* and *E. coli*, respectively.

#### *5.2.7.2.* ***Bacterial Adhesion Assay***

The sample substrates were immersed into 400 µL of bacterial inoculation at $OD_{600}$ 0.001 in the culture medium. The bacterial inoculation was incubated in contact with film samples at 37°C for 1.5 h to allow the bacteria to adhere to the sample surface. After 1.5 h, the bacteria growing in planktonic state and number of adhered bacteria onto the sample surfaces were analyzed. 100 µL of the supernatant was taken in a 96-well plate reader to measure optical density at 600 nm ($OD_{600}$) to probe the planktonic growth. To analyze the number of bacteria adhered onto the substrates, the samples were carefully rinsed with PBS in a dilution manner to avoid the creation of sample surface-air interface to prevent the removal of attached bacteria. The membrane integrity and number of adhered bacteria were analyzed by observing the samples with confocal microscopy (Zeiss LSM-710, ×63) using Live/Dead staining described below. The quantification was performed on three images per samples on at least seven samples.

#### *5.2.7.3.* ***Bacterial Proliferation Assay***

The samples substrates were immersed into 400 µL of inoculated medium in an incubator at 37°C. After 1.5 h of incubation, the inoculation was replaced with fresh medium free of bacteria, and the adhered bacteria were allowed to proliferate for 24 h at 37°C in an incubator without agitation to maximize the bacteria settling on the sample surface under gravity. After 24 h of proliferation, the film samples were observed by fluorescence confocal microscopy (Zeiss LSM-710, ×63). For this purpose, the samples were carefully rinsed with PBS in a dilution manner to avoid the creation of surface-air interface to prevent the removal of attached bacteria. Finally, the samples were observed using Live/Dead staining procedures. The quantification was performed on 3 images per samples on at least 7 samples.

#### *5.2.7.4.* ***Bacteria Live/Dead Assays***

To observe the viability and number of bacteria present on the surfaces for both adhesion and proliferation experiments, two Live/Dead assays were used, and all the results are presented in terms of number of bacteria per $mm^2$. SYTO® dyes are cell-permanent nucleic acid stains that show a large fluorescence enhancement upon binding nucleic acid. SYTO®-9 and SYTO®-24 dyes can stain RNA and DNA in both alive and dead eukaryotic cells, thus counting all the cells present on the surfaces. The first Live/Dead assay was based on Propidium iodide (PI, excitation/emission: 530/620 nm) and SYTO®-9 (excitation/emission: 485/498 nm). PI, a red-fluorescent nucleic acid stain, penetrates only the bacteria with damaged or porous membranes, and causes a reduction in the fluorescence of SYTO®-9 stain due to FRET phenomenon. Thus, with an appropriate mixture, SYTO®-9 stains alive bacteria with intact cell membranes in green and PI stains bacteria with damaged membranes in red. With this staining combination, we could

determine the percentage of damaged bacteria adhered onto the surfaces by calculating the ratio of number of damaged cells (PI staining) versus the total number of bacteria (PI and SYTO®-9 staining). To that aim, the samples were stained using PI (30 µM) and SYTO®-9 (6 µM) staining (Invitrogen, LIVE/DEAD BacLight Bacterial Viability Kit, L7012) for 25 min at room temperature in dark, followed by a fixation step using 4% paraformaldehyde solution. Then, the samples were mounted with the help of a mounting medium (Invitrogen, ProLong™ Diamond Antifade Mountant, P36965) for the confocal microscopy (Zeiss LSM-710) observation by utilizing a 63× Plan Apo (1.4 NA) objective immersed in oil.

To confirm the bacteria vitality after 24 h of proliferation, the samples were also stained with 5-cyano-2, 3-ditolytetrazolium chloride (CTC, Invitrogen, B34956, excitation/emission: 450/630 nm) and SYTO®-24 (Invitrogen, B34956, excitation/emission: 490/515 nm). Bacterial cell activity converts CTC, a tetrazolium salt, into formazan crystals (emitting a red fluorescence). CTC staining enables to evaluate the respiratory or metabolic activity of bacterial cells. Healthy cells are respiring via the electron transport chain and will absorb and reduce the tetrazolium salt. Only viable or alive bacterial cells can thus be stained by CTC and detected by fluorescent microscope. Thus, SYTO®-24 stains all the bacteria in green and CTC the alive bacteria in red. With this staining combination, we could determine the percentage of active bacteria adhered onto the surfaces by calculating the ratio of number of active cells (CTC staining) versus the total number of bacteria (SYTO®-24 staining). To that aim, the samples were stained by immersion in 400 µL mixture of CTC (5 mM) and SYTO®-24 (0.2 µM) staining for 30 min at room temperature in dark, followed by a fixation step using 4% paraformaldehyde solution. Finally,

the samples were mounted for the fluorescence microscopy (Zeiss LSM-710) observations with the help of the mounting medium (Invitrogen, P36965).

#### *5.2.7.5.* ***Planktonic growth of bacteria***

100 µL of the supernatant was taken in a 96-well plate reader to measure optical density at 600 nm ($OD_{600}$). Several controls were used: LbL films in contact with medium free of bacteria were used as negative control; corresponding to 0% growth of bacteria (ensuring sterility). Uncoated glass substrates in contact with inoculated medium (with bacteria) were taken as negative control; that corresponds to 100% growth of bacteria. The uncoated glass substrates immersed into free of bacteria medium were taken as blank. To calculate the normalized planktonic growth (%), following equation was used:

$$\text{Normalized Growth (\%)} = \frac{OD_{600}(\text{film with bacteria}) - OD_{600}(\text{film without bacteria})}{OD_{600}\,(\text{uncoated glass coverslips with bacteria}) - OD_{600}(\text{film without bacteria})} \times 100$$

#### *5.2.7.6.* ***Biofilm Assays***

The formation of *S. aureus* biofilm was evaluated on CNC-ending oriented and non-oriented film samples in comparison to the uncoated glass substrate, as control. *S. aureus* was precultured aerobically overnight in MH medium at 37 °C in an agitator. The bacteria pre-culture was centrifuged at 3000 rpm for 20 min. The supernatant was replaced with fresh medium, and the final optical density was adjusted to $OD_{600}$=0.01 in RPMI medium. The samples were incubated with 1 mL of the bacteria inoculation at 37°C in an incubator without agitation. After 48 h of incubation, 100 µL of the supernatant was taken to measure the absorbance ($OD_{600}$). The samples were carefully rinsed three times with 1 mL of PBS in a dilution manner to avoid the creation of sample surface-air interface to prevent damage to the biofilm.

The biofilm biomass was quantified by staining with Safranin (5 mg/mL in water, B21674, Alfa Aesar). To that aim, the samples were incubated with 500 µL of methanol (99%) at room temperature. After 15 min, methanol was discarded safely, and the samples were air dried. Then, the samples were incubated with 500 µL of safranin solution for 20 min at room temperature, followed by extensive rinsing with ultrapure water by using a disposable pipette. The adsorbed safranin was resolubilized by immersing the samples in 500 µL of aqueous acetic solution (33% by vol) for at least 30 min at room temperature. 100 µL of the supernatants were taken to measure the absorbance at 540 nm. The biofilm was also observed by confocal microscopy using CTC/SYTO®-24 labelling. The biofilm quantification was performed on eight samples divided in two individual experiments.

### 5.2.8. Fibroblast Viability Assays

Non-oriented CNC-ending films and oriented CNC based films ending with $Fe^{3+}$, TA, TA/ $Fe^{3+}$, CNC, prepared on 1×1 $cm^2$ glass slides, were tested towards fibroblasts from murine (NIH3T3) regarding the adhesion and proliferation. The fibroblast cells were seeded on top of the multilayer substrates at a cell density of $5\times10^4$ cells per mL and maintained at 37°C with 5% $CO_2$ in High Glucose DMEM medium supplemented with 10% decomplemented Fetal Bovine Serum (FBS), 1% Penicillin/Streptomycin for cell adhesion and proliferation assays.

#### *5.2.8.1.* ***Cell Adhesion Assay***

*In vitro* cytotoxicity of the oriented and non-oriented LbL films was assessed via an acidic phosphatase assay on NIH3T3 cell line. After an incubation time of 4 h, the films were washed twice with 1 mL of PBS. Then, 500 µl of 100 mM sodium acetate (NaOAC) solution containing 1% triton X-100 and 0.5 mg/mL of p-Nitrophenyl phosphate (pNPP) was dispensed on the

samples and incubated at 37°C with 5% CO2 for 1 h. Then, 10 µl of 1 M NaOH was added to stop the reaction between the phosphatases and pNPP and to deprotonate the p-nitrophenol, the product of the reaction, to give yellow colored p-nitrophenolate. To evaluate the amount of p-nitrophenolate, 100 µL of the reaction media in each well was transferred to a 96 well plate. The absorbance at 405 nm was recorded with spectrofluorometer (SAFAS Xenius XC). The uncoated glass slides and TCPS were used as controls.

#### *5.2.8.2.* ***Cell Proliferation Assay***

*In vitro* cell proliferation on the oriented and non-oriented LbL films was evaluated by incubating with NIH3T3 cells. After an initial incubation time of 4 h the cell solutions were discarded, followed by two rinsing steps using 1 mL of PBS. Then, the samples were incubated with 1 mL of the supplemented DMEM medium without cell for the second incubation of 18 h. After 18 h of proliferation, the samples were rinsed twice with 1 mL of PBS, followed by a fixation step using 500 µL of 4% paraformaldehyde solution in PBS for 15 min at room temperature. After thoroughly rinsing with PBS, the cells were permeabilized with 500 µL of 0.1% (v/v) Triton X-100 (BP151, Fischer Scientific) for 15 min in PBS, and finally stained with 500 µL of Alexa Fluor 568 conjugated-Phalloidin (Invitrogen A12380, 1/400) for 30 min in PBS at room temperature. Nuclei were counterstained with Hoechst 33342 (Invitrogen, B2261, 5 µg/mL) in PBS for 10 min.-Stained cells were then mounted and imaged by confocal microscopy (Zeiss LSM-710, ×60).

### 5.2.9. AFM imaging, force measurement & analysis

AFM force measurements were performed in Peak Force QNM mode or contact mode in liquid using a Bruker Dimension ICON AFM. Negatively charged AFM probes were prepared by

immersing the AC-40 AFM probes (spring constant ~0.1 N/m, tip radius ~10 nm; Bruker, CA, USA) in 14 mL of ethanol containing 12-Mercaptododecylphosphonic acid ($HS-(CH_2)_{13}-PO(OH)_2$) for 24 h, rinsed with ethanol and air-dried in a chemical hood. The modified AFM probe spring constant was calibrated before the force measurement experiment by measuring the thermal noise of the free cantilever in liquid.[75] Over 500 force-distance (F-D) curves were recorded with at least three separate combinations of probe/bacteria samples. All F-D curve measurements between modified probes and characterized surfaces were collected in liquid conditions with PBS (without metallic salt). The control experiments were carried out under the same conditions. Data analysis was performed with the Bruker Nanoscope Analysis software.

#### 5.2.10. Statistical analysis:

The two-tail student t-test was performed on all microbiology experimental data to determine the statistical significance of differences between the oriented and the non-oriented multilayer films with uncoated glass substrates (control). The obtained *p-value*s are indicated on the corresponding graphs with symbols such as *, **, ***, and **** for $p \leq 0.05$, 0.01, 0.001, and 0.0001, respectively.

## 5.3. Results and Discussion

### 5.3.1. Characterization of CNC

CNCs were characterized using Dynamic Light Scattering (DLS) and Atomic Force Microscopy (AFM). The developed CNCs showed strong cationic character with zeta potential of +48.3 mV. The size of anisotropic elongated nanostructured CNCs **(Figure 5.3a)** is found to be

approximately 116 nm calculated using DLS measurements **(Figure 5.3b)** which is confirmed by AFM with 116.2 ± 8.4 nm.

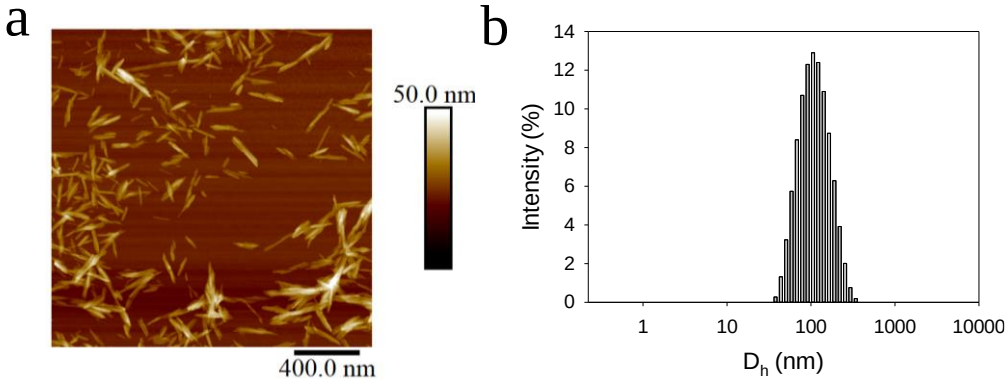


***Figure 5.3: (a)*** *Typical AFM topography image of chitin nanocrystals drop casted on a silicon wafer, rinsed with water and air dried.* ***(b)*** *Dynamic light scattering (DLS) measurement showing the intensity of the hydrodynamic diameter of CNC solution (0.09% w/v).*

### 5.3.2. Buildup and topography of CNC/TA LbL films

Herein, we report the development of CNC-based LbL films using the dipping and brushing methods, both with 10 s contact with the compounds at each deposition step. The buildup method should dramatically influence the orientation of the deposited CNC layers which is expected due to the shearing effect of brushing deposition method.[27] In the first experiments, the buildup of CNC with $Fe^{3+}$ or TA as sole partner was not possible by the brushing method. Indeed, the film thicknesses did not increase after 1 or 2 deposited layers (data not shown). As CNC and TA are both known to interact with $Fe^{3+}$, the deposition of (TA/$Fe^{3+}$/CNC/$Fe^{3+}$) quadrilayer was performed by the brushing and dipping methods, to obtain oriented and non-oriented CNC/TA films, respectively. The thickness of oriented CNC/TA films increased linearly as a function of the last deposition step reaching up to 24.8 ± 0.8 nm after 8 quadrilayers **(Figure 5.4a).** Non-oriented CNC/TA films showed an irregular growth reaching 121.3 ± 2.8 nm

after 8 quadrilayers (*i.e.* $(TA/Fe^{3+}/CNC/Fe^{3+})_8$). The dipping method induced a significant increase of the thickness at each CNC deposition reaching a plateau after 7 quadrilayers. Highly anisotropic nanostructures are known to show slightly different refractive index values in a direction parallel or perpendicular to their long axis.[76] To confirm the results obtained by ellipsometry, the thickness of oriented $(TA/Fe^{3+}/CNC/Fe^{3+})_7$-$TA/Fe^{3+}$/CNC film was determined by AFM using the cross-section of scratched films **(Figure 5.4b)**. It was defined as the minimal z distance between the bare substrate and the surface of the film that covers the whole substrate. The film thickness was measured at 23.1 ± 2.7 nm in agreement with the value obtained by ellipsometry **(Figure 5.4c)**. In comparison, chitosan/alginate-micelles LbL films followed a similar linear buildup with comparable thicknesses when obtained by the brushing or dipping methods.[26] The reduced amount of suspension in contact combined with a high shearing effect of the brushing method leads probably to less deposition of the nanostructured components (CNC) in comparison to the dipping method.[77] Both oriented and non-oriented CNC/TA films were stable in contact with PBS for 1 h with no significant loss of dry thickness **(Figure 5.4a)**. The CNC/TA films were then imaged using AFM to investigate the topography and characterize the degree of orientation of the nanocrystals using OrientationJ, an ImageJ plug-in that allows pixel-based characterization of the orientation (**Figure 5.4c-h)**. This software allows visualizing the general direction of orientation (main color) and the degree of alignment of the AFM images. Each pixel is color-coded according to the alignment direction.

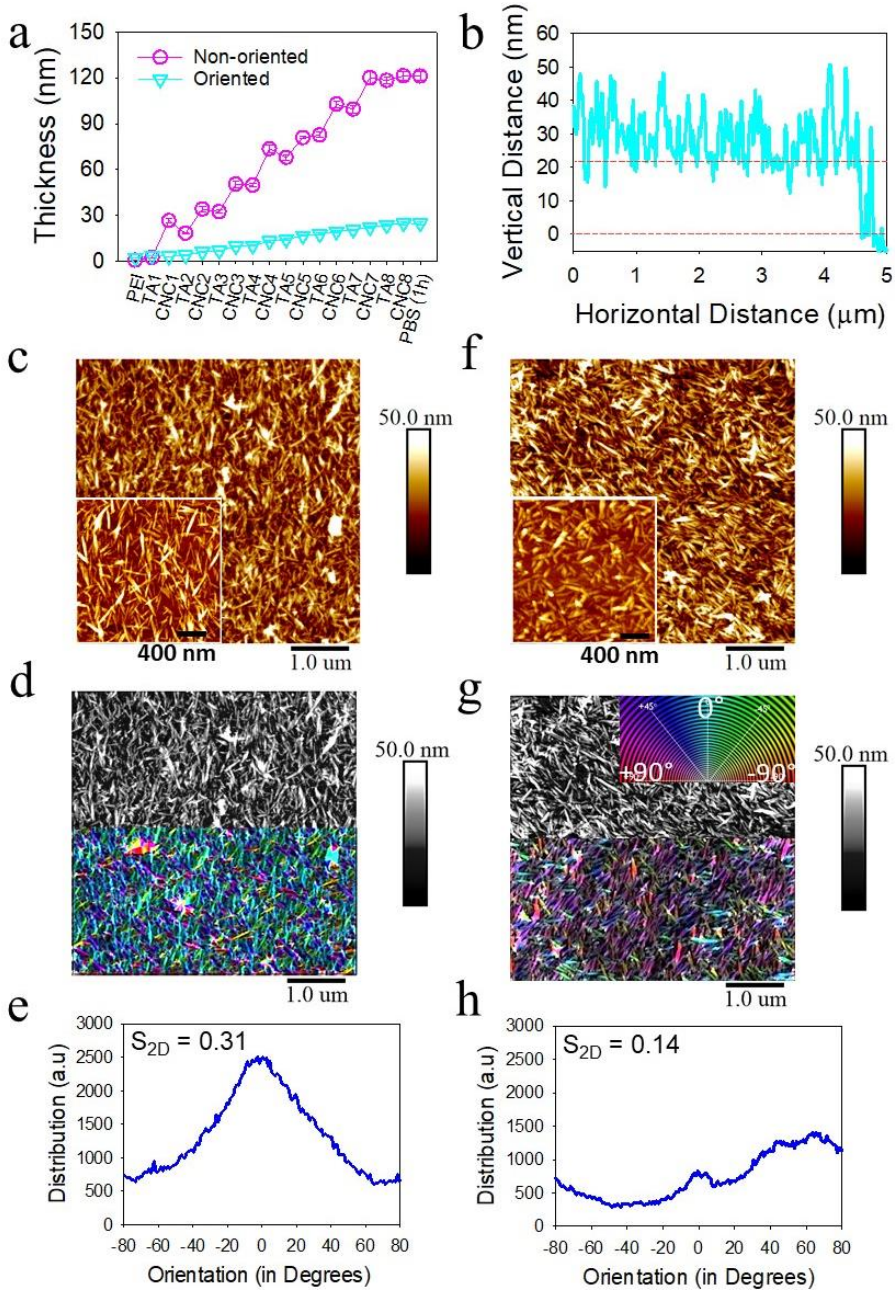


***Figure 5.4:*** *Characterization of CNC/TA films* ***(a)*** *Evolution of the thickness, determined by ellipsometry, as a function of the last deposited layer of the oriented (turquoise triangles) and the non-oriented (pink circles) films. The film thickness was also measured after 1h contact with PBS. For sake of clarity, the incremental thickness of $Fe^{3+}$ is not reported as it was less than 1 nm. AFM characterization of $(TA/Fe^{3+}/CNC/Fe^{3+})_7$-$TA/Fe^{3+}/CNC$ films, in dry state,* ***(b)*** *typical 3D cross-section profile after scratching of the oriented film and* ***(c-i)*** *typical AFM topography images, with the black and white version image (top) and the colorized output (bottom), and orientation distribution, with the order parameter $S_{2D}$, of* ***(c, d, e)*** *the oriented and* ***(f, g, h)*** *the non-oriented CNC films, obtained by OrientationJ.*

The oriented CNC/TA films showed a preferential orientation of the nanocrystals in the direction of brushing, adjusted to 0° (vertical) in the images (**Figure 5.4c-d**), which is confirmed by the orientation distribution following a Gaussian curve with the maximum at 0° **(Figure 5.4e)**. In comparison, non-oriented CNC films showed a random distribution of CNC (**Figure 5.4f-h**). To evaluate whether the ending layer impacts the orientation of the nanocrystals, the following oriented CNC/TA films were characterized by AFM: CNC/$Fe^{3+}$-ending film (*i.e.* $(TA/Fe^{3+}/CNC/Fe^{3+})_8$), TA-ending film (*i.e.* $(TA/Fe^{3+}/CNC/Fe^{3+})_7$-TA), oriented TA/$Fe^{3+}$-ending film (*i.e.* $(TA/Fe^{3+}/CNC/Fe^{3+})_7$-TA/$Fe^{3+}$) (**Figure 5.5**) in comparison to CNC-ending film (*i.e.* $(TA/Fe^{3+}/CNC/Fe^{3+})_7$-TA/$Fe^{3+}$/CNC) **(Figure 5.4d-f)**.

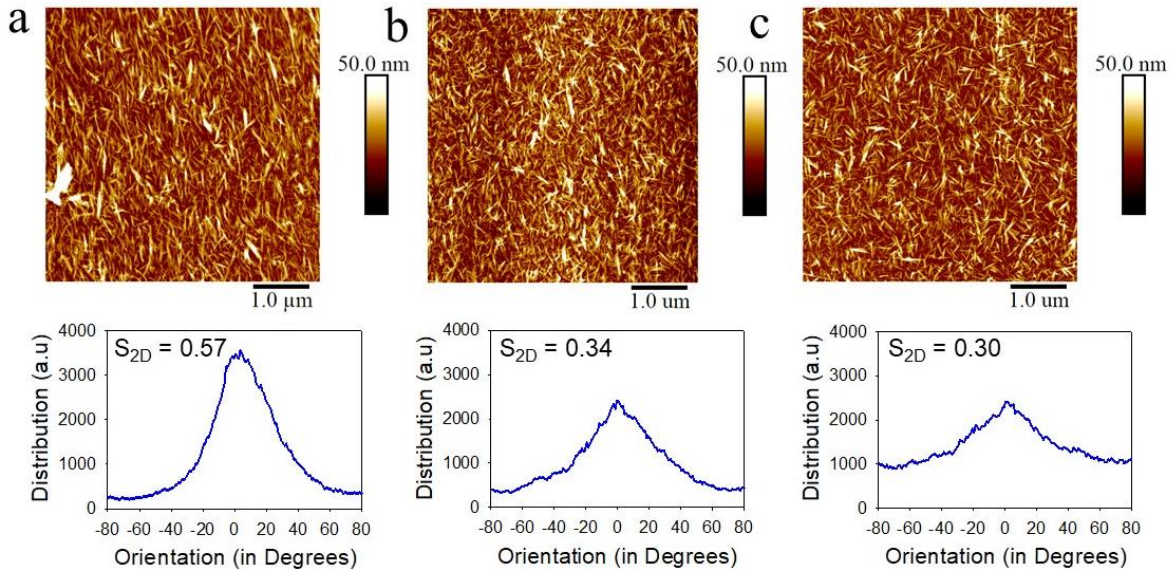


***Figure 5.5:*** *Typical 2D AFM images of the oriented CNC/TA films* ***(a)*** *TA-ending film,* ***(b)*** *TA/$Fe^{3+}$-ending film,* ***(c)*** *CNC/$Fe^{3+}$-ending film and orientation distribution, obtained by OrientationJ. The slight deviation of the peak from 0° comes from the AFM experimental setup, where film samples are manually placed approximately perpendicular to scan axis.*

The orientation of the films was evaluated also by calculating the order parameter ($S_{2D}$), defined as the angular change in the unidirectionality of oriented nanocrystals, calculated using the following:

$$S_{2D} = 2\cos\theta^2 - 1$$

with "θ" the angle between CNC main axis and the vertical direction (0°), *i.e.*, the brushing direction. The $S_{2D}$ value changes from zero (random isotropic distribution) to 1 (perfect orientation).

The ending layer has a small effect on the orientation of the oriented CNC/TA films with $S_{2D}$ values of 0.31, 0.57, 0.34, and 0.30 for oriented CNC-ending, TA-ending, TA/$Fe^{3+}$-ending, and CNC/$Fe^{3+}$-ending films, respectively. In comparison, the non-oriented CNC/TA films showed the order parameter of 0.14.

### 5.3.3. Antibacterial activity of CNC-ending CNC/TA films

The antibacterial activity of the oriented and the non-oriented CNC/TA films ended by CNC was analyzed towards *S. aureus* and *E. coli* to evaluate bacteria adhesion, proliferation, and biofilm formation. *S. aureus*, a Gram-positive pathogen, is known to cause nosocomial and device related infections[78] and is the most common reason in osteomyelitis which is a bone infection that causes pain, redness, weakness, fever etc..[79] *E. coli*, a gram-negative pathogen, is the most frequent reason for catheter associated infections.[80] The experiments were conducted in static conditions to allow maximum settling or contact of bacteria on the substrates under gravity.

#### *5.3.3.1.* ***Bacterial adhesion***

After 1.5 h of bacterial incubation with the CNC/TA films, PI/SYTO®-9 Live/Dead staining was performed to evaluate the antiadhesive property of the films using confocal microscopy (**Figure 5.6a-d**). The SYTO®-9 staining (in green) corresponds to alive bacteria and the propidium iodide (PI) staining (in red) represents the damaged bacteria. A clear difference can be observed in the confocal optical microscopy images where less *S. aureus* bacteria are observed in both channels on the oriented CNC-ending CNC/TA films in comparison to the non-oriented films and the uncoated glass control (**Figure 5.6a-c**).

The oriented CNC-ending CNC/TA films showed a strong anti-adhesive property with approximately 86% reduction of the alive adhered bacteria number (SYTO®-9 green staining) in comparison to the uncoated glass control (with *p-value* $\leq$ 0.0001) **(Figure 5.6d).** *S. aureus* adhesion is also significantly reduced about 43% on the non-oriented CNC-ending films vs the uncoated glass (with *p-value* $\leq$ 0.01). The orientation of CNC showed a strong difference in the antiadhesive property of CNC/TA films. The vitality of bacteria was evaluated by calculating the ratio of the number of damaged bacteria (PI red staining) and all bacteria (SYTO®-9 green staining+ PI red staining), 46% of attached bacteria are damaged on the oriented CNC/TA films whereas only 26% on the non-oriented CNC/TA films. The control uncoated glass showed 16% of damaged bacteria. A strong contact killing property of the oriented CNC ending CNC/TA films is observed after 1.5 h of contact. Regarding the planktonic state, there is no effect on the bacterial growth in the supernatant in contact with CNC/TA films **(Figure 5.6e)**. The contact killing effect is localized on the surface and did not prevent the growth in the supernatant.

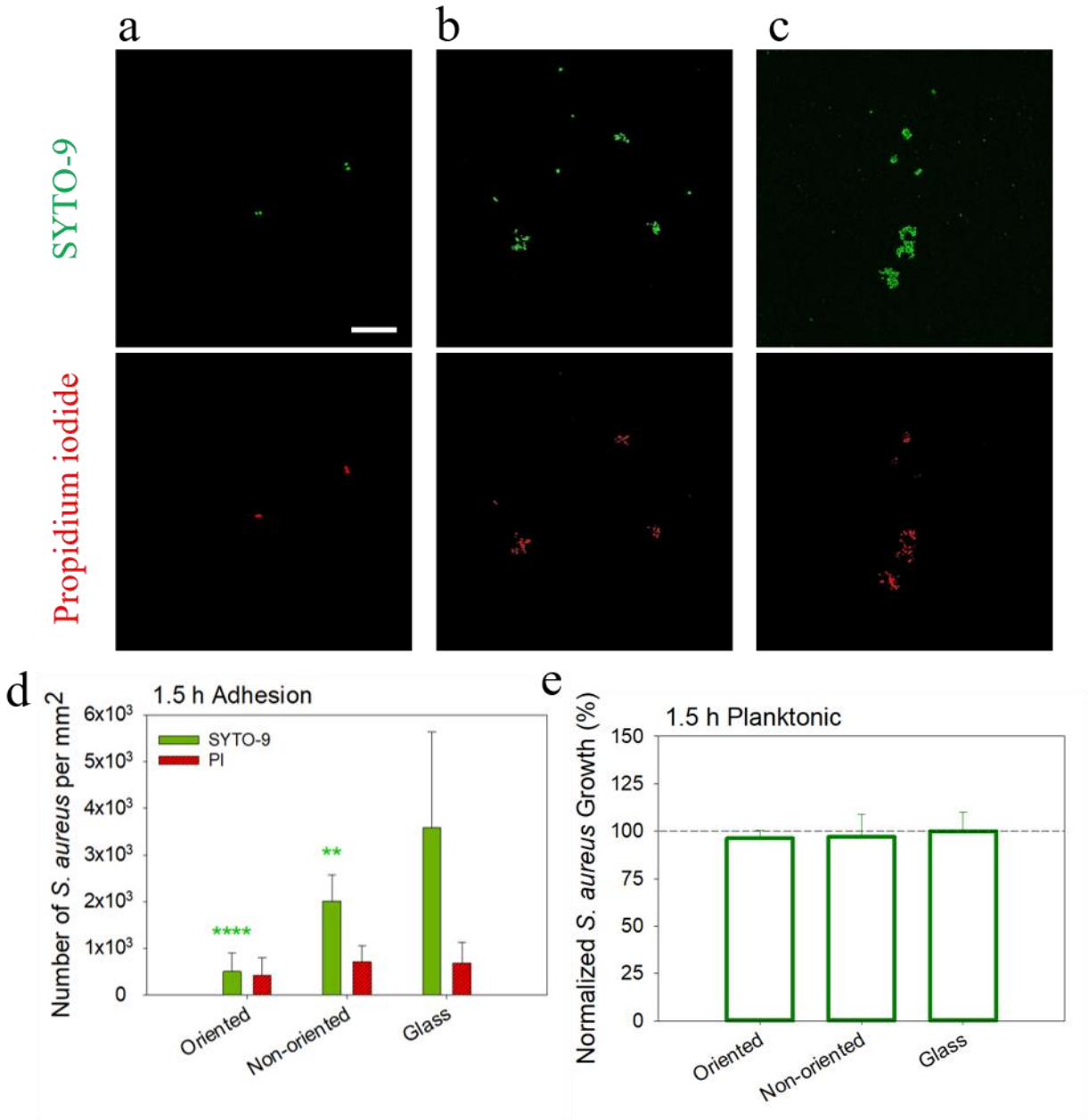


***Figure 5.6:*** *Bacterial adhesion of S. aureus on CNC ending CNC/TA films after 1.5 h incubation at 37°C under static condition.* ***(a-c)*** *Typical confocal microscopy images, in green and red channels, of* ***(a)*** *oriented and* ***(b)*** *non-oriented CNC/TA films and* ***(c)*** *uncoated glass (control) with* ***(d)*** *the corresponding number of bacteria adhered per mm² and* ***(e)*** *bacteria growth in planktonic state. The SYTO®-9/PI LIVE/DEAD assay was used to stain the alive bacteria in green (SYTO®-9) and damaged ones in red (PI). Scale bar: 20 µm. The number of bacteria per mm² were determined from three different images of the 1×1 cm² film taken on at least seven samples (21 images in total) with the significance level in t-test of SYTO®-9 staining in comparison to the uncoated glass ** $p \leq 0.01$ and **** $p \leq 0.0001$.*

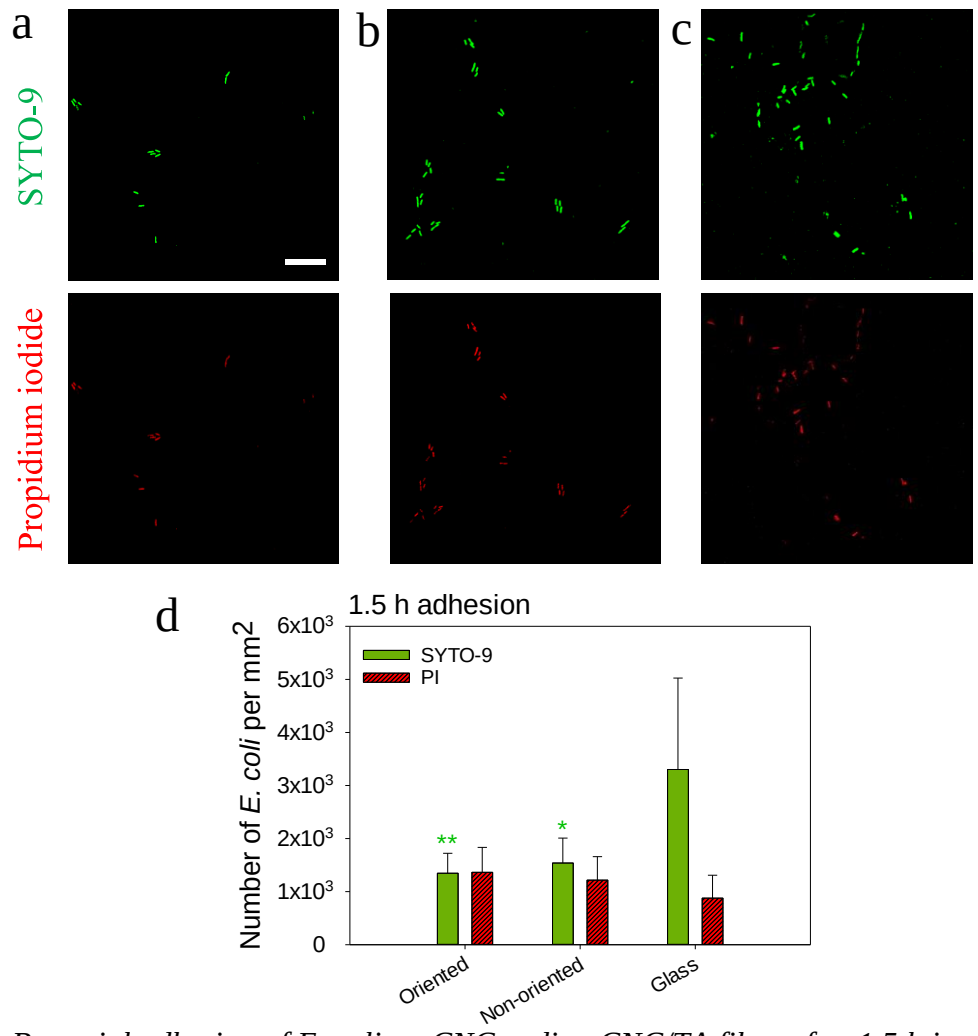


***Figure 5.7:*** *Bacterial adhesion of E. coli on CNC ending CNC/TA films after 1.5 h incubation at 37°C under static condition.* ***(a-c)*** *Typical confocal microscopy images, in green and red channels, of* ***(a)*** *oriented and* ***(b)*** *non-oriented CNC/TA films and* ***(c)*** *uncoated glass (control) with* ***(d)*** *the corresponding number of bacteria adhered per mm². The SYTO®-9/PI LIVE/DEAD assay was used to stain the alive bacteria in green (SYTO®-9) and damaged ones in red (PI). Scale bar: 20 µm. The number of bacteria per mm² are determined from three different images of the 1×1 cm² film taken on at least seven samples (21 images in total) with the significance level in t-test of SYTO-9 staining in comparison to the uncoated glass ** $p \leq 0.01$ and * $p \leq 0.1$.*

The same study was performed on *E. coli* to evaluate the antiadhesive and contact-killing effect of CNC/TA films (**Figure 5.7**). *E. coli* adhesion is also decreased at about 41% (with *p-value* ≤

0.01) and 46% (with *p-value* ≤ 0.1) on the oriented and non-oriented CNC/TA films with respect to uncoated glass. The viability of *E. coli* is dramatically reduced with 50% and 44% of damaged bacteria on the oriented and non-oriented CNC-ending CNC/TA films. For comparison, 20% of damaged bacteria are found on the uncoated glass. Thus after 1.5 h of incubation, the oriented CNC-ending surfaces exhibit both antiadhesive and contact killing property on *S. aureus* and *E. coli*. Regarding the planktonic state, there is no effect on the bacterial growth in the supernatant in contact with CNC/TA films (data not shown).

#### *5.3.3.2.* ***Bacterial proliferation***

To evaluate the bacterial proliferation, the adhered bacteria were allowed to proliferate for 24 h under the harsh non-agitated conditions. After 1.5 h of initial incubation, the bacterial supernatant was replaced by fresh culture medium and incubated for 24 h at 37°C. The confocal microscopy images of *S. aureus* after Live/Dead staining showed a dramatic effect of CNC orientation on the number of bacteria observed on the samples on both channels (**Figure 5.8a)**. Indeed, on the contrary to non-oriented CNC-ending CNC/TA films and uncoated glass substrate, only few alive and dead bacteria were visible on the oriented CNC-ending CNC/TA films.

The oriented CNC-ending CNC/TA films decreased by almost 2-log (98.6%) the number of alive bacteria (SYTO®-9 green staining) in comparison the uncoated glass control (with *p-value* ≤ 0.0001) (**Figure 5.8b)**. Moreover, the viability of the adhered *S. aureus* is critically compromised with approximately 48% of damaged bacteria on the oriented CNC-ending films. Hence, longer incubation time on the oriented CNC-ending films led to an efficient contact killing effect besides a drastic decrease of the bacterial proliferation. The non-oriented CNC/TA films showed

a similar proliferation as the uncoated glass with a similar percentage of damaged bacteria 10.7% and 8.2 %, respectively.

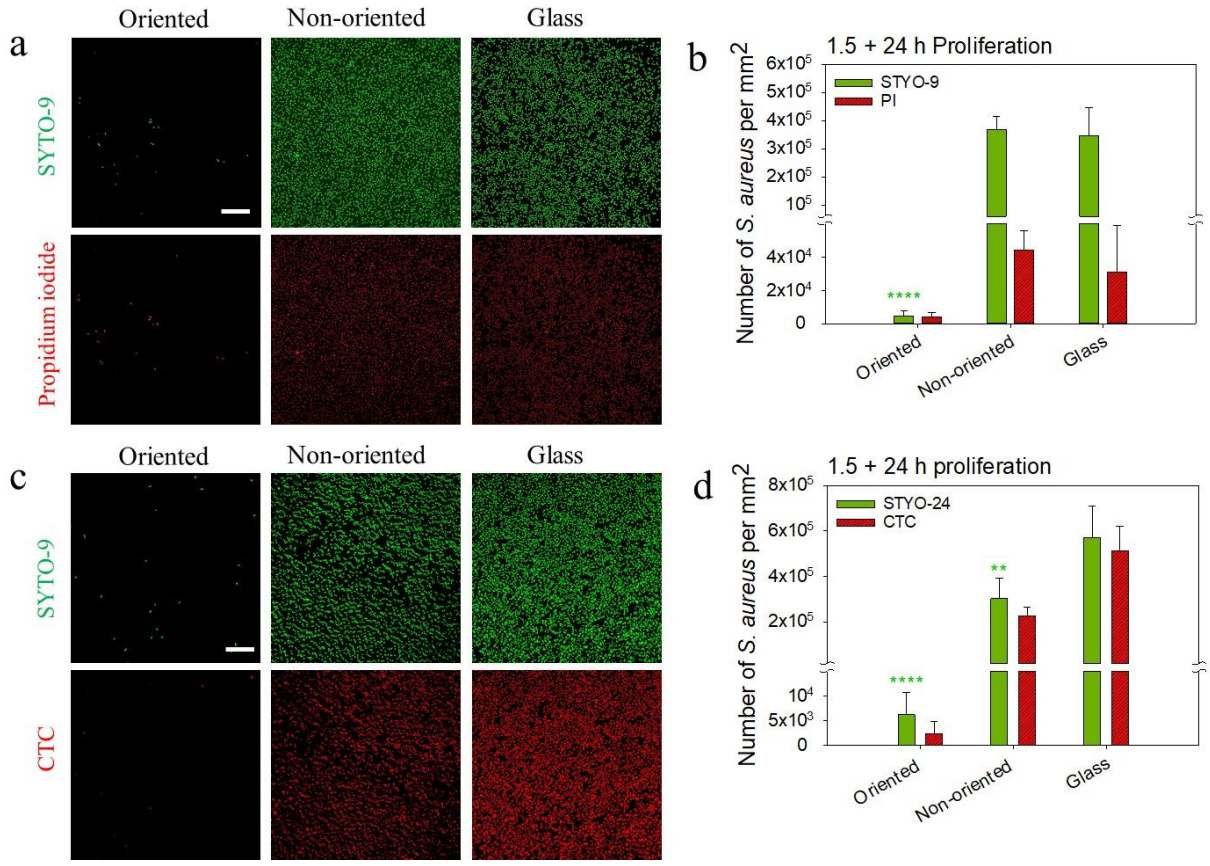


***Figure 5.8:*** *Bacterial proliferation of S. aureus on CNC ending CNC/TA films after 24 h incubation of the adhered bacteria at 37°C under static condition.* ***(a, b)*** *SYTO®-9/PI (LIVE/DEAD) assay was used to stain alive bacteria in green (SYTO®-9) and damaged ones in red (PI) and* ***(c, d)*** *SYTO®-24/CTC assay to stain all bacteria in green (SYTO®-24) and active ones in red (CTC).* ***(a, c)*** *Typical confocal microscopy images in green and red channels (Scale bar: 20 µm).* ***(b, d)*** *Number of bacteria per mm$^2$ determined from three different images of the 1×1 cm² film taken on at least seven samples (21 images in total) with the significance level in t-test of SYTO®-9 or SYTO®-24 staining in comparison to the uncoated glass ** $p \leq 0.01$ and **** $p \leq 0.0001$.*

To differentiate between metabolically inactive and damaged bacteria, the bacteria metabolic activity was also determined with SYTO®-24/CTC Live/dead assay staining all bacteria in green

(SYTO®-24) and viable ones with respiratory activity in red (CTC) (**Figure 5.8c-d**). Only 38% of *S. aureus* attached on CNC-ending oriented CNC/TA films exhibited a metabolic activity. The SYTO-9/PI staining showed 52% of not-damaged bacteria. Such observation is not a surprise as PI is found to slightly miscalculate the viability of attached bacteria.[81] Some metabolically active bacteria might have compromised membranes allowing PI to diffuse. Non-oriented CNC/TA films and glass substrate have 74% and 90% of attached bacteria that are metabolically active. SEM images allowed to address the integrity of the bacteria membranes **(Figure 5.9)**. Very few bacteria were attached on the oriented CNC-ending films, all with severely damaged membranes. On the contrary, a great number of healthy bacteria were observed on non-oriented CNC and uncoated glass.

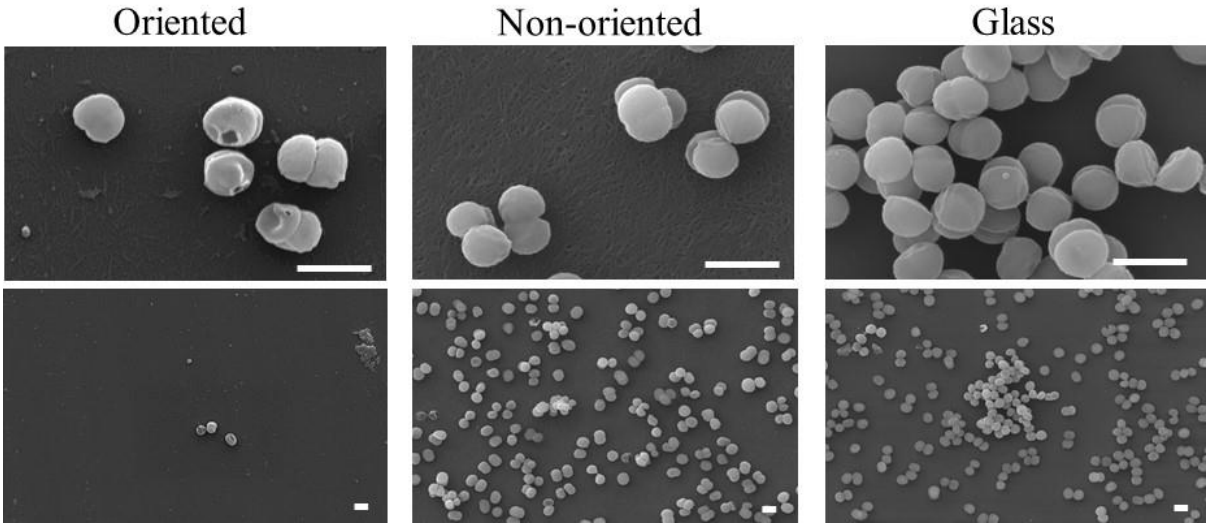


***Figure 5.9:*** *Morphology of S. aureus after proliferation, observed by SEM, on the oriented and the non-oriented CNC-ending CNC/TA films and uncoated glass substrate (Scale bar: 1 µm). Each image is a representative of images taken out on random locations on 1×1 cm² samples in duplicates from two individual experiments.*

The proliferation test was also performed on *E. coli* to evaluate the antiadhesive and contact-killing effect of the CNC-ending CNC/TA films (**Figure 5.10**).

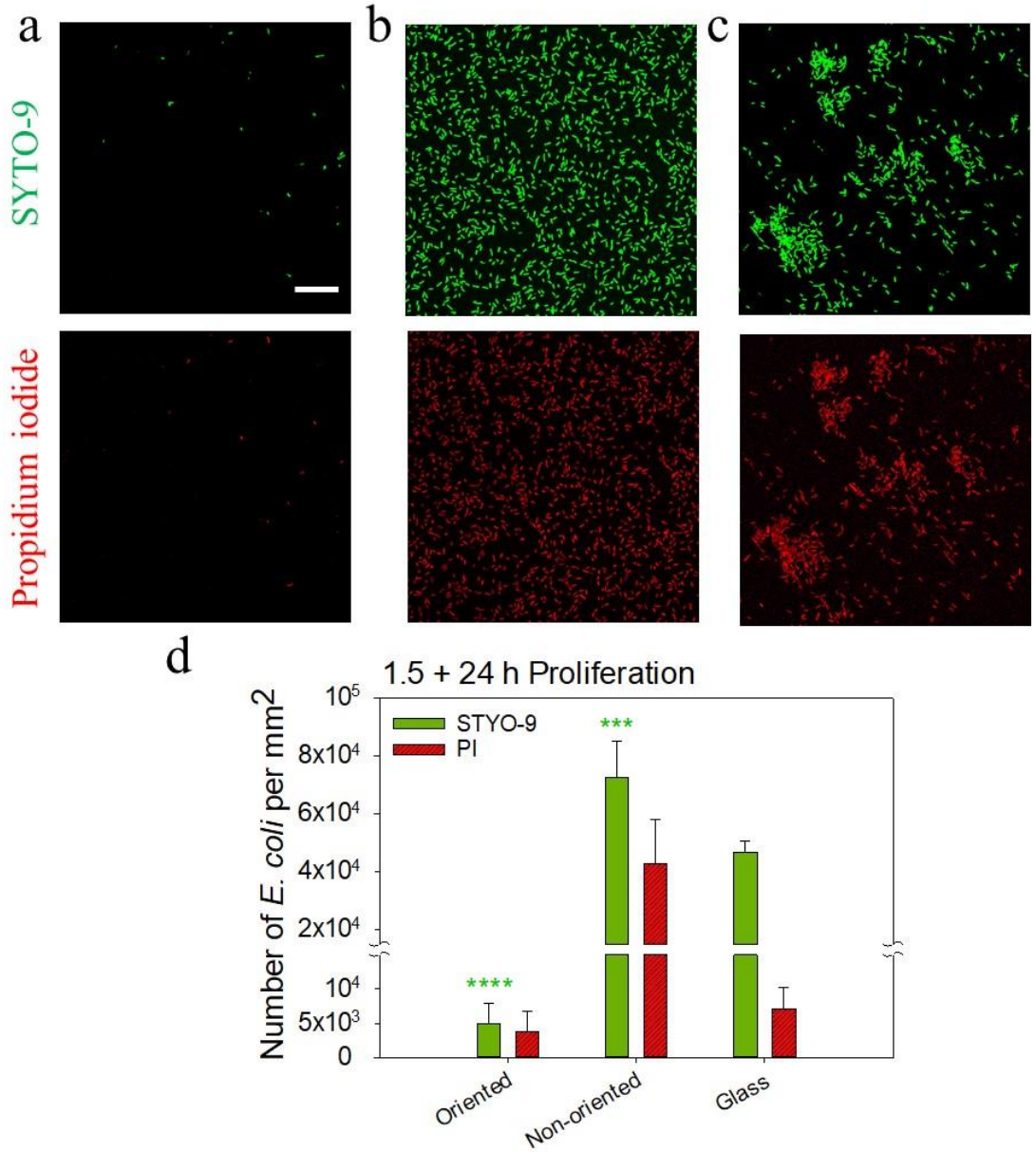


***Figure 5.10:*** *Bacterial proliferation of E. coli on CNC ending CNC/TA films after 1.5 h incubation at 37°C under static condition.* ***(a-c)*** *Typical confocal microscopy images, in green and red channels, of* ***(a)*** *the oriented and* ***(b)*** *the non-oriented CNC/TA films and* ***(c)*** *uncoated glass (control) with* ***(d)*** *the corresponding number of bacteria present per mm². The SYTO®-9/PI LIVE/DEAD assay was used to stain the alive bacteria in green (SYTO®-9) and damaged ones in red (PI). Scale bar: 20 µm. The number of bacteria per mm² are determined from three different images of the 1×1 cm² film taken on at least seven samples (20 images in total) with the significance level in t-test of SYTO®-9 staining in comparison to the uncoated glass *** $p \leq 0.001$ and **** $p \leq 0.0001$.*

Confocal microscopy images confirmed the anti-adhesive effect of CNC orientation with only few bacteria visible (**Figure 5.10a**). In comparison to the uncoated glass, the oriented CNC-ending films showed 90% decrease in number of adhered *E. coli* (with *p-value* ≤ 0.0001) with 44% of damaged ones (**Figure 5.10a and c**). Non-oriented CNC ending CNC/TA films showed an increase of the number of *E. coli* in comparison to the uncoated glass (with *p-value* ≤ 0.001) with however a contact-killing effect with 37% of damaged *E. coli* compared to 13% for the uncoated glass. Regarding the planktonic state, there is no effect on the bacterial growth in the supernatant in contact with TA/CNC films (data not shown).

#### *5.3.3.3.* ***Formation of S. aureus biofilm***

To investigate long-term surface activity in contact with bacteria, biofilm assays were performed by both qualitative and quantitative methods. To that aim, the surfaces were incubated with *S. aureus* at elevated optical density (OD) values for 48 h in non-agitated conditions at 37°C. Qualitatively, the samples were stained by STYO-24®/CTC staining to probe all bacteria and metabolically active ones which clearly shows the presence of only few bacteria on oriented CNC-ending CNC/TA films (**Figure 5.11a**). The anti-adhesive property of the oriented film is maintained even in harsh conditions of higher initial bacterial density.

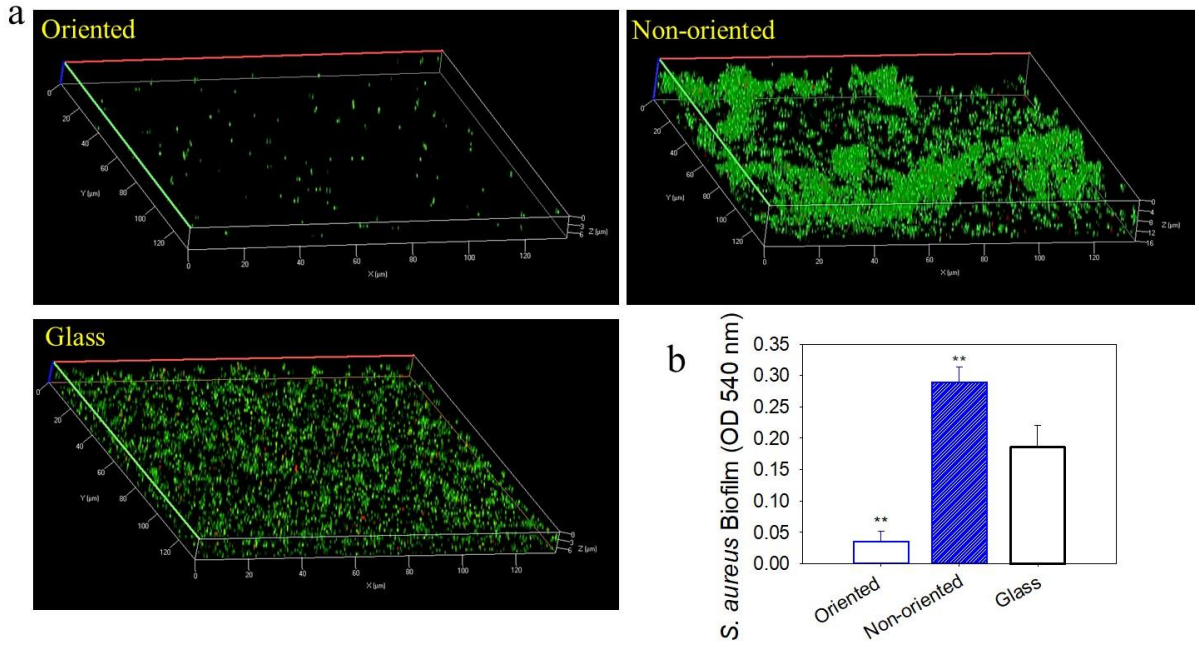


***Figure 5.11:*** *Formation of S. aureus biofilm on the CNC-ending CNC/TA films and uncoated glass after 48 h of incubation at 37 °C without agitation.* ***(a)*** *Typical 3D confocal microscopy images of the biofilm after STYO-24®/CTC staining of all bacteria in green (SYTO®-24) and active ones in red (CTC). (Image size: 130 µm²) The images are representative of three different images of the 1×1 cm² film taken randomly on eight samples (24 images in total).* ***(b)*** *Biofilm biomass quantification obtained by Safranin staining with the significance level in t-test in comparison to the uncoated glass ** $p \leq 0.01$. The experiment was repeated twice with four samples each.*

Furthermore, the biofilm biomass was quantitatively determined by using Safranin staining **(Figure 5.11b)**. Similarly, the biomass formation on the oriented CNC-ending films is 81 % lower than the one obtained on the uncoated glass control (with *p-value* $\leq 0.01$). Non-oriented CNC films appeared to promote the biofilm formation in comparison to uncoated glass (with *p-value* $\leq 0.01$). Conclusively, oriented CNC-ending CNC/TA films exhibit both antiadhesive and contact killing properties on *S. aureus* and *E. coli*. Moreover, this film prevents the formation of *S. aureus* biofilm.

### 5.3.4. Influence of the ending layer on the antibacterial activity of oriented CNC/TA films

The influence of the ending layer of the oriented CNC/TA films was then evaluated regarding the proliferation of *S. aureus*. Despite a similar nanotopography **(Figure 5.5)** the nature of the ending layer is of a paramount importance towards bacterial proliferation and viability. Indeed, oriented CNC/$Fe^{3+}$-, TA- and TA/$Fe^{3+}$-ending CNC/TA films showed a weaker antiadhesive effect with more adhered bacteria in comparison to CNC-ending films **(Figure 5.12 and Figure 5.6).** The quantitative data showed a similar number of not-damaged bacteria for CNC/$Fe^{3+}$, TA and TA/$Fe^{3+}$-ending films, around $2 \times 10^5$ bacteria per $mm^2$, which is statistically lower than the number of bacteria on the uncoated glass (with *p-value* $\leq 0.0001$) but not as low as CNC-ending films at $5 \times 10^3$. More interestingly, the percentage of damaged bacteria (PI vs SYTO®-9+PI staining) is of only around 10% for other ending films (similar to uncoated glass) in comparison to the high efficiency of CNC-ending films (48%). The good proliferation of *S. aureus* on CNC/$Fe^{3+}$ and TA/$Fe^{3+}$ -ending films can be explained by the fact that iron is a nutrient for bacteria.[82] TA possesses a strong antibacterial property towards *S. aureus* in solution[83] and upon efficient release from LbL films.[84] However, TA is strongly bound on TA-ending films rendering its antibacterial activity ineffective.[85] Only antifungal properties were reported for TA/$Fe^{3+}$ LbL films without TA release.[86]

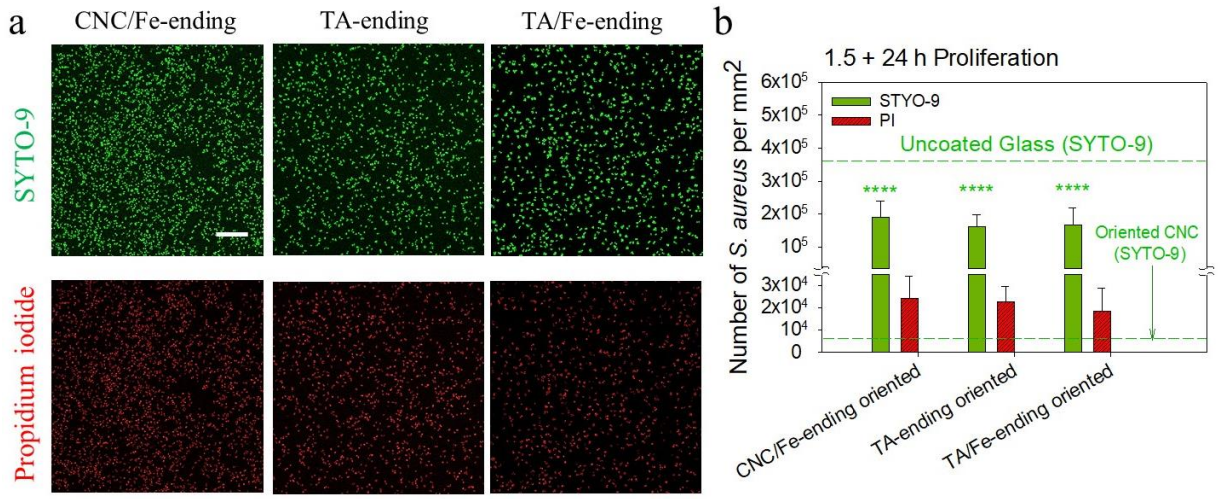


***Figure 5.12:*** *Bacterial proliferation of S. aureus on the oriented CNC/TA films with different ending layers after 24 h incubation of adhered bacteria at 37°C under static condition. SYTO®-9/PI LIVE/DEAD assay was applied to stain alive bacteria in green (SYTO®-9) and damaged ones in red (PI).* ***(a)*** *Typical confocal microscopy images in green and red channels (Scale bar: 20 µm).* ***(b)*** *Number of bacteria per mm$^2$ determined from three different images of the 1×1 cm² film taken randomly on at least seven samples (21 images in total) with the significance level in t-test of SYTO®-9 staining in comparison to the uncoated glass **** $p \leq 0.0001$. The values obtained in SYTO®-9 staining for the uncoated glass and the oriented CNC-ending CNC/TA films are represented by two dashed green lines.*

The nature of the ending layer of the oriented CNC/TA films is thus a crucial factor to obtain an efficient antibacterial activity against *S. aureus* colonization both by preventing the adhesion and by contact killing. The mode of action remains unclear as the research on antibacterial properties of chitin is particularly limited. Chitin nanowhiskers/starch blend membranes were reported to be only bacteriostatic against *L. monocytogenes* (Gram-positive) but not against *E. coli* (Gram-negative).[87] The antifungal activity of α-chitin nanofibers towards *Aspergillus Niger* was attributed to their small compact size and high surface area/charge ratio.[52] Finally, the antibacterial chitin based materials were mostly obtained by incorporating TA[58, 88] or blending with chitosan.[56,53, 89] On the contrary, chitosan (CHI), its deacetylated counterpart, has been

extensively reported as an antibacterial material component.[50-51] The exact mechanism of antibacterial activity is yet to be fully understood with the influence of several factors. The proposed antibacterial activity of chitosan is by binding to the negatively charged bacterial cell wall, altering the membrane permeability, followed by attachment to DNA causing inhibition of DNA replication and subsequently cell death.[90] Another proposed mechanism is the chelation of trace metal elements by chitosan causing toxin production and inhibiting microbial growth.[91]

### 5.3.5. Influence of the film composition on the antibacterial activity

A part from the ending layer, it has been reported that the antibacterial properties of LbL films are strongly dependent not only on the buildup conditions or post-buildup treatments[25] but also on the polycation/polyanion couple.[92] To gain more insight on the mechanism of action of oriented CNC-ending CNC/TA films, the antibacterial activity of other LbL films with different chemical compositions were tested against *S. aureus* by replacing TA/$Fe^{3+}$ by Hyaluronic acid (HA) or CNC by chitosan (CHI) in the architecture keeping a positive layer as the ending layer CNC and CHI, respectively. Oriented CNC/HA, *i.e.* $(HA/CNC)_n$, films were obtained by the brushing method using the same protocol as described for CNC/TA films (**Figure 5.13a-b)**. Oriented CNC/HA films reached a thickness of 72.9 ± 0.3 nm after 7 bilayers and showed anisotropic orientation of CNC crystals observed by AFM and confirmed by image treatment with an order parameter $S_{2D}$ is of 0.48.

The buildup of CHI/TA films by the brushing method was not possible. CHI/TA, *i.e.* $(TA/Fe^{3+}/CHI/Fe^{3+})_n$, films were then obtained by the dipping method (**Figure 5.13c-d)**. The film reached a thickness of 23 nm after 8 bilayers showing granular topography with no preferential orientation.

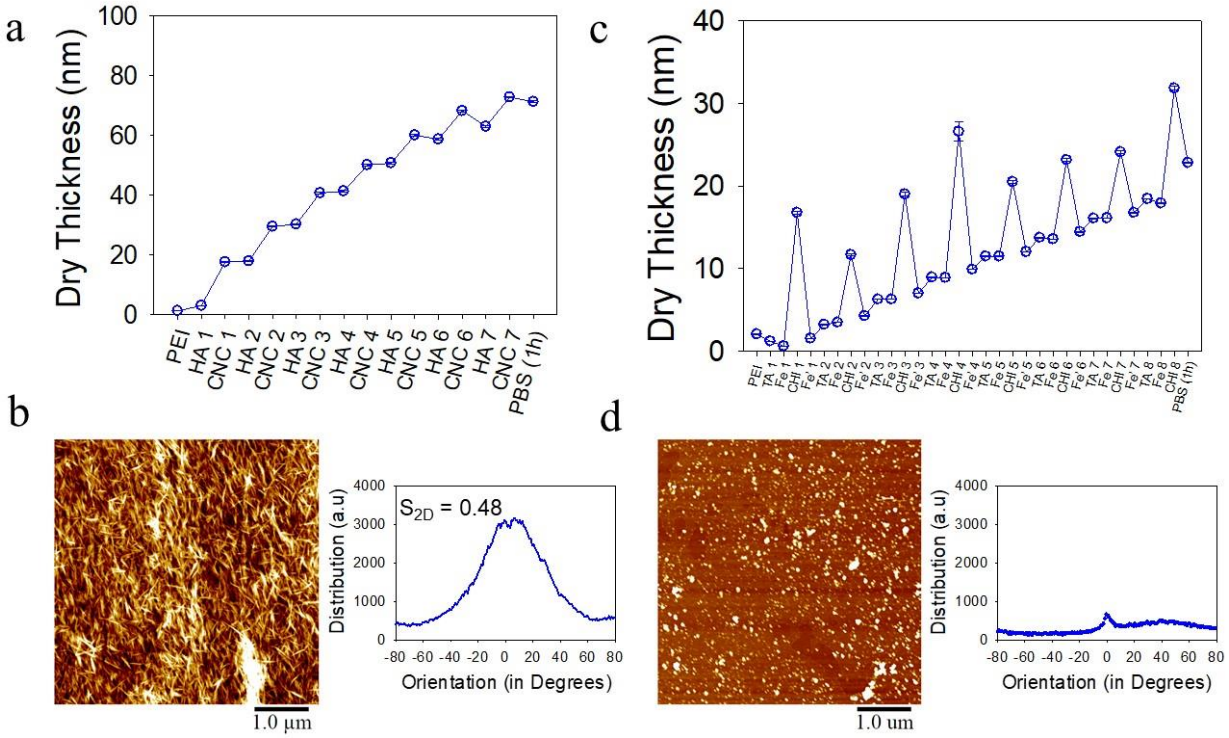


***Figure 5.13: (a-c)*** *Evolution of the thickness, determined by ellipsometry, as a function of the last deposited layer, and* ***(b-d)*** *typical 2D AFM topography images (z-scale of 50 nm) with orientation distribution curves obtained via OrientationJ analysis of oriented CNC-ending HA/CNC* ***(a, b)*** *and non-oriented CHI-ending TA/CHI i.e. (TA/$Fe^{3+}$/CHI/$Fe^{3+}$)$_n$, LbL films* ***(c, d)****. The film thickness was also measured after 1h contact with PBS.*

A higher proliferation of *S. aureus* (SYTO®-9 green staining) was observed on oriented CNC-ending CNC/HA and CHI-ending CHI/TA films with 29 % and 25 % of damaged bacteria, respectively **(Figure 5.14)**. The antibacterial effect was totally lost by replacing TA/$Fe^{3+}$ par HA and CNC by CHI.

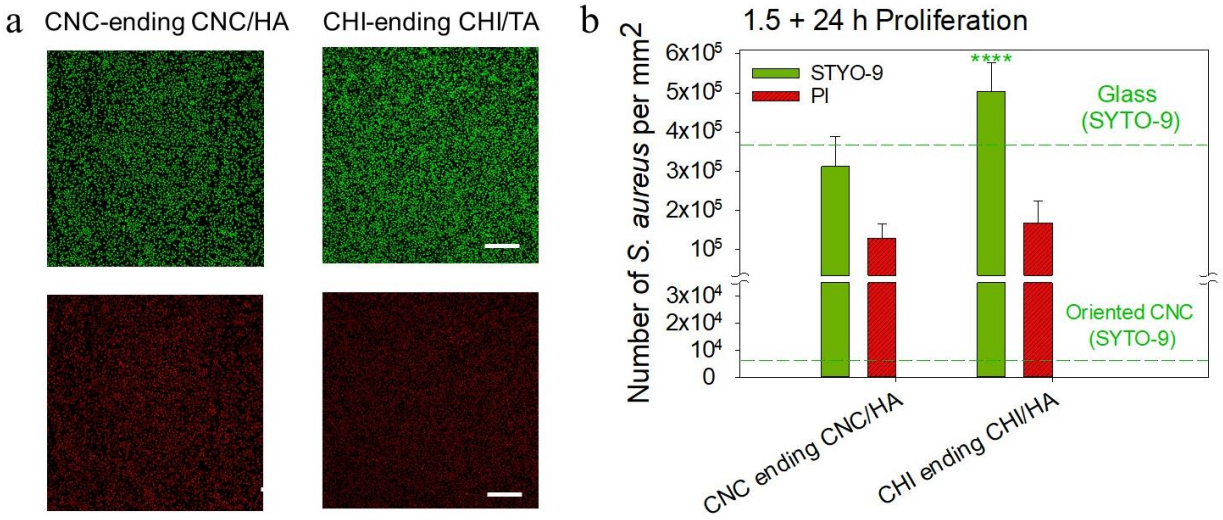


***Figure 5.14:*** *Bacterial proliferation of S. aureus on the oriented $(HA/CNC)_n$ and non-oriented $(TA/Fe^{3+}/CHI/\ Fe^{3+})_n$-$TA/Fe^{3+}/CHI$ films after 24 h incubation of adhered bacteria at 37°C under static condition. The SYTO®-9/PI LIVE/DEAD assay was used to stain alive bacteria (SYTO®-9 green) and damaged ones (PI red)* ***(a)*** *Typical confocal microscopy images in green and red channels (Scale bar: 20 µm).* ***(b)*** *Number of bacteria per $mm^2$ determined from three different images of the 1×1 $cm^2$ film taken on at least seven samples (21 images in total) with the significance level in t-test of SYTO®-9 staining in comparison to the uncoated glass **** $p \leq 0.0001$. The values obtained in SYTO®-9 staining for the uncoated glass and the oriented CNC-ending CNC/TA films are represented by two dashed green lines.*

### 5.3.6. Insight on the mechanism of action of oriented CNC-ending CNC/TA films

Oriented CNC-ending CNC/TA films, *i.e.* $(TA/Fe^{3+}/CNC/Fe^{3+})_n$-$TA/Fe^{3+}/CNC$, showed a strong antibacterial activity coupled with an antiadhesive property. These properties are lost when (i) the CNCs are not oriented, (ii) the last layer is not the CNC, (iii) $Fe^{3+}/TA$ is replaced by HA or (iv) CNC replaced by CHI. We were then interested to characterize the nanotopography and the surface charge density of these films to gain more insight on the mechanism of action of the oriented CNC-ending CNC/TA films.

#### *5.3.6.1. **Nanotopography characterization***

The AFM cross-section profiles of the oriented and the non-oriented CNC-ending CNC/TA films are shown in **Figure 5.15a,b**. The oriented film shows more frequent and bigger peaks (20-30 nm height) compared to the non-oriented film. To evaluate the nanotopography, the AFM images were used to evaluate the gaussian distribution of depths of the nanocrystal topography via the bearing analysis. The bearing analysis is a method used to plot and analyze the distribution of surface height over a surface by revealing what percentage of the surface (*y*-axis on **Figure 5.15c**), *i.e*. the bearing area ratio, is below or above any selected height (*x*-axis on **Figure 5.15c**).[75]

The bearing area curves showed a sharp rise starting from 60 and 20 nm for the oriented CNC/TA and the non-oriented CNC/TA films, respectively **(Figure 5.15c)**. The increasing trend in the bearing area ratio starting from higher values of heights represents a surface with a rougher topography and bearing capacity, with spike-like topographical features confirmed from AFM cross-section profile **(Figure 5.15a)**. The bearing capacity is directly linked to the contact area of the surface. In fact, the distribution and the maximum of depths are clearly different for the oriented CNC/TA films compared to the non-oriented one **(Figure 5.15d)**.[93]

Similarly, the CNC/TA films with different ending layers showed the bearing area curves and the depth distributions similar to the oriented CNC-ending CNC/TA film **(Figure 5.16a,b)**. The films with other compositions, CNC/HA and CHI/TA, showed a behavior closer to the non-oriented CNC-ending film **(Figure 5.16c,d)**. Even if the orientation of CNC is similar to CNC/TA films with even a better $S_{2D}$ value **(Figure 5.5)**, the association of HA with CNC

prevent probably the nanocrystals to be distributed with spike-like topography when they are brushed.

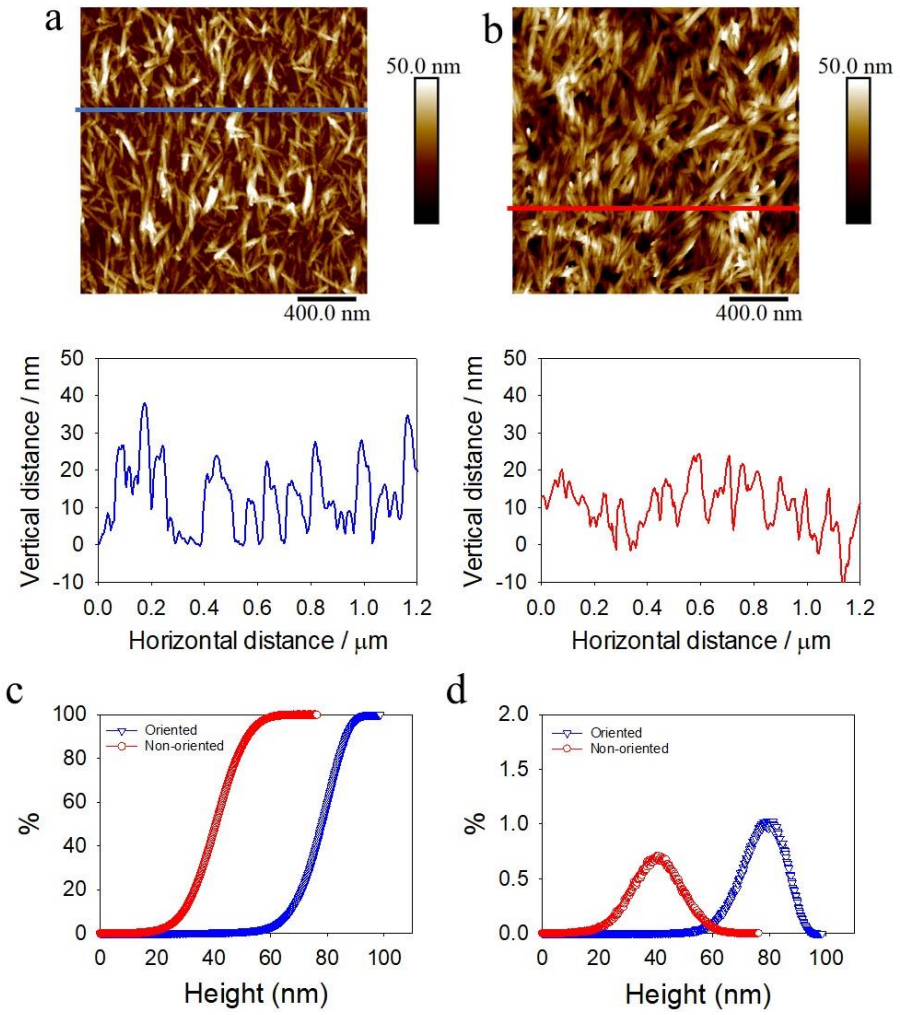


***Figure 5.15:*** *Typical 3D cross-section profiles of the* ***(a)*** *oriented and the* ***(b)*** *non-oriented CNC-ending films obtained by AFM analysis. Bearing analysis of the oriented and the non-oriented CNC-ending CNC/TA films,* ***(c)*** *the surface bearing area ratio and* ***(d)*** *the depth histograms calculated from the corresponding AFM topography images (5×5 µm²).*

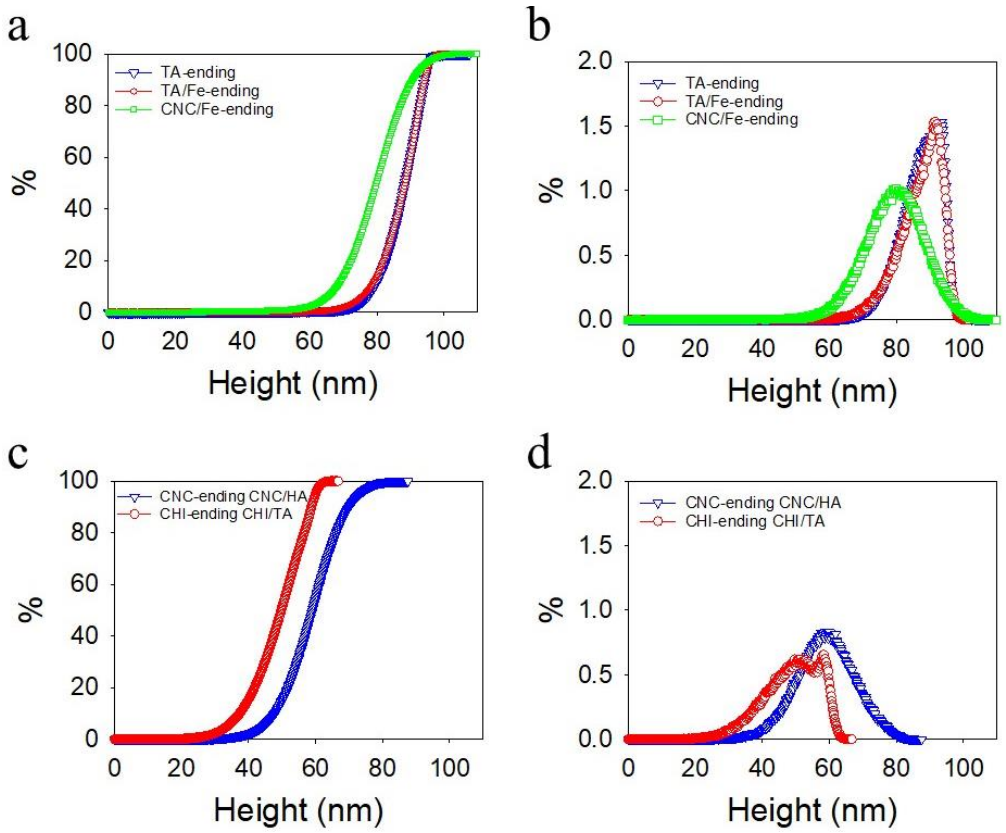


***Figure 5.16:*** *Bearing analysis of the oriented CNC/TA films with different ending layers* ***(a-b)****, and CNC/HA and CHI/TA films* ***(c-d)****. The surface bearing area ratio curves* ***(a, c)****, and the depth histograms* ***(b, d)*** *calculated from the corresponding AFM topography images (5×5 µm²).*

*5.3.6.2 Surface charge density*

In collaboration with Gregory Francius (LCPME, Vandoeuvre), chemical force microscopy (CFM) was used to characterize the surface charge density of the different studied films. To this aim, CFM uses chemical interactions between a functionalized atomic force microscope (AFM) tip and a sample. The chemical interaction is measured by the deflection of the AFM cantilever during the AFM tip approach and withdrawal.[75] The deflection can be converted into the force needed to pull the functionalized AFM tip from the sample using the spring constant of the cantilever and Hooke's law.[94] The AFM probe pull-off force during withdrawal from the sample

can be quantified as a measurement of adhesion force and can be used to compare the surface chemistry of samples. A carboxylic acid-modified AFM probe has been reported to determine the surface charge of biological samples.[95-96]

In our case, the positive surface charge of the films was characterized using phosphate-functionalized AFM probe, to mimic the bacteria cell membranes, in PBS at pH 7.2. To measure small molecular binding interactions, a very soft, Au-coated Bruker AC-40 AFM probe (tip radius ~10 nm) was used. To confirm the probe functionalization, the force was measured between the phosphate coated probe and a positively charged SAM-$NH_3^+$-modified control surface in PBS at pH 7.2. Adhesion histogram and mapping of the adhesion force (positive charges) have been obtained for oriented CNC/TA films ended by different layers, non-oriented CNC-ending CNC/TA film, oriented CNC-ending CNC/HA film and CHI-ending CHI/HA film in comparison to SAM-$NH_3^+$ and uncoated glass **(Figure 5.17)**.

***Table 5.1:*** *A summary of one-way analysis of variance (ANOVA) test performed on adhesion force measurements presented in Figure 5.17.*

| Adhesion forces with $-PO_3^-$ AFM-tip | | |
|---|---|---|
| **Comparison of** | **with** | **P** |
| Oriented CNC (CNC/TA) | Glass | <0.001 |
| Non-oriented CNC (CNC/TA) | Glass | <0.001 |
| Oriented CNC/Fe (CNC/TA) | Glass | <0.001 |
| Oriented TA (CNC/TA) | Glass | <0.001 |
| Oriented TA/Fe (CNC/TA) | Glass | <0.001 |
| Oriented CNC (CNC/HA) | Glass | <0.001 |
| CHI | Glass | <0.001 |
| SAM $NH_3$+ | Glass | <0.001 |
| Non-oriented CNC (CNC/TA) | Oriented CNC (CNC/TA) | 0.677 |
| Oriented CNC/Fe (CNC/TA) | Oriented CNC (CNC/TA) | 0.952 |
| Oriented TA (CNC/TA) | Oriented CNC (CNC/TA) | 0.956 |
| Oriented TA/Fe (CNC/TA) | Oriented CNC (CNC/TA) | 0.999 |
| Oriented CNC (CNC/HA) | Oriented CNC (CNC/TA) | 0.029 |
| CHI | Oriented CNC (CNC/TA) | <0.001 |
| SAM $NH_3$+ | Oriented CNC (CNC/TA) | 0.859 |

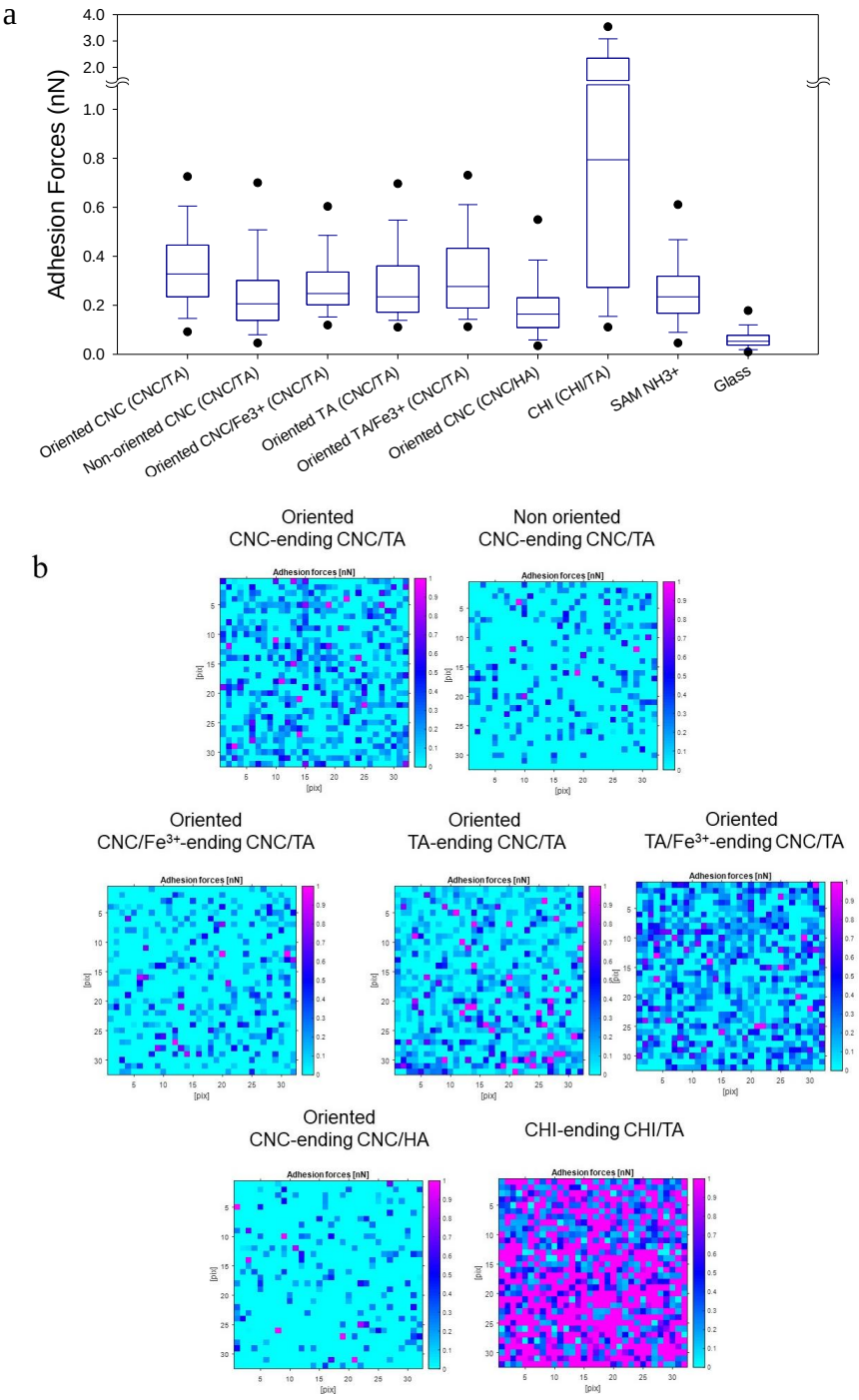


***Figure 5.17:*** *Adhesion force, measured by CFM using phosphate functionalized AFM tip,* ***(a)*** *Box-charts show the median (line), the 5% and 95% quartiles (p-value ≤ 0.001 for all) and* ***(b)*** *mapping on 1 × 1 µm² area on the surface of different studied films. The notation of the film is as follows: Oriented CNC (CNC/TA) means the oriented CNC-ending CNC/TA film.*

Oriented CNC-ending CNC/TA films showed a higher adhesion force with a median value at 0.35 nN than the non-oriented CNC-ending film, revealing probably a stronger interaction with the phosphate functionalized tip and thus strong electrostatic interactions **(Figure 5.17a)**. However, the one-way analysis of variance (ANOVA) test applied on the recorded data show no significant difference **(Table 5.1)**. The mapping of both film surfaces showed a higher density of charges for the oriented film (**Figure 5.17b**). Oriented CNC-ending CNC/HA films present a lower adhesion force in comparison to oriented CNC-ending CNC/TA films, with the median value at 0.18 nN which is significant according to the ANOVA test ($p$ value$<0.05$). We can point out that the orientation of CNC combined with TA/$Fe^{3+}$ allowed to obtain a higher density of charges and interactions between the phosphate tip and the surface. This probably explain the antibacterial activity of the oriented CNC ending CNC/TA films. By comparing the oriented CNC/TA films with different ending layers, the adhesion force distribution and the mapping of the surface showed quite similar results for TA/$Fe^{3+}$ and TA ending films. This could be explained by the electrostatic interactions of phosphate moieties of the tip with $Fe^{3+}$ and hydrogen bond interactions with TA.[97] It can be noticed that CHI-ending CHI/HA films (without CNC) presented the strongest interactions reaching 0.8 nN as a median value with poor antibacterial activity of the film. However, this induces a higher proliferation of *S. aureus* **(Figure 5.17).** In this case, the positive charges on the surface favor probably the adhesion of bacteria by attractive electrostatic interaction with no perturbation of the cell membrane. The combination of positive charges with spike like topographical features seems to be essential to obtain an antibacterial activity by contact-killing.

We hypothesize that here in the case of the oriented CNC-ending CNC/TA films, the specific orientation obtained by the brushing allowed probably to immobilize CNCs' positively charges amino groups ($NH^{3+}$) on the surface such that they become accessible to the bacteria. The positively charged spikes of oriented CNC-films perhaps apply a shear force on the cell membrane leading to its puncture. **(Scheme 5.1)**.

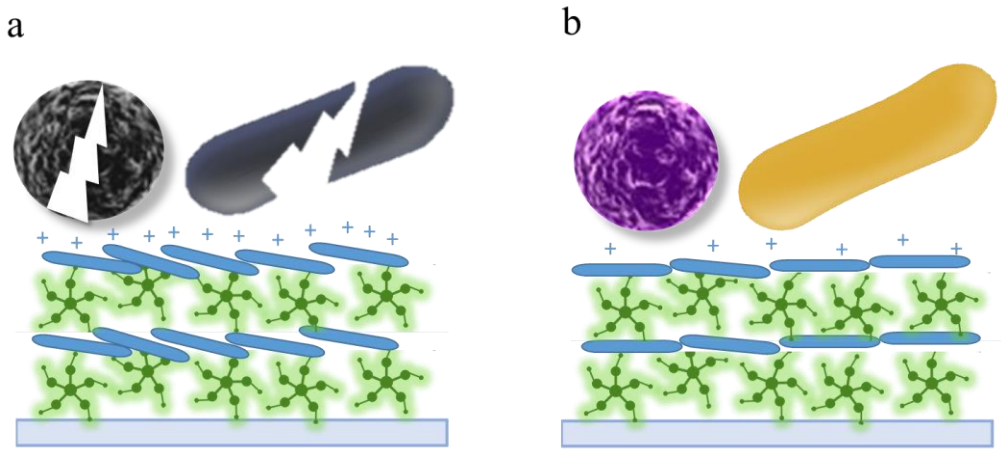


***Scheme 5.1:*** *A schematic representation of the antibacterial activity by contact-killing of* ***(a)*** *the oriented and* ***(b)*** *the non-oriented CNC-ending CNC/TA films in contact with S. aureus and E. coli. The antibacterial activity of the oriented CNC/TA LbL films is associated to nanotopographical orientation of CNC in a spike like features with high surface charge density. In comparison, the non-oriented films present a smoother topography with less density of charges.*

### 5.3.7. Cytotoxicity of CNC/TA films

The cytocompatibility of CNC/TA films was evaluated towards murine NIH3T3 fibroblasts after 4 h of adhesion and 18 h of proliferation **(Figure 5.18)**. Interestingly whatever the ending layer, oriented CNC/TA films showed a good cell viability after 4 h similarly to uncoated glass and TCPS.

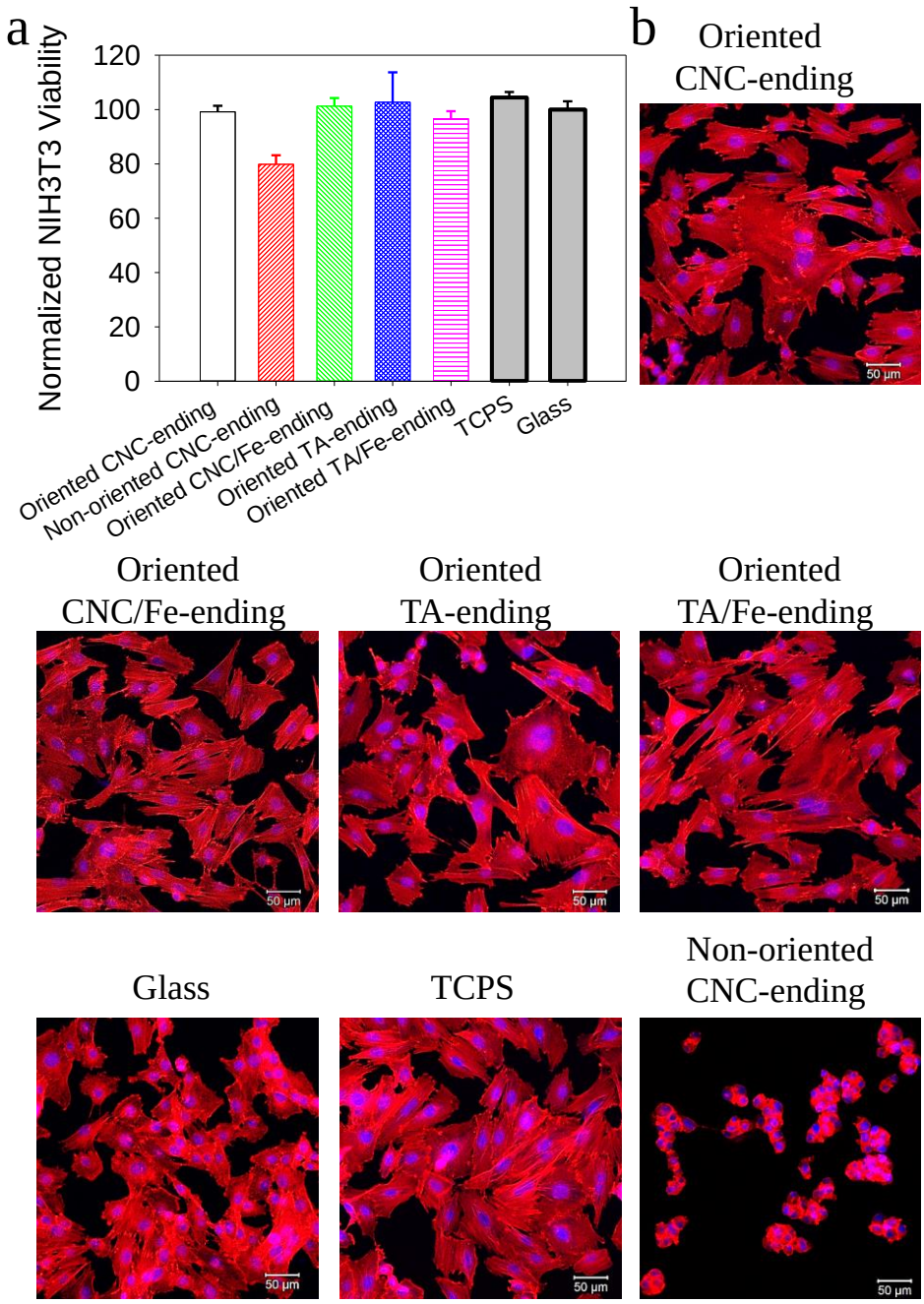


***Figure 5.18:*** ***(a)*** *Adhesion and* ***(b)*** *proliferation of CNC/TA films towards murine NIH3T3 fibroblasts.* ***(a)*** *Acidic phosphatase assay of the adhered cells after 4 h of incubation.* ***(b)*** *Fluorescent microscopy images of labelled cells seeded for 4 h followed by a PBS rinsing step and further incubating in supplemented medium for 18 h (scale bars = 50 µm, red = F-actin, Phalloidin and blue = nuclei, DAPI).*

On the other hand, the non-oriented CNC-ending films shows around 80% cell viability. After 18 h of proliferation on oriented CNC/TA films, well spread NIH3T3 cells were observed with a typical fibroblastic cell shape whatever the ending layer, similarly to the uncoated glass and TCPS substrates **(Figure 5.18b)**. On the contrary, the cells adopted a round shape morphology when seeded on non-oriented CNC ending CNC/TA films which indicates that the cells cannot adhere on the surface (**Figure 5.18b)**. Even if chitin is known for its good biocompatibility for mammalian cells,[98-101] the cytotoxicity of chitin nanocrystals had been reported a few times due to high chitin content in chitosan matrix[54], increase of surface roughness in chitosan scaffolds[101] and agglomeration in hydrogels.[60] In this work, the non-oriented CNC/TA films, obtained by the dipping method, are thicker with higher deposition of CNCs on the surface in comparison to the oriented CNC/TA films **(Figure 5.4)**. This explains probably the cytotoxicity of the non-oriented films.

## 5.4. Conclusion

To the best of our knowledge, we reported the first CNC based LbL films with antiadhesive and contact-killing properties against *S. aureus* and *E. coli* preventing also bacterial biofilm formation. On the contrary to reported studies, CNC was not modified or associated with another antibacterial compound. Even if TA is known to be antibacterial, its immobilization prevents its action. The non-oriented films, obtained by the dipping method, showed only a contact killing effect with a higher bacteria adhesion in comparison to uncoated glass.

The antibacterial property is due to the orientation of CNC, obtained by the brushing method, in combination with TA and Iron(III) as partner allowing to obtain spike-like nanotopographies

with high density of positive charge on the surface. The positively charged spikes of oriented CNC-films probably apply a shear force on the cell membrane leading to its puncture. This hypothesis should be further studied with the characterization of the mechanical properties of the bacteria membranes and TEM analysis of the bacteria in contact with the surface. The mode of action could be similar to nanotextured surface of organisms, such as cicada or dragonfly wings, both composed of chitin and proteins. In the case of cicada wings nanopillars, the membrane rupture was explained by direct contact of the bacterial cell membrane with the nanopillars, which are strong enough to damage the bacterial membrane.[9] In the case of dragonfly wing's,[102] a combination of two phenomena were reported: (i) the strong adhesion between nanopillars and bacterium and the shear force when immobilized bacterium attempts to move away from the unfavorable surface topography.

## 5.5. Bibliography:

1. Costerton, J. W.; Stewart, P. S.; Greenberg, E. P., Bacterial biofilms: a common cause of persistent infections. *Science* **1999,** *284* (5418), 1318-22.
2. Davies, D., Understanding biofilm resistance to antibacterial agents. *Nature Reviews Drug Discovery* **2003,** *2* (2), 114-22.
3. Lopez, G. U.; Gerba, C. P.; Tamimi, A. H.; Kitajima, M.; Maxwell, S. L.; Rose, J. B., Transfer efficiency of bacteria and viruses from porous and nonporous fomites to fingers under different relative humidity conditions. *Appl Environ Microbiol* **2013,** *79* (18), 5728-5734.
4. Wang, Y.; Yang, Y.; Shi, Y.; Song, H.; Yu, C., Antibiotic-Free Antibacterial Strategies Enabled by Nanomaterials: Progress and Perspectives. *Advanced Materials* **2020,** *32* (18), 1904106.
5. Wang, M.; Tang, T., Surface treatment strategies to combat implant-related infection from the beginning. *Journal of orthopaedic translation* **2019,** *17*, 42-54.
6. Allegranzi, B.; Bagheri Nejad, S.; Combescure, C.; Graafmans, W.; Attar, H.; Donaldson, L.; Pittet, D., Burden of endemic health-care-associated infection in developing countries: systematic review and meta-analysis. *Lancet (London, England)* **2011,** *377* (9761), 228-41.
7. Fadeeva, E.; Truong, V. K.; Stiesch, M.; Chichkov, B. N.; Crawford, R. J.; Wang, J.; Ivanova, E. P., Bacterial Retention on Superhydrophobic Titanium Surfaces Fabricated by Femtosecond Laser Ablation. *Langmuir* **2011,** *27* (6), 3012-3019.
8. Tiller, J. C.; Liao, C.-J.; Lewis, K.; Klibanov, A. M., Designing surfaces that kill bacteria on contact. *Proceedings of the National Academy of Sciences* **2001,** *98* (11), 5981-5985.
9. Ivanova, E. P.; Hasan, J.; Webb, H. K.; Truong, V. K.; Watson, G. S.; Watson, J. A.; Baulin, V. A.; Pogodin, S.; Wang, J. Y.; Tobin, M. J.; Löbbe, C.; Crawford, R. J., Natural Bactericidal Surfaces: Mechanical Rupture of Pseudomonas aeruginosa Cells by Cicada Wings. *Small* **2012,** *8* (16), 2489-2494.
10. Barthlott, W.; Neinhuis, C., Purity of the sacred lotus, or escape from contamination in biological surfaces. *Planta* **1997,** *202* (1), 1-8.
11. Lee, H.; Lee, B. P.; Messersmith, P. B., A reversible wet/dry adhesive inspired by mussels and geckos. *Nature* **2007,** *448* (7151), 338-341.
12. Peng, Y. L.; Lin, C. G.; Wang, L., The Preliminary Study on Antifouling Mechanism of Shark Skin. *Advanced Materials Research* **2009,** *79-82*, 977-980.
13. Salta, M.; Wharton, J.; Stoodley, P.; Dennington, S.; Goodes, L.; Werwinski, S.; Mart, U.; Wood, R.; Stokes, K., Designing biomimetic antifouling surfaces. *Philosophical transactions. Series A, Mathematical, physical, and engineering sciences* **2010,** *368*, 4729-54.
14. Medilanski, E.; Kaufmann, K.; Wick, L. Y.; Wanner, O.; Harms, H., Influence of the Surface Topography of Stainless Steel on Bacterial Adhesion. *Biofouling* **2002,** *18* (3), 193-203.
15. Chung, K. K.; Schumacher, J. F.; Sampson, E. M.; Burne, R. A.; Antonelli, P. J.; Brennan, A. B., Impact of engineered surface microtopography on biofilm formation of Staphylococcus aureus. *Biointerphases* **2007,** *2* (2), 89-94.
16. Kelly, P. J.; Li, H.; Whitehead, K. A.; Verran, J.; Arnell, R. D.; Iordanova, I., A study of the antimicrobial and tribological properties of TiN/Ag nanocomposite coatings. *Surface and Coatings Technology* **2009,** *204* (6), 1137-1140.

17. Etienne, O.; Picart, C.; Taddei, C.; Haikel, Y.; Dimarcq, J. L.; Schaaf, P.; Voegel, J. C.; Ogier, J. A.; Egles, C., Multilayer polyelectrolyte films functionalized by insertion of defensin: a new approach to protection of implants from bacterial colonization. *Antimicrobial agents and chemotherapy* **2004,** *48* (10), 3662-9.
18. Boulmedais, F.; Frisch, B.; Etienne, O.; Lavalle, P.; Picart, C.; Ogier, J.; Voegel, J. C.; Schaaf, P.; Egles, C., Polyelectrolyte multilayer films with pegylated polypeptides as a new type of anti-microbial protection for biomaterials. *Biomaterials* **2004,** *25* (11), 2003-11.
19. Price, J. S.; Tencer, A. F.; Arm, D. M.; Bohach, G. A., Controlled release of antibiotics from coated orthopedic implants. *Journal of Biomedical Materials Research Part A* **1996,** *30* (3), 281-6.
20. Lin, J.; Qiu, S.; Lewis, K.; Klibanov, A. M., Mechanism of bactericidal and fungicidal activities of textiles covalently modified with alkylated polyethylenimine. *Biotechnology and bioengineering* **2003,** *83* (2), 168-72.
21. Richert, L.; Lavalle, P.; Payan, E.; Shu, X. Z.; Prestwich, G. D.; Stoltz, J.-F.; Schaaf, P.; Voegel, J.-C.; Picart, C., Layer by Layer Buildup of Polysaccharide Films: Physical Chemistry and Cellular Adhesion Aspects. *Langmuir* **2004,** *20* (2), 448-458.
22. Decher, G., Fuzzy Nanoassemblies: Toward Layered Polymeric Multicomposites. *Science* **1997,** *277* (5330), 1232-1237.
23. Jiang, C.; Markutsya, S.; Tsukruk, V. V., Collective and individual plasmon resonances in nanoparticle films obtained by spin-assisted layer-by-layer assembly. *Langmuir* **2004,** *20* (3), 882-890.
24. Schlenoff, J. B.; Dubas, S. T.; Farhat, T., Sprayed Polyelectrolyte Multilayers. *Langmuir* **2000,** *16* (26), 9968-9969.
25. Séon, L.; Lavalle, P.; Schaaf, P.; Boulmedais, F., Polyelectrolyte Multilayers: A Versatile Tool for Preparing Antimicrobial Coatings. *Langmuir* **2015,** *31* (47), 12856-12872.
26. Park, K.; Choi, D.; Hong, J., Nanostructured Polymer Thin Films Fabricated with Brush-based Layer-by-Layer Self-assembly for Site-selective Construction and Drug release. *Scientific Reports* **2018,** *8* (1), 3365.
27. Zhao, X.; Zhou, C.; Lvov, Y.; Liu, M., Clay Nanotubes Aligned with Shear Forces for Mesenchymal Stem Cell Patterning. *Small* **2019,** *15* (21), 1900357.
28. Gordon, L. M.; Joester, D., Nanoscale chemical tomography of buried organic–inorganic interfaces in the chiton tooth. *Nature* **2011,** *469* (7329), 194-197.
29. Gyliene, O.; Rekertas, R.; Salkauskas, M., Removal of free and complexed heavy-metal ions by sorbents produced from fly (Musca domestica) larva shells. *Water research* **2002,** *36* (16), 4128-36.
30. Revol, J. F.; Marchessault, R. H., In vitro chiral nematic ordering of chitin crystallites. *International Journal of Biological Macromolecules* **1993,** *15* (6), 329-335.
31. Peter, M. G., Chitin and Chitosan from Animal Sources. In *Biopolymers Online*.
32. Duan, B.; Zheng, X.; Xia, Z.; Fan, X.; Guo, L.; Liu, J.; Wang, Y.; Ye, Q.; Zhang, L., Highly Biocompatible Nanofibrous Microspheres Self-Assembled from Chitin in NaOH/Urea Aqueous Solution as Cell Carriers. *Angewandte Chemie International Edition* **2015,** *54* (17), 5152-5156.

33. Das, P.; Heuser, T.; Wolf, A.; Zhu, B.; Demco, D. E.; Ifuku, S.; Walther, A., Tough and Catalytically Active Hybrid Biofibers Wet-Spun From Nanochitin Hydrogels. *Biomacromolecules* **2012,** *13* (12), 4205-4212.
34. Fan, Y.; Fukuzumi, H.; Saito, T.; Isogai, A., Comparative characterization of aqueous dispersions and cast films of different chitin nanowhiskers/nanofibers. *International Journal of Biological Macromolecules* **2012,** *50* (1), 69-76.
35. Wu, J.; Zhang, K.; Girouard, N.; Meredith, J. C., Facile Route to Produce Chitin Nanofibers as Precursors for Flexible and Transparent Gas Barrier Materials. *Biomacromolecules* **2014,** *15* (12), 4614-4620.
36. Qi, Z.-D.; Saito, T.; Fan, Y.; Isogai, A., Multifunctional Coating Films by Layer-by-Layer Deposition of Cellulose and Chitin Nanofibrils. *Biomacromolecules* **2012,** *13* (2), 553-558.
37. Salaberria, A. M.; H Diaz, R.; Andrés, M. A.; Fernandes, S. C. M.; Labidi, J., The Antifungal Activity of Functionalized Chitin Nanocrystals in Poly (Lactid Acid) Films. *Materials (Basel)* **2017,** *10* (5), 546.
38. Heath, L.; Zhu, L.; Thielemans, W., Chitin Nanowhisker Aerogels. *ChemSusChem* **2013,** *6* (3), 537-544.
39. Araki, J.; Yamanaka, Y.; Ohkawa, K., Chitin-chitosan nanocomposite gels: reinforcement of chitosan hydrogels with rod-like chitin nanowhiskers. *Polymer Journal* **2012,** *44* (7), 713-717.
40. Tian, Y.; Liang, K.; Wang, X.; Ji, Y., Fabrication of Nanocomposite Bioelastomer Porous Scaffold Based on Chitin Nanocrystal Supported Emulsion-Freeze-Casting. *ACS Sustainable Chemistry & Engineering* **2017,** *5* (4), 3305-3313.
41. Elbaz, A.; Lu, J.; Gao, B.; Zheng, F.; Mu, Z.; Zhao, Y.; Gu, Z., Chitin-Based Anisotropic Nanostructures of Butterfly Wings for Regulating Cells Orientation. *Polymers* **2017,** *9* (9), 386.
42. Boltoeva, M. Y.; Dozov, I.; Davidson, P.; Antonova, K.; Cardoso, L.; Alonso, B.; Belamie, E., Electric-Field Alignment of Chitin Nanorod–Siloxane Oligomer Reactive Suspensions. *Langmuir* **2013,** *29* (26), 8208-8212.
43. Nge, T. T.; Hori, N.; Takemura, A.; Ono, H.; Kimura, T., Synthesis and orientation study of a magnetically aligned liquid-crystalline chitin/poly(acrylic acid) composite. *Journal of Polymer Science Part B: Polymer Physics* **2003,** *41* (7), 711-714.
44. João, C. F. C.; Echeverria, C.; Velhinho, A.; Silva, J. C.; Godinho, M. H.; Borges, J. P., Bio-inspired production of chitosan/chitin films from liquid crystalline suspensions. *Carbohydrate Polymers* **2017,** *155*, 372-381.
45. Mendoza-Galvan, A.; Muñoz, E.; Järrendahl, K.; Arwin, H., Birefringence of nanocrystalline chitin films studied by Mueller-matrix spectroscopic ellipsometry. *Optical Materials Express* **2016,** *6*, 671.
46. Torres-Rendon, J. G.; Schacher, F. H.; Ifuku, S.; Walther, A., Mechanical Performance of Macrofibers of Cellulose and Chitin Nanofibrils Aligned by Wet-Stretching: A Critical Comparison. *Biomacromolecules* **2014,** *15* (7), 2709-2717.
47. Rinaudo, M., Chitin and chitosan: Properties and applications. *Progress in polymer science* **2006,** *31* (7), 603-632.
48. Li, J.; Revol, J.; Marchessault, R., Rheological properties of aqueous suspensions of chitin crystallites. *Journal of colloid and interface science* **1996,** *183* (2), 365-373.

49. Fu, J.; Ji, J.; Yuan, W.; Shen, J., Construction of anti-adhesive and antibacterial multilayer films via layer-by-layer assembly of heparin and chitosan. *Biomaterials* **2005,** *26* (33), 6684-6692.
50. Sudarshan, N. R.; Hoover, D. G.; Knorr, D., Antibacterial action of chitosan. *Food Biotechnology* **1992,** *6* (3), 257-272.
51. Jia, Z.; shen, D.; Xu, W., Synthesis and antibacterial activities of quaternary ammonium salt of chitosan. *Carbohydrate Research* **2001,** *333* (1), 1-6.
52. Salaberria, A. M.; Fernandes, S. C. M.; Diaz, R. H.; Labidi, J., Processing of α-chitin nanofibers by dynamic high pressure homogenization: Characterization and antifungal activity against A. niger. *Carbohydrate Polymers* **2015,** *116*, 286-291.
53. Ma, B.; Qin, A.; Li, X.; Zhao, X.; He, C., Structure and properties of chitin whisker reinforced chitosan membranes. *International Journal of Biological Macromolecules* **2014,** *64*, 341-346.
54. Salaberria, A. M.; Diaz, R. H.; Labidi, J.; Fernandes, S. C. M., Role of chitin nanocrystals and nanofibers on physical, mechanical and functional properties in thermoplastic starch films. *Food Hydrocolloids* **2015,** *46*, 93-102.
55. Zhang, Y.; Jiang, J.; Liu, L.; Zheng, K.; Yu, S.; Fan, Y., Preparation, assessment, and comparison of α-chitin nano-fiber films with different surface charges. *Nanoscale Research Letters* **2015,** *10* (1), 226.
56. Panariello, L.; Coltelli, M.-B.; Buchignani, M.; Lazzeri, A., Chitosan and nano-structured chitin for biobased anti-microbial treatments onto cellulose based materials. *European Polymer Journal* **2019,** *113*, 328-339.
57. Xu, H.; Fang, Z.; Tian, W.; Wang, Y.; Ye, Q.; Zhang, L.; Cai, J., Green Fabrication of Amphiphilic Quaternized β-Chitin Derivatives with Excellent Biocompatibility and Antibacterial Activities for Wound Healing. *Advanced Materials* **2018,** *30* (29), 1801100.
58. Wang, Y.; Li, J.; Li, B., Nature-Inspired One-Step Green Procedure for Enhancing the Antibacterial and Antioxidant Behavior of a Chitin Film: Controlled Interfacial Assembly of Tannic Acid onto a Chitin Film. *Journal of Agricultural and Food Chemistry* **2016,** *64* (28), 5736-5741.
59. Solairaj, D.; Rameshthangam, P.; Muthukumaran, P.; Wilson, J., Studies on electrochemical glucose sensing, antimicrobial activity and cytotoxicity of fabricated copper nanoparticle immobilized chitin nanostructure. *International Journal of Biological Macromolecules* **2017,** *101*, 668-679.
60. Li, W.; He, X.; Liu, K.; Wen, W.; Lu, L.; Liu, M.; Zhou, C.; Luo, B., Creating Ultrastrong and Osteogenic Chitin Nanocomposite Hydrogels via Chitin Whiskers with Different Surface Chemistries. *ACS Sustainable Chemistry & Engineering* **2020,** *8* (47), 17487-17499.
61. Xu, H.; Zhang, L.; Cai, J., Injectable, Self-Healing, β-Chitin-Based Hydrogels with Excellent Cytocompatibility, Antibacterial Activity, and Potential As Drug/Cell Carriers. *ACS Applied Bio Materials* **2019,** *2* (1), 196-204.
62. Villares, A.; Moreau, C.; Capron, I.; Cathala, B., Chitin Nanocrystal-Xyloglucan Multilayer Thin Films. *Biomacromolecules* **2014,** *15* (1), 188-194.
63. Tanaka, C.; Shiratori, S., Fabrication of the durable low refractive index thin film with chitin-nanofiber by LBL method. *MATEC Web of Conferences* **2013,** *4*, 05006.

64. Manabe, K.; Tanaka, C.; Moriyama, Y.; Tenjimbayashi, M.; Nakamura, C.; Tokura, Y.; Matsubayashi, T.; Kyung, K.-H.; Shiratori, S., Chitin Nanofibers Extracted from Crab Shells in Broadband Visible Antireflection Coatings with Controlling Layer-by-Layer Deposition and the Application for Durable Antifog Surfaces. *ACS Applied Materials & Interfaces* **2016,** *8* (46), 31951-31958.
65. Taniguchi, T.; Kyung, K.-H.; Shiratori, S., Layer-by-layer self-assembled thin films of chitin fibers and heparin with anti-thrombus characteristics. *RSC Advances* **2015,** *5* (130), 107488-107496.
66. Ejima, H.; Richardson, J. J.; Liang, K.; Best, J. P.; van Koeverden, M. P.; Such, G. K.; Cui, J.; Caruso, F., One-Step Assembly of Coordination Complexes for Versatile Film and Particle Engineering. *Science* **2013,** *341* (6142), 154-157.
67. Wang, W.; Meng, Q.; Li, Q.; Liu, J.; Zhou, M.; Jin, Z.; Zhao, K., Chitosan Derivatives and Their Application in Biomedicine. *International Journal of Molecular Sciences* **2020,** *21* (2), 487.
68. Shukla, A.; Fang, J. C.; Puranam, S.; Jensen, F. R.; Hammond, P. T., Hemostatic Multilayer Coatings. *Advanced Materials* **2012,** *24* (4), 492-496.
69. Goodrich, J. D.; Winter, W. T., Alpha-chitin nanocrystals prepared from shrimp shells and their specific surface area measurement. *Biomacromolecules* **2007,** *8* (1), 252-7.
70. Narkevicius, A.; Steiner, L. M.; Parker, R. M.; Ogawa, Y.; Frka-Petesic, B.; Vignolini, S., Controlling the Self-Assembly Behavior of Aqueous Chitin Nanocrystal Suspensions. *Biomacromolecules* **2019,** *20* (7), 2830-2838.
71. Püspöki, Z.; Storath, M.; Sage, D.; Unser, M., Transforms and Operators for Directional Bioimage Analysis: A Survey. In *Focus on Bio-Image Informatics*, De Vos, W. H.; Munck, S.; Timmermans, J.-P., Eds. Springer International Publishing: Cham, 2016; pp 69-93.
72. Barattin, R.; Voyer, N., Chemical Modifications of Atomic Force Microscopy Tips. In *Atomic Force Microscopy in Biomedical Research: Methods and Protocols*, Braga, P. C.; Ricci, D., Eds. Humana Press: Totowa, NJ, 2011; pp 457-483.
73. Mi, X.; Heldt, C. L., Single-particle chemical force microscopy to characterize virus surface chemistry. *BioTechniques* **2020,** *69* (5), 363-370.
74. Dague, E.; Alsteens, D.; Latgé, J.-P.; Verbelen, C.; Raze, D.; Baulard, A. R.; Dufrêne, Y. F., Chemical Force Microscopy of Single Live Cells. *Nano Letters* **2007,** *7* (10), 3026-3030.
75. Santos, N. C.; Carvalho, F. A., *Atomic Force Microscopy*. Springer: 2019.
76. Cranston, E. D.; Gray, D. G., Morphological and Optical Characterization of Polyelectrolyte Multilayers Incorporating Nanocrystalline Cellulose. *Biomacromolecules* **2006,** *7* (9), 2522-2530.
77. Merindol, R.; Diabang, S.; Mujica, R.; Le Houerou, V.; Roland, T.; Gauthier, C.; Decher, G.; Felix, O., Assembly of Anisotropic Nanocellulose Films Stronger than the Original Tree. *ACS Nano* **2020,** *14* (12), 16525-16534.
78. Katneni, R.; Hedayati, S. S., Central venous catheter-related bacteremia in chronic hemodialysis patients: epidemiology and evidence-based management. *Nature Clinical Practice Nephrology* **2007,** *3* (5), 256-266.
79. Jensen, A. G.; Espersen, F.; Skinhøj, P.; Rosdahl, V. T.; Frimodt-Møller, N., Increasing frequency of vertebral osteomyelitis following Staphylococcus aureus bacteraemia in Denmark 1980–1990. *Journal of Infection* **1997,** *34* (2), 113-118.

80. Jacobsen, S. M.; Stickler, D. J.; Mobley, H. L. T.; Shirtliff, M. E., Complicated catheter-associated urinary tract infections due to Escherichia coli and Proteus mirabilis. *Clin Microbiol Rev* **2008,** *21* (1), 26-59.
81. Rosenberg, M.; Azevedo, N. F.; Ivask, A., Propidium iodide staining underestimates viability of adherent bacterial cells. *Scientific Reports* **2019,** *9* (1), 6483.
82. Finkelstein, R. A.; Sciortino, C. V.; McIntosh, M. A., Role of iron in microbe-host interactions. *Reviews of infectious diseases* **1983,** *5 Suppl 4*, S759-77.
83. Payne, D. E.; Martin, N. R.; Parzych, K. R.; Rickard, A. H.; Underwood, A.; Boles, B. R., Tannic acid inhibits Staphylococcus aureus surface colonization in an IsaA-dependent manner. *Infection and immunity* **2013,** *81* (2), 496-504.
84. Iqbal, M. H.; Schroder, A.; Kerdjoudj, H.; Njel, C.; Senger, B.; Ball, V.; Meyer, F.; Boulmedais, F., Effect of the Buffer on the Buildup and Stability of Tannic Acid/Collagen Multilayer Films Applied as Antibacterial Coatings. *ACS Applied Materials & Interfaces* **2020,** *12* (20), 22601-22612.
85. Reitzer, F.; Allais, M.; Ball, V.; Meyer, F., Polyphenols at interfaces. *Advances in colloid and interface science* **2018,** *257*, 31-41.
86. Park, J. H.; Choi, S.; Moon, H. C.; Seo, H.; Kim, J. Y.; Hong, S.-P.; Lee, B. S.; Kang, E.; Lee, J.; Ryu, D. H.; Choi, I. S., Antimicrobial spray nanocoating of supramolecular Fe(III)-tannic acid metal-organic coordination complex: applications to shoe insoles and fruits. *Scientific Reports* **2017,** *7* (1), 6980.
87. Qin, Y.; Zhang, S.; Yu, J.; Yang, J.; Xiong, L.; Sun, Q., Effects of chitin nano-whiskers on the antibacterial and physicochemical properties of maize starch films. *Carbohydrate Polymers* **2016,** *147*, 372-378.
88. Tan, L.; Zhou, X.; Wu, K.; Yang, D.; Jiao, Y.; Zhou, C., Tannic acid/CaII anchored on the surface of chitin nanofiber sponge by layer-by-layer deposition: Integrating effective antibacterial and hemostatic performance. *International Journal of Biological Macromolecules* **2020,** *159*, 304-315.
89. Zhang, Q.; Wei, S.; Huang, J.; Feng, J.; Chang, P. R., Effect of surface acetylated-chitin nanocrystals on structure and mechanical properties of poly (lactic acid). *Journal of Applied Polymer Science* **2014,** *131* (2).
90. Nagy, A.; Harrison, A.; Sabbani, S.; Munson, R. S., Jr.; Dutta, P. K.; Waldman, W. J., Silver nanoparticles embedded in zeolite membranes: release of silver ions and mechanism of antibacterial action. *International journal of nanomedicine* **2011,** *6*, 1833-52.
91. Divya, K.; Vijayan, S.; George, T. K.; Jisha, M. S., Antimicrobial properties of chitosan nanoparticles: Mode of action and factors affecting activity. *Fibers and Polymers* **2017,** *18* (2), 221-230.
92. Mutschler, A.; Betscha, C.; Ball, V.; Senger, B.; Vrana, N. E.; Boulmedais, F.; Schroder, A.; Schaaf, P.; Lavalle, P., Nature of the Polyanion Governs the Antimicrobial Properties of Poly(arginine)/Polyanion Multilayer Films. *Chemistry of Materials* **2017,** *29* (7), 3195-3201.
93. Stoica, I.; Epure, E.-L.; Constantin, C.-P.; Damaceanu, M.-D.; Ursu, E.-L.; Mihaila, I.; Sava, I., Evaluation of Local Mechanical and Chemical Properties via AFM as a Tool for Understanding the Formation Mechanism of Pulsed UV Laser-Nanoinduced Patterns on Azo-Naphthalene-Based Polyimide Films. *Nanomaterials* **2021,** *11* (3), 812.

94. Kámán, J., Young's Modulus and Energy Dissipation Determination Methods by AFM, with Particular Reference to a Chalcogenide Thin Film. *Periodica Polytechnica Electrical Engineering and Computer Science* **2015,** *59* (1), 18-25.
95. Mi, X.; Bromley, E. K.; Joshi, P. U.; Long, F.; Heldt, C. L., Virus Isoelectric Point Determination Using Single-Particle Chemical Force Microscopy. *Langmuir* **2020,** *36* (1), 370-378.
96. Ahimou, F.; Denis, F. A.; Touhami, A.; Dufrêne, Y. F., Probing Microbial Cell Surface Charges by Atomic Force Microscopy. *Langmuir* **2002,** *18* (25), 9937-9941.
97. Shin, M.; Ryu, J. H.; Park, J. P.; Kim, K.; Yang, J. W.; Lee, H., DNA/Tannic Acid Hybrid Gel Exhibiting Biodegradability, Extensibility, Tissue Adhesiveness, and Hemostatic Ability. *Advanced Functional Materials* **2015,** *25* (8), 1270-1278.
98. Hirano, S., Applications of chitin and chitosan in the ecological and environmental fields. In *Applications of chitin and chitosan*, CRC Press: 2020; pp 31-54.
99. Ge, Z.; Baguenard, S.; Lim, L. Y.; Wee, A.; Khor, E., Hydroxyapatite–chitin materials as potential tissue engineered bone substitutes. *Biomaterials* **2004,** *25* (6), 1049-1058.
100. He, M.; Wang, X.; Wang, Z.; Chen, L.; Lu, Y.; Zhang, X.; Li, M.; Liu, Z.; Zhang, Y.; Xia, H.; Zhang, L., Biocompatible and Biodegradable Bioplastics Constructed from Chitin via a "Green" Pathway for Bone Repair. *ACS Sustainable Chemistry & Engineering* **2017,** *5* (10), 9126-9135.
101. Thein-Han, W. W.; Misra, R. D. K., Biomimetic chitosan–nanohydroxyapatite composite scaffolds for bone tissue engineering. *Acta Biomaterialia* **2009,** *5* (4), 1182-1197.
102. Bandara, C. D.; Singh, S.; Afara, I. O.; Wolff, A.; Tesfamichael, T.; Ostrikov, K.; Oloyede, A., Bactericidal Effects of Natural Nanotopography of Dragonfly Wing on Escherichia coli. *ACS Applied Materials & Interfaces* **2017,** *9* (8), 6746-6760.

Muhammad Haseeb IQBAL

# Surface Engineering of Bio-based Polymeric Nanofilms for Biomedical Applications


## Résumé

Les propriétés de surface des biomatériaux agissent comme une première ligne de défense à l'interface cellule-biomatériau pour combattre les infections et favoriser la bio-intégration. Au cours de cette thèse, trois volets ont été abordés dans ce contexte. Dans la première partie, des films multicouches à base d'acide tannique et de collagène (TA/COL) ont été développés par la méthode couche-par-couche afin d'obtenir des films antibactériens. Construit à pH 4, le tampon utilisé a eu un impact non seulement sur les propriétés physico-chimiques mais aussi sur les propriétés antibactériennes. A contrario des films obtenus dans le tampon acétate de sodium, les films TA/COL obtenus dans le tampon citrate ont montré des propriétés antibactériennes envers les bactéries *Staphylococcus aureus* grâce à leurs topographies granulaires. Dans la deuxième partie, Les films TA/COL ont été développés en utilisant la méthode LbL pour obtenir l'orientation des fibres COL dans les films. La différenciation des myoblastes humains a été obtenue en seulement 12 jours de contact avec les films TA/COL orientés grâce à deux propriétés distinctes : l'orientation du COL qui aligne les myoblastes favorisant leur contact étroit et la libération de TA qui favorise la différenciation. Les fibres de collagène ainsi orientées peuvent être utilisées pour régénérer des tissus anisotropes. Dans la troisième partie, nous avons développé des films LbL ayant différentes nanotopographies avec des propriétés antiadhésives et antibactériennes de contact contre *Staphylococcus aureus* et *Escherichia coli*, empêchant également la formation de biofilms bactériens. Les caractéristiques nanotopographiques des films LbL chargées positivement appliquent probablement une force de cisaillement sur la membrane cellulaire, entraînant sa perforation.



## Résumé en anglais

The surface properties of biomaterials act as a first line of defense at cell-biomaterial interface to fight infections and promote bio-integration. Three biomedical aspects were addressed in this thesis. In the first part, tannic acid/collagen (TA/COL) layer-by-layer films were built at pH 4 using acetate or citrate buffer. The buffer used not only impacted the physico-chemical properties of the film but also its antibacterial properties. Thanks to the granular film topography obtained by using citrate buffer, TA/COL films showed a strong release-killing property towards *Staphylococcus aureus*. In the second part, TA/COL films were developed by using LbL method to obtain orientation of COL fibers in the films. The differentiation of human myoblasts was obtained in only 12 days of contact with the oriented TA/COL films, thanks to two distinct properties: COL orientation which aligns myoblasts favoring their close contact and TA release which favors their differentiation. On the developed oriented TA/COL LbL films, the powerful topography cues and the strong links between cells and the collagen can be used to mimic the complexity of *in vivo* conditions and design new model tissues to regenerate anisotropic tissues. In the third part, we reported the development of LbL films having different nanotopographies with antiadhesive and contact-killing properties against *Staphylococcus aureus* and *Escherichia coli*, preventing also bacterial biofilm formation. The positively charged nanotopographical features of the LbL films probably apply a shear force on the cell membrane leading to its puncture.